UiO : University of Oslo

Julie Denise Josette Héron

C-H Activation and CuAAC Reactions with 1,8-Naphthyridine Based Dicopper Complexes from a Computational Perspective

Thesis submitted for the degree of Philosophiae Doctor

Department of Chemistry

Faculty of Mathematics and Natural Sciences

2021

Series of dissertations submitted to the
Faculty of Mathematics and Natural Sciences, University of Oslo
No. 2459

ISSN 1501-7710

Cover: Hanne Baadsgaard Utigard.
Print production: Reprosentralen, University of Oslo.

Table of contents

Preface

This thesis is submitted in partial fulfilment of the requirements for the degree of Philosophiae Doctor at the University of Oslo. The research presented here was conducted at the Hylleraas Centre for Quantum Molecular Sciences, a centre of excellence funded by the Research Council of Norway. During my PhD, I was supervised by Dr. David Balcells, Dr. Ainara Nova and Prof. Mats Tilset. This work has been founded by the Research Council of Norway and by the Norwegian Supercomputing Program NOTUR.

Acknowledgements

I want like to acknowledge my supervisors; Dr. David Balcells, Dr. Ainara Nova and Prof. Mats Tilset; for their guidance and advices through my years at the CTCC and the Hylleraas Centre. I am also profoundly grateful to Prof. Odile Eisenstein and Prof. Mohamed Amedjkouh for our many scientific discussions. I must also thanks Prof. Trygve Helgaker and Jan Ingar Johnsen for welcoming me at the Centre and helping me settling down in Norway.

I would like to express my gratitude to my colleagues from the Hylleraas Centre and the Catalysis group: Lluís, Mahika, Abril, Glen, Jon, Mauritz, Isabelle, Sarah, Inga, Thibaud, Karolina and Jerome to name a few of them. Your moral support and friendship have been essential.

I also want to thanks Prof. T Don Tilley for our collaboration on this project and for welcoming me in his group for a research visit in May 2019.

I am profoundly grateful to my friends and family, both here in Oslo and back home in France, for their support and encouragements through this PhD.

List of papers

This is the list of articles concerning the work presented in this thesis. A copy of the published papers or a draft are available in the annexes.

1. Title: Unsymmetrical Naphthyridine-Based Dicopper (I) Complexes: Synthesis, Stability and Carbon-Hydrogen Bond Activations.
   Authors: Nicolay, Amelie; Héron, Julie; Shin, Chungkeun; Kuramarohit, Serene; Ziegler, Micah; Balcells, David; Tilley, T. Don.
   Organometallics 2021, 40, 12, 1866–1873
   DOI: 10.1021/acs.organomet.1c00188

2. Title: Concerted Cycloaddition Mechanism in the CuAAC Reaction Catalyzed by Naphthyridine Dicopper Complexes
   Authors: Héron, Julie; Balcells, David.
   Draft in the Annexes.

I - Introduction

1 - Naphthyridine based complexes

The synthesis and the use of bimetallic complexes in homogeneous catalysis has been under an increasing attention over the last decades. The close interaction between two metal centres can allow for a larger range of reactivity due to higher activity, selectivity or multi-electron transfer processes. The proximity between the metals can be enforced by either covalent bonding or by multidentate ligands. In nature, these effects are observed primarily in metalloenzymes in which the active sites comprise metals in close proximity to each other and with the surrounding environment (1st and 2nd coordination spheres). This yields an active site enabling otherwise challenging or inaccessible reactions. In regards to transferring these concepts to catalyst design, one type of metalloenzymes is particularly of interest: some enzymes incorporate a carboxylate ligand[1–4] (glutamic and aspartic amino acids) used as the template to coordinate two metals and therefore enforce their proximity without the necessity of a strong bond between them. The presence of a bridging ligand does not inhibit the flexibility at the active site as the carboxylate is small and the metals can be either in or out of the plane of the ligand, accommodating a large variety of positions while still being coordinated to the carboxylate. In these metalloenzymes, the distance between the metals varies from 2.5 to 4.4 Å.

To design bimetallic complexes in homogeneous catalysis, carboxylate-based ligands can be used as a template or any other molecule that share similar properties (distance between the coordinating atoms and allowing for flexibility). A popular option is the 1,8-naphthyridine ligand, an aromatic heterocyclic compound belonging to the diazanaphthalene class ($C_8H_6N_2$) and consisting of two pyridines fused (Figure I.1a). The distance between two nitrogens is 2.31 Å[5], allowing for a similar range of metal-metal distances as the carboxylate ligands. Metals can coordinate to a 1,8 naphthyridine in three ways: κN_1, $\kappa^2 N_1,N_8$ and $\mu\text{-}\kappa N_1{:}\kappa N_8$ but only the last one involves two metals (Figure I.1). The naphthyridines can be functionalized in the positions 2 and 7, adding new coordination sites and making the resulting complexes more

stable. The functionalization allows for differentiating the two coordination sites of the naphthyridine, defining which site coordinates to which metal in heterobimetallic complexes. In 1979, Evens and Caluwe published one of the first reports[6] on the synthesis of a series of functionalized 1,8 naphthyridines, including bpnp, which became a popular ligand in the following years (Figure I.2).

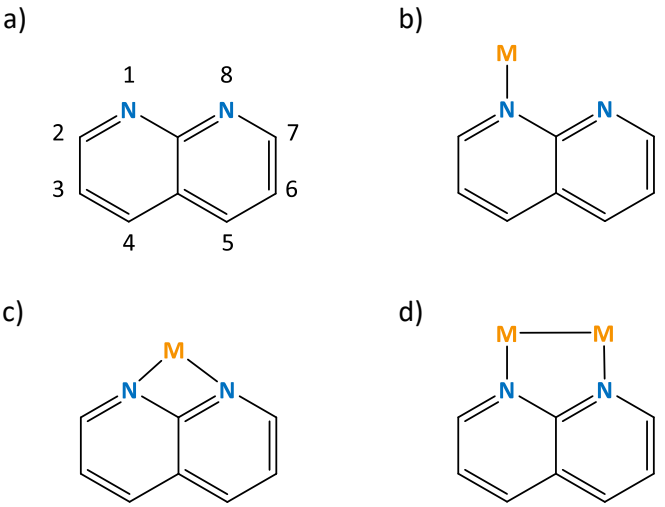

Figure I.1. a) Atom numeration in 1,8 naphthyridine and coordination modes to 1,8 naphthyridine by one or two metals: b) κN_1, c) $\kappa^2 N_1,N_8$ and d) μ-κN_1:κN_8.

1,8-naphthyridine was first used as ligand in the 1970's in coordination chemistry (Figure I.2). The goals were to synthesize either metal complexes with a high coordination number[7–9] (8 for Fe, Ni, Co, Cu, Zn or 12 for Pr) or bimetallic complexes with a large variety of metal ions[10–15] (Rh, Ru, Cu, Mo, Fe, Zn, Pd, etc…). The research focused on the synthesis and characterisation of these complexes. Two papers are especially worth mentioning. The first one is the work of Ford and Kasha[16–19] on the ligand exchange from acetate to naphthyridine, highlighting the similarities between the coordination of the metals to them and making a comparison to metalloenzymes (Figure I.2c). The second is the synthesis of the heterobimetallic Rh/Ni complexes by Balch,[20] which were the first ones to be published to my knowledge.

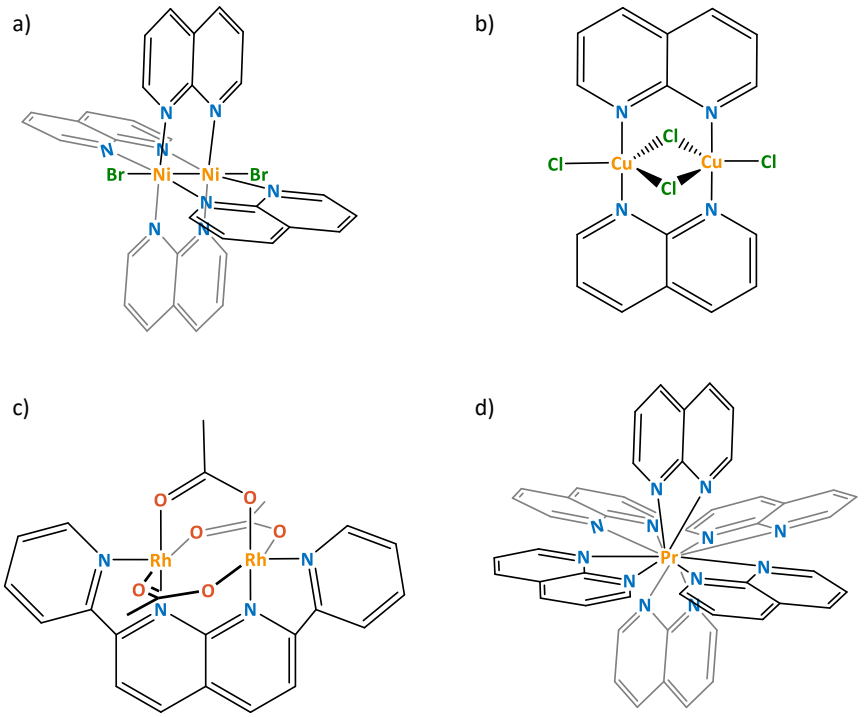

Figure I.2. Selection of 1,8-naphthyridine based complexes from the 1970's and 1980's: a) $[Ni_2(napy)_4Br_2]^+$ from Sacconi et *al.*,[13] b) $[Cu_2(napy)_2Cl_4]$ from Mealli et *al.*,[11] c) $[Rh_2(OAc)_3(bpnp)]^+$ from Tikkanen et *al.*[16] and d) $[Pr(napy)_6]^{3+}$ from Clearfield et *al.*[9]

A renewed interest in the naphthyridine based complexes started on the 2000's, with the focus shifting from their properties to their reactivity and catalytic abilities. The Lippard group[21–25] published one of the first examples of homogeneous catalysis for the transesterification of an RNA mimic by a Zn_2 complex (Figure I.3). The dinuclear catalyst was six times faster than the mononuclear one, highlighting the interest of multi-nuclear complexes as efficient catalysts.

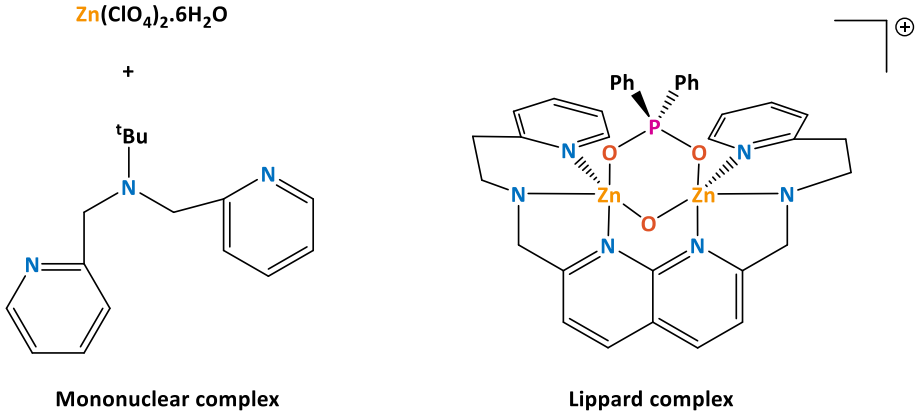

Figure I.3. Catalyst for the transesterification of an RNA mimic by Lippard.[24]

Several research groups specialized in the design of new ligands based on 1,8-naphthyridine and the reactivity of their corresponding complexes, including Uyeda, Bera, Broere and Tilley. A few examples from each group are described here, to give an overview of the state of the art. The main types of reactions done with these complexes are either cyclisations or C-H activations, which are those studied in this thesis. Other types of reactions[26–35] have also been published, like the dehydrogenation of alcohols into ketones[31] and the formation of imines.[30,32] The Uyeda group specialized in the cyclisation reaction: they synthesized dinickel complexes with a 1,8-naphthyridine ligand having imine substituents in positions 2 and 7. To complete the coordination sphere of the nickels, a benzene was introduced as a π-bridging ligand (Figure I.4a).[36] This specific complexes can promote a large variety of cyclisations[37–43] like alkyne cyclotrimerisation, [4+1] cycloaddition of diene, cyclopropanation and the Pauson-Khand reaction. The groups of Bera[44] and Tilley,[45] both published on the cyclisation of alkynes with azides catalysed by dicopper complexes (CuAAC reaction; Figure I.4b).

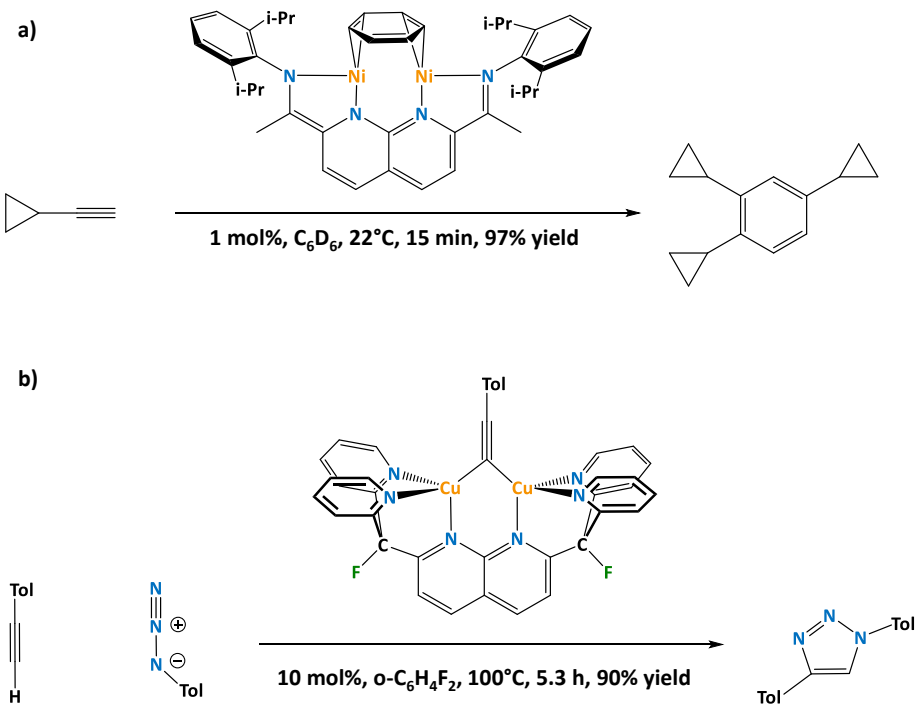

Figure I.4. Examples of cyclisation reactions with naphthyridine based catalysts: a) cyclotrimerisation of alkyne by Uyeda[38] and b) alkyne azide cycloaddition by Tilley.[45]

In naphthyridine complexes, the C-H reaction can occur on the naphthyridine ligand itself or on another reactant coordinated to the metal(s). In the former case, the Bera's group synthesized Ru and Pd complexes[46,47] in which the naphthyridine is substituted on one side only, with a phenyl or a heterocycle. This substituent can be deprotonated to become an additional coordination site to the metal (Figure I.5a). In another work by Broere's group,[48,49] the naphthyridine ligand can undergo a reversible deprotonation that can dearomatize the naphthyridine core (Figure I.5b). This deprotonation can happen on both sides of the ligand and can be done on the free ligand or on the corresponding dicopper complexes. The C-H activation of other molecules by naphthyridine complexes has been reported. The Tilley group reported copper complexes[45,50,51] (with di-pyridine substituents) promoting the proton transfer from an alkyne to a phenyl ligand and producing benzene and an alkynyl dicopper complex. Deolka et *al.*[52] reported a similar reaction done

with a Pt^{II}/Cu^{I} complex in which the 2 and 7 substituents of the naphthyridine were different (one acting as a hard coordinating ligand, and the other as a soft) to promote the selective coordination of the two metals. This system yielded also an alkynyl complex and the formation of methane. Isaac et al.[53] described the electrochemical activation of the sp^3 aliphatic C-H bond in toluene and acetonitrile by Cu^{II}/Cu^{III} complexes based on the ligand synthesized by the Tilley group. This reaction is done both in stoichiometric and catalytic fashions.

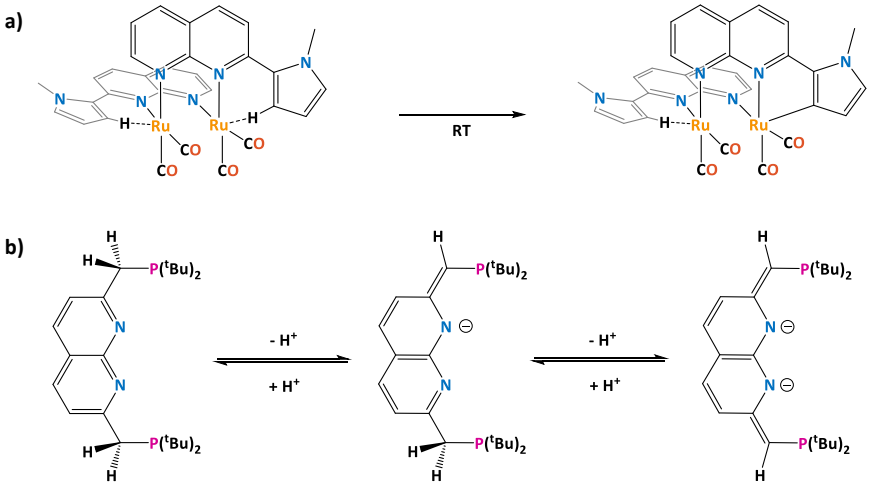

Figure I.5. Examples of C-H activation reactions a) on a substituent of the naphthyridine[46] and b) with the dearomatisation of the naphthyridine ring.[48]

2 - Activation of alkynes by copper complexes

The first organocopper ever reported was the copper alkynyl Cu_2C_2 (ethyne 1,2 diylcopper (I)) in 1859 by Böttger.[54] This complex is stable under wet conditions but highly explosive if dry. In the absence of any additional ligand, the copper alkynyl adopts a polymeric form,[55,56] which confers it a thermal and shock stability, contrary to the earlier complexes. In presence of a Lewis base (phosphine, carbine, amine, etc.), the polymeric structure breaks down into clusters, poly- and mononuclear complexes as the base coordinates to the coppers.

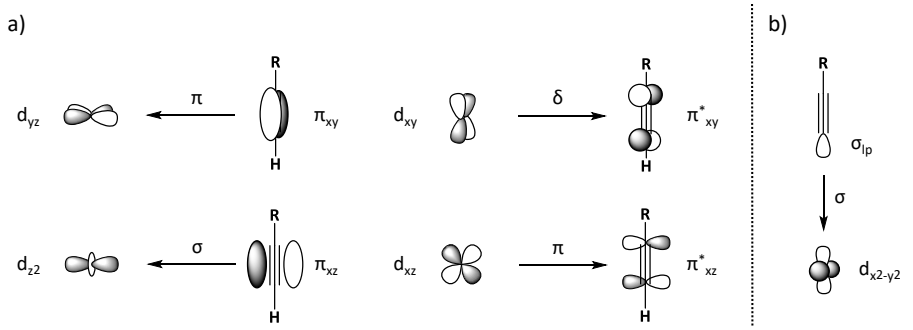

Figure I.6. Orbital type and interaction between a copper and a) an alkyne in η^2 coordination mode, b) an alkynyl in a κ^1 coordination mode.

In copper-alkyne complexes, the metal coordinates to the π-system of the alkyne (4-electrons π-donor), delocalizing the electron density between 3 centres (Cu and C≡C). The molecular orbitals of the alkyne involved in the donation to the metal are the π_{xy} and π_{xz} (Figure I.6). The coordination of the alkyne to the copper breaks its linearity, with the substituents at an angle up to 140° compared to the linearity of triple bond in the free alkyne. The alkyne is also a π-acceptor with its π^*_{xy} and π^*_{xz} orbitals. However, the Cu^I ion is a poor back-donor on its own but this ability can be increased with the presence of suitable ancillary ligands[57–60] (1,10-phenanthroline or β-diketimide, for example). The alkynyl ligand (deprotonated alkyne) coordinates mainly to the copper via its lone pair (2-electrons σ-donor) but its π-system can also be involved in back-donation and can coordinate to additional coppers centres. It is worth noticing that Cu^I has a d^{10} electronic configuration and thus the antibonding orbitals are partially filled, activating the C≡C bond. All these donor/acceptor combinations allows for a large variety of coordination modes in which the alkyne/alkynyl can be bonded to one or several coppers, allowing the formation of multi-metallic complexes and polymers. The figure I.7 shows a selection of different coordination modes.

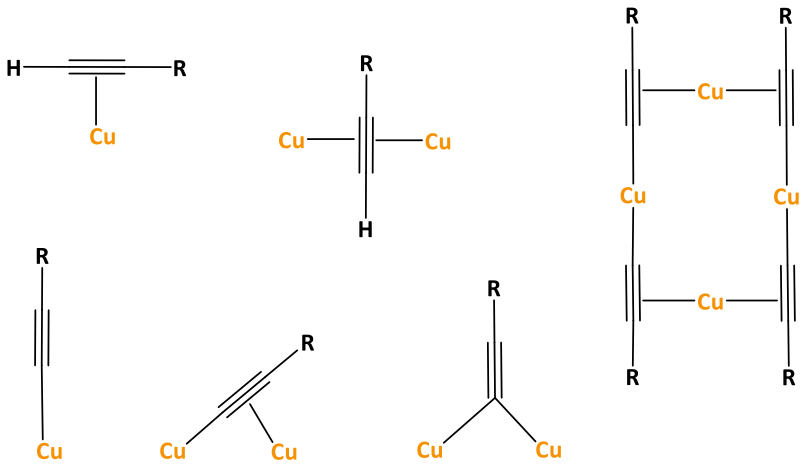

Figure I.7. Selection of coordination modes of alkyne and alkynyl to copper(s).

Copper-alkynyl complexes are involved in a large variety of reactions[61–64] from cross-couplings to propargylic substitutions (Figure I.8).[65] All these types of reactivity will not be describe here. Instead, the focus will be centred on the Glaser-Hay coupling and cycloadditions as they are the most relevant to this thesis.

The Glaser-Hay coupling is the name for the homocoupling reaction of two terminal alkynes (Figure I.9a). It was first discovered by Glaser in 1869 with the report of the synthesis of the 1,4 diphenyl 1,3 butadiyne.[66] In this coupling reaction O_2 is used as an oxidant reagent. The main drawback of Glaser reaction is that it was explosive. This problem was fixed by Hay in 1962 with the use of a bidentate ligand to stabilize the copper complexes.[67] The Glaser-Hay reaction[68–74] is a good example of a green reaction as it is done under mild reaction conditions, uses no hazardous nor toxic reagents and provides diynes in excellent yield with water as the only side product. As this reaction only need terminal alkynes in presence of copper (I), the Glaser-Hay reaction often yields side products in the other reactions shown in Figure I.8.

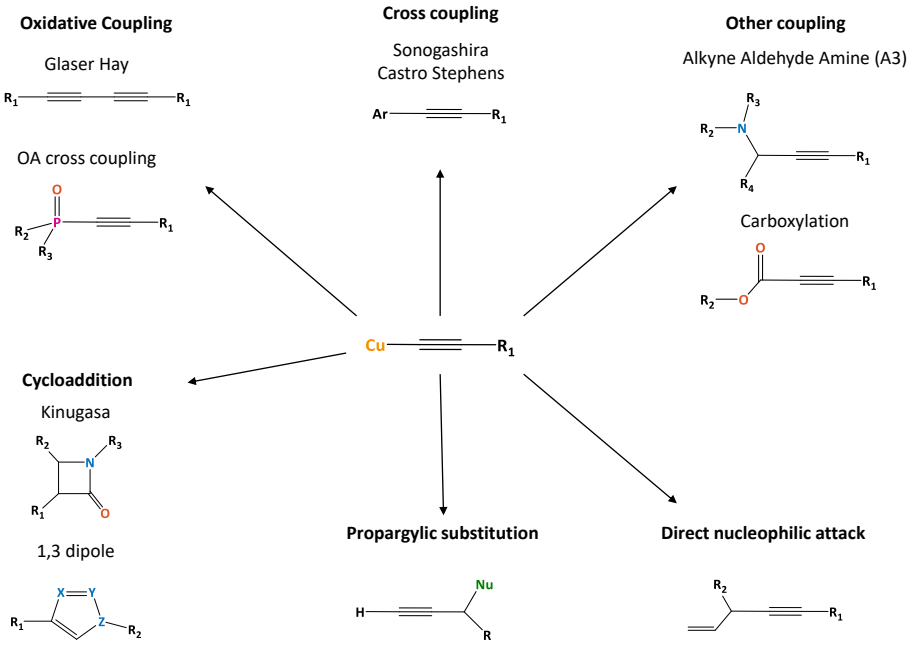

Figure I.8. Summary the reactivity of alkynes with copper complexes.

There are two main types of cycloadditions with alkynyl-copper complexes and they both involve 1,3 dipoles to form either 4-membered ring (Kinugasa reaction) or 5-membered ring products (Figure I.9b and c). The Kinugasa reaction[75] is the synthesis of 2-azetidione (also called β-lactam) from the cyclisation of nitrone with alkyne in the presence of copper (I). This reaction can be done at room temperature, uses accessible and stable reactants and the copper catalysis allows for better diastereoselectivity than the organic version of this reaction.[76–82] β-lactam are very common in pharmaceutical drugs like antibiotics (penicillin and its derivatives) and others used in the treatment of several diseases (cancer, AIDS, high cholesterol level, etc.). To synthesize these drugs a high level of selectivity is needed and the Kinugasa reaction is very important to reduce waste, excluding the formation of unwanted side products. The formation of 5-membered rings between a 1,3 dipole and an alkyne is very well known in the case of the azide (to form triazole) but other dipoles can be used, like oxine. This reactions provides

access to a large library of heterocycles. The specific case of the cyclisation with azide is discussed at length in the next section of the introduction.

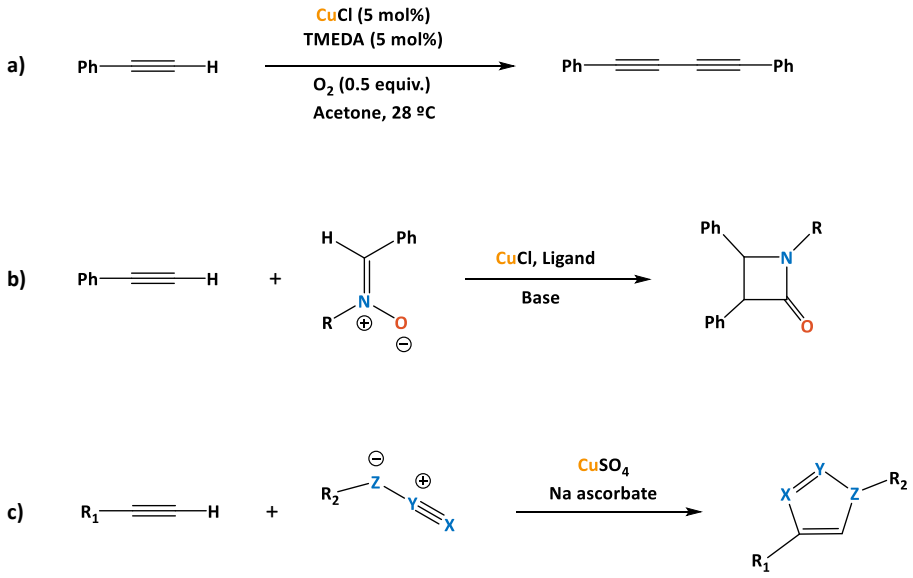

Figure I.9. Example of a) the Glaser-Hay reaction,[67] b) the Kinugasa reaction[76] and c) the formation of 5-membered rings from 1,3 dipoles.[63]

3 - Synthesis of 1,2,3 triazole and the CuAAC reaction

The earliest report of the synthesis of 1,2,3 triazole was published in 1893 by Michel.[83] It detailed the cyclisation of dimethyl acetylene dicarboxylate (DMAD) with phenyl azide (Figure I.10a) and mentioned the two isomers of the product. The electronic structure of both the reactant and the product seems questionable to modern eye as none of the usual characterization methods were available at the time. The reaction between an alkyne and a 1,3 dipole is a part of a type of reactions called the 1,3 dipolar cycloadditions[84–90] (also called the Huisgen reaction) and these reactions went under a huge development during the 1960's. This type of reaction enables the relatively easy synthesis of 5-membered heterocycles. It involved two different types of reactant: a 1,3 dipole (molecule with separation of charge over three atoms and π-delocalized electrons) and a dipolarophile (molecule containing a multiple bond). The 1,3 dipole participates in the reaction with

four π-electrons while the dipolarophile brings in two π-electrons. In the case of the synthesis of triazoles, the dipolarophile is an alkyne and the 1,3 dipole is an azide. The product of the resulting cycloaddition leads to two isomers: the 1,4 and the 1,5 triazoles (Figure I.10b).

Computational works to understand the mechanism of this reaction were published since 1963,[91] with the work of Polenski on the calculation of activation enthalpies. The current understanding of the mechanism[90,92,93] of the Huisgen reaction is as follows: in the vast majority of cases the cycloaddition occurs in one concerted step in which the two C-N bonds are formed. In some instance, a stepwise mechanism can be more favourable if the intermediate is extremely well stabilized by its substituents. Depending on the systems, the reactivity is either controlled by the distortion of the 1,3 dipole or by the orbital interactions between the HOMO of the 1,3 dipole and the LUMO of the dipolarophile.

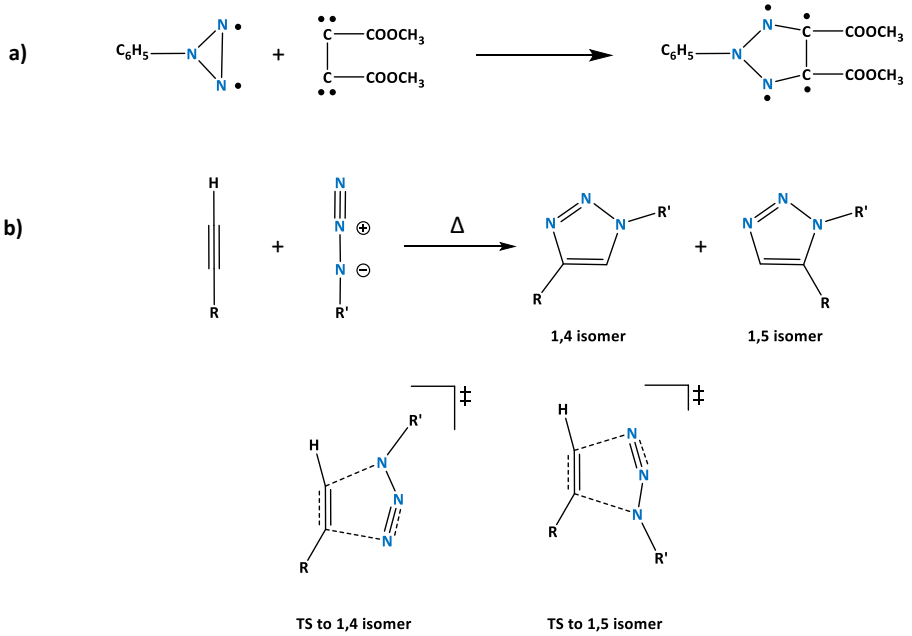

Figure I.10. Early attempt at 1,2,3 triazole synthesis by Michel[83] as written in 1893 (a) and Huisgen reaction[84] with the transition states (b).

The latest big improvement in the synthesis of triazole occurred in 2002 with the works of Medal[94] and Sharpless[95] (Figure I.11). They both reported the copper catalysed version of the 1,3 dipolar cycloaddition between alkyne and azide[96–101] (CuAAC for short). This reaction is one of the most relevant example of click chemistry.[102] This branch of organic synthesis focus on the development of reactions to link building blocks via cross-couplings, cycloadditions and other reactions leading to carbon-heteroatom bond. The term click chemistry refers to both the synthetic processes as well as the type of reactions. Indeed, a reaction has to fulfil several rigorous criteria to be regarded as click chemistry: high yield, high selectivity, wide scope, harmless by-products removable without chromatography, non-toxic reaction conditions and easily available reactants. The CuAAC reaction fits perfectly in this framework as the reaction produces selectively 1,4 triazole at very high yield (often > 95%) at room temperature. The reaction is very robust, supporting a wide pH range (4-12), a variety of solvents (from organic to pure water) and with a low catalyst loading (0.25-2 mol%). Side products[95,103–106] are rarely reported and almost any type of functional group is tolerated on both the azide and alkyne. The catalyst for this reaction is usually Cu^{II} salts in presence of sodium ascorbate to produce the Cu^{I} active species. Cu^{I} salts are less often used as catalyst as they are more easily poisoned by disproportionation.

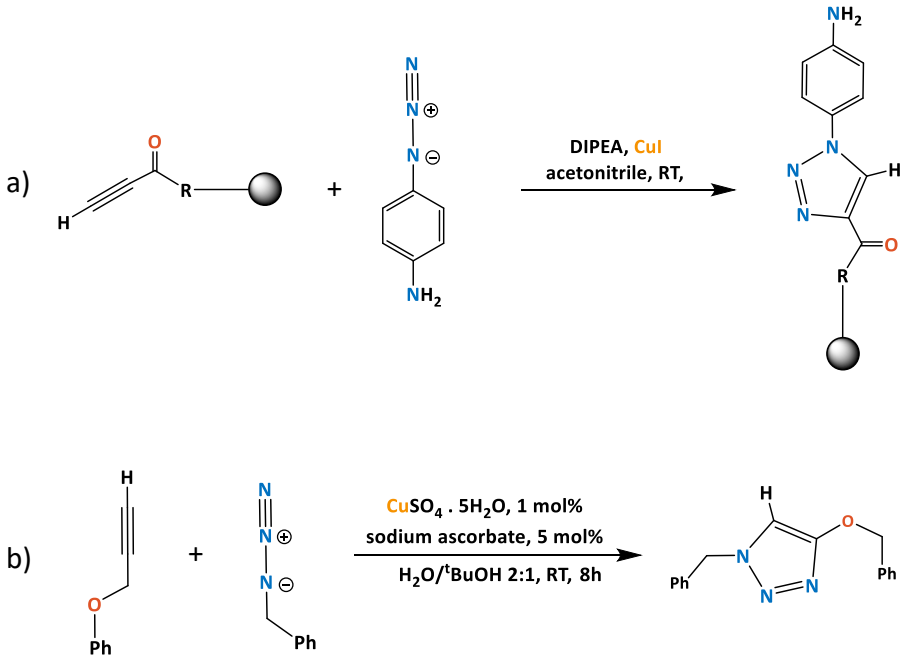

Figure I.11. CuAAC reaction as first reported by a) Medal[94] and b) Sharpless.[95]

The CuAAC reaction is very efficient but it is not the only procedure to selectively synthesize 1,4 triazoles: Ag,[107,108] Ru[109] complexes, heterogeneous Zn/C, Au(111) and Raney-Ni catalysts have been also reported. If these reactions are less efficient than the CuAAC, most of them do not need to undergo a catalyst activation like the Cu^{II} salt does (reduction to Cu^{I}). The CuAAC reaction has two main limitations: 1) it can only work for terminal alkynes as the mechanism requires their deprotonation and 2) the 1,5 triazole isomer cannot be synthesized due to the larger distortions the reactants have to overcome to be aligned in the transition state compared to the one leading to the 1,4 triazole. To tackle these issues, other metal-based catalysts[110] were develop over the last 20 years. To synthesize the 1,5 isomer of the 1,2,3 triazole, several complexes have been already developed based on Ru, Zn and some lanthanides.[111] The catalysed cyclisation of internal alkynes is possible with Ir[112] and Ru complexes, leading to 1,4,5 trisubstituted 1,2,3 triazole. The Figure I.12 regroups a selection of these catalysts for the MAAC reaction (Metal catalysed Alkyne Azide Cycloaddition).

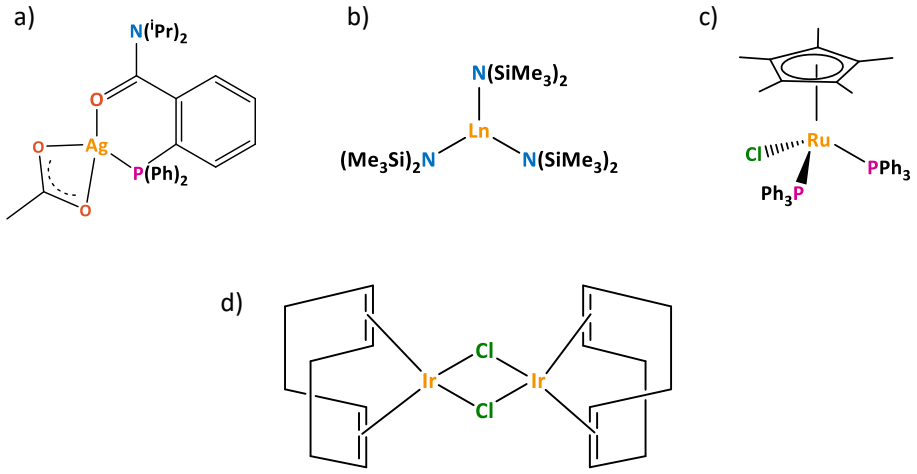

Figure I.12. Example of catalyst for the MAAC for 1,4 triazole synthesis[108] (a); for 1,5 triazoles synthesis[109,111,113] (b and c) and for 1,4,5 triazoles synthesis from internal alkynes[112] (d).

The CuAAC reaction is typically done using Cu^{II} salts that are first reduced to Cu^{I} before entering the catalytic process. The reduction can occur via the addition of a reducing agent (like sodium ascorbate) or via the Glaser-Hay homocoupling of alkynes. UV and EPR results[114] support the reduction of Cu^{II} into Cu^{I} during the induction period of the CuAAC reaction. The mechanism of the CuAAC reaction was first supposed to be monomeric[95,115] *i.e.* only one Cu^{I} centre is involved in the active species of the catalytic cycle. This mechanism involves four steps and is shown in the Figure I.13. It starts with an alkynyl Cu^{I} complex, formed during the catalyst activation. The first step consists of the coordination of the azide to the complex, followed by the formation of the first C-N bond leading to a 6-membered metallacycle. The second C-N bond is created by reductive elimination forming a copper-triazolyl intermediate.[116] The 1,4 triazole product is released after a proton transfer with the alkyne, regenerating the copper alkynyl complex. The cyclisation of the azide with the alkynyl occurs in a stepwise manner, contrarily to the Huisgen reaction in which it is concerted, and this mechanism is supported by a computational study.[115] However, Quirante et al.[117] nuances that concerted vs stepwise cyclisation preference: it depends of the ability of the system to stabilize the metallacycle intermediates. Thus, the preferred pathway depends on the

nature of the substituent of the alkyne and the azide as well as of the reaction conditions. This work also examined the causes of the observed regioselectivity: there is a 12.4 kcal/mol difference between the transition states for the 1,4 and 1,5 isomers, explaining the exclusive synthesis of the former. The transition state of the 1,5 cyclisation is higher in energy due to the higher distortion needed to align the atoms and to the arrangment of the charges of the carbons and nitrogens that are less ideal than for the 1,4 cyclisation.

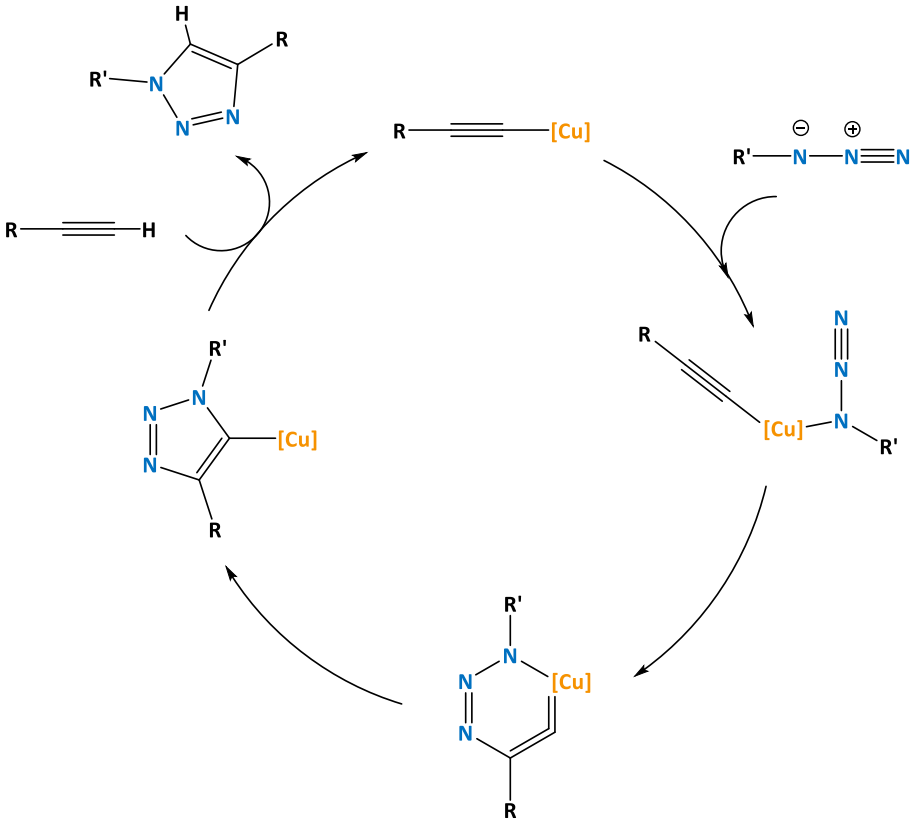

Figure I.13. Catalytic cycle of the CuAAC reaction with a mononuclear catalyst.

However, the number of coppers involved in the reaction started to be questioned in 2005, with the publication of a kinetic study[118] showing a second order in copper, *i.e.* the active species in the catalytic cycle involve more than one copper centre. As copper salts are usually used as catalyst with

the addition of some ligand, a large variety of nuclearities are potentially accessible in solution, from mononuclear complexes to clusters. The bimetallic nature of the active species was corroborated by a computational study in 2007[119] that compared the energy of the cyclisation step for the CuAAC reaction with mono, di(σ,σ), di(σ,π) and tetra-copper alkynyl complexes. The lowest barrier is given by di(σ,σ) alkynyl complex. Since then, several computational[120–126] papers arrived at the same conclusion that dicopper species are more active than their monocopper equivalent and therefore are the actual active species. Monocopper complexes can still be formed and/or be the resting state[127] of the reaction but their participation to the production of the 1,4 triazole is minimal. The bimetallic character of the catalyst for the CuAAC reaction was further established via diverse experimental methods:[127–133] ESI-MS, isotope exchange, kinetic studies and characterization of intermediates. The CuAAC reaction has also been done with well defined dicopper complexes based on naphthyridine ligand, showing that the reaction can work properly and efficiently with a dicopper active site.

The mechanism with dicopper active species is shown in Figure I.14. The mechanism is not very different from the mononuclear ones: it also starts with an alkynyl Cu^{I} complex and another copper complex coordinates to the alkynyl to further active it, either to its π-system or in a σ mode. Then, the azide coordinates to the dicopper and the formation of the first C-N bond leads to a 6-membered metallacycle. The triazolyl intermediate is formed by the creation of the second C-N bond and the dissociation of one of the coppers. A proton transfer from the alkyne to the triazolyl allows the regeneration of the alkynyl Cu^{I} complex and the release of the 1,4 triazole product. Due to the flexibility of the system, the exact geometries of the active species can vary depending on the ligands and the reaction conditions but the general steps remain the same. As for the mononuclear catalyst, the cyclisation happens in two steps instead of a concerted one like in the Huisgen reaction. The rate determining step depends on the reaction conditions. Turzun and al.[134] showed that in aprotic conditions, the proton transfer from the alkyne to the triazolyl complex happen in one concerted step and is the RDS. But in protic conditions, the deprotonation of the alkyne and the protonation of the

triazolyl are decoupled in two different steps and their respective transition states are stabilized compared to the concerted one. Thus, in the whole cycle, there is three transition states (deprotonation, cyclisation, protonation) with similar energies and therefore the RDS can vary easily depending on specific reaction conditions and on the environment around the coppers.

Overall, the CuAAC reaction mechanism is extremely flexible but the fundamental nature of the catalytic cycle remains unchanged. It is the composition and geometry of the active species that vary significantly, adapting to the reactants and reaction conditions. The efficiency and robustness of this reaction arise from its adaptive behaviour.

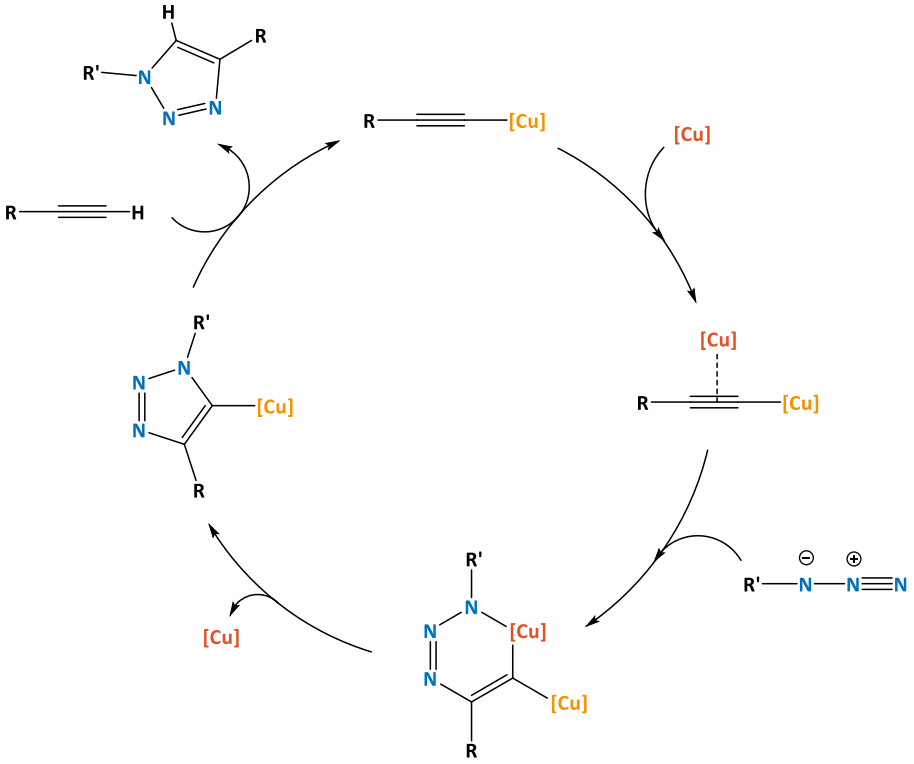

Figure I.14. Catalytic cycle of the CuAAC reaction with a dinuclear catalyst.

To be active, the CuAAC catalyst needs to contain a Cu^{I} centre but if not stabilized enough, it can deactivate easily. The poisoning of the catalyst is

usually due to an oxidation back to Cu^{II} or a disproportionation of two Cu^{I} into Cu^{II} and Cu^{0}. The use of ligand for stabilizing Cu^{I} is a way to prevent the poisoning of the catalyst and to make it more efficient (Figure I.15). The cheapest ligand for the CuAAC reaction is the acetate ion.[114,129,135,136] It provides a template for the coordination of two coppers in close proximity (2.64 Å in $[Cu^{II}_2(C_2H_3O_2)_4]\cdot 12H_20$), increasing the efficiency of the catalyst as two coppers are needed in the active species. Several attempts were made to use other ligands that can chelate two coppers (1,8 naphthyridine or di-NHC ligands). Another common type of ligand for the CuAAC reaction is the polyamine/heterocycle ones[137–141] which despite being polydentate seem to coordinate to one copper only. These ligands have large sizes but they are often flexible enough to preserve the ability of the catalyst to adapt to specific reactants and reaction conditions. The third most common type of ligand is the heterocyclic carbene (NHC),[116,127,130,131,142–144] which provided some of the most efficient CuAAC catalysts (high yields at room temperature with catalyst loading of 75 ppm in 6 hours[143]). Other types of ligand like phosphine[132,133,145], thioester[146] and pincer based on pyridine[147] or naphthyridine[44] can also be used even if less commonly. The reactant can compete with the ligand for the coordination to the metal centre. Thus, there is a need for a balance between stabilizing the catalyst promoting the CuAAC reaction and poisoning it by creating very stable but unreactive complexes or bulky species in which the active site is blocked.

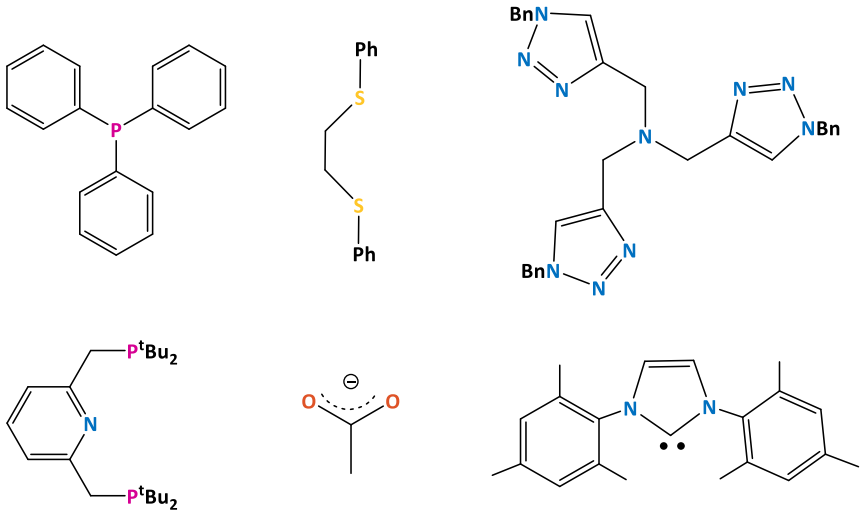

Figure I.15. Example of ligands for the CuAAC reaction.

4- Outline of this thesis

This thesis describes the computational investigations done on Cu^I/Cu^I DPEOPN complexes (Figure I.16). These systems are challenging as the mechanisms of the reactions presented here are very complex due to the flexibility of the coordination environment of the coppers, the presence of a counter-ion and the asymmetric nature of the DPEOPN ligand. The goal of this thesis is to take a deep look into these factors and their influence on the properties and the reactivity of these complexes. After introducing the chemistry of these metal complexes in the Chapter I, Chapter II provides a summary of the computational details, including benchmarks. Chapter III reports the properties of the complexes $\mathbf{1}^+$ and $\mathbf{2}^+$ ($[Cu_2(DPEOPN)(\mu\text{-}Ph)]^+$ and $[Cu_2(DPEOPN)(\mu\text{-}CC(\rho\text{-}CF_3\text{-}C_6H_4)]^+$, respectively). Chapter IV focuses on the mechanism of C-H activation of alkyne by $\mathbf{1}^+$ (Figure I.16a) and Chapter V covers the water catalysis of this reaction. Chapter VI describes the mechanism of the CuAAC reaction using $\mathbf{2}^+$ as catalyst (Figure I.16b). Finally, Chapter VII discusses on the design of new complexes based on the DPEOPN ligand to improve the C-H activation of alkynes by $\mathbf{1}^+$.

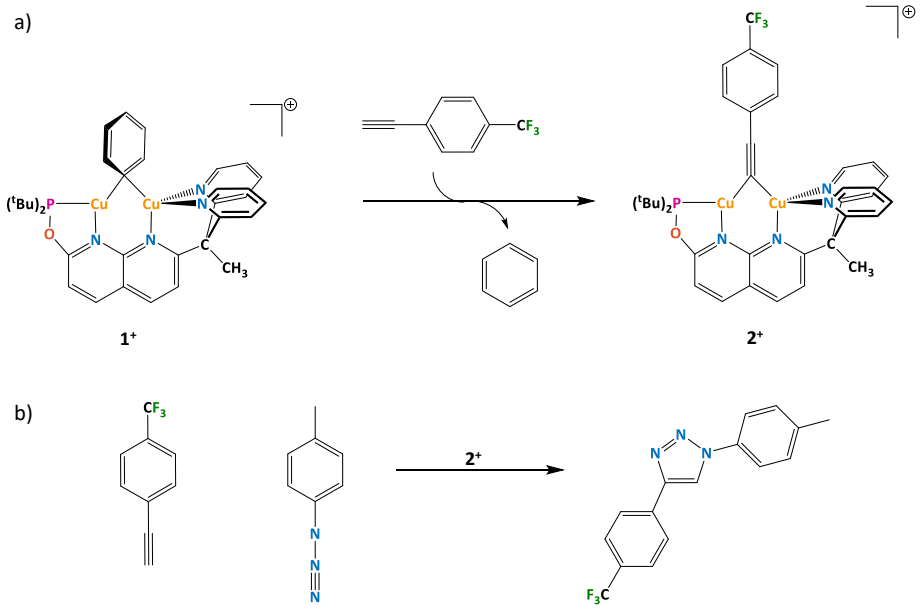

Figure I.16. The main reactions described in this thesis: a) C-H activation of alkynes by 1^+ and b) CuAAC reaction catalyzed by 2^+.

Part of the work reported in this thesis is the results of a collaboration with the Tilley group (UC Berkeley). Over the last decade, this group has published several articles[45,50,51,148–152] on 1,8-naphthyridine complexes, mostly involving copper (Cu^I/Cu^I or Cu^I/Cu^{II}, Cu^I/M^{II} with M = Mn, Fe, Co, Ni and Zn). They developed two main ligand types (Figure I.17): one with the same dipyridine substituents[148,150] (later referred as "arms" in this thesis) on positions 2 and 7 (DPFN and DPEN) and one with a phosphine and a dipyridine substituents[152,153] on the same positions (DPEOPN). The study of the reactivity of these complexes focuses on the C-H activation of alkynes or pentafluorobenzene[45,50,51] and on the CuAAC reaction.[45] The purpose of this collaboration was to achieve a better understanding of the properties and the reactivity of dicopper complexes based on 1,8-naphthyridine. In particular, Chapters III and IV describe the work done for our join publication of June 2021 (see article 1 in the annexes).

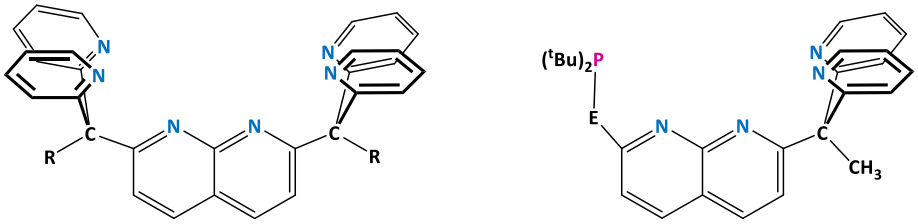

R = Me (DPEN)
R = F (DPFN)

E = O (DPEOPN)
E = CH_2 (DPEPN)

Figure I.17. 1,8-naphthyridine based ligands from the Tilley group.

II - Computational details

The methods used in this thesis will not to be explained here. Theoretical and technical details can be found in the literature for DFT,[154–156] solvation models[157] and microkinetics modelling.[158,159] This chapter focuses on the benchmarks realized to choose the DFT functional and a short overview of the methods used to carry out the calculations.

1 - Benchmark

At the beginning of this project, a benchmark was carried out to choose an appropriate DFT functional. A pool of seven different functionals[160–168] (B3LYP+GD3, BMK+GD3, CAM-B3LYP+GD3, M06+GD3, MN15, PBE0+GD3, and TPSSh) was used to compute the geometry and the energies of $\mathbf{1}^{+}$ and $\mathbf{2}^{+}$. For all functionals, the geometry of $\mathbf{1}^{+}$ and $\mathbf{2}^{+}$ were optimized in gas phase and compared to their X-Ray crystal structure. The quality of the DFT geometries was assessed by considering the distances between the two metals and between the metals and the ligands (Figure II.1). For both complexes, TPSSh and PBE0+GD3 give the lowest values for the root mean square deviation (RMSD) and thus were kept for the second part of the benchmark.

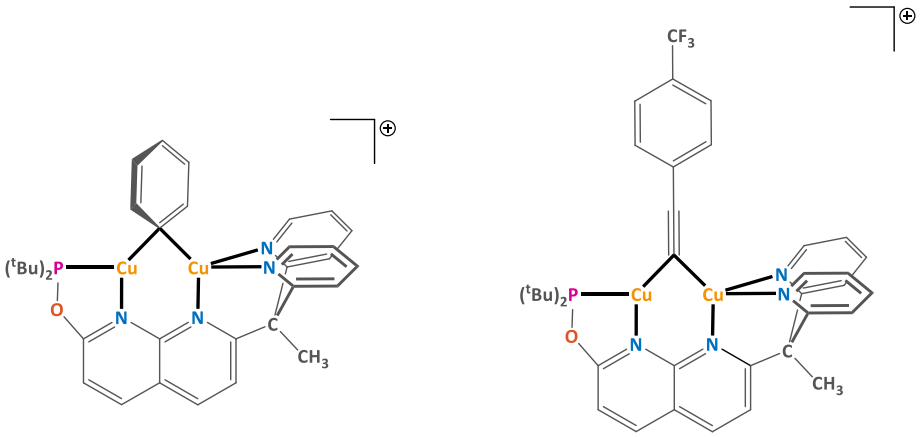

Functional	RMSD	MaxDev
B3LYP	0.056	0.086
BMK	0.084	0.163
CAM-B3LYP	0.038	0.077
M06	0.054	0.083
MN15	0.036	0.058
PBE0	0.029	0.065
TPSSh	0.021	0.047

Functional	RMSD	MaxDev
B3LYP	0.045	0.088
BMK	0.167	0.088
CAM-B3LYP	0.034	0.069
M06	0.036	0.072
MN15	0.085	0.195
PBE0	0.025	0.052
TPSSh	0.030	0.057

Figure II.1. Key distances (in bold black) selected to calculate RMSD and the maximum deviation (MaxDev) of the bonds in bold black in 1^+ (left) and 2^+ (right) for the different functionals.

In order to evaluate the functionals performance for energy barrier estimation, several energy profiles were computed with TPSSh and PBE0+GD3. In all cases, PBE0+GD3 yielded lower $\Delta G^{\ddagger}$ barriers than TPSSh. For example, the barrier is 6.6 kcal/mol lower in the case of the C-H activation of alkyne (Figure II.2). TPSSh always yields to energy barriers that are too high to be plausible under the experimental reaction conditions. This is likely due to the different description of dispersion forces in each case. The PBE0 functional does not account for dispersion therefore the Grimme dispersion correction GD3[169] was used in all calculations. The TPSSh functional was formulated to describe both strong and weak interactions. Thus, it accounts for non-

covalent interactions to some extent. Nevertheless the GD3 corrections was also develop for TPSSh and thus was tested on the pathway for the same reaction as PBE0+GD3 and TPSSh (Figure II.2). The barrier decreases by 8.0 kcal/mol relative to TPSSh, showing the dramatic importance of dispersion in this system. However, the calculation of the frequencies at the TPSSh+GD3 level failed in the Gaussian release used to perform this work. Thus, the thermal corrections cannot be computed with the GD3 correction, yielding unreliable the energies. Therefore, the PBE0+GD3 functional was used for all the calculations in this project.

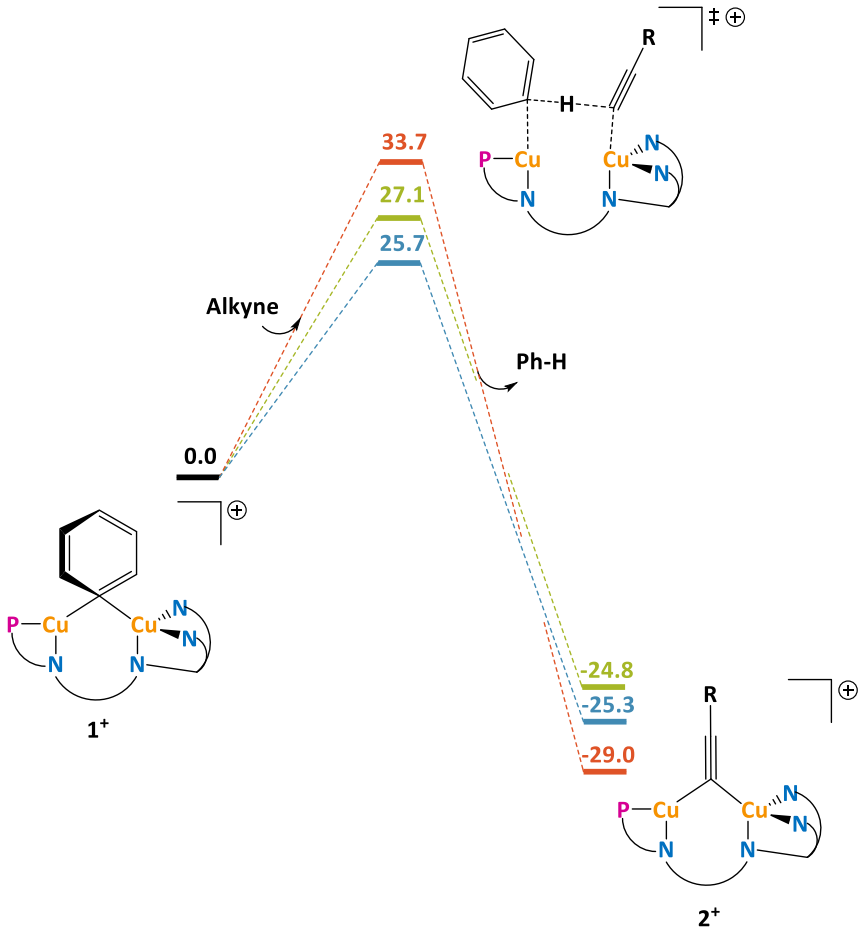

Figure II.2. Energy comparison between PBE0+GD3 (green), TPSSh (red) and TPSSh+GD3 (blue) for the C-H activation of alkyne by 1^+.

2 - Methods

DFT calculations were carried out with the hybrid PBE0 GGA functional,[166] as implemented in the Gaussian 16 software package.[170] The Grimme dispersion model GD3[169] was used to correct the PBE0 functional. Two different basis sets,[171] one of double-ζ quality (def2SVP) and one of triple-ζ quality (def2TZVP), were used. All the structures were fully optimized without any geometry or symmetry constraint with the def2SVP basis set. Frequency calculations were also carried out with the same basis set, to confirm the energy-minimum nature of all stationary points (*i.e.* all-real frequencies) and to estimate the thermal corrections at 298.15K (E_T, including zero-point, thermal and entropy energies). A selection of transition states were relaxed with IRC calculations to verify that they belong to the reaction pathway connecting **1**$^+$ to **2**$^+$. The potential energy of the optimized geometries was refined by means of single-point calculations with the def2TZVP basis set (E). The ultrafine (99,590) pruned grid was used for higher accuracy in the computation of the two-electron integrals. When not specified, the calculations were performed in THF (CPCM continuum model).[172,173] Orbital analysis and spin densities were obtained from natural population analysis with the NBO7 software.[174] The calculations were done using the def2TZVP basis set. The free energies reported in the manuscript (G) were obtained by adding the thermal corrections to the refined potential energies as show in Eq. 1 and corrected to the 1M standard state.

$$G = E + E_T \qquad \textbf{Eq1}$$

Microkinetic models were constructed with the COPASI software (version 4.24).[175] Association reactions were assumed to have low Gibbs energy barriers ($\Delta G^{\ddagger} \leq 5$ kcal mol^{-1}), thus having no impact on the global kinetics of the reaction. The initial concentrations used in the simulations were those reported in experimentally and are detailed in the corresponding sections of this thesis. The model was simulated at 1 atm and 48.5 ºC in accordance with the experimental conditions. The rate equations were solved using deterministic time course simulations with the LSODA algorithm. The elementary steps of the mechanism underlying the microkinetic models are

given in later sections of this thesis, together with the $\Delta G^{\ddagger}$ values derived from the DFT calculations. The model was optimized with the Hooke & Jeeves algorithm to fit the experimental values.

III - Properties of the DPEOPN based complexes

In this chapter, the focus has been emphasized on the properties of the complexes **1**$^+$ and **2**$^+$. As it will become evident in latter chapters, several properties of these complexes have a large impact on reactivity and are therefore essential to describe. To ease the description of the complexes and their analysis, the key atoms have been labelled as shown in Figure III.1. These labels do not change depending on the presence of additional molecules (counter-ion or solvent molecule).

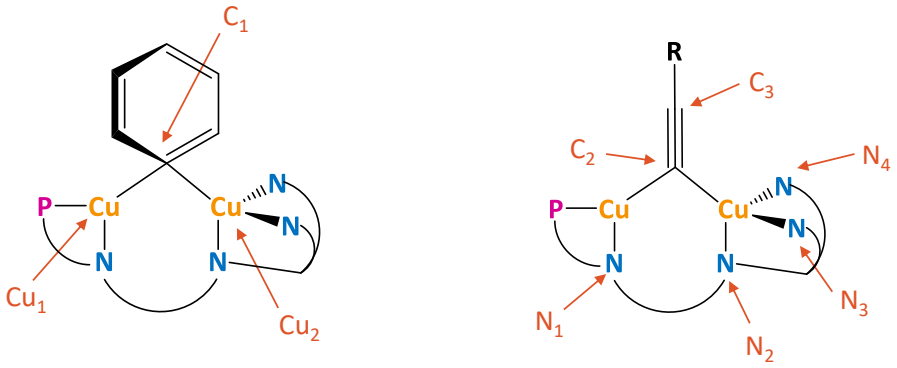

Figure III.1. Labels of the key atoms in the complexes 1$^+$ and 2$^+$.

1 - Coordination modes of the alkynyl ligand

Experimentally, two coordination modes of the alkynyl ligands are observed in the crystal structures[153] (Figure III.2). In **2**$^+$, the bridging ligand, μ-CC(*p*-CF_3-C_6H_4), is coordinated symmetrically to the coppers in a σ,σ mode. Conversely, the bridging alkynyl group in **3**$^+$ ([Cu_2(DPEOPN)(μ-CC(*p*-CH_3-C_6H_4))]$^+$) is coordinated asymmetrically to the coppers in a σ,π mode.

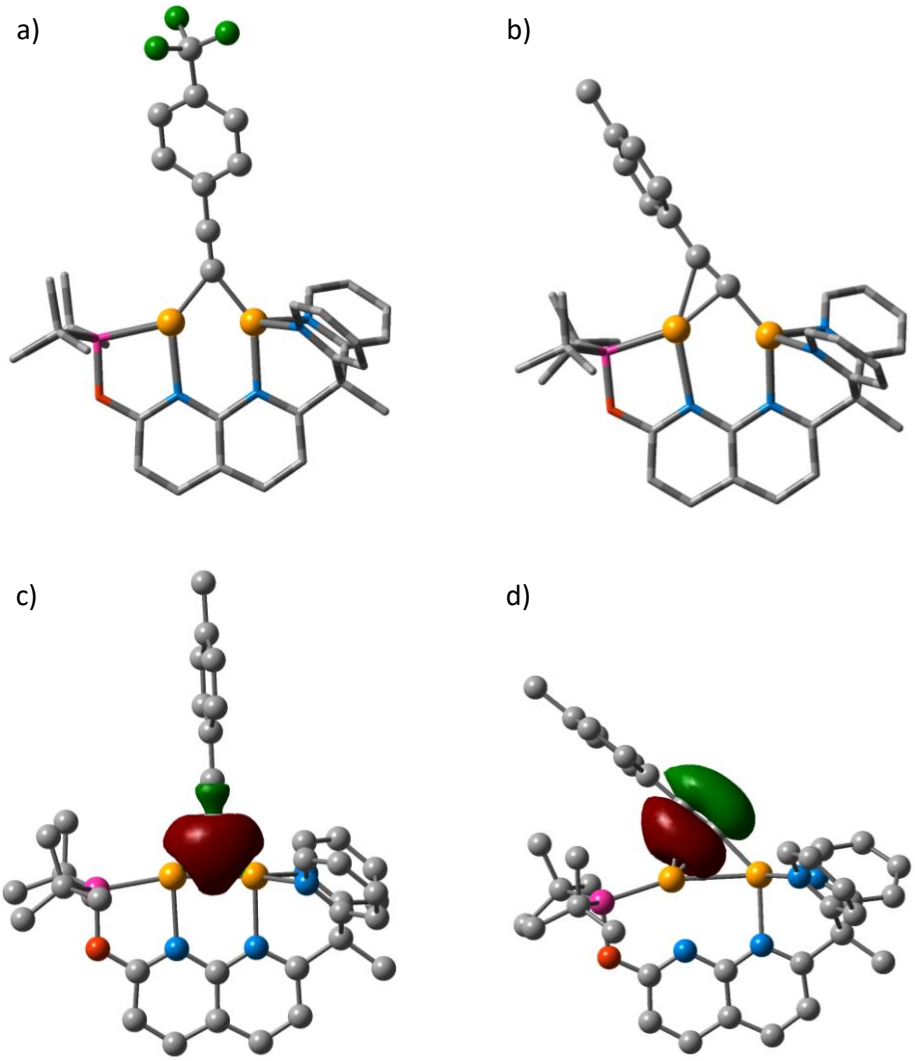

Figure III.2. Two coordination modes of the alkynyl: a) σ,σ in 2^+ and b) σ,π in 3^+ and the NLMOs involved in the coordination of the alkynyl: c) lone pair of C_2 in $3^+_{\sigma,\sigma}$ and d) π_{xy} orbital of the triple bond between C_2 and C_3 in $3^+_{\sigma,\pi}$.

To assess the origin of this difference, both coordination modes were computed for $\mathbf{2}^+$ and $\mathbf{3}^+$, in gas phase and in THF (Table III.1). In all cases, the σ,σ binding mode is more stable than the σ,π, though by small energy differences within the 1.6-2.7 kcal/mol range. Thus, the σ,π coordination mode observed in $\mathbf{3}^+$ is likely due to packing effects in the crystal structure,

which are not taken into account in our DFT model. Further experimental ^{1}H NMR data confirm this explanation as the σ,σ binding mode of the alkynyl is the only one observed for both **2**$^+$ and **3**$^+$ in solution.

Complexes	Gas phase	THF
2$^+_{σ,σ}$	0.0	0.0
2$^+_{σ,π}$	2.1	2.7
3$^+_{σ,σ}$	0.0	0.0
3$^+_{σ,π}$	1.7	1.6

Table III.1. Relative free energies of 2$^+$ and 3$^+$ with the σ,σ and σ,π coordination modes. All the energies are in kcal/mol.

A NBO analysis on **3**$^+_{σ,σ}$ and **3**$^+_{σ,π}$ gives more details about their coordination modes and about the different orbitals involved. In **3**$^+_{σ,σ}$, the alkynyl coordinates to the coppers by its lone pair (Figure III.2c) with similar interaction strengths: 49.6 and 53.1 kcal/mol for Cu_1 and Cu_2, respectively. In **3**$^+_{σ,π}$, the lone pair of the alkynyl also interacts with both coppers but the interaction is stronger with Cu_2 (68.9 kcal/mol) than with Cu_1 (16.5 kcal/mol). In addition to the lone pair, the $π_{xy}$ orbital of the triple bond (Figure III.2d) coordinates to Cu_1 (23.6 kcal/mol). This interaction is occurring due the bending of the alkynyl toward Cu_1, reducing the distance with the carbons to 2.01 and 2.28 Å for C_2 and C_3, respectively.

2 - Coordination of a THF molecule

Another properties worth checking before investigating any reactivity is the ability of a THF molecule to coordinate to **1**$^+$ and **2**$^+$, leading to **1**$^+_{THF}$and **2**$^+_{THF}$. The energy of the association between a THF molecule and the complexes was computed. In the case of **1**$^+$, THF do not coordinate to the copper as there is steric hindrance between the solvent molecule and the phenyl ligand (Figure III.3). For **2**$^+$, the THF molecule can coordinate to Cu_1 (2.17 Å), the least sterically crowded copper. The association is thermoneutral with a ΔG of 0.5 kcal/mol. In the rest of this work, the assumption made is that the solvent do not coordinate to the complexes if not explicitly stated and THF is only modelled implicitly.

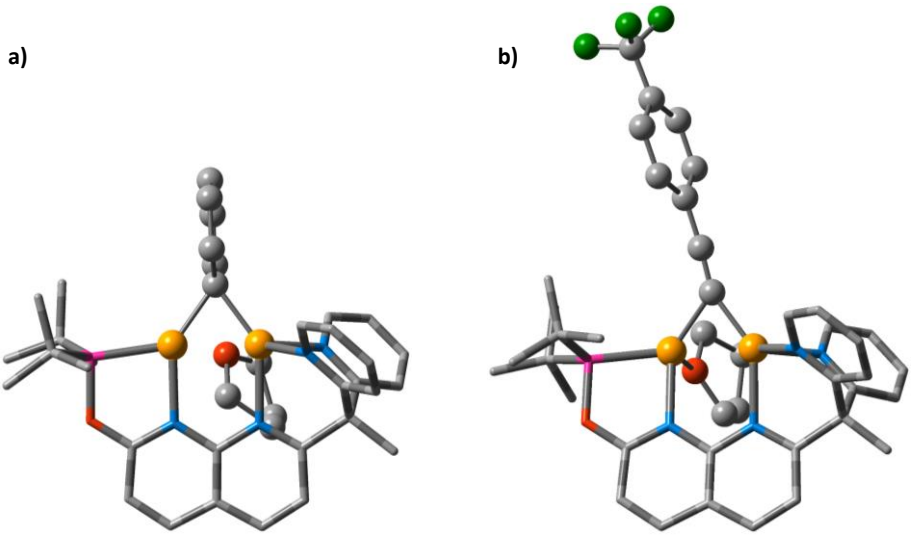

Figure III.3. 3D representation of a) 1^{+}_{THF} and b) 2^{+}_{THF}.

3 - Partial dissociation of DPEOPN

DPEOPN is a polydentate ligand κ^5 that can partially dissociate from the two coppers. The dissociation could lead to more space in the active site and/or create new favourable interactions with potential reactants. Thus, the thermodynamics of three partial dissociations have been considered (Figure III.4) to assess if they are easily accessible under experimental conditions. These dissociations are done by a rotation of the following bonds:

- O-naphthyridine
- C_{sp3}-naphthyridine
- C_{sp3}-pyridine

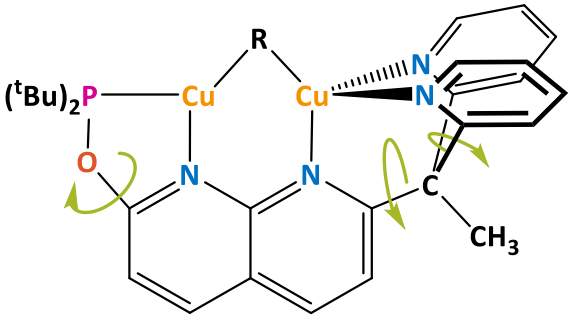

Figure III.4. The three partial dissociations of DPEOPN considered for 1^+ and 2^+, R = Ph or CC(*p*-CF_3-C_6H_4).

All the partial dissociations of $\mathbf{1}^+$ and $\mathbf{2}^+$ are accessible and the same trends are observed for both complexes (Figure III.5 and III.6). The highest intermediates are the ones with the phosphine dissociated ($\mathbf{1}^+_{phos}$ and $\mathbf{2}^+_{phos}$) with energies above 15 kcal/mol compared to the fully coordinated complexes. The dissociation of the pyridines arm ($\mathbf{1}^+_{arm}$ and $\mathbf{2}^+_{arm}$) is more favourable, with energies between 10 and 15 kcal/mol. The most favourable dissociation is caused by the rotation of one of the pyridines ($\mathbf{1}^+_{pyr}$ and $\mathbf{2}^+_{pyr}$), which is close to thermoneutrality for $\mathbf{2}^+$ and slightly exergonic for $\mathbf{1}^+$. The partial dissociation of DPEOPN introduce geometrical modifications: in $\mathbf{X}_{phos}$ and $\mathbf{X}_{arm}$ (where X stands for $\mathbf{1}^+$ or $\mathbf{2}^+$), the remaining bonds are shortened for the copper centre undergoing dissociation, whereas the bonds involving the other copper are weakened. No significant geometry changes are observed in the $\mathbf{X}^+_{pyr}$ complexes. The energetic cost of the dissociations can be ascribed to the strength of the coordination bond: Cu-P > [Cu-N]x2 > Cu-N. For $\mathbf{X}^+_{phos}$ and $\mathbf{X}^+_{arm}$, the coordination of a THF molecule on the vacant site can slightly stabilize the complexes, from 0.1 to 2.6 kcal/mol. No coordination of THF is reported for the $\mathbf{X}^+_{pyr}$ complexes as the decoordination of one pyridine does not open a large enough vacant site to fit a THF molecule.

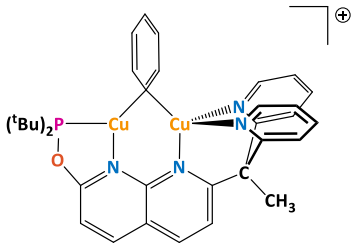

1^+ **0.0**

1^+_THF **0.0**

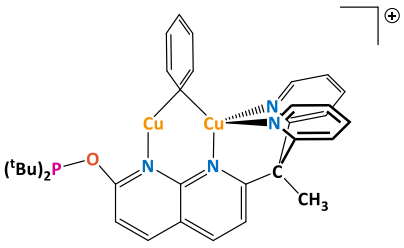

1^+_{phos} **16.4**

$1^+_{phos\_THF}$ **16.3**

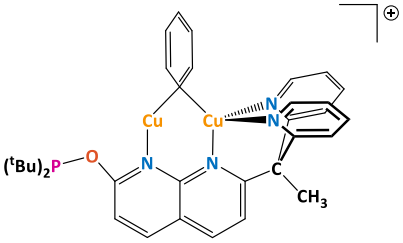

1^+_{arm} **10.7**

$1^+_{arm\_THF}$ **9.8**

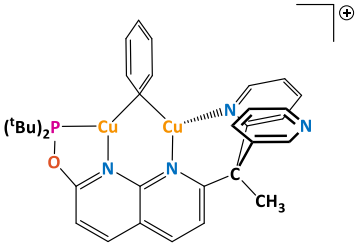

1^+_{pyr} **-1.4**

Figure III.5. Partial dissociations of DPEOPN for 1^+ in kcal/mol.

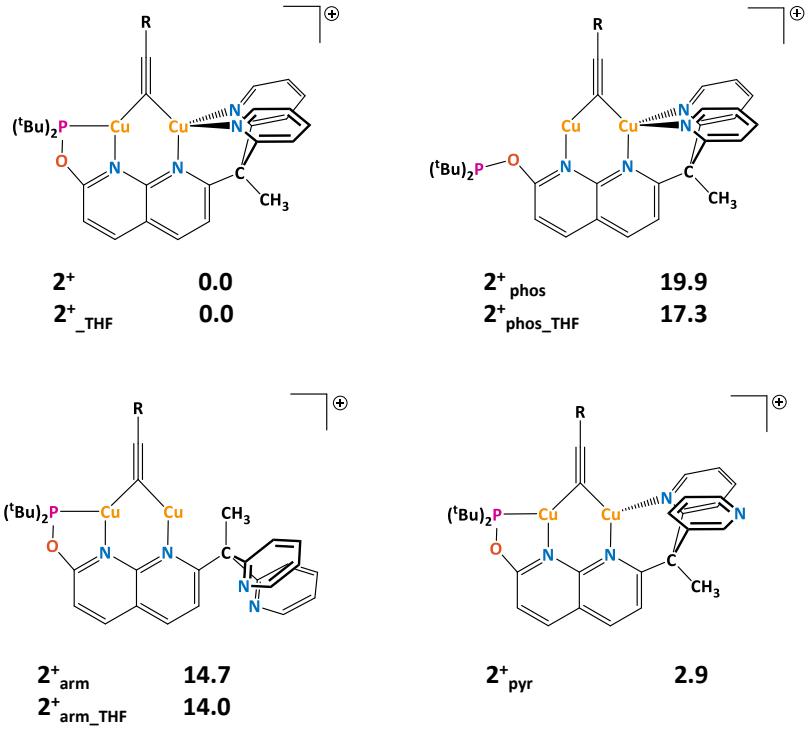

Figure III.6. Partial dissociations of DPEOPN for 2^+ in kcal/mol.

To further study the impact of the partial dissociation of DPEOPN on $\mathbf{1}^+$, an NBO analysis was carried out (Table III.2). All the significant interactions between the ligands and the coppers involve a σ(sp) orbital centred on the coordinating atoms of DPEOPN and the phenyl with an accepting σ(s)* orbital mainly centred on the coppers (Figure III.7). As stated above, the energetic cost of the dissociation correlates to the strength of the coordination to the coppers. This is highlighted by the energy of the interaction between P (59.5 kcal/mol) and N (21.8 kcal/mol on average) with the coppers. In $\mathbf{1}^+_{pyr}$, the strength of the interactions between the ligands and the coppers do not change compared to $\mathbf{1}^+$, displaying the small effect of the partial dissociation of one pyridine. On the contrary, the dissociations yielding $\mathbf{1}^+_{arm}$ and $\mathbf{1}^+_{phos}$ have a large effect on the energy of the remaining interactions. In $\mathbf{1}^+_{arm}$, there are three less bond less between the coppers and DPEOPN than in $\mathbf{1}^+$. As a result, the remaining interactions have higher energies (+17.6, +25.8 and

+25.3 kcal/mol for P, N_2 and C_1, respectively). In $\mathbf{1}^+_{phos}$, due to the loss of the coordination of the phosphine, the energy of the interactions involving Cu_1 increases (+27.6 and +23.3 kcal/mol for N_1 and C_1) while the C_1-Cu_2 interaction is weakened (-8.6 kcal/mol)

	P-Cu$_1$	**N$_1$-Cu$_1$**	**N$_2$-Cu$_2$**	**N$_3$-Cu$_2$**	**N$_4$-Cu$_2$**	**C$_1$-Cu$_1$**	**C$_1$-Cu$_2$**
$\mathbf{1}^+$	59.5	24.7	21.0	20.0	21.6	53.2	44.5
$\mathbf{1}^+_{pyr}$	60.5	24.1	25.5	25.3	-	56.0	47.3
$\mathbf{1}^+_{arm}$	77.1	-	46.8	-	-	54.6	69.8
$\mathbf{1}^+_{phos}$	-	52.9	15.9	22.3	22.3	76.5	35.9

Table III.2. Energies (in kcal/mol) of the interaction between a donating σ(sp) orbital centred on the coordinating atoms of DPEOPN and the phenyl with an accepting σ(s)* orbital mainly centred on the coppers.

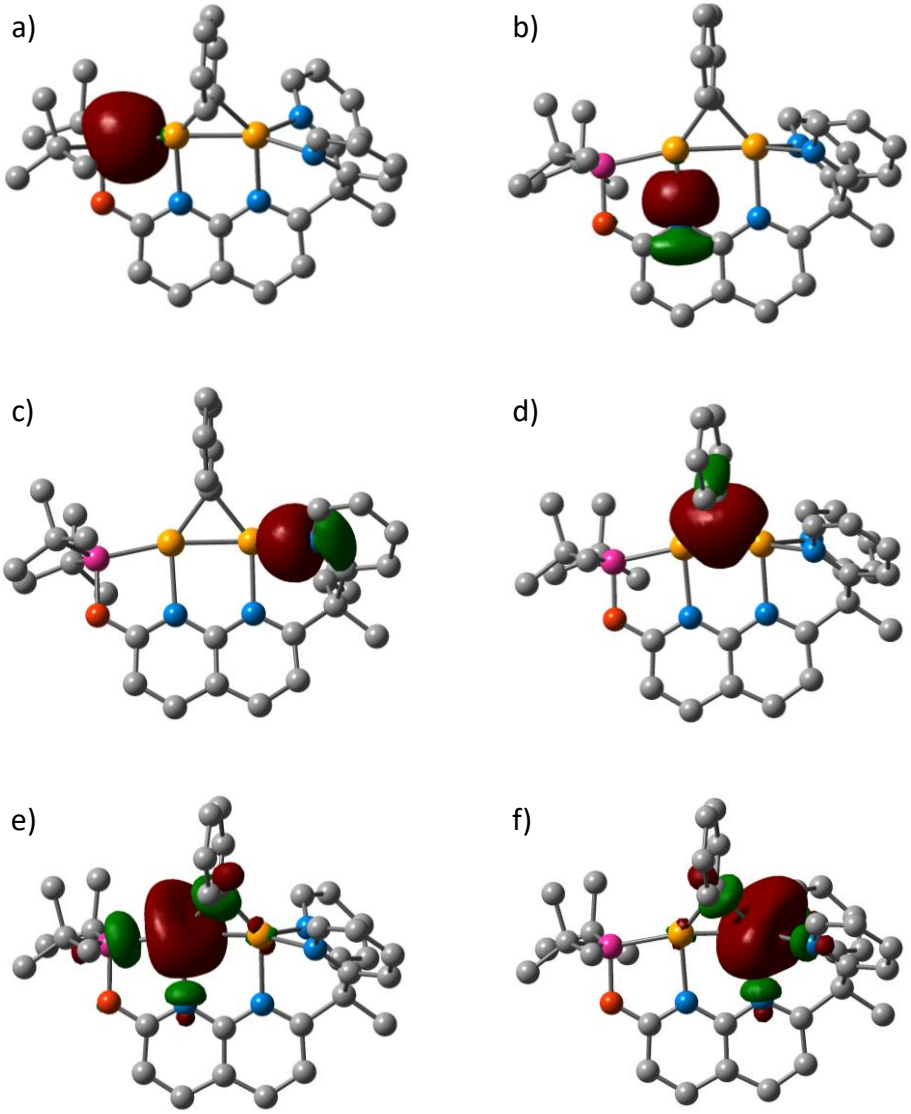

Figure III.7. 3D representation of the NLMOs involved in the σ(sp) donation from a) P, b) N_1, c) N_3, d) C_1 to the σ(s)* of e) Cu_1 and f) Cu_2 in the complex 1^+.

4 - Ion-pairing of NTf_2^- with 1^+ and 2^+

Another important property to consider is the energy of association of the complexes $\mathbf{1}^+$ and $\mathbf{2}^+$ with the counter-ion NTf_2^-, which was computed in THF with an implicit solvent model. Five positions for NTf_2^- are defined around the complexes (Figure III.8) and these series of calculations are noted $\mathbf{1_X}$ and $\mathbf{2_X}$, where X stands for the position of the counter-ion (*i.e.* **A** to **E**). In symmetrical complexes, the positions **C** and **E** are equivalent, as in $\mathbf{1}^+$, but they differ when one of the pyridines dissociates, as in $\mathbf{1}^+_{\mathbf{pyr}}$.

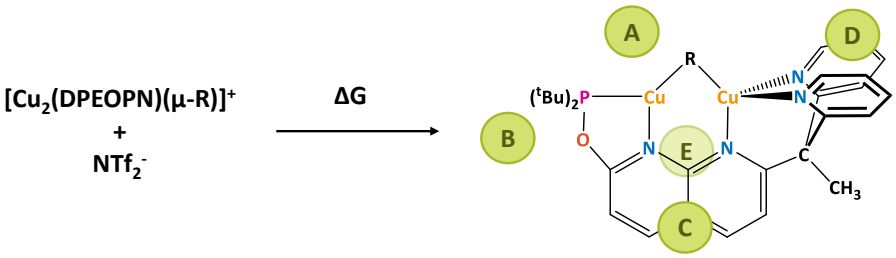

Figure III.8. Positions A to E of NTf_2^- around the complexes $[Cu_2(DPEOPN)(\mu\text{-}R)]^+$ represented by green circles.

The association of $\mathbf{1}^+$ with NTf_2^- is favourable as the free energies are thermoneutral in one case and slightly exergonic in the others (Table III.3). The most favourable position is **C** with -2.5 kcal/mol. In all cases, there is no direct coordination to the metal centres and the counter-ion is only interacting with the complex via weak dispersion interactions (Figure III.9). Overall, the geometries of the $\mathbf{1_X}$ series are not impacted by the presence of NTf_2^- and are very similar to the one of $\mathbf{1}^+$. As shown in the previous section, the partial dissociation of one pyridine leads to the stable intermediate $\mathbf{1}^+_{\mathbf{pyr}}$. Thus, its association with NTf_2^- was also computed (Table III.3). The complexes $\mathbf{1_{pyrX}}$ are also close to thermoneutrality or exergonic. $\mathbf{1_{pyrC}}$ is the most stable complex of all the computed $\mathbf{1}^+$ isomers, with -4.3 kcal/mol. The position **E** is also very stable, by -4.1 kcal/mol, as expected from its similarity with the position **C**. In most cases, the geometry is not affected by the presence of NTf_2^-, except for $\mathbf{1_{pyrA}}$ (Figure III.10) in which the counter-ion is coordinated (2.30

Å) to Cu_1 and leads to an elongation of the bonds between the latter and DPEOPN.

Position of NTf_2^-	ΔG (kcal/mol)	Position of NTf_2^-	ΔG (kcal/mol)
$\mathbf{1}_A$	0.0	$\mathbf{1}_{pyrA}$	1.3
$\mathbf{1}_B$	-2.3	$\mathbf{1}_{pyrB}$	-0.9
$\mathbf{1}_C$	-2.5	$\mathbf{1}_{pyrC}$	-4.3
$\mathbf{1}_D$	-1.2	$\mathbf{1}_{pyrD}$	-1.2
		$\mathbf{1}_{pyrE}$	-4.1

Table III.3. Free energy of the ion-paring for 1^+ and 1^+_{pyr}. The energy reference is the energy 1^+ added to the energy of NTf_2^- for both series.

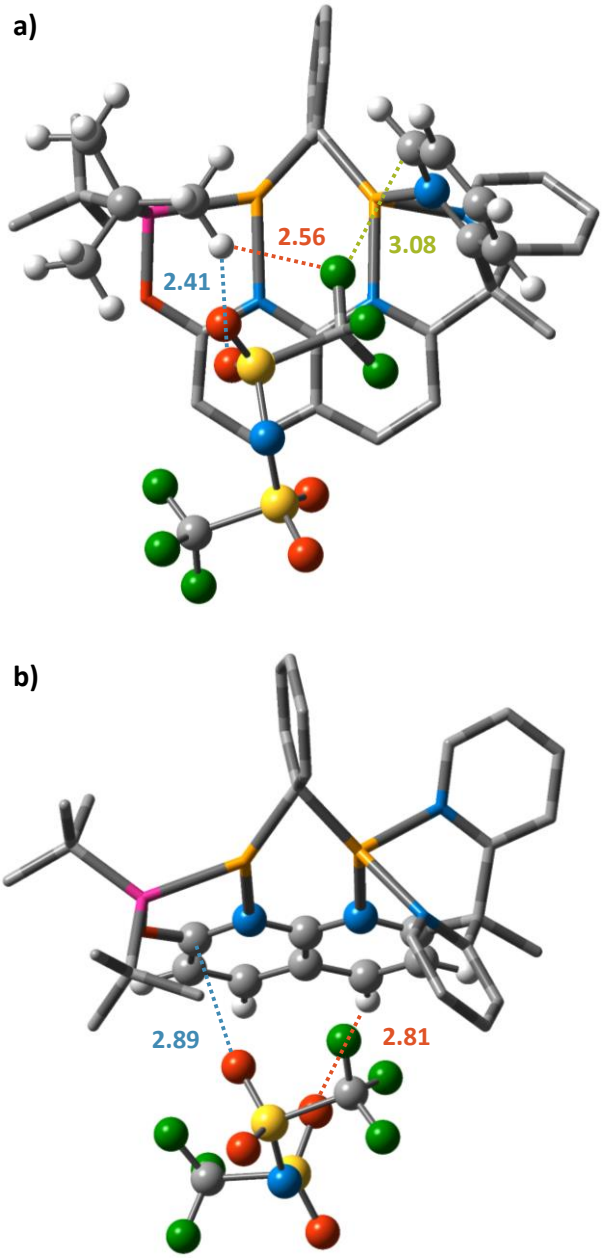

Figure III.9. 3D representation of 1_C from different perspectives showing the position of NTf_2^- relative to a) the pyridine and the phosphine and b) the naphthyridine backbone. All the distances are in Angstrom (Å).

The association of $\mathbf{2}^+$ with the counter-ion is also close to thermoneutrality or slightly exergonic (Table III.4). In this case the most stable position is **B**, by -3.4 kcal/mol. The counter-ion is associated only via weak interactions with the ligands and does not have a significant impact on the geometry (Figure III.10c). The only noticeable change occurs for $\mathbf{2_D}$, in which the alkynyl bends toward the pyridines arm and NTf_2^-. However, the bridging carbon is still equidistant from the coppers so the coordination mode is not modified by this bending. As for $\mathbf{1}^+$, the association of $\mathbf{2}^+_{\mathbf{pyr}}$ with NTf_2^- was investigated. The energies of the $\mathbf{2_{pyrX}}$ series are thermoneutral but not low enough to be more stable than $\mathbf{2_B}$. The positions **A**, **B** and **C** yield geometries very similar to that of $\mathbf{2}^+_{\mathbf{pyr}}$ and the only differences between them are the weak interactions involving NTf_2^-. The two remaining complexes, $\mathbf{2_{pyrD}}$ and $\mathbf{2_{pyrE}}$, have a different coordination mode: the C_{ipso} of the alkynyl is binding in an σ fashion to one copper and in a π fashion to the other, like in $\mathbf{3}^+$. In $\mathbf{2_{pyrD}}$, the C_{ipso} is σ bonded to Cu_2 while it is σ bonded to Cu_1 in $\mathbf{2_{pyrE}}$ (Figure III.10c). For the latter, the geometrical changes also involved an interaction between the coppers and one oxygen of NTf_2^-: with distances of 2.39 Å with Cu_1 and 2.62 Å with Cu_2. Therefore, the ion-pairing of $\mathbf{1}^+$ and $\mathbf{2}^+$ with NTf_2^- is an important effect that stabilizes the complexes and leads to low-energy intermediates with interesting features including different coordination modes and direct interactions with the metals centres.

Position of NTf_2^-	ΔG (kcal/mol)	Position of NTf_2^-	ΔG (kcal/mol)
$\mathbf{2_A}$	2.3	$\mathbf{2_{pyrA}}$	2.0
$\mathbf{2_B}$	-3.4	$\mathbf{2_{pyrB}}$	-1.1
$\mathbf{2_C}$	-1.4	$\mathbf{2_{pyrC}}$	-0.3
$\mathbf{2_D}$	-1.5	$\mathbf{2_{pyrD}}$	0.5
		$\mathbf{2_{pyrE}}$	-1.1

Table III.4. Free energy of ion-paring for 2^+ and 2^+_{pyr}. The energy reference is the energy 2^+ is added to the energy of NTf_2^- for both series.

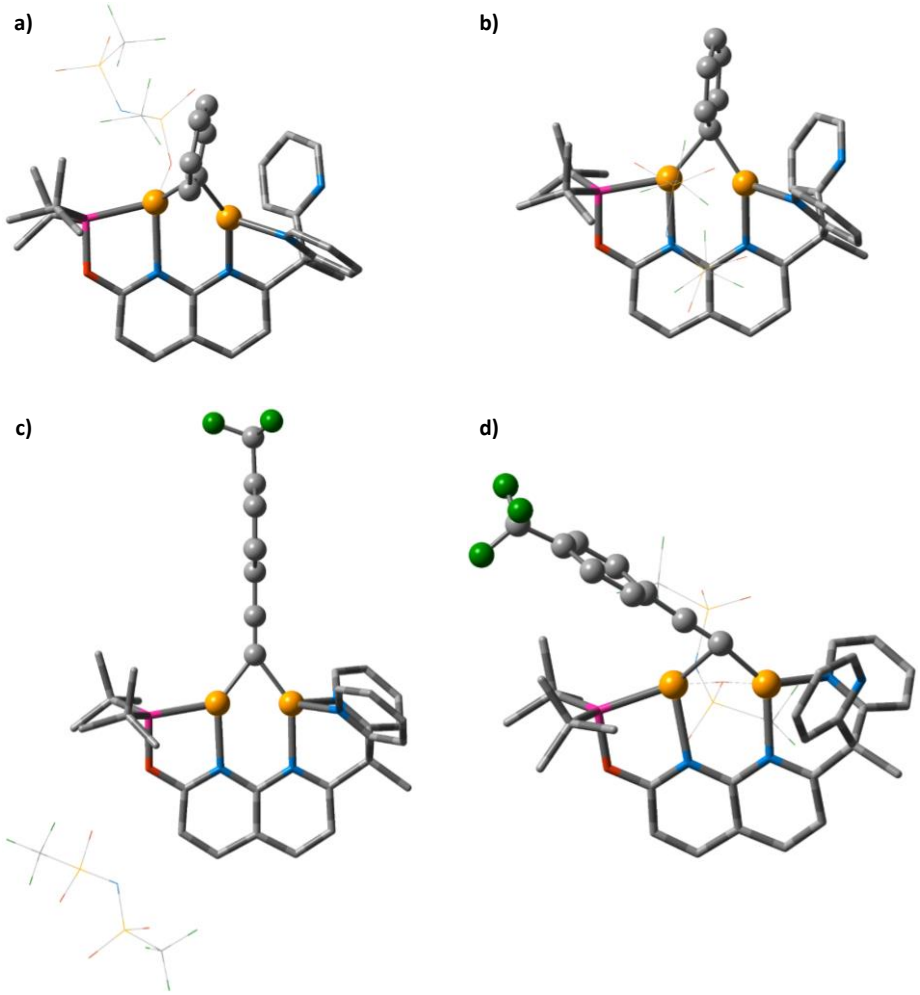

Figure III.10. 3D representation of a) 1_{pyrA}, b) 1_{pyrC}, c) 2_{B} and d) 2_{pyrE}.

5 - Redox potentials of 1^{+} and orbital analysis

The redox potentials of $\mathbf{1}^{+}$ were measured experimentally and it was hypothesized that the complex undergoes a quasi-reversible reduction involving the naphthyridine ligand.[153] Thus, the redox potentials were computed to determine which orbitals were involved. Both the oxidation and reduction lead to species with one unpaired electron, $\mathbf{1}^{2+}$ and $\mathbf{1}^{0}$, respectively. The spin ladder of $\mathbf{1}^{+}$, $\mathbf{1}^{2+}$ and $\mathbf{1}^{0}$ were computed to verify that the lowest spin

states used to calculate the redox potentials are the ground states. For both $\mathbf{1}^{2+}$ and $\mathbf{1}^{0}$, the lower spin state is the doublet by a large energy difference while $\mathbf{1}^{+}$ is a singlet, as expected for a $3d^{10}$ complex (Table III.5).

$\mathbf{1}^{+}$	**ΔG**	$\mathbf{1}^{2+}$	**ΔG**	$\mathbf{1}^{0}$	**ΔG**
S = 1	0.0	S = 2	0.0	S = 2	0.0
S = 3	29.2	S = 4	49.0	S = 4	50.0
S = 5	98.4				

Table III.5. Spin ladder for 1^{+}, 1^{2+} and 1^{0}; all energies are in kcal/mol.

Then, the most stable spin states of $\mathbf{1}^{+}$, $\mathbf{1}^{2+}$ and $\mathbf{1}^{0}$ were selected to calculate the redox potentials. A significant deviation is observed for the computed oxidation potential compared the experimental one with 0.46 V versus 0.17 V, respectively; inducing a difference of 0.29 V. The HOMO of $\mathbf{1}^{+}$ has strong contributions from the 3d orbitals of the coppers and the σ lone pairs of the coordinating atoms of DPEOPN. This orbital also involves the π-system of the phenyl bridging ligand (Figure III.11), indicating the presence of a three-centre-two-electron interaction (3c2e) with the coppers. The spin density of $\mathbf{1}^{2+}$ is very similar to the HOMO of $\mathbf{1}^{+}$ and thus suggests that the oxidation takes place at the dicopper core of the complex, in which the local spins (0.49 and 0.15 α) and charges (-0.36 and -0.39 *e*) of each metal centre are significantly different.

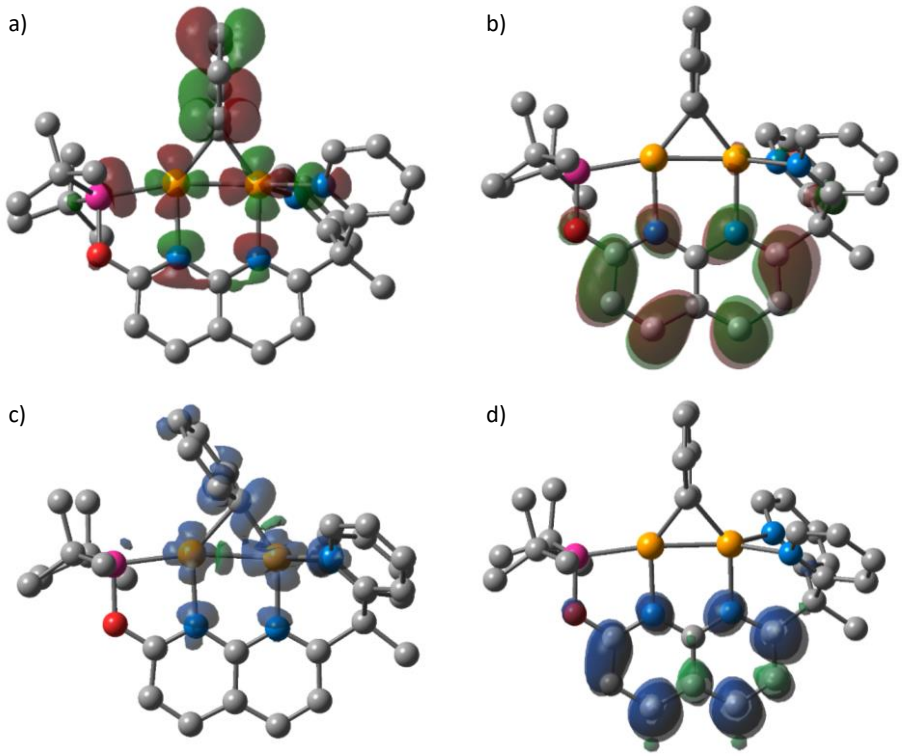

Figure III.11. Computed orbitals and densities relevant to the electrochemical behaviour of 1^{+}; a) HOMO of 1^{+}, b) LUMO of 1^{+}, c) spin density of 1^{2+}, d) spin density of 1^{0}.

For the reduction potential, there is a better agreement between the experimental and the computed values; -1.70 and -1.58 V, respectively; with a smaller deviation of 0.12 V. The LUMO of $\mathbf{1}^{+}$ is an antibonding orbital centred on the naphthyridine backbone (Figure III.11). The spin density of $\mathbf{1}^{0}$ matches very well with the LUMO of $\mathbf{1}^{+}$, confirming that the populated orbital in the reduction process is ligand-based.

The redox potentials were also computed using $\mathbf{1}^{+}_{pyr}$, as the most stable form of $\mathbf{1}^{+}$ is $\mathbf{1}_{pyrC}$. However, the counter-ion was not considered in the redox potential calculations. The oxidation leads the complexes $\mathbf{1}^{2+}_{pyr}$ and the reduction to $\mathbf{1}^{0}_{pyr}$. As done for the redox calculations with $\mathbf{1}^{+}$, the spin ladder for the three complexes and the results are gathered in Table III.6. The most

stable spin state is the lowest one for all the complexes, as expected since the lowest spin state are the most stable in the previous redox calculations and there is no major changes between $\mathbf{1}^{+}$ and $\mathbf{1}^{+}_{pyr}$.

$\mathbf{1}^{+}_{pyr}$	ΔG	$\mathbf{1}^{2+}_{pyr}$	ΔG	$\mathbf{1}^{0}_{pyr}$	ΔG
S = 1	0.0	**S = 2**	0.0	**S = 2**	0.0
S = 3	31.3	**S = 4**	43.8	**S = 4**	50.9
S = 5	108.2				

Table III.6. Spin ladder for $\mathbf{1}^{+}_{pyr}$, $\mathbf{1}^{2+}_{pyr}$ and $\mathbf{1}^{0}_{pyr}$; all energies are in kcal/mol.

Then, the most stable spin state of $\mathbf{1}^{+}_{pyr}$, $\mathbf{1}^{2+}_{pyr}$ and $\mathbf{1}^{0}_{pyr}$ were used to calculate the redox potentials. A large deviation is observed for the computed oxidation potential compared the experimental one: 0.73 V versus 0.17 V, giving an error of 0.54 V. The deviation is even larger than with $\mathbf{1}^{+}$ and is becoming too substantial to represent the experimental data correctly. Thus, no orbital analysis was carried out for the oxidation potential. The reduction potential with $\mathbf{1}^{+}_{pyr}$ is -1.58 V versus -1.70 V experimentally, giving an error of 0.22 V. As with $\mathbf{1}^{+}$, the reduction potential is better fitting the experiments than the oxidation one. However, the experimental reduction potential is better represented by $\mathbf{1}^{+}$ than by $\mathbf{1}^{+}_{pyr}$ and therefore was not investigated further.

IV - C-H activation of alkynes with 1^+

The C-H activation of alkyne by $\mathbf{1}^+$ consist of a stoichiometric reaction where a proton is transferred from the alkyne to the phenyl bridging the two coppers in $\mathbf{1}^+$, leading to the formation of benzene and $\mathbf{2}^+$. Experimentally,[153] the activation of alkynes has been performed in THF at 48.5°C using the alkyne HCC(*p*-CF_3-C_6H_4). This chapter details the search of a mechanism to explain this reaction and the assessment of its accuracy by comparing some computed properties with experimental data.

1 - Search of the transition states

A concerted step in which the proton transfers from the terminal alkyne to the bridging phenyl ring was assumed as a starting point. For this mechanism, the transition state has two isomers, due to the two different arms of the naphthyridine backbone. The alkyne coordinates to the copper either on the pyridine side or on the phosphine side and are further referred as the $\mathbf{TS_1}$ and $\mathbf{TS_2}$ series, respectively. All the transition states are represented schematically on the Figures IV.2 and IV.3 for the $\mathbf{TS_1}$ series and Figures IV.6 and IV.7 for the $\mathbf{TS_2}$ series. All the energy of the transition states reported in this thesis are gathered in tables in the annex A.

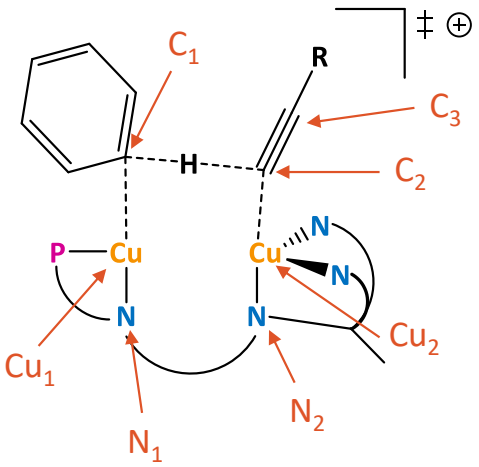

Figure IV.1. Labels of the key atoms in the transition states connecting 1^+ to 2^+.

To ease the description of the transition states and their analysis, the key atoms have been labelled as shown in Figure IV.1. These labels do not change depending on the isomers nor on the presence of additional molecules to the transition state (counter-ion or solvent molecule). For all the energy barriers mentioned below, $\mathbf{1}^+$ and $\mathbf{1_C}$ were used as the energy reference instead of $\mathbf{1}^+_{\mathbf{pyr}}$ and $\mathbf{1_{pyrC}}$ isomers. The two latter converged with lower DFT energies, but the experimental ^{1}H NMR and the redox potential calculations do not support the partial dissociation of the pyridines in the DPEOPN as the most stable form of $\mathbf{1}^+$.

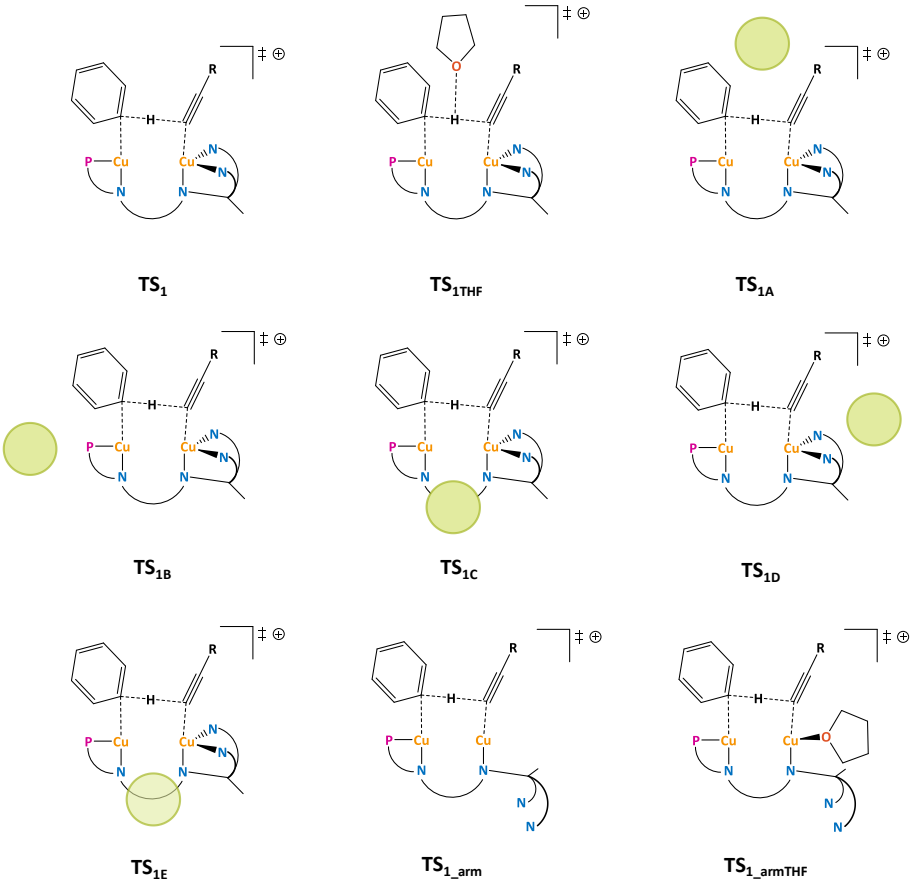

Figure IV.2. Schematic representations and labels of all the transition states computed for the TS_1 series; the green circles represent the position of NTf_2^- (1/2).

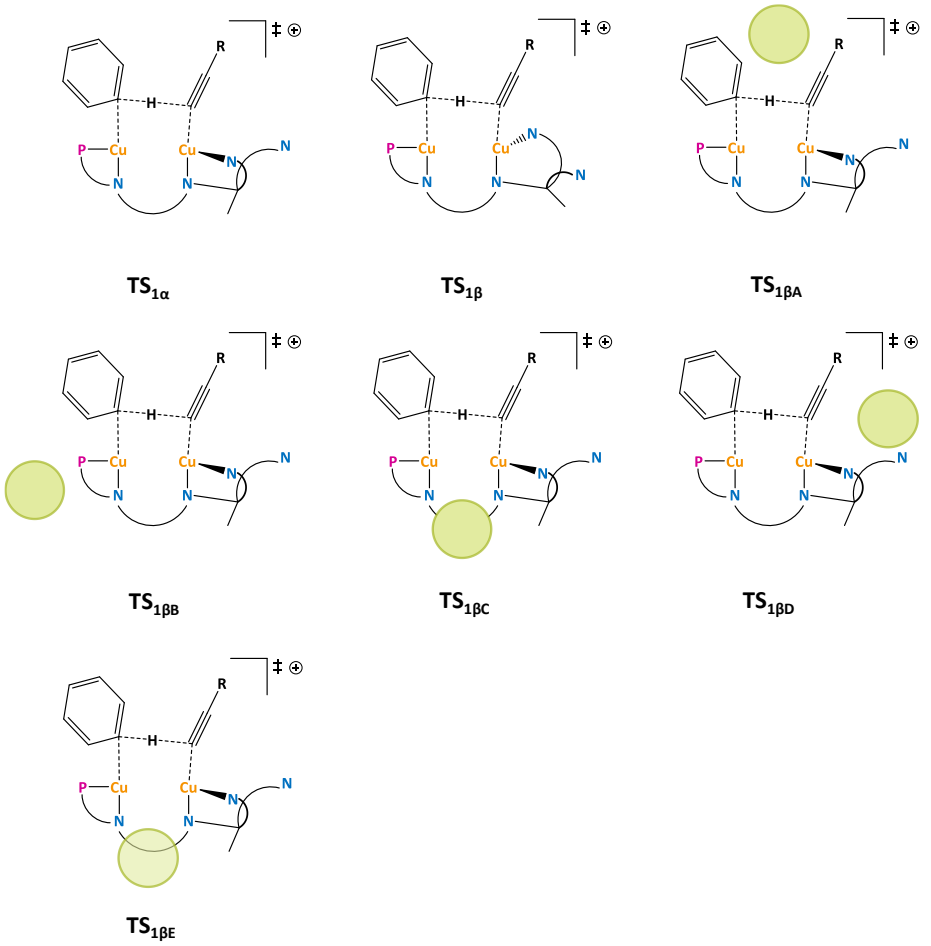

Figure IV.3. Schematic representations and labels of all the transition states computed for the TS_1 series; the green circles represent the position of NTf_2^- (2/2).

For the **TS_1** series, 16 transition states were considered. The simplest one is **TS_1** (in red in Figure IV.4 and Figure IV.5a), where all the part of DPEOPN are coordinated to the coppers and the counter-ion is not included. **TS_1** is distorted compared to **1^+** and **2^+**, with the distance between the coppers increased by 0.5 Å and the dihedral angle Cu_1-N_1-N_2-Cu_2 is 21.9°, compared to 4.1° in **1^+**. However, all the other distances are quite similar to the ones in **1^+** and **2^+**. The alkynyl bends over one of the ^{t}Bu substituent of the phosphine, creating dispersion interactions with it. The barrier $\Delta G^‡$ of 27.1 kcal/mol

associated to this transition state is too high compared to what is expected from the experiments (*i.e.* <24.0 kcal/mol). The first attempt to lower the energy of **TS_1** consisted in adding a THF molecule to "solvate" the transferred proton (**TS_{1THF}**, in dotted red in Figure IV.4). The oxygen of THF is pointing toward the proton at a distance of 2.84 Å, thus it is close enough to interact with it. To accommodate the THF molecule on top of the active site, the complex has to distort even more: the distance between the copper is 3.03 Å and the distances between Cu_1 and the phenyl and between Cu_2 and the alkynyl are elongated by 0.8 and 0.12 Å, respectively. All these geometrical changes, increase the energy of the transition state by 3.3 kcal/mol, up to 30.4 kcal/mol and thus, the presence of a solvent molecule around the active site is not favourable.

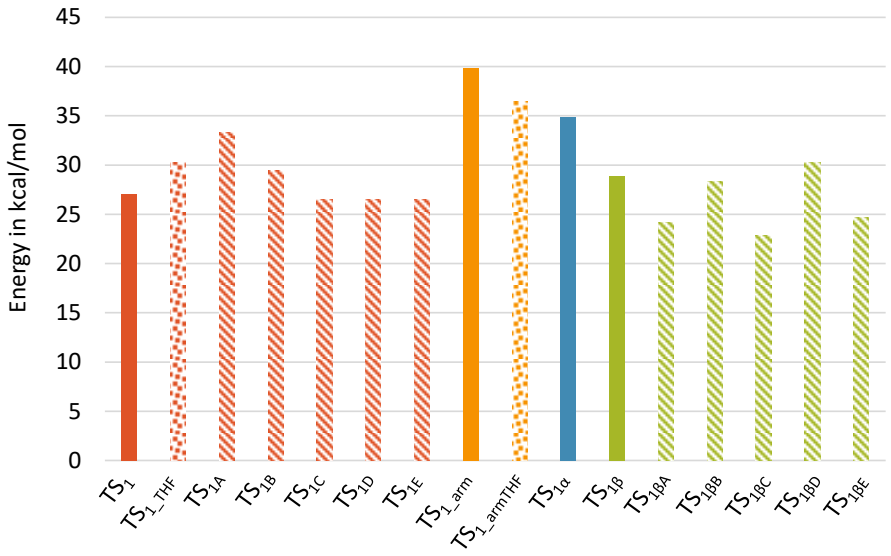

Figure IV.4. Free energy of all the transition states of the TS_1 series.

The counter-ion is added to **TS_1** to create the **TS_{1X}** series (diagonally red dashed in Figure IV.4), with X describing the position of the counter-ion around the complex (**A** to **E** see Figure IV.2). The energy range varies from 26.5 to 33.3 kcal/mol. **TS_{1A}** has a very interesting structure where NTf_2^- is bound to Cu_1, causing its partial dissociation from the naphthyridine ligand,

due to steric hindrance (Figure IV.5b). Thus, the distance between the coppers increases to 3.91 Å. **TS_{1A}** yields to an energy barrier of 33.3 kcal/mol, which is too high to be relevant. On the contrary, **TS_{1C}**, **TS_{1D}** and **TS_{1E}** have structures extremely close to **TS_1**, where the only difference is the bending of the alkynyl over the phosphine. In these transition states, NTf_2^- interacts only via dispersion with the ligands: DPEOPN, phenyl and alkynyl. In the case of these three positions, the association of **TS_1** and NTf_2^- is isoenergetic.

As previously shown for **1^+** and **2^+**, DPEOP is a chelating ligand that can partially dissociate from the coppers. These isomers could be more reactive, yielding lower energy barriers that would not be accessible otherwise. Thus, several dissociations were considered for **TS_1**. The first one is the rotation of the pyridines arm (**TS_{1_arm}**), which opens space around Cu_2. This dissociation has a dramatic effect on the geometry. The remaining bond between Cu_2 and DPEOPN is strengthened to balance the loss of the pyridines, including the shortening of -0.1 Å of the bond with the naphthyridine backbone. The coordination of Cu_2 to the alkynyl and the naphthyridine is close to linearity with an angle of 173.0°. Conversely, the bond between Cu_1 and the naphthyridine elongates to full dissociation at 2.81 Å. The phenyl does a hydrogen bond with the pyridine on the back of **TS_{1_arm}**, with a distance of 2.85 Å between the hydrogen and the nitrogen atoms. The alkynyl does not interact with the phosphine substituents, unlike in **TS_1**. The coordination sphere of Cu_1 is also more linear than is in the previous transition states, with an angle of 167.7° between the phosphine, Cu_1 and the phenyl. The energy barrier associated to **TS_{1_arm}** is very high (39.9 kcal/mol) and thus these modifications and new interactions are not favourable enough to compensate the dissociation of the two pyridines. The coordination of a THF molecule in the vacant site of Cu_2 mitigates the structural distortion, lowering the energy barrier to 36.5 kcal/mol (**TS_{1_armTHF}** in dotted orange in Figure IV.4). For example, the Cu_1 bond to the naphthyridine backbone is elongated to 2.31 Å, but not dissociated. However, the energy of **TS_{1_armTH}** remains high and therefore the coordination of THF does not make this reaction pathway plausible.

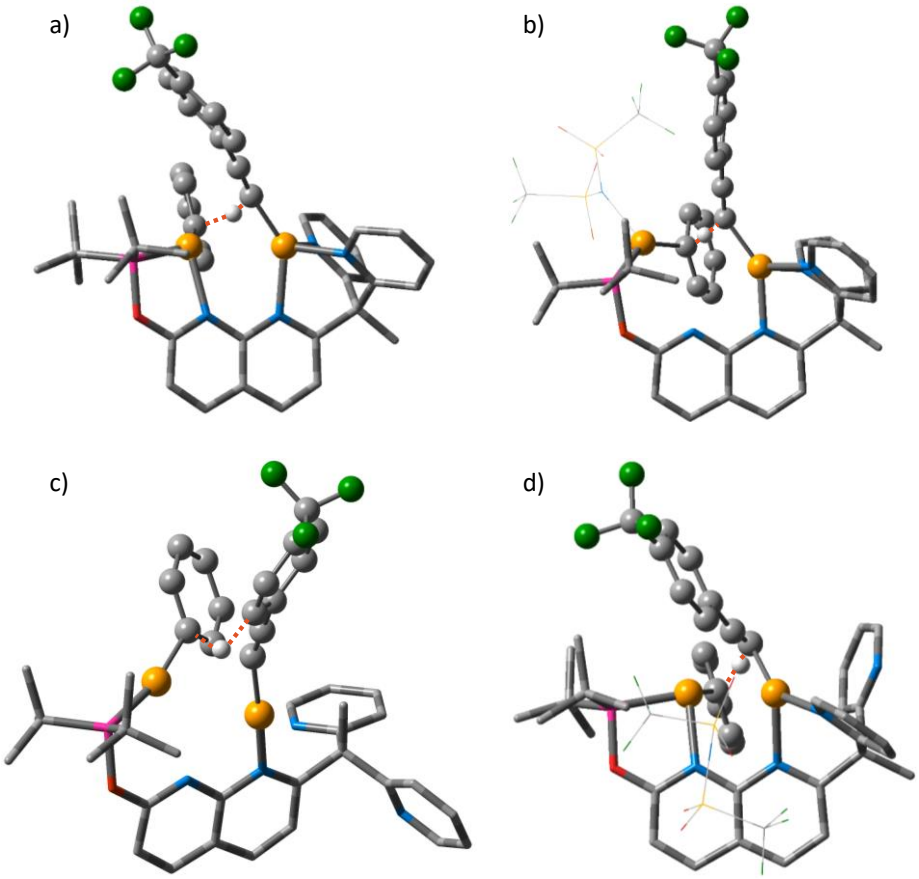

Figure IV.5. 3D representation of a) TS_1, b) TS_{1A}, c) TS_{1_arm} and d) $TS_{1\beta C}$. The red dashed lines account for the cleavage and formation of C-H bonds between the phenyl and alkynyl moieties.

As the dissociation of the pyridines arm leads to very high barriers, the dissociation of the phosphine is excluded, as the related intermediates are even at higher energies. The only partial dissociation remaining is the rotation of one pyridine. Starting from **TS_1**, two different dissociations can be done. Either the pyridine in the front rotates or the one in the back, leading to **$TS_{1\alpha}$** and **$TS_{1\beta}$**, respectively (Figures IV.2 and IV.3). On one hand, **$TS_{1\alpha}$** has an unusual geometry, with the phenyl group still bridging the coppers evenly but with longer distance than in **1^+** (2.17 Å on average). As the coppers are still bridged, the distances between them is much smaller than in **TS_1**, with only

2.55 Å. The alkynyl group is coordinated to Cu_1; and not on Cu_2 as the transition states from the **TS_1** series are supposed to; and orientated in parallel to naphthyridine backbone with which it interacts by π-stacking. Contrary to the previous transition states, the transferred proton is equidistant from the phenyl and the alkynyl (1.44 Å). Regardless of these unusual features, **$TS_{1\alpha}$** has a high energy (34.9 kcal/mol). On the other hand, **$TS_{1\beta}$** has a geometry very close to **TS_1** with similar distances (between all the key distances involving the coppers) and the same orientation of the alkynyl and phenyl groups (Figure IV.5c). Despite these similarities, the loss of one pyridine in the coordination sphere of Cu_2 destabilizes the transition state to 28.9 kcal/mol. Overall, the partial dissociation of DPEOPN does not lead to the lowering of the energy of **TS_1** on its own.

The last possibility to lower the energy of **TS_1** series is to combine the effects of the partial dissociation of DPEOPN and of the ion-pairing with NTf_2^-. As **$TS_{1\beta}$** is the lowest transition state with a partial dissociation, it is the only one considered for the association with NTf_2^-, leading to the **$TS_{1\beta X}$** series, with X referring the position of counter-ion (Figure IV.3). In **$TS_{1\beta A}$**, NTf_2^- is on top of the complex, in the plane of the naphthyridine backbone and coordinated to Cu_1 by one of its oxygen (2.18 Å). Like in **TS_{1THF}**, the complex has to be even more distorted than usual to fit NTf_2^- in the active site: the distance between the copper increases to 3.74 Å and Cu_1 dissociates from the naphthyridine backbone (3.08 Å). Due to its unusual position, NTf_2^- interacts with all parts of the ligands (distances below 2.80 Å), except the naphthyridine. This particular geometry is surprisingly quite stable as the free energy associated to **$TS_{1\beta A}$** is 24.2 kcal/mol. **$TS_{1\beta B}$**, **$TS_{1\beta C}$** and **$TS_{1\beta D}$** have very similar geometries to **$TS_{1\beta}$**, except for the Cu_1-naphthyridine bond which is elongated by 0.1 Å. The counter-ion is not coordinated to the coppers in these transition states and it only does weak interactions with the ligand. The energy range for these transitions states is from 22.9 to 28.3 kcal/mol (green dashed line on Figure IV.4) and the differences are mainly due to the interactions with the counter-ion. These interactions maximize in the case of **$TS_{1\beta C}$**, which yields the lowest energy barrier (22.9 kcal/mol), involving most of the DPEOPN ligand and the alkynyl (Figure IV.5d).

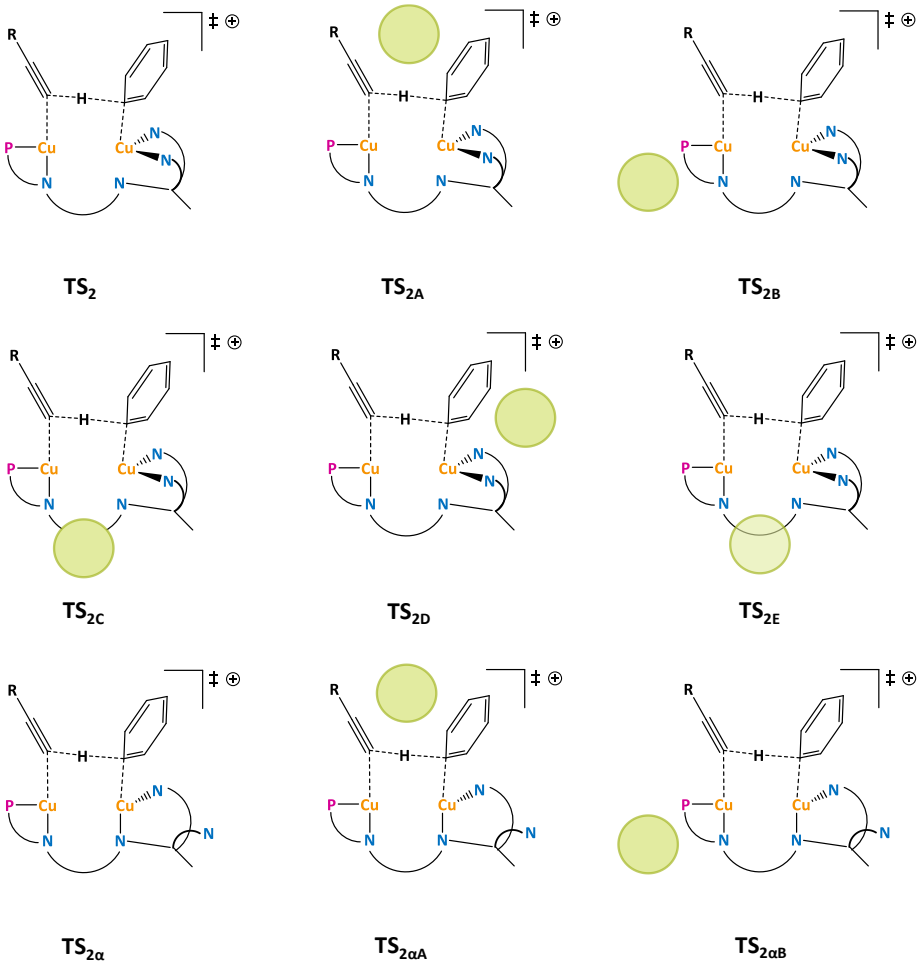

Figure IV.6. Schematic representations and labels of all the transition states computed for the TS_2 series; the green circles represent the position of NTf_2^- (1/2).

For the **TS_2** series, 13 transition states were computed and are listed in Figures IV.6 and IV.7. The simplest one is **TS_2** (Figure IV.9a), where DPEOPN is fully coordinated to the coppers and the counter-ion is excluded. **TS_2** is much more distorted than **TS_1**. This is caused by the higher steric hindrance of the phenyl with the pyridines than with the phosphine. To fit the two pyridines and the phenyl around Cu_2, the pyridines arm is pushed forward and Cu_2 dissociates from the naphthyridine backbone (2.67 Å). Thus, the distance between the coppers increases up to 3.58 Å. The position of the transferred proton is

similar to the one in **TS_1**: the distance between H^+ and the alkynyl is shorter (1.30 Å) than the one between H^+ and the phenyl (1.78 Å). The geometry of **TS_2** is the only one with this geometrical feature in the series and gives its second lowest energy barrier (27.3 kcal/mol, in red in Figure IV.8).

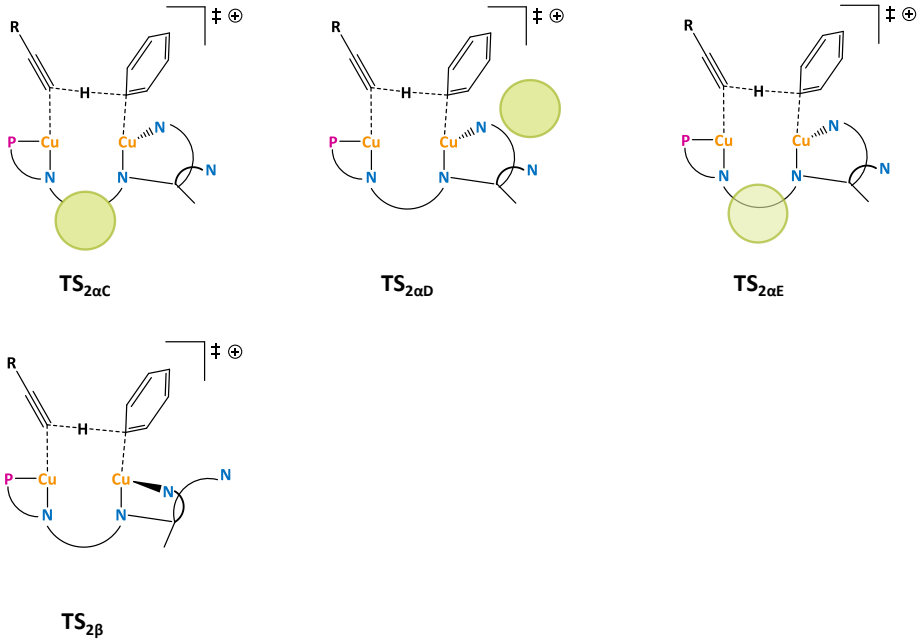

$TS_{2\alpha C}$ **$TS_{2\alpha D}$** **$TS_{2\alpha E}$**

$TS_{2\beta}$

Figure IV.7. Schematic representations and labels of all the transition states computed for the TS_2 series; the green circles represent the position of NTf_2^- (2/2).

As for the **TS_1** series, the ion-paring between **TS_2** and NTf_2^- was also explored, yielding the **TS_{2X}** series (red dashed in Figure IV.8), with X describing the position of the counter-ion. **TS_{2A}** and **TS_{2B}** are both compact transition states, with a distance between the coppers of 2.60 and 2.66 Å, respectively. In **TS_{2A}**, NTf_2^- is on top of the complex and it interacts with the most parts of the ligands, including the phosphine, the pyridines, the phenyl and the alkynyl. NTf_2^- is also in contact with the transferred proton through one of the fluorine (2.71 Å).The presence of NTf_2^- on top of the complex forces the bond between the proton and the alkynyl to elongate to 2.21 Å. In **TS_{2B}**, NTf_2^- is only interacting with the ^{t}Bu of the phosphine. These two transition states yield high energy barriers: 35.2 and 35.8 kcal/mol for **TS_{2A}** and **TS_{2B}**, respectively.

TS_{2C} and **TS_{2E}** are more distorted, with a distance of 2.76 and 2.86 Å between the coppers (Figure IV.9b). Most of the distances between the coppers and the ligands are the same as in **1^+** and **2^+**, except for one between the naphthyridine backbone and Cu_2, which is elongated by 0.1 Å. This distortion is quite small compared to the same bond in **TS_2**. As there is more space within the active site, the alkynyl is closer to the coppers and thus the distance between the H^+ and the alkynyl is shortened to 1.53 and 1.48 Å for **TS_{2C}** and **TS_{2E}**, respectively. The energy of these transition states are the lowest in this **TS_{2X}** series, *i.e.* 31.1 and 29.4 kcal/mol. The **TS_{2X}** series gives interesting geometries and NTf_2^- has a clear impact on both the energy and the geometry of **TS_2**. However, the energy of the associations of **TS_2** and NTf_2^- varies from isoenergetic to unfavourable, within the 0.7-7.1 kcal/mol range of energies. As for **TS_1**, the ion-pairing effects alone are not enough to lower the energy of **TS_2**.

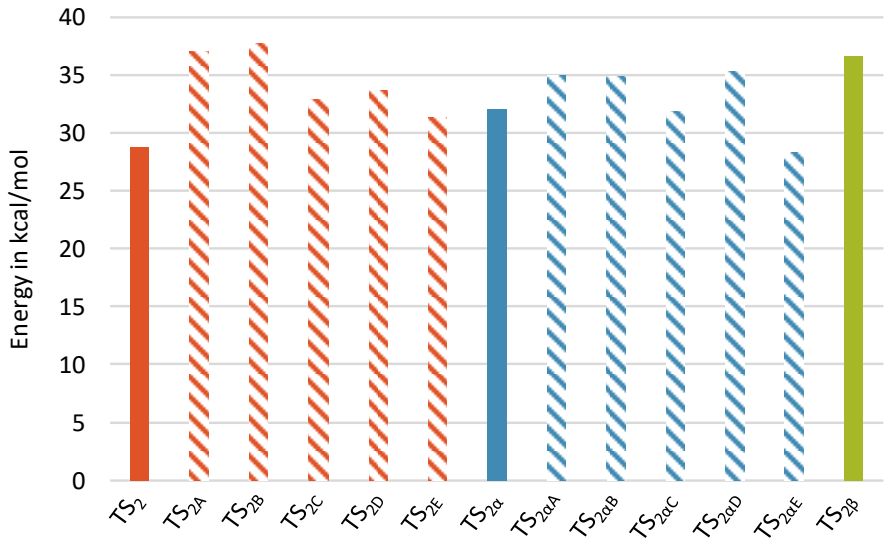

Figure IV.8. Free energy of all the transition states of the TS_2 series.

The transition states of the **TS_2** series appeared to be higher in energy than the ones of **TS_1**. However, to be consistent, the effect of the partial dissociation of DPEOPN was also investigated for **TS_2**. Considering the results obtained with **TS_1**, only the partial dissociation of one pyridine was kept. This

yields two different transition states, $\mathbf{TS_{2\alpha}}$ and $\mathbf{TS_{2\beta}}$, for the dissociation of the pyridine on each of the opposite faces of the complex (Figures IV.6 and IV.7). These two transition states have a very different geometry compared to $\mathbf{TS_2}$: On one hand, $\mathbf{TS_{2\alpha}}$ is moderately open with a distance of 2.73 Å between the coppers and the distances between the coppers and the ligands are similar to the ones in $\mathbf{1}^+$ and $\mathbf{2}^+$. The phenyl and the dissociated pyridine are parallel to each other and are separated by 3.90 Å on average, suggesting the presence of π-stacking interactions (Figure IV.9c). $\mathbf{TS_{2\alpha}}$ is quite high in energy, yielding a barrier of 32.1 kcal/mol. One the other hand, $\mathbf{TS_{2\beta}}$ has a particular geometry: the distance between the coppers is extremely short, with only 2.58 Å, corresponding to an elongation of 0.1 Å compared to $\mathbf{1}^+$ and $\mathbf{2}^+$. As the active site is extremely compact, the bond between the alkynyl and Cu_1 is elongated to 2.23 Å and the alkynyl adopts an unusual position: orientated downward and parallel to the naphthyridine backbone. This transition state yielded the highest energy barrier for the $\mathbf{TS_2}$ series, with 36.6 kcal/mol. Thus, likewise the ion-pairing, the partial dissociation of DPEOPN alone cannot lower the energy of $\mathbf{TS_2}$.

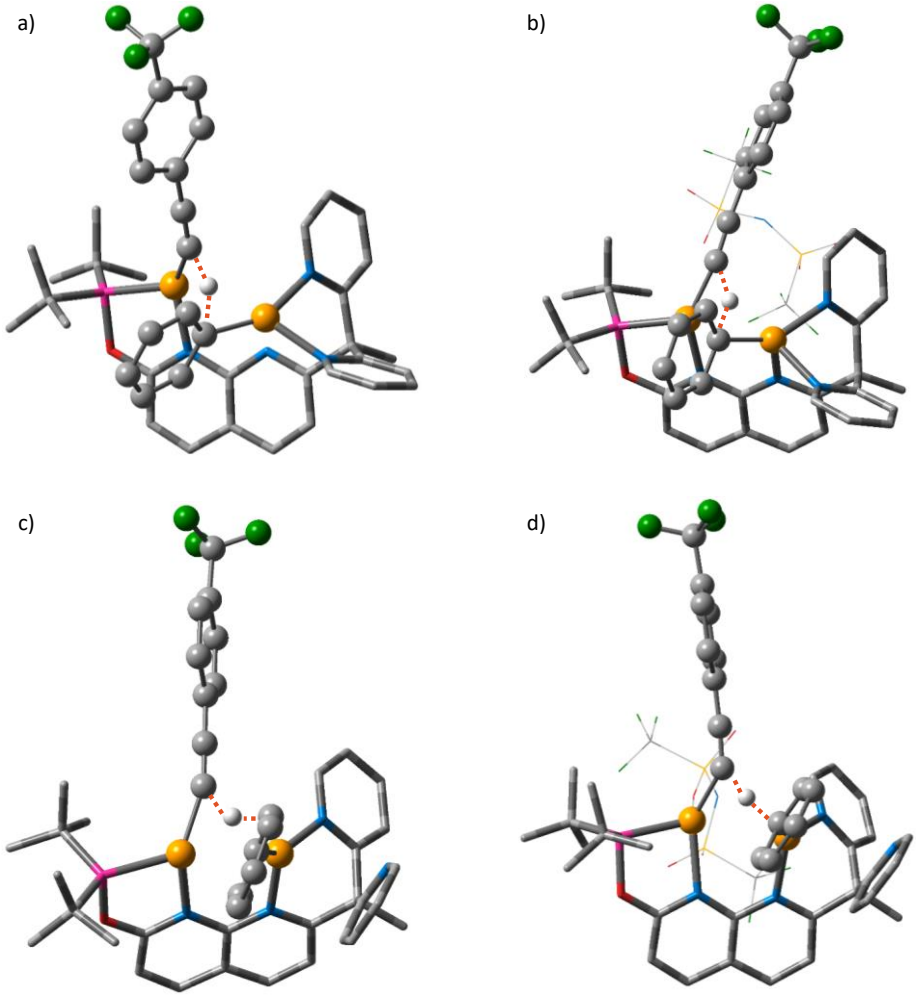

Figure IV.9. 3D representation of a) TS_2, b) TS_{2E}, c) $TS_{2\alpha}$ and d) $TS_{2\alpha E}$. The red dashed lines account for the cleavage and formation of C-H bonds between the phenyl and alkynyl moieties.

The last attempt to lower the $\Delta G^{\ddagger}$ in the **TS_2** series is to combine the effects of the ion-pairing and the partial dissociation. Only **$TS_{2\alpha}$** is considered, as **$TS_{2\beta}$** is too high to be lowered enough by these effects. This attempt is labelled **$TS_{2\alpha X}$**, with X denoting the position of NTf_2^- (Figures IV.6 and IV.7). **$TS_{2\alpha A}$**, **$TS_{2\alpha B}$**, **$TS_{2\alpha C}$** and **$TS_{2\alpha D}$** have a geometry close to the one of **$TS_{2\alpha}$**, even if small variations are observed. For example, **$TS_{2\alpha D}$** is more compact than the others with a

distance of 2.64 Å between the coppers. But overall, they are all quite similar and the main difference is the position of NTf_2^- and the interactions it makes with the complex. The energy varies between 31.9 and 35.3 kcal/mol, showing that these associations of NTf_2^- to **$TS_{2\alpha}$** are either isoenergetic or unfavourable. **$TS_{2\alpha E}$** is much different from the other transition states of this series. Its geometrical characteristics are very similar to **$TS_{1\beta C}$,** even if the position of the phenyl and the alkynyl are reversed: the distance between the coppers is 2.92 Å (Figure IV.9d). The transition state is therefore quite distorted but the coppers are still coordinated to the naphthyridine backbone. Since the active space is quite open, the alkynyl is close to Cu_1, so its C-H bond is elongated only up to 1.27 Å. The forming C-H bond of the benzene is longer with 1.66 Å. As in **$TS_{1\beta C}$**, NTf_2^- is involved in weak interactions with most parts of the ligands; including the pyridine **β**, the naphthyridine backbone, the phosphine and the alkynyl. These geometrical characteristics appear to be favourable, as the energy barrier of **$TS_{2\alpha E}$** is 26.7 kcal/mol. It is the lowest transition state found for the **TS_2** series, even if it is only 0.6 kcal/mol lower than **TS_2**.

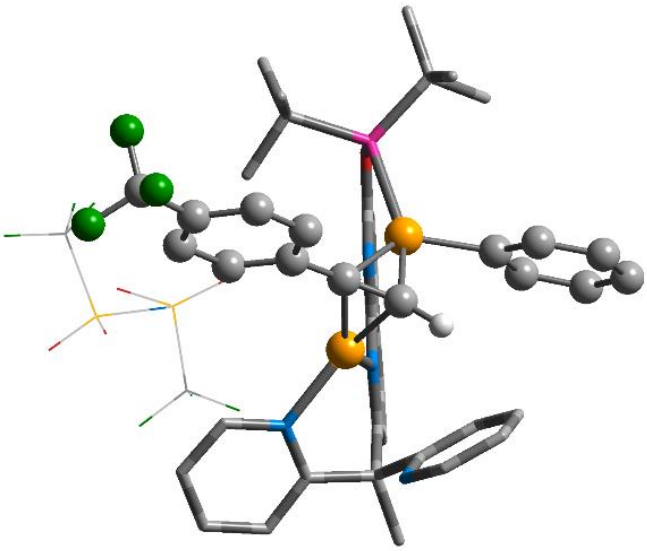

Figure IV.10. 3D representation of the intermediate between 1_C to $TS_{1\beta C}$.

Overall, **$TS_{1\beta C}$**, is the lowest transition state for the C-H activation of alkyne by **1^+**, with a $\Delta G^{\ddagger}$ of 22.9 kcal/mol. This energy barrier involves both the partial dissociation of DPEOPN and the ion-pairing with NTf_2^-, highlighting the relevance of these effects and their combination. An Intrinsic Reaction Coordinate (IRC)-driven relaxation has been done on a selection of transition states, coming from both **TS_1** and **TS_2** series. In some cases, the IRC leads to an intermediate where the alkyne reactant or the benzene product appear coordinated to the dicopper core. These intermediates do not change the concerted nature of the C–H activation step. In the case of **$TS_{1\beta C}$**, the IRC leads to the products directly, while yielding an intermediate on the reactants side at 9.8 kcal/mol (Figure IV.10). This intermediate has a particular geometry: the phenyl is only coordinated to Cu_1 with a distance of 1.98 Å, while the alkyne is bridging the two coppers via its π-system with distances of 2.00 Å for C_2 and 2.12 Å for C_3. No associative transition state was found connecting **1^+** to this pre-reaction complex despite multiple attempts, and thus a low potential energy barrier was postulated for this step. The full mechanism is summarize in Figure IV.11. Through this pathway, the natural charge of H is relatively stable (from +0.22 in the benzene up to +0.29 in the intermediates) due to the similarity of the atoms bonded to it (carbons C_1 and C_2 from the phenyl and the alkyne). However, the charge of these carbons varies largely (-0.22 to -0.62 in the case C_2 for example) depending on their coordination to the coppers, increasing the polarity of the Cu-C bonds.

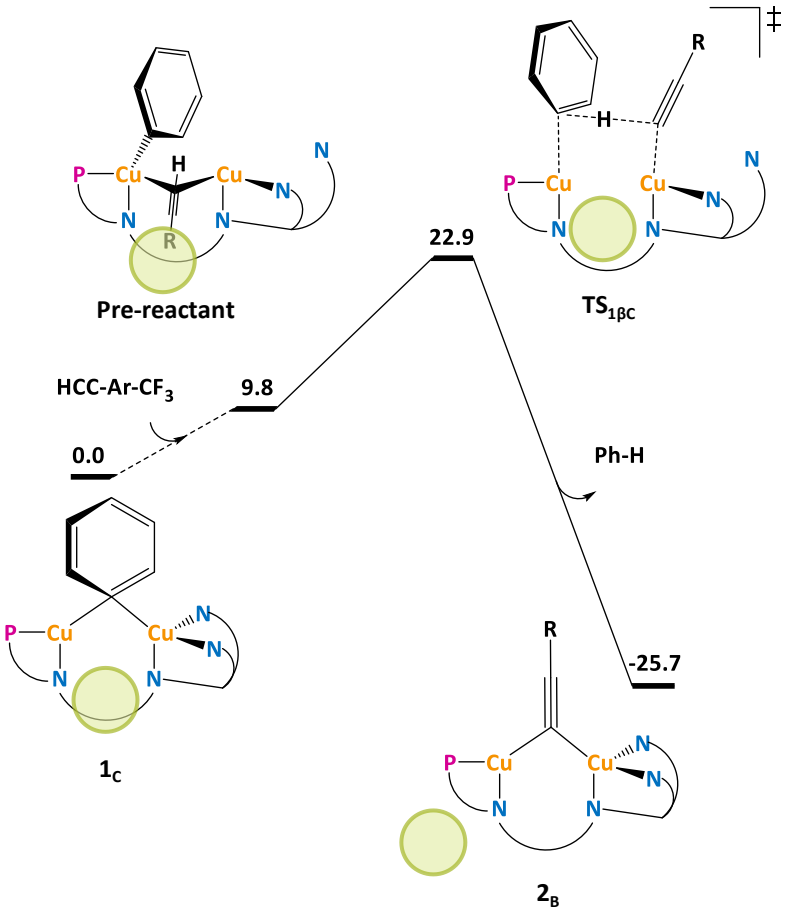

Figure IV.11. Schematic representation of the concerted mechanism of 1_C to 2_B; the green circles represent the positions on NTf_2^-.

2 - Descriptors analysis of the transition states

The 29 transitions states found for the concerted mechanism were analysed with the aim of finding which descriptors yield the lowest energy barriers. 15 different descriptors were considered, including the following geometrical and electronic parameters:

- Position of NTf_2^-
- Distance between Cu_1 and Cu_2
- Distance between C_1 and C_2
- Distance between H and C_1
- Distance between H and C_2
- Dihedral angle Cu_1-N_1-N_2-Cu_2
- Natural charge of Cu_1
- Natural charge of Cu_2
- Difference of natural charge between Cu_1 and Cu_2
- Natural charge of the C_1
- Natural charge of the C_2
- Difference of natural charge between C_1 and C_2
- Natural charge of H
- Difference of natural charge between H and C_1
- Difference of natural charge between H and C_2

In the following Figures IV.12 and IV.13 and in the additional *Descriptors file* (see Annexes) are scattered plots of the descriptors analysis of the **TS_1** and **TS_2** series. All the transition states related to the **TS_1** series are represented in blue dots while the ones related to the **TS_2** series are in green dots. There is three trends that can be extracted from this descriptors analysis. First, the transition states of the **TS_1** series tend to be lower in energy than the one of the **TS_2** series (Figure IV12). Second, the position of the counter-ion relative the

complex influences the energy and the most stable transition states are the ones where NTf_2^- is near the alkynyl; *i.e.* position **C** for $\mathbf{TS_1}$ and **E** for $\mathbf{TS_2}$ (Figure IV.12). Third, the descriptor yielding the strongest correlation is the distance between the coppers (Figure IV.13). The ideal distance seems to be 2.95 Å, at which both coppers are still coordinated to the naphthyridine backbone, and yet distant enough to accommodate the incoming alkyne. If the distance between the copper is shorter, the active site is very compact and steric hindrance destabilizes the transition state. If the coppers distance is longer, one of the copper dissociates from the naphthyridine backbone and thus the energy of the transition states increases. From this perspective, the energy barrier appears to be mostly controlled by steric effects.

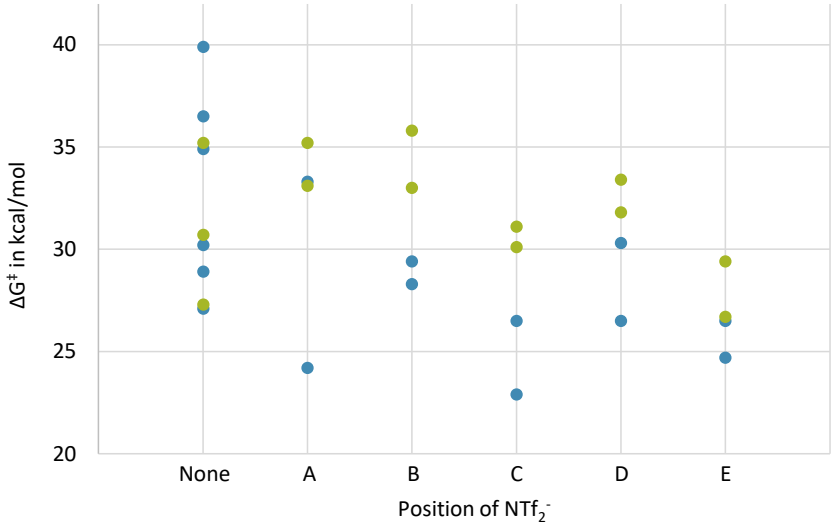

Figure IV.12. Energy of the transition states as function of the position of NTf_2^-.

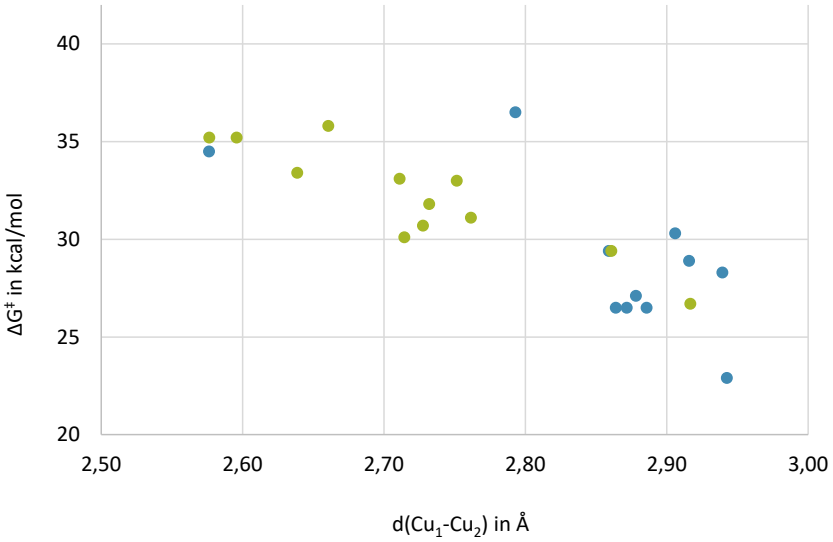

Figure IV.13. Energy of the transition states as function of the distance between the coppers, R^2 = 0.7080. Four points were off the trend and have been removed: [2.95;39.9], [3.58;27.3], [3.74;24.2] and [3.91;33.3].

3 - KIE calculations

The possibility of having kinetic isotope effects (KIE) was also considered in the DFT studies by replacing the transferred hydrogen atom in **$TS_{1\beta C}$** by deuterium. The KIE was modelled for the same substrate (*p*-tolylacetylene) and solvent (dichloromethane) used in the experiments, yielding k_H/k_D = 9.3. The experimental KIE,[153] k_H/k_D = 1.8 ± 0.2, was measured by exposing **1^+** to an excess of an equimolar mixture of *p*-tolylacetylene and *p*-tolylacetylene-d_1. There is a significant difference between the DFT and the experimental values of k_H/k_D but both are consistent with a normal and primary KIE. Further, this difference corresponds to a small energy quantity of only 1.0 kcal/mol. Two factors may exaggerate the KIE in the DFT calculations: overestimated linearity of the C···H···C moiety, on one hand, and underestimated contribution of the heavier elements (C and Cu) to the transition state vector, on the other.

4 - Microkinetics modelling of the C-H activation

To assess the agreement of our DFT mechanism with the experiments, a microkinetics model was created. By comparing the experimental conversion to the one predicted with the DFT mechanism, we can determine if our model represents the experiments well and estimate the error in the DFT barriers. In the experimental kinetics data, 50 and 100% conversion are reached at 15 and 90 minutes, respectively. To compute the microkinetics, the same conditions as in the kinetic experiments were used: 10 mM of $\mathbf{1}^{+}$, 21mM of alkyne, at 48.5°C in THF with 1 atm. The microkinetics model comprise two elementary steps (Figure IV.14): the reaction of $\mathbf{1_C}$ to $\mathbf{2_B}$ via $\mathbf{TS_{1\beta C}}$ and its reverse reaction. For the forward step, the $\Delta G^{\ddagger}_{f}$ is 22.9 kcal/mol while the reverse step has a $\Delta G^{\ddagger}_{r}$ of 48.6 kcal/mol. The coordination of the reactant and the dissociation of the product have been neglected as they do not have an impact on the microkinetics simulations. The conversion was computed via a time course simulation, with one point generated every 30 seconds for 90 min. The final conversion achieved with the DFT parameters was 18.2%. This conversion is too low compared to the experimental data.

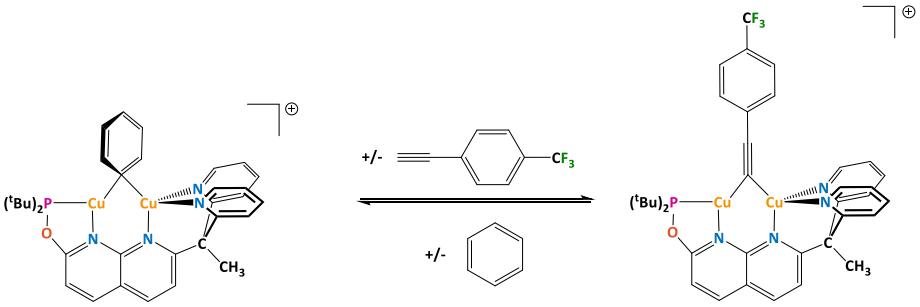

Figure IV.14. Elementary reactions considered for the microkinetics model of the $\mathbf{1_C}$ to $\mathbf{2_B}$ bridging ligand exchange.

To estimate the error in the DFT $\Delta G^{\ddagger}$ barrier, the simulated conversion was fitted to the experimental one by varying the free energy of $\mathbf{TS_{1\beta C}}$ (Figure IV.15 and Table IV.1). The fitted model with an error correction of -2.0 kcal/mol matches well with the experimental data: the conversion is 49.8 and 95.5 % at 15 and 90 minutes, respectively. Thus, the fitted $\Delta G^{\ddagger}$ values are 20.9 and

44.8 kcal/mol for the forward and reverse elementary steps. An error of -2.0 kcal/mol is within the range expected for DFT methods in the calculation of energy barriers. The overestimation of the barrier may originate from the complex features of our system, including:

- The involvement of 3 molecular entities: $\mathbf{1}^+$, NTf_2^- and the alkyne; increasing the sources of error in the computation of the free energies.
- The NTf_2^- ligand interactions, which have proven to be relevant, might be influenced by a complex combination of dispersion forces and solvation effects.

	Conversion at 15 min	Conversion at 90 min
Experiment	50	100
DFT model	3.4	18.2
Fitted model (-0.5)	7.3	34.2
Fitted model (-1.0)	14.9	56.9
Fitted model (-1.5)	28.7	80.3
Fitted model (-2.0)	49.8	95.5
Fitted model (-2.5)	74.0	99 (at 66 min)
Fitted model (-3.0)	92.3	99 (at 30 min)

Table IV.1. Comparison of the conversion between the experiments, the unfitted DFT model and the fitted model (error in kcal/mol).

Experimentally, the reaction rate is a first order in $\mathbf{1}^+$ and fractional in the alkyne (*p*-tolylacetylene). In contrast, the mechanistic model derived from the DFT calculations is first order in both $\mathbf{1}^+$ and the alkyne. This difference can be related to the following points:

- Our model considers only one reaction pathway but due to the complexity of this system, it is likely that multiple pathways are available and several equilibriums involving complexes formed from $\mathbf{1}^+$ and the alkynes potentially exist.
- Experimentally, to obtain the order in the alkyne, its concentration varied from 15 to 60 equivalent to $\mathbf{1}^+$. These reaction conditions are different to the rest of the experiment were the ratio was closer to 1:1 (alkyne:$\mathbf{1}^+$). With high concentration, the aggregation of the

alkyne or the creation of complexes involving several alkyne molecules cannot be excluded. Our model does not include these possibilities as it considers a 1:1 ratio.

- The solubility of the reactants can also play a role in this difference. Experimentally the solubility was reported as potentially challenging, with few solvents able to support the reaction. Computationally, the solvent is modelled implicitly only, thus dismissing interactions requiring the use of explicit models.

Overall, the DFT results suggest a viable pathway for C–H bond activation of alkyne at the dicopper centre. Even if it is not possible to connect fully the experimental and computational results together in a comprehensive way, the DFT results suggest a viable pathway for C–H bond activation at the dicopper centre. A more detailed description of the reaction mechanism, including competing pathways, will require more in-depth experimental and computational investigations.

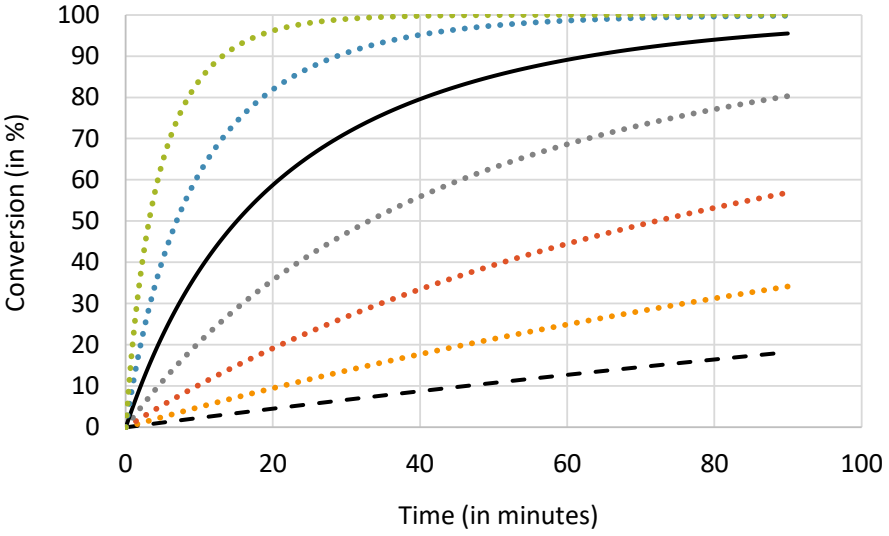

Figure IV.15. Comparison of the fitted microkinetics model: unfitted DFT model (black dashed line), fitted model with energy corrections in kcal/mol of -0.5 (orange dots), -1.0 (red dots), -1.5 (grey dots), -2.0 (black line), -2.5 (blue dots) and -3.0 (green dots).

V - C-H activation of alkynes catalyzed by water

At the beginning of this project, the experimental work was performed at room temperature. Back then, the preliminary results estimated the time required to complete the reaction from $\mathbf{1}^+$ to $\mathbf{2}^+$ to be 175h, *i.e.* over a week. Therefore, we searched a way to accelerate the reaction, considering the mechanistic details discussed in the previous chapter. Based on this knowledge, we proposed that water could be added to the reaction, since it could potentially ease the transfer of the proton from the alkyne substrate to the phenyl bridging ligand. The water molecule can assist the reaction in three different manners. The first possibility is related to the nature of $\mathbf{TS_{1THF}}$, and corresponds to a concerted mechanism where the water molecule solvates the transferred proton (Figure V.1a). However, this transition state never converged and H_2O always dissociated from the active site during the optimization. The second possibility is a proton shuttle: H^+ of the alkyne is transfer to H_2O that gives an H^+ to the phenyl (Figure V.1b), but no transition state could be converged, despite multiple attempts. The last attempt to find a water-assisted mechanism has a two steps (Figure V.1c). First, H^+ is transfer from H_2O to $\mathbf{1}^+$, leading to the release of benzene and the formation of the intermediate $\mathbf{4}^+$, in which a hydroxyl group is the bridging ligand (step A). Then, the H^+ is transferred from the alkyne to $\mathbf{4}^+$, recovering H_2O and forming $\mathbf{2}^+$ (step B). Thus, water catalyses the formation of $\mathbf{2}^+$. To assess its plausibility, we compute the thermodynamics of $\mathbf{4}^+$ compared to $\mathbf{1}^+$ and $\mathbf{2}^+$. $\mathbf{4}^+$ was found to be more stable than $\mathbf{1}^+$ by -7.8 kcal/mol and higher in energy than $\mathbf{2}^+$, which is -24.8 kcal/mol lower than $\mathbf{1}^+$. Thus, this reaction pathway is plausible, at least from the thermodynamics point of view. Before exploring this mechanism any further, it is worth mentioning that the addition of water has been experimentally tested. The presence of water has a dramatic effect on the kinetics of the reaction: the time to reach full conversion decreased from 90 to 60 min at 48.5°. This effect is consistent with a change in the mechanism towards a reaction pathway involving water through a lower energy barrier. Therefore, the mechanism for the water-assisted activation of alkynes was further explored.

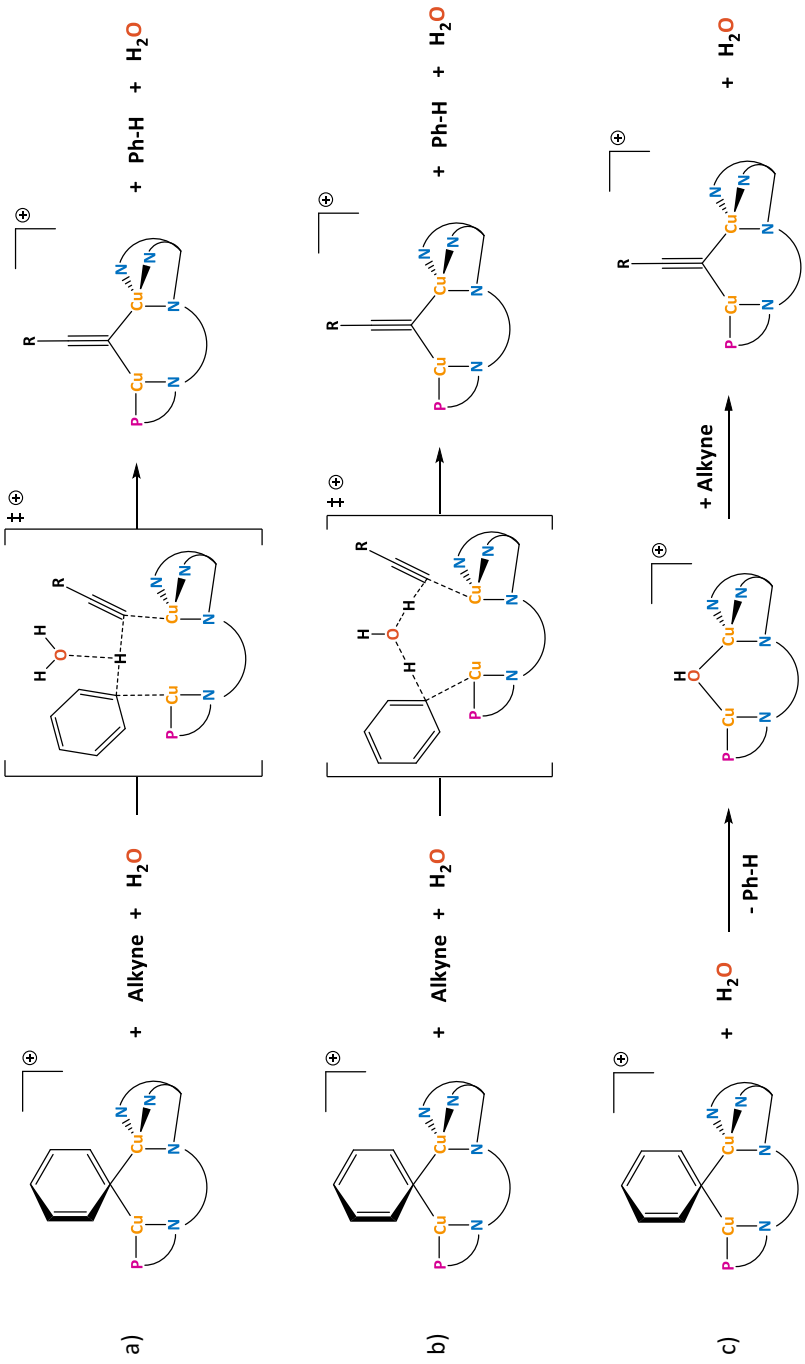

Figure V.1. Possible mechanisms for the activation of alkyne with water.

1 - Properties of the complex 4^+

Before searching for transition states, the properties of $\mathbf{4}^+$ were computed as it is a new intermediate and its geometry is different from the ones of $\mathbf{1}^+$ and $\mathbf{2}^+$ (Figure V.2a). The copper on the phosphine side is decoordinated from the naphthyridine backbone (2.45 Å), leading to an asymmetric bonding of the hydroxyl to the copper, with 1.89 and 1.97 Å for Cu_1 and Cu_2, respectively. It also results in a shorter bond between Cu_1 and the phosphine (2.18 Å) and the distance between the coppers is elongated to 2.67 Å. The effects of the partial dissociation of DPEOPN and the association with the counter-ion are described below. To compare the energetic impact of these effects, $\mathbf{4}^+$ is used as the energy reference.

To look at the association of $\mathbf{4}^+$ with NTf_2^-, the same five positions described in Figure III.8 are computed. The associations are thermoneutral or exergonic in one case (see Table V.1). $\mathbf{4_A}$ is the most stable complex, with an energy of -3.2 kcal/mol relative to $\mathbf{4}^+$, and the presence of NTf_2^- on top of the active site does not affect its geometry. However, the counter-ion interacts extensively with the ligands: it makes dispersion interactions with the phosphine and the pyridines and a hydrogen bond with the hydroxyl via one of its oxygen (2.10 Å). The relevance of such interactions is highlighted by the comparison between $\mathbf{4_A}$ and $\mathbf{4_B}$: they have extremely similar geometries but the latter is 3.7 kcal/mol higher than the former. This difference is due to the lack of interactions between the complex and NTf_2^-: as the counter-ion is on the side of the phosphine, it can only do weak interactions with the ^{t}Bu substituents. The complexes $\mathbf{4_C}$, $\mathbf{4_D}$ and $\mathbf{4_E}$ have similar geometries that vary only in two ways: the position of NTf_2^- and the length of the bond between Cu_1 and the naphthyridine backbone, varying between 2.30 and 2.53 Å. These differences do not impact the energy of these complexes, as there are in a range of 0.4 kcal/mol.

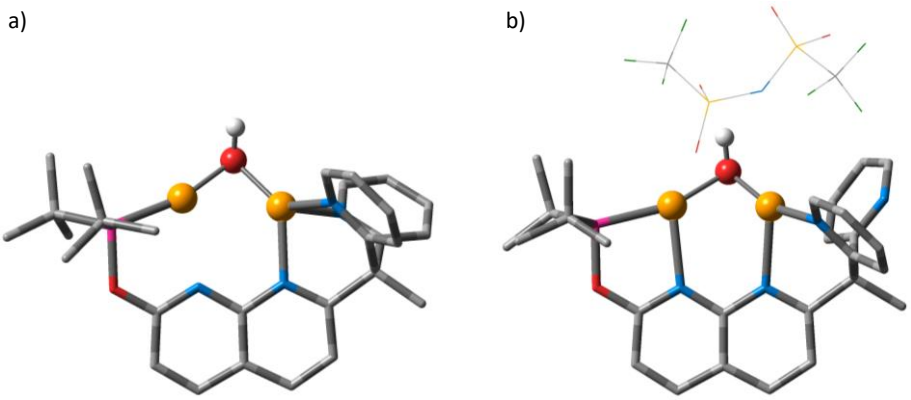

Figure V.2. 3D representation of a) 4^+ and b) 4_{pyrD}.

The three partial dissociations considered for $\mathbf{4}^+$ are the same ones as for $\mathbf{1}^+$ and $\mathbf{2}^+$: the rotation of the phosphine, of the pyridines arm and of one of pyridine (see Figure III.4 for more details), leading to the complexes $\mathbf{4}^+_{phos}$, $\mathbf{4}^+_{arm}$ and $\mathbf{4}^+_{pyr}$. The loss of the phosphine in $\mathbf{4}^+_{phos}$ leads to a very distorted complex, where the remaining bonds involving Cu_1 are contracted: the distance between the coppers is reduced by 0.2 Å, and the bonds to the hydroxyl and the naphthyridine backbone shorten to 1.86 and 1.91 Å, respectively. To allow this closer interaction, Cu_2 dissociates from the naphthyridine with a distance of 2.51 Å. These important changes in the geometry of $\mathbf{4}^+$, due to the dissociation of the phosphine, are not favourable as the energy of $\mathbf{4}^+_{phos}$ is 18.1 kcal/mol above $\mathbf{4}^+$. The dissociation of the pyridines arm also causes major changes to the geometry of $\mathbf{4}^+$: the distance between Cu_1 and the naphthyridine backbone increases even more to 2.72 Å, allowing the coordination sphere of Cu_1 to be nearly linear, with an angle of 176.6° between the phosphorus, Cu_1 and the oxygen of the hydroxyl versus 165.4° in $\mathbf{4}^+$. The coordination sphere of Cu_2 is also influenced: the Cu_2–ligand bonds are shortened (1.83 Å with the hydroxyl, and 1.94 Å with the naphthyridine), and its coordination sphere straightened (160.8° in $\mathbf{4}^+_{arm}$ and 134.2° in $\mathbf{4}^+$ for the angle between the naphthyridine, Cu_2 and the hydroxyl). These changes do not have a huge energetic impact, as $\mathbf{4}^+_{arm}$ is only 5.0 kcal/mol higher than $\mathbf{4}^+$. In contrast with $\mathbf{4}^+_{phos}$ and $\mathbf{4}^+_{arm}$, the dissociation of one pyridine causes small structural changes in $\mathbf{4}^+_{pyr}$: the coordination of the

hydroxyl to the coppers is even, with a bond length of 1.90 Å, and the distance between the coppers and the DPEOPN ligand vary within 0.2 Å. This dissociation lead to a low-energy intermediate at -2.7 kcal/mol. These three dissociations have the same energy range as the dissociations of $\mathbf{1}^+$ and $\mathbf{2}^+$ and they follow the same trend: their energetic cost is related to the strength of the coordination of the broken bonds: Cu-P > (Cu-N) x2 > Cu-N.

Position of NTf_2^-	ΔG (kcal/mol)	Position of NTf_2^-	ΔG (kcal/mol)
$\mathbf{4}_A$	-3.2	$\mathbf{4}_{pyrA}$	-5.1
$\mathbf{4}_B$	0.5	$\mathbf{4}_{pyrB}$	-2.2
$\mathbf{4}_C$	-0.3	$\mathbf{4}_{pyrC}$	-2.7
$\mathbf{2}_D$	-0.2	$\mathbf{4}_{pyrD}$	-6.1
$\mathbf{4}_E$	-0.6	$\mathbf{4}_{pyrE}$	-2.5

Table V.1. Free energy of ion-paring for 4^+ and 4^+_{pyr}. The energy reference is the energy of 4^+ added to the energy of NTf_2^- for both series.

The combined effects of both the ion-pairing with NTf_2^- and the partial dissociation of DPEOPN on $\mathbf{4}^+$ were investigated and only $\mathbf{4}^+_{pyr}$, the most stable dissociation was kept. Again, the same five positions around the complex (**A** to **E**) were computed leading to the $\mathbf{4}_{pyrX}$ series. The two most stable structures are $\mathbf{4}_{pyrD}$ (Figure V.2b) and $\mathbf{4}_{pyrA}$, with -6.1 and -5.1 kcal/mol, respectively. They have several common characteristics. NTf_2^- is on top of the complex and does a hydrogen bond with the hydroxyl via one of its oxygen atoms (2.00 and 2.04 Å for $\mathbf{4}_{pyrD}$ and $\mathbf{4}_{pyrA}$, respectively). The hydroxyl is coordinated symmetrically to the coppers with a distance of 1.91 Å in both cases. The main difference between $\mathbf{4}_{pyrA}$ and $\mathbf{4}_{pyrD}$ is the coordination of the coppers to the naphthyridine backbone: in the latter the coordination is symmetrical, with a distance of 2.25 Å, while asymmetrical in the former. The bond involving Cu_2 is 0.1 Å longer than the one with Cu_1 (2.20 and 2.31 Å). The complexes $\mathbf{4}_{pyrC}$ and $\mathbf{4}_{pyrE}$ share similar features, the main one being the coordination of NTf_2^- to Cu_1 by one of its oxygen, with distances of 2.32 and 2.23 Å, respectively. This coordination does not affect the geometry of $\mathbf{4}_{pyrC}$ and modify slightly the distances between the coppers and the naphthyridine backbone (0.1 Å) in $\mathbf{4}_{pyrE}$. As expected with such similarities, the energy of

these two complexes are very close, differing by only 0.2 kcal/mol. The most stable isomer of $\mathbf{4}^+$ is $\mathbf{4}_{\mathbf{pyrD}}$, which include the effects of the ion-pairing with NTf_2^- and the dissociation of one pyridine. $\mathbf{4}_{\mathbf{pyrD}}$ is 11.4 kcal/mol lower than $\mathbf{2}_{\mathbf{B}}$, showing that this reaction is thermodynamically favourable.

2 - Step A: the formation of 4^+

To ease the description of the transition states and their analysis, the key atoms have been labelled as shown in Figure V.3. These labels do not change depending on the isomers or on the presence of additional molecules like the counter-ion. For all the energy barriers mentioned below, $\mathbf{1}^+$ and $\mathbf{1}_{\mathbf{C}}$ were used as the energy reference, depending on the presence of NTf_2^-. All the energy of the transition states reported in this chapter are listed in tables in the annex A.

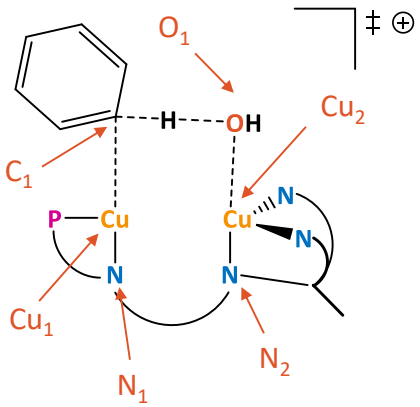

Figure V.3. Labels of the key atoms in the transition states connecting 1^+ to 4^+.

a) Search of the transition states

The first step of the mechanism of the water-assisted activation of alkyne corresponds to a proton transfer between the phenyl in $\mathbf{1}^+$ and H_2O. A concerted transition state is postulated for this step and as for the concerted C-H activation mechanism (see the previous chapter), there are two different isomers: the water molecule can coordinate to the copper on the pyridine side or on the phosphine side of $\mathbf{1}^+$. This approaches are not equivalent and

are further referred as the **TS$_3$** and **TS$_4$** series and all their related transition states are represented schematically on the Figures V.4 and V.5 for the former and V.8 and V.9 for the latter.

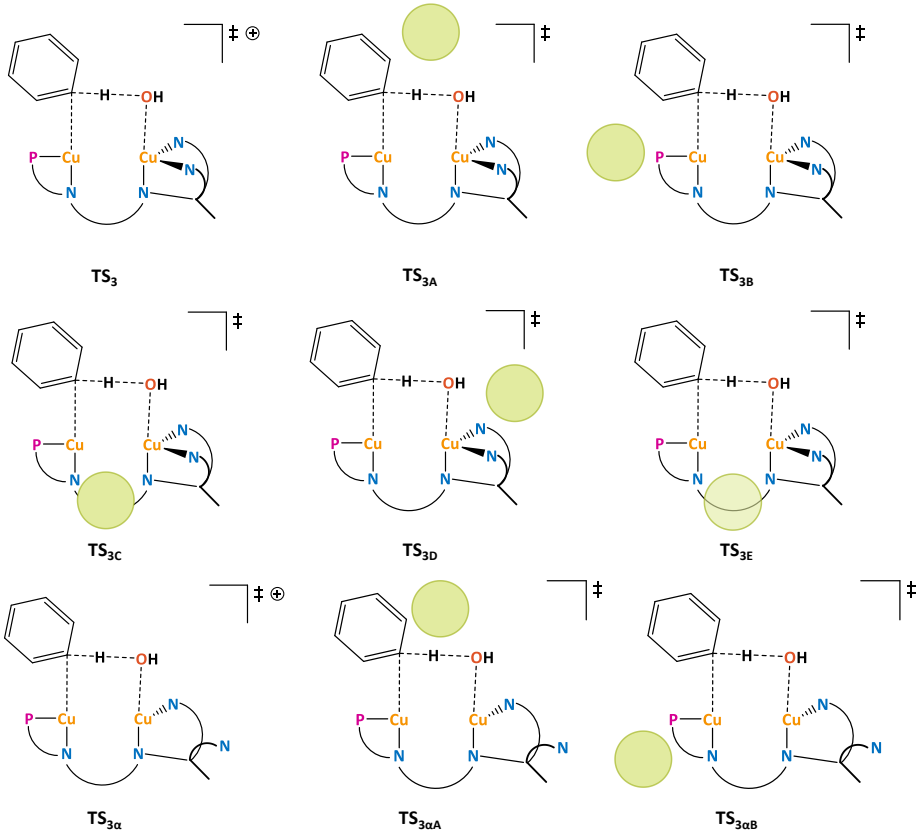

Figure V.4. Schematic representations and labels of all the transition states computed for the TS$_3$ series; the green circles represent the position of NTf_2^- (1/2).

For **TS$_3$** series, 18 transition states were considered and are shown in Figures V.4 and V.5. The simplest one is **TS$_3$** (in red in Figure V.6 and Figure V.7a), in which DPEOPN is fully coordinated to the coppers and the counter-ion is not included. **TS$_3$** is quite distorted with a distance between the coppers of 2.81 Å, in the same range as **TS$_1$**, and a dihedral angle Cu_1-N_1 -N_2-Cu_2 of 32.2°. Both the naphthyridine backbone and the pyridines are coordinated asymmetrically to the coppers, with a difference of 0.09 Å for the formers and

0.07 Å for the latter. The phenyl and hydroxyl groups have similar bond length with the coppers, 2.04 Å for the former and 2.00 Å for the latter, respectively. The proton is much closer to the hydroxyl than the phenyl: 1.18 vs 1.48 Å, thus the forming bond is more elongated than the breaking one, like in the **TS_1** and **TS_2** series. Overall, this transition state has a geometry similar to the previous ones but with a much lower $\Delta G^{\ddagger}$ barrier of 23.0 kcal/mol. This result is consistent with the increased reactivity observed in the experiments.

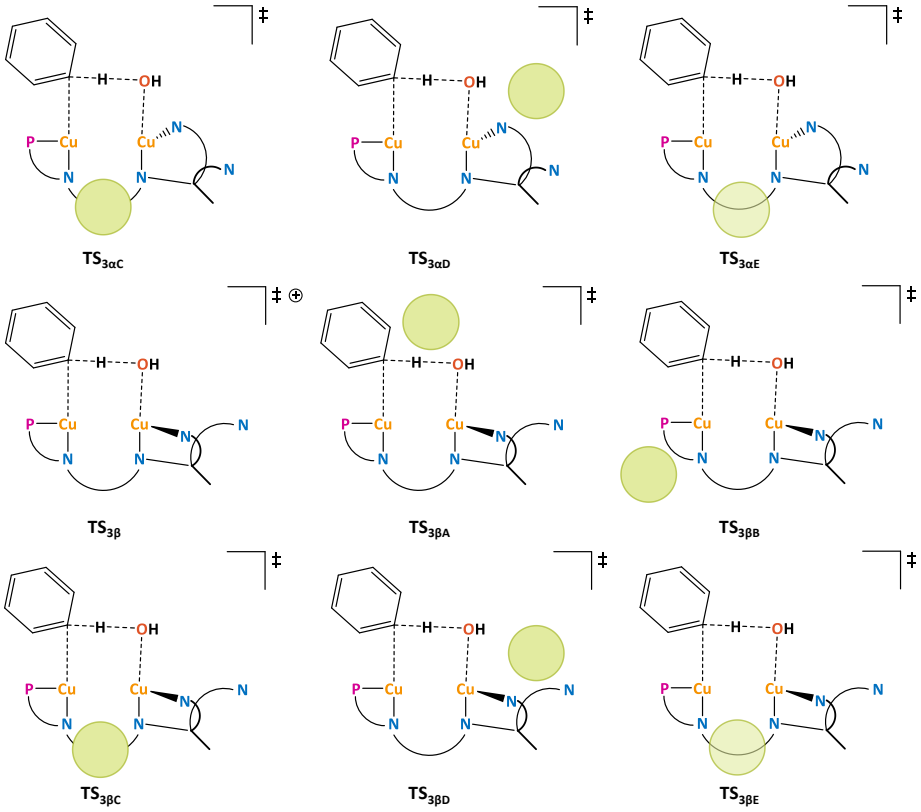

Figure V.5. Schematic representations and labels of all the transition states computed for the TS_3 series; the green circles represent the position of NTf_2^- (2/2).

As this water-assisted pathway seemed promising, the effects of the ion-paring with NTf_2^- and of the partial dissociation of DPEOPN were inquired, to allow its comparison to **$TS_{1\beta C}$**, the most stable transition state of the concerted activation of the alkynes. First, the effects of the ion-paring are described and

it corresponds to the **TS_{3X}** series, where X stands for the position of NTf_2^- around the complex (Figure V.4). The changes introduced by NTf_2^- have little impact on the energy as the five **TS_{3X}** are within a narrow energy range of 1.5 kcal/mol (in red dashed in the Figure V.6) and the association varies from being isoenergetic (**TS_{3E}**) to slightly unfavourable (**TS_{3D}**). The geometry of the transition states of this series share some common traits: the distance between the coppers and the ligands are similar to the ones in **TS_3**, as well as the distances of the breaking and forming bonds involving the proton. However, the distances between the two coppers show larger fluctuations, with values varying from 2.68 Å in **TS_{3D}** to 2.97 Å in **TS_{3A}**. In the **TS_{3X}** series, NTf_2^- never interacts directly with the coppers but does many weak interactions with DPEOPN. In **TS_{3A}** (Figure V.7b), **TS_{3B}** and **TS_{3D}**, there is a hydrogen bond between the hydroxyl and one of the oxygens of NTf_2^- and another with one of its fluorine atoms, with distances of 1.86 and 2.54 Å, respectively. Thus, the association of NTf_2^- to **TS_3** induce some geometrical changes resulting in slightly higher energy barriers.

To investigate the effects of the partial dissociation of DPEOPN on **TS_3**, only the dissociations involving one pyridine were kept, leading to **$TS_{3\alpha}$** and **$TS_{3\beta}$**. The overall geometry of these transition states are not impacted by the dissociation compared to **TS_3**: the remaining bond between Cu_2 and DPEOPN is only shortened by 0.05 Å, while the distance between the coppers increases by 0.1 Å and 0.05 Å in **$TS_{3\alpha}$** and **$TS_{3\beta}$** (Figure V.7c). The energy of **$TS_{3\alpha}$** is 23.5 kcal/mol and thus, this dissociation has no energy cost. However, the dissociation of the pyridine **β** is favourable by 2.3 kcal/mol, giving a barrier of 20.7 kcal/mol.

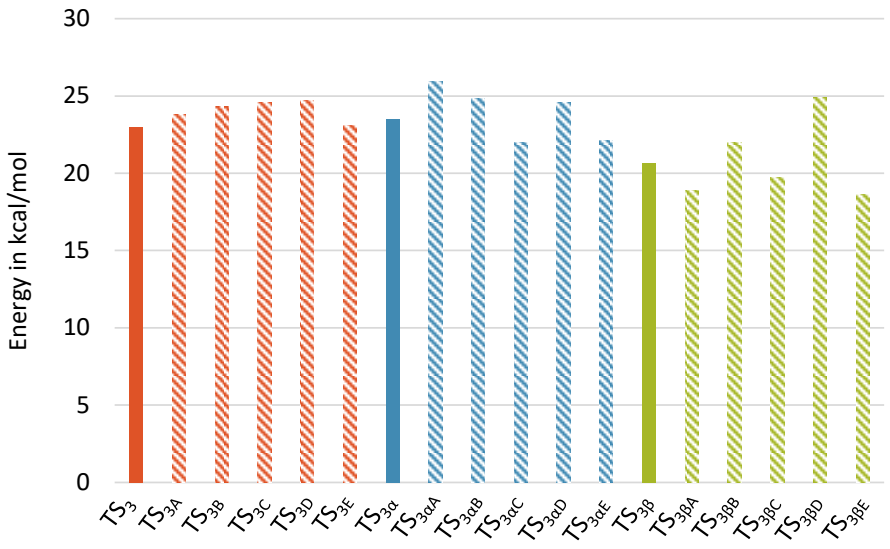

Figure V.6. Free energy of all the transition states for the TS_3 series.

These two transition states are 2.8 kcal/mol apart and while this difference is significant, they were both kept to unravel the effects of combining the ion-paring with the partial dissociation of DPEOPN. The **$TS_{3\alpha X}$** series is composed of five transition states corresponding to the association of NTf_2^- (positions X = **A** to **E**) with **$TS_{3\alpha}$**. The energy of these transition states are reported in blue dashed in Figure V.6. The two lowest transitions states of this series are **$TS_{3\alpha C}$** and **$TS_{3\alpha E}$**, with an energy of 22.1 and 22.0 kcal/mol. Their geometry are extremely similar to **TS_3**. The only difference between them is the position of NTf_2^- but it does weak interactions with the ^{t}Bu substituents of the phosphine and with the naphthyridine backbone in both cases. In **$TS_{\alpha C}$**, NTf_2^- interacts also with the coordinated pyridine while it interacts with the dissociated pyridine and the phenyl ring in **$TS_{3\alpha E}$**. These differences do not impact their energy. In the **$TS_{3\alpha X}$** series, two other transition states have very close geometries: **$TS_{3\alpha A}$** and **$TS_{3\alpha D}$**. They have a distance between the coppers of 2.80 Å, 0.1 Å longer than in **$TS_{3\alpha}$** and NTf_2^- does a hydrogen bond with the hydroxyl via one of its oxygen (1.82 Å). The energy of these transition states is higher, with 25.9 and 24.6 kcal/mol, showing again that a closer interaction

between the complex and the counter-ion does not necessarily lead to a lower energy.

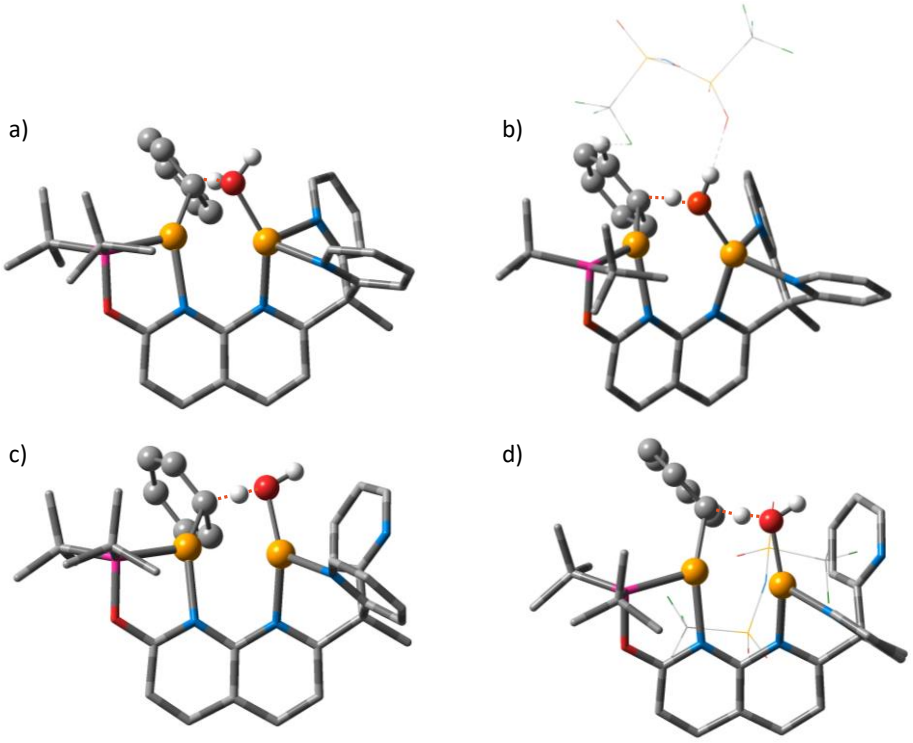

Figure V.7. 3D representation of a) TS_3, b) TS_{3A}, c) $TS_{3\beta}$ and d) $TS_{3\beta E}$. The red dashed lines account for the cleavage and formation of bonds between the phenyl and hydroxyl moieties.

The **$TS_{3\beta X}$** series (Figure V.5) is more homogeneous: the geometries of the five transition states are similar to **$TS_{3\beta}$**. The only difference is the position of NTf_2^- which yields an energy range of 6.3 kcal/mol, going from 18.6 kcal/mol for **$TS_{3\beta E}$** up to 24.9 kcal/mol for **$TS_{3\beta D}$**. As they are all akin, only the lowest is described here (Figure V.7d). In **$TS_{3\beta E}$**, the distance between the coppers is 2.72 Å and the remaining bonds between the coppers and DPEOPN are not impacted by the loss of the back pyridine. A dissymmetry exists in the coordination of the coppers to the naphthyridine backbone (2.16 Å for Cu_1 and 2.00 Å for Cu_2), but this difference was already present in **TS_3**. The hydroxyl and the phenyl are closely coordinated to Cu_2 (1.94 Å) and to Cu_1

(2.04 Å), respectively. The transferred proton is closer to the hydroxyl than to the phenyl, with interatomic distances of 1.18 and 1.45 Å, respectively. The counter-ion is located in the cavity created by the two arms of the naphthyridine backbone. It only does weak interactions with DPEOPN and the phenyl, and it has no interaction with the coppers nor the hydroxyl. **$TS_{3\beta E}$** is the lowest transition state of the **TS_3** series. It shows the importance of combining the effects of the partial dissociation of DPEOPN and the ion-pairing with NTf_2^-, despite that these effects can increase the energy of the transition states when considered separately.

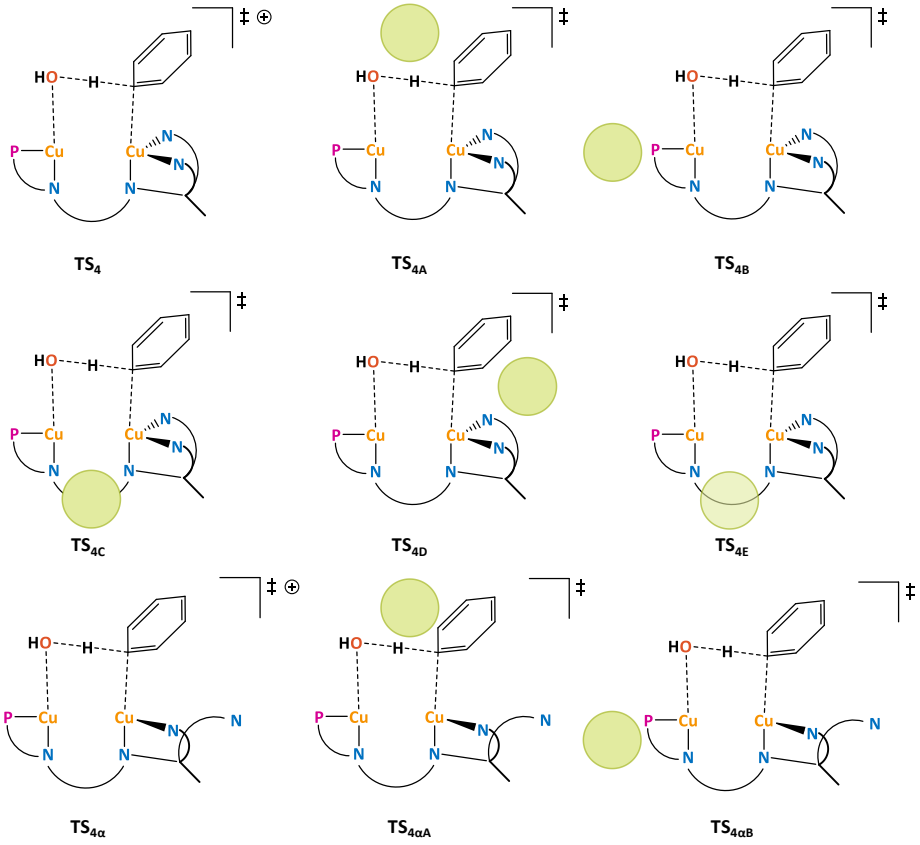

Figure V.8. Schematic representations and labels of all the transition states computed for the TS_4 series; the green circles represent the position of NTf_2^- (1/2).

The **TS_4** series was also investigated and the 18 transition states considered are displayed in the Figures V.8 and V.9. The simplest one is **TS_4** (in red in Figure V.10 and Figure V.11a), where all the part of DPEOPN are coordinated to the coppers and the counter-ion is excluded. The geometry of **TS_4** shares similar features with **TS_3**, despite the isomerism. **TS_4** is quite distorted, with a distance of 2.85 Å between the coppers and a dihedral angle of 30.8° between Cu_1-N_1-N_2-Cu_2. The hydroxyl is closely coordinated to Cu_1 while the phenyl has a longer bond with Cu_2, with distances of 1.94 and 2.04 Å, respectively. The transferred proton is also closer to the hydroxyl than to the phenyl with distances of 1.18 and 1.40 Å. Due to the presence of the bulky phenyl ring on Cu_2, the pyridines arm shifts in front of the complex to ease the steric hindrance in the active site. **TS_4** has a $\Delta G^{\ddagger}$ of 23.6 kcal/mol, which is only 0.6 kcal/mol higher than **TS_3**. Thus, the impact of the ion-paring with NTf_2^- and of the partial dissociation of DPEOPN on **TS_4** were investigated.

TS_4 is more affected by the presence of NTf_2^- in its environment than **TS_3**, with a wide range of energies; from 19.6 to 25.8 kcal/mol (red dashed in Figure V.10). The lowest one is **TS_{4A}** and it is the lowest transition state of the entire **TS_4** series. Its geometry is heavily impacted by the presence of NTf_2^- on top of the complex. The pyridines arm is pushed forward even more, leading to the dissociation of Cu_2 from the naphthyridine backbone, with a distance of 2.77 Å (Figure V.11b). The bond between Cu_1 and the naphthyridine is elongated to 2.18 Å, causing a shortening of the other bonds with Cu_1 to 2.18 Å with the phosphine and 1.88 Å with the hydroxyl. These modifications lead to an increasing distance between the coppers, as they are 4.00 Å apart. In **TS_{4A}**, NTf_2^- interacts mainly with the hydroxyl, with which it does two hydrogen bonds via two of its oxygens, at 1.97 and 2.33 Å. These interactions are supposedly the ones that stabilize **TS_{4A}** compared to the other transition states of the **TS_4** series. The other positions of NTf_2^- lead to higher energies, from 22.6 kcal/mol for **TS_{4E}**, up to 25.8 kcal/mol for **TS_{4B}**. The impact of the counter-ion on geometry is smaller in these cases: there is no decoordination or elongation of the bonds between the coppers and DPEOPN. However, the distance between the coppers varies significantly from 2.73 Å in **TS_{4C}** to 3.05 Å on **TS_{4B}**. In these four transition states, NTf_2^- interacts only via dispersion interactions with the ligands. Overall, the counter-ion has an important effect

on **TS$_4$**, as it lowers the barrier by 4.0 kcal/mol and influence the geometry dramatically.

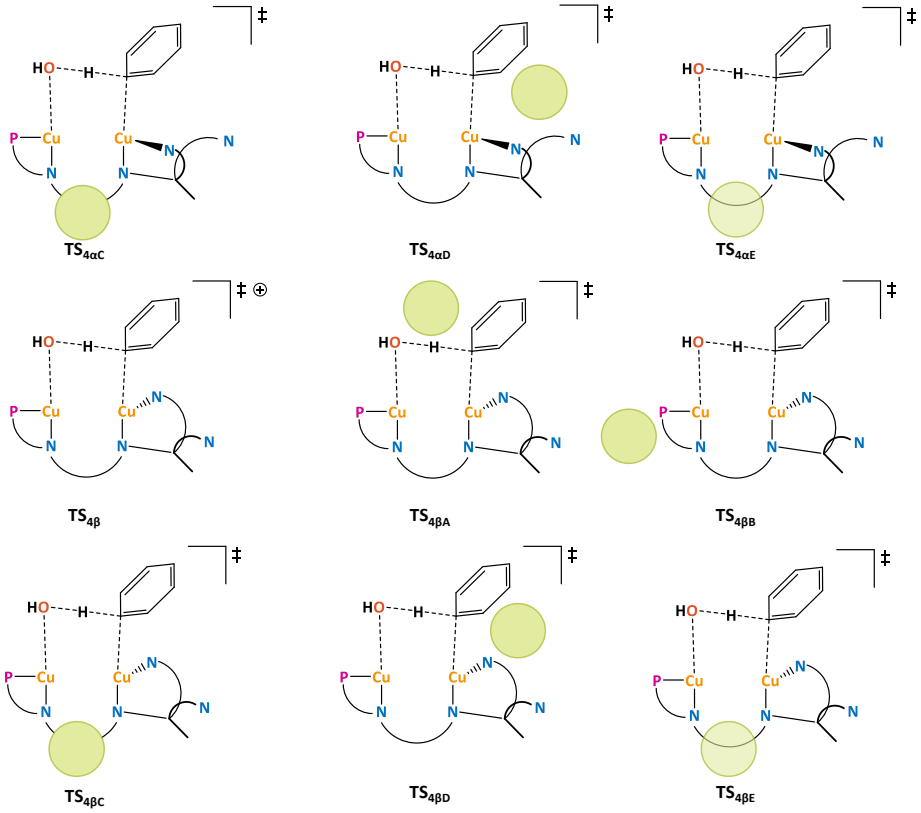

Figure V.9. Schematic representations and labels of all the transition states computed for the TS$_4$ series; the green circles represent the position of NTf_2^- (2/2).

To be consistent with the **TS$_3$** series, the only partial dissociation considered is the rotation of one pyridine, leading to **TS$_{4\alpha}$** and **TS$_{4\beta}$** for the dissociation of the front and back pyridine, respectively (Figures V.8 and V.9). These two transition states have extremely similar geometries where the only difference is the distance between the coppers: it is longer in **TS$_{4\beta}$** than in **TS$_{4\alpha}$** (2.91 and 2.80 Å). The other distances between the coppers and the ligands are the same as in **TS$_4$**, except for a slight dissymmetry in the coordination of the coppers to the naphthyridine backbone (2.05 Å for Cu_1 and 2.16 Å for Cu_2 on average). These minimal modifications of the geometry lead to lower

energies: 22.1 kcal/mol for **TS$_{4\alpha}$** and 20.8 kcal/mol for **TS$_{4\beta}$** (Figure V.11c). It displays once more the importance of the partial dissociation of DPEOPN in the reactivity of **1**$^{+}$.

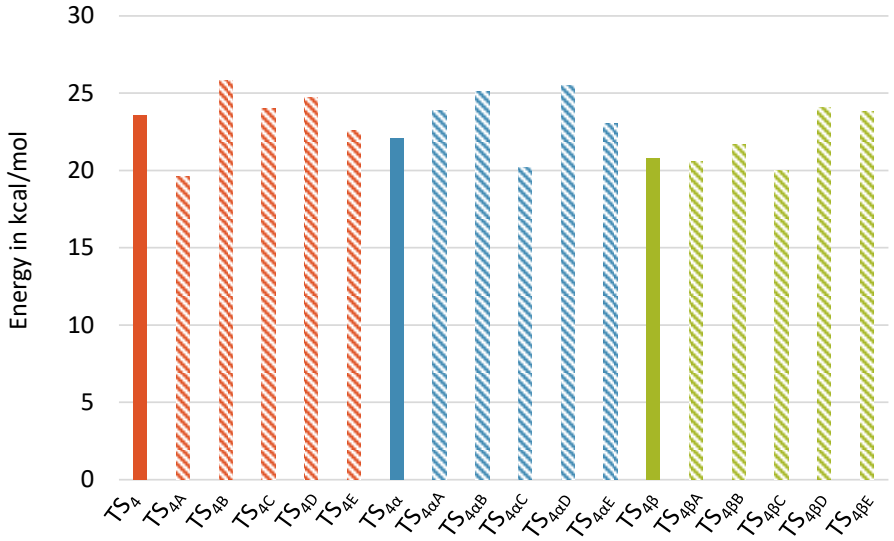

Figure V.10. Free energy of all the transition states of the TS$_4$ series.

Both **TS$_{4\alpha}$** and **TS$_{4\beta}$** were kept for the investigation on the combined effects of the ion-pairing and of the partial dissociation of DPEOPN, as they are only separated by 1.3 kcal/mol, leading to the **TS$_{4\alpha X}$** and **TS$_{4\beta X}$** series. All the transition states in the former series are akin to **TS$_{4\alpha}$**. The distance between the coppers varies only between 2.76 and 2.83 Å and the most noticeable difference is in the way the coppers coordinate to the naphthyridine backbone. In some transition states, they are coordinated symmetrically, as in **TS$_{4\alpha C}$**, or unsymmetrical like in **TS$_{4\alpha A}$** (with the largest difference being 0.2 Å) but there is no dissociation from the naphthyridine backbone. The energy range of this series is from 20.2 to 25.5 kcal/mol (blue dashed Figure V.10). The lowest one is **TS$_{4\alpha C}$**, where NTf_2^- is in the cavity formed by the two arms of the naphthyridine backbone. It allows the counter-ion to interact with all the parts of DPEOPN as well as with the phenyl ring but there is no direct

contact with the coppers nor the hydroxyl. The addition of NTf_2^- to **$TS_{4\alpha}$** lowers its energy by 1.9 kcal/mol.

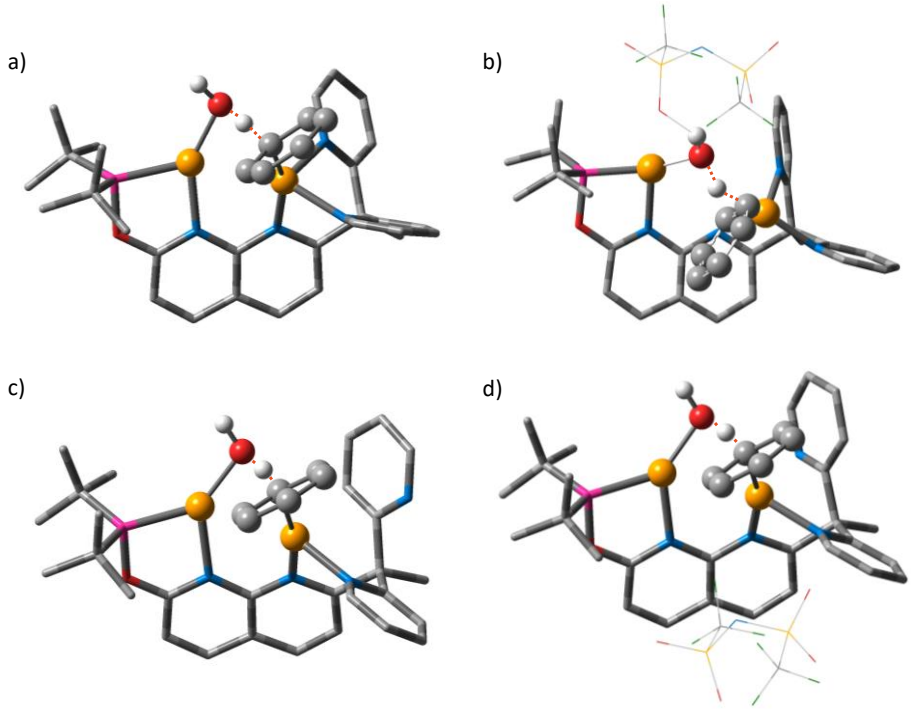

Figure V.11. 3D representation of a) TS_4, b) TS_{4A}, c) $TS_{4\beta}$ and d) $TS_{4\beta C}$. The red dashed lines account for the cleavage and formation of bonds between the phenyl and the hydroxyl moieties.

The association of NTf_2^- with **$TS_{4\beta}$** prompts to a large variety of geometries within an energy range of 20.0 to 24.1 kcal/mol (green dashed Figure V.10). The two lowest transitions states have very similar energies; 20.0 kcal/mol for **$TS_{4\beta C}$** (Figure V.11d) and 20.6 kcal/mol for **$TS_{4\beta A}$**; but very different characteristics. **$TS_{4\beta A}$** is extremely distorted, with a distance of 3.67 Å between the coppers, due to the dissociation of Cu_1 from the naphthyridine backbone (2.95 Å). As Cu_1 is further away from DPEOPN, it is more accessible to NTf_2^-, which coordinates to it via one of its oxygen (1.42 Å). Another oxygen does a hydrogen bond with the hydroxyl (1.87 Å), which is usual for the position **A**. In contrast, there is no impact on the geometry of **$TS_{4\beta}$** when paired with NTf_2^- in the position **C**. The counter-ion is interacting via dispersion with the

phosphine, the naphthyridine backbone, the dissociated pyridine and the phenyl but there is not direct interactions with the coppers nor the hydroxyl. Overall, the ion-pairing with NTf_2^- is the most relevant effect on **TS$_4$** at it gives the lowest transition state of the series with **TS$_{4A}$**. However, it is important to note that several transition states that also include the partial dissociation of DPEOPN are close to the energy of **TS$_{4A}$** (3 within 1 kcal/mol).

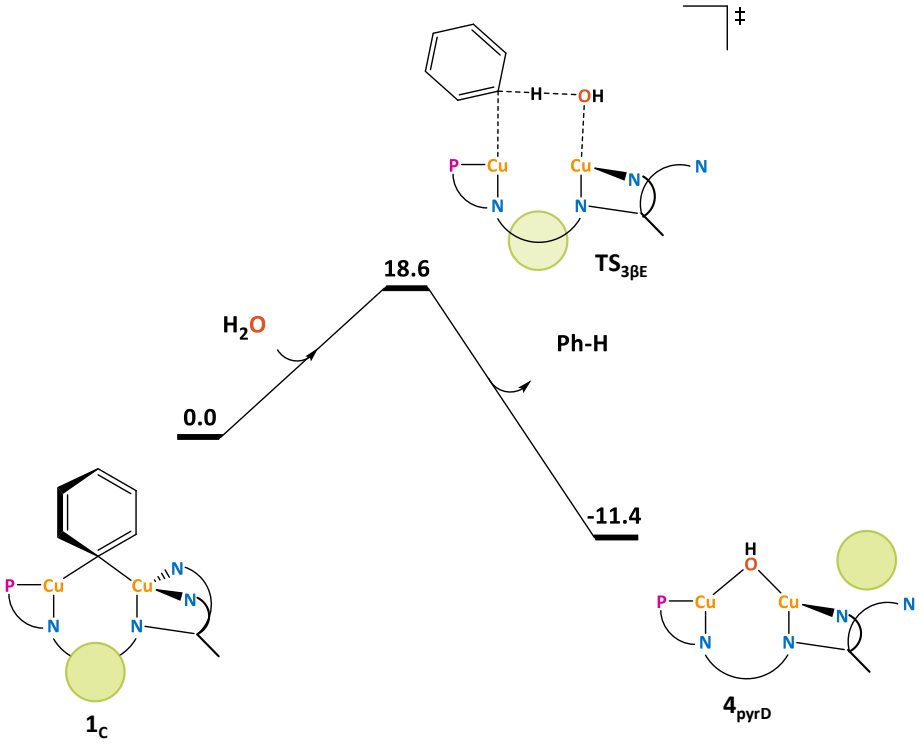

Figure V.12. Schematic representation of the mechanism from 1^+ to 4^+; the green circles represent the position of NTf_2^-.

The **TS$_4$** series leads to several low lying transition states; however, none of them are lower than **TS$_{3βE}$**, the lowest transition state for the first step of the water-assisted activation of alkynes by **1**$^+$, with a $\Delta G^‡$ of 18.6 kcal/mol. As for the concerted mechanism, both the partial dissociation of DPEOPN and the ion-pairing with NTf_2^- are involved in this mechanism, enforcing their relevance. A collection of transition states, from both the **TS$_3$** and **TS$_4$** series,

have been selected to undergo an IRC-driven relaxation. In most cases, including **$TS_{3\beta E}$**, the transition states relax directly to **1^+** and **4^+**. The mechanism for this first step is summarized in Figure V.12. Through this mechanism, the natural charge of H decreases as it transfers from H_2O to the phenyl (+0.47 to +0.22) consistently with the electronegativity of the atoms it is bonded to (O_1 or C_1). The charge of O_1 increases (-0.94 to -1.14) as it coordinates to the coppers while the charges of C_1 decreases (-0.60 to -0.22) as it dissociates from them.

b) Descriptors analysis of the transition states

The 36 transition states obtained for the first step of the water-assisted activation of alkynes were analysed using descriptors, defined by 15 different geometrical and electronic parameters. These descriptors include:

- Position of NTf_2^-
- Distance between Cu_1 and Cu_2
- Distance between the C_1 and O_1
- Distance between H and C_1
- Distance between H and O_1
- Dihedral angle Cu_1-N_1-N_2-Cu_2
- Natural charge of Cu_1
- Natural charge of Cu_2
- Difference of natural charge between Cu_1 and Cu_2
- Natural charge of the C_1
- Natural charge of the O_1
- Difference of natural charge between C_1 and O_1
- Natural charge of H
- Difference of natural charge between H and C_1
- Difference of natural charge between H and O_1

The following Figures V.13 and V.14 and in the additional *Descriptors file* (see annexes) are scatter plots showing the potential correlations between these descriptors and the energy barriers of the transition states. All the transition states related to the **TS_3** series are represented in blue dots while the ones related to the **TS_4** series are in green dots. As previously stated, the lowest transitions states are taking into account the ion-pairing, the partial dissociation of DPEOPN or both combined. The first noticeable feature is that the transition states are less distorted, with most of the transition states having their distance between the coppers ranging from 2.65 to 2.85 Å, versus 2.70 and 3.00 Å in the transition states of the concerted C-H activation mechanism. The lower distortions in the **TS_3** and **TS_4** series can be due to the smaller size of the incoming reactant (water versus alkyne). The second characteristic that arise from these figures is that the two series form clusters when looking at the natural charge of Cu_1 (Figure V.13): all the transition states from **TS_3** series have a δ_{Cu1} around 0.40 while the one from the **TS_4** series have a δ_{Cu1} around 0.50. This clustering might be cause by the different ligand coordinated to Cu_1 in these series. In **TS_3**, the phenyl ligand is bounded to Cu_1 while it is the hydroxyl in **TS_4**. The hydroxyl polarizes it bond with Cu_1 more than the phenyl, causing the δ_{Cu1} to be higher for **TS_4** series than **TS_3**. With this hypothesis, the reverse should be expected for Cu_2: a natural charge higher for the **TS_3** series than for **TS_4**. The trend is not as clear (Figure V.14) as no cluster are observed even if the values from the **TS_4** series tend to be lower. There is no other correlation to report since the highest R^2 value is 0.1642 for the natural charge of Cu_2.

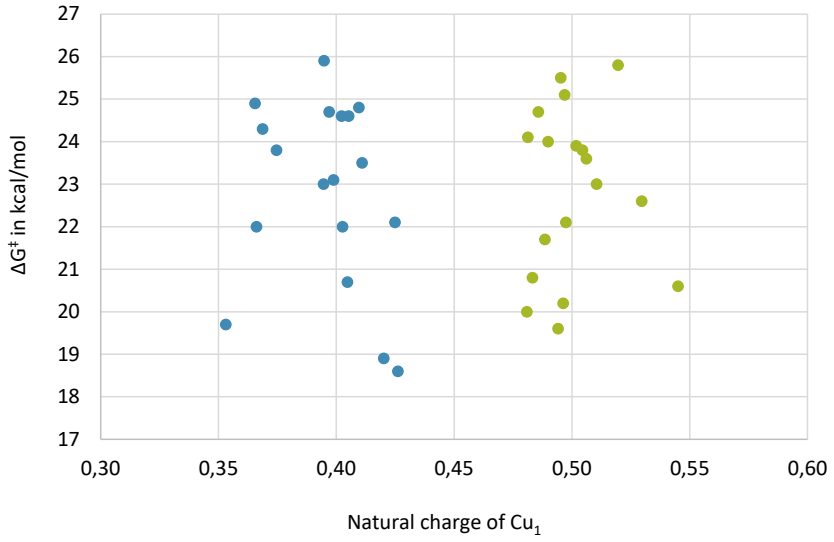

Figure V.13. Energy of the transition states as function of the natural charge of Cu_1, R^2 = 0.0017. No point has been removed.

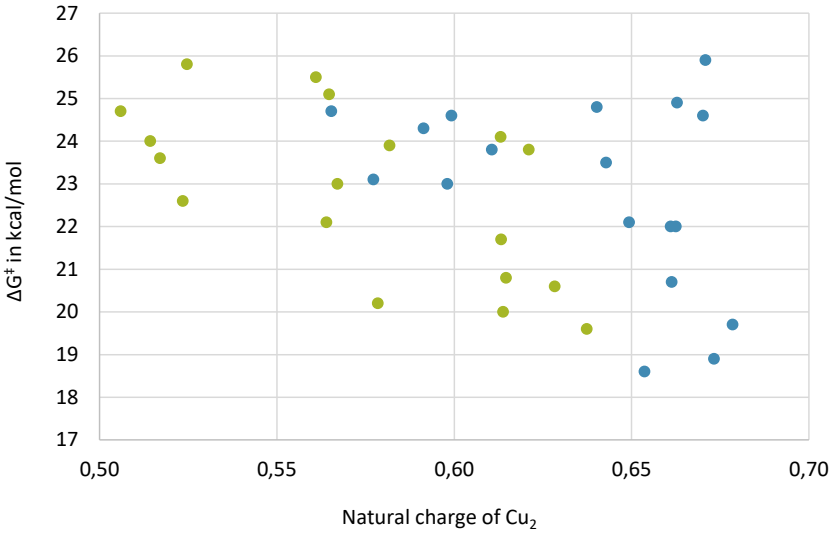

Figure V14. Energy of the transition states as function of the natural charge of Cu_2, R^2 = 0.1642. No point has been removed.

3 - Step B: the formation of 2^+

To ease the description of the transition states and their analysis, the key atoms have been labelled as shown in Figure V.15. These labels do not change depending on the isomers or on the presence of additional molecules to the transition state, like the counter-ion. For all the energy barriers mentioned below, $\mathbf{4}^+_{pyr}$ and $\mathbf{4}_{pyrD}$ were used as the energy reference as they are the lowest isomers of $\mathbf{4}^+$, depending on the presence of the counter-ion.

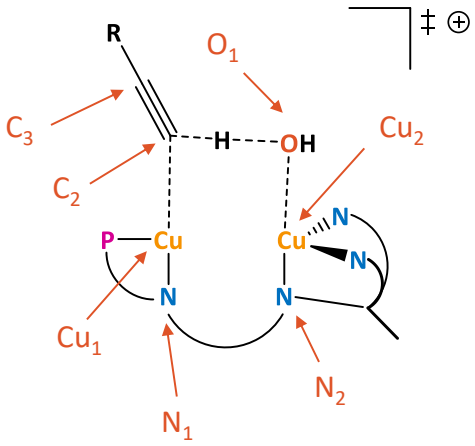

Figure V.15. Labels of the key atoms in the transition states connecting 4^+ to 2^+.

a) Search of the transition states

The second step of the water-assisted activation of alkynes consists of the proton transfer between the hydroxyl in $\mathbf{4}^+$ and an alkynyl to form $\mathbf{2}^+$ and regenerate H_2O. As for the previous step (see above), there are two isomers of the transition state: the alkyne can coordinate on the pyridine side or on the phosphine side and these approaches are not equivalent and are further referred as the $\mathbf{TS_5}$ and $\mathbf{TS_6}$ series. All the transition states are represented schematically on the Figure V.16 for the $\mathbf{TS_5}$ series and on the Figures V.19 and V.20 for the $\mathbf{TS_6}$ series.

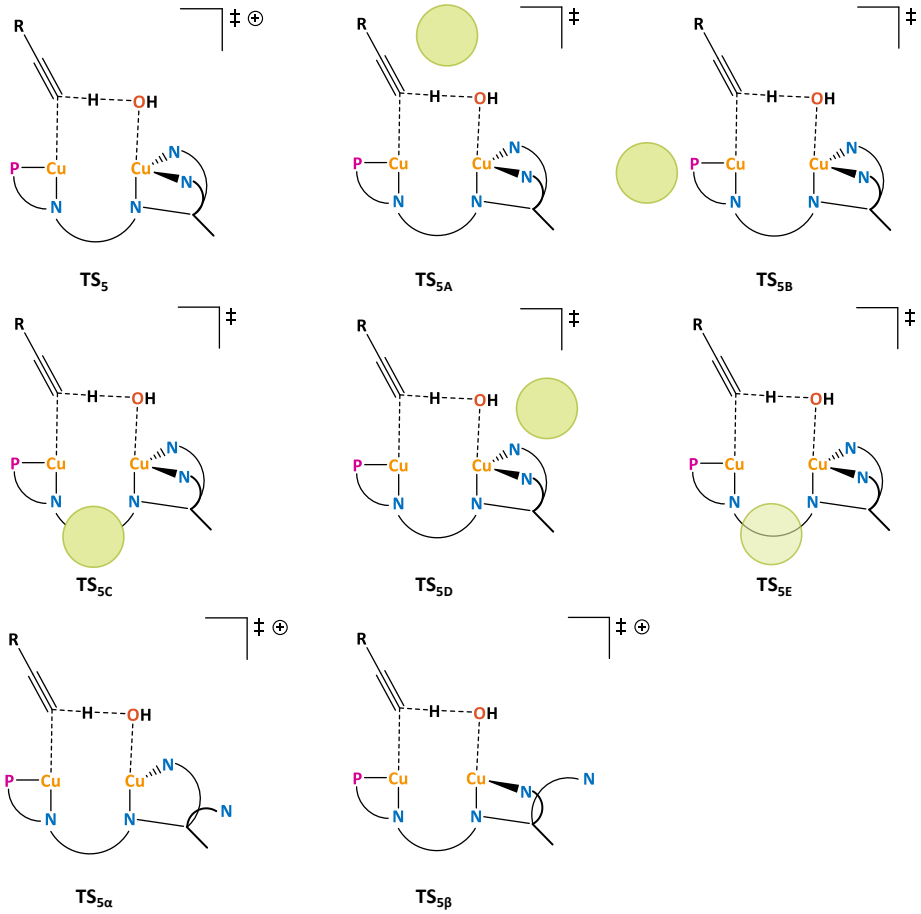

Figure V.16. Schematic representations and labels of all the transition states computed for the TS_5 series; the green circles represent the position of NTf_2^-.

For the **TS_5** series, 8 transition states (Figure V.16) have been considered. The simplest one is **TS_5**, where DPEOPN is fully coordinated and the association with the counter-ion is neglected (in red Figure V.17 and Figure V.18a). The most noticeable characteristic is how compact this transition state is compared to the previous ones, with a distance of 2.64 Å between the coppers, similar to the one in **4^+**. As the coppers are close together, the hydroxyl is asymmetrically bound to both (2.00 Å to Cu_2 and 2.29 Å to Cu_1) while the alkynyl group is only coordinated to Cu_1 (2.13 Å). **TS_5** has a free energy of 17.0 kcal/mol and thus is lower than **TS_3** by 6.0 kcal/mol. It indicates

that the rate limiting step of this reaction is the first one; *i.e.* the formation of **4**$^{+}$. It also shows that this water assisted mechanism has a lower barrier than the concerted of activation of alkynes. The effects of the ion-pairing with NT_2^- and the partial dissociation of DPEOPN on **TS$_5$** are summarized below.

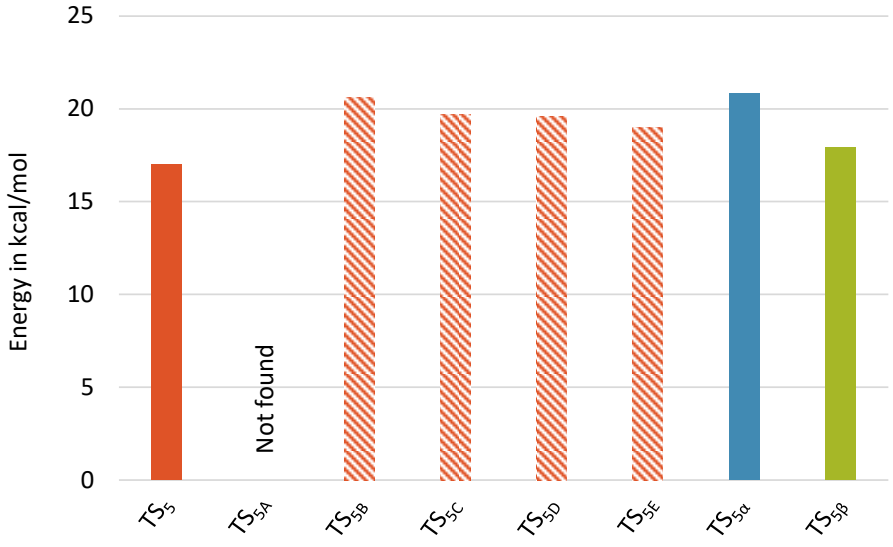

Figure V.17. Free energy of all the transition states of the TS$_5$ series.

The **TS$_{5X}$** series come from the association of **TS$_5$** with NTf_2^- in five positions (A to E, see Figure V.16). However only four are reported here, as **TS$_{5A}$** did not converge. There is an overall destabilization of **TS$_5$** due to the presence of NTf_2^- in its environment, as the energy of these transition states varies from 19.0 to 20.6 kcal/mol (in red dashed in Figure V.17). The energy range is narrow and coincides with similar geometry of the transition states. Their key features are a short distance between the coppers, around 2.66 Å, a symmetric coordination to DPEOPN (coppers to the naphthyridine backbone and Cu_2 to the pyridines) and no direct interaction between the coppers and the counter-ion. In the position **B**, **C** and **E**, the substituents are oriented in the same manner as in **TS$_5$**: the alkynyl is pointing to the outside of the active centre and the hydroxyl is slightly in front of the coppers. In **TS$_{5D}$**, the naphthyridine backbone and the alkynyl are parallel to each other (3.70 Å) and do a π-

stacking interaction together. This new geometry is not particularly favourable as the associated energy is in the same range as the rest of the **TS_{5X}** series. The counter-ion interacts with the complex by the usual dispersion and other weak interaction as a hydrogen bond with the hydroxyl group in **TS_{5C}**. Overall, the interaction between **TS_5** and NTf_2^- increases the barriers $\Delta G^{\ddagger}$.

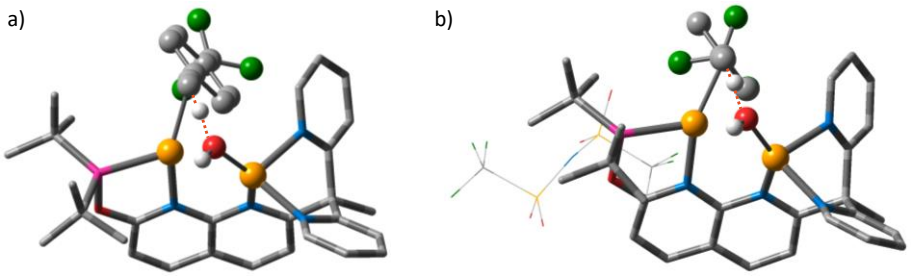

Figure V.18. 3D representation of a) TS_5, b) TS_{5E}. The red dashed lines account for the cleavage and formation of C-H bonds between the hydroxyl and alkynyl moieties.

As for the step A, only the dissociation of one pyridine is considered, leading to **$TS_{5\alpha}$** and **$TS_{5\beta}$** (Figure V.16). The geometry of **$TS_{5\alpha}$** is not impacted by the dissociation. The only modification is the slight asymmetry in the coordination of the coppers to the naphthyridine backbone: it is closer to Cu_2 than Cu_1, with 2.05 and 2.17 Å, respectively. The dissociation of the pyridine **α** heads to an increase of $\Delta G^{\ddagger}$ by 3.8 kcal/mol. Conversely, the geometry of **$TS_{5\beta}$** is more affected by the dissociation as the distance between the coppers increases to 2.84 Å. There is also an asymmetry in the coordination of the coppers to the naphthyridine core: the bond with Cu_1 is 0.14 Å longer than the one with Cu_2. Otherwise, the bonds have similar length than the ones in **TS_5**. The energy of **$TS_{5\beta}$** is 17.9 kcal/mol, which is similar to the one of **TS_5**, indicating that the dissociation of the pyridine **β** do not affect the energy. It is not atypical to obtain higher barrier when the ion-pairing with NTf_2^- or the partial dissociation of DPEOPN are taken into account separately (see IV). However, as the transition states of **TS_6** are much lower, no further computational work has been done on the **TS_5** series.

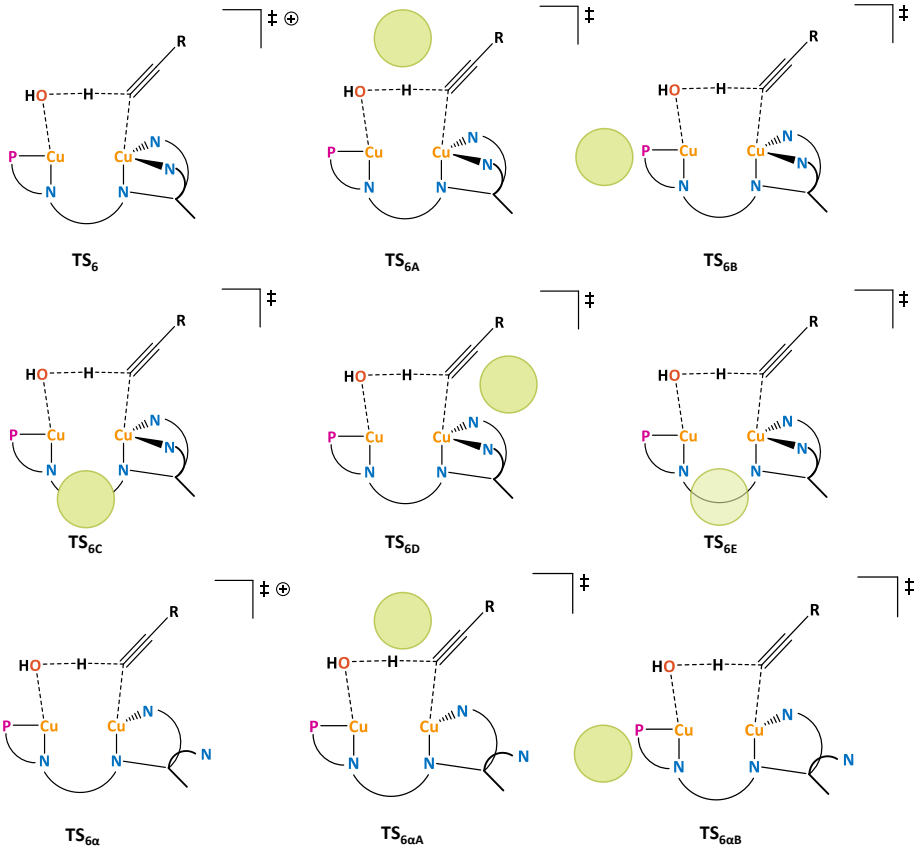

Figure V.19. Schematic representations and labels of all the transition states computed for the TS_6 series; the green circles represent the position of NTf_2^- (1/2).

Then, the last 18 transition states for this water-assisted mechanism were investigated and form the **TS_6** series (Figures V.19 and V.20). The simplest one is **TS_6** (Figure V.22a), where all the part of DPEOPN are coordinated to the coppers and the counter-ion is neglected. The geometry of **TS_6** is much more distorted than **TS_5**, with a distance between the copper of 2.84 Å. This elongation is due to the dissociation of Cu_1 from the naphthyridine backbone (2.55 Å). As there is more space in the active site, the alkynyl group can coordinate to Cu_2 via its π system, with similar bond distances for the two carbons: 2.05 Å for C_2 and 2.08 Å for C_3. The hydroxyl is coordinated to Cu_1, with a distance longer than usual and akin to the alkynyl ones (2.04 Å). The

forming bond is longer than the breaking one: the proton is at 1.43 Å of the hydroxyl and at 1.22 Å of the alkynyl. All this features seem favourable as the energy of **TS_6** is only 14.3 kcal/mol (red in Figure V.21)

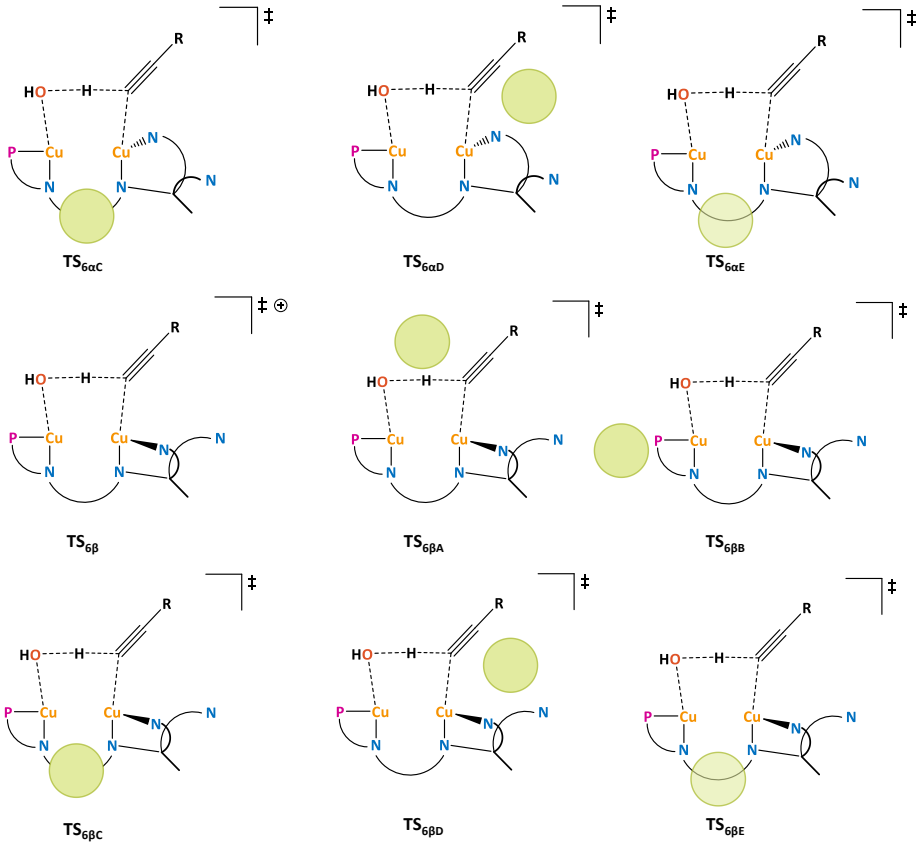

Figure V.20. Schematic representations and labels of all the transition states computed for the TS_6 series; the green circles represent the position of NTf_2^- (2/2).

The association of **TS_6** and NTf_2^- leads to the five transition states **TS_{6X}** (X = **A** to **E**). They are all in a range of 4.1 kcal/mol (red dashed in Figure V.21) and the two lowest transition states, **TS_{6C}** and **TS_{6D}**, have similar energies as **TS_6** with $\Delta G^{\ddagger}$ are 14.6 and 14.7 kcal/mol, respectively. Their geometry are also akin, with a distance between the copper around 2.82 Å and with the distances of the proton with the hydroxyl and the alkynyl of 1.20 and 1.46 Å, respectively. The main difference between **TS_{6C}** and **TS_{6D}** is the coordination

sphere of Cu_1: in the former the bond with the naphthyridine core is elongated (2.21 Å) while Cu_1 is decoordinated from the nitrogen in the latter (2.48 Å). However, this difference does not have much repercussions on the rest of the geometry. Another difference is the interaction with NTf_2^-. In **TS_{6C}**, the counter-ion is located in the cavity formed by the two arms of the naphthyridine backbone and interacts with all the parts of DPEOPN and the alkynyl (Figure V.22b) while it only interacts with the pyridines arm in **TS_{6D}**. Overall, the association of **TS_6** with NTf_2^- is isoenergetic or unfavourable and the geometry of the **TS_6** is impacted only to a small extend.

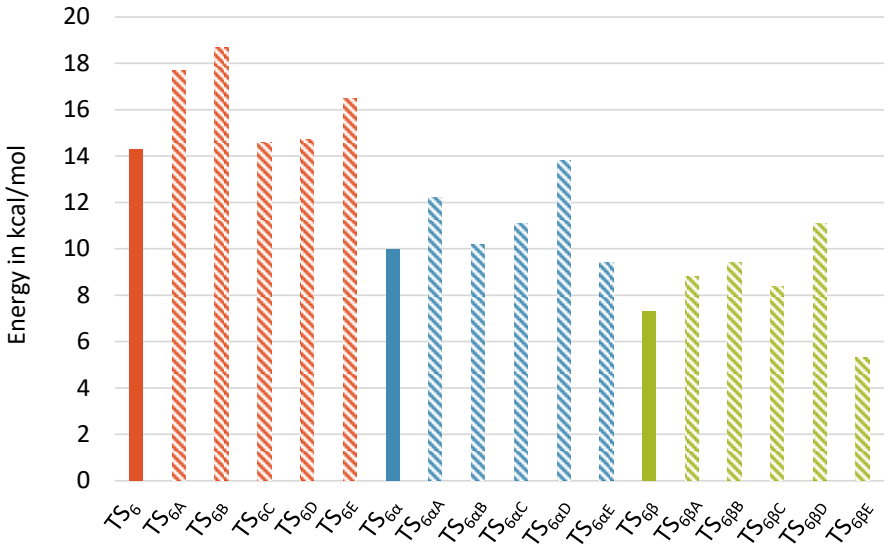

Figure V.21. Free energy of all the transition states of the TS_6 series.

As for **TS_5**, the only dissociations of DPEOPN considered were the rotation of one of the pyridine leading to **$TS_{6\alpha}$** and **$TS_{6\beta}$**. In this case, the partial dissociation of DPEOPN has a huge impact on the energy of **TS_6**, leading to low-lying transition states: 10.0 and 7.3 kcal/mol for **$TS_{6\alpha}$** and **$TS_{6\beta}$**, respectively (in blue and green in Figure V.21). The biggest geometrical impact of these dissociations is the elongation of the distance between the coppers: it increases up to 3.29 Å for **$TS_{6\alpha}$** and to 3.57 Å for **$TS_{6\beta}$**. In the first case, it is caused by the elongation of the distance between Cu_1 and the naphthyridine

backbone up to 3.03 Å, while it is due to the orientation of Cu_1 toward the back of the complex in **$TS_{6\beta}$**, with an unchanged distance between Cu_1 and the naphthyridine backbone (Figure V.22c). In both transition states, the transferred hydrogen is closer to the hydroxyl than to the alkynyl, with average values of 1.23 and 1.35 Å, respectively. The coordination mode of the alkynyl is retained as the two carbons involved in the π-system of the alkynyl are at 2.05 Å from Cu_2 on average.

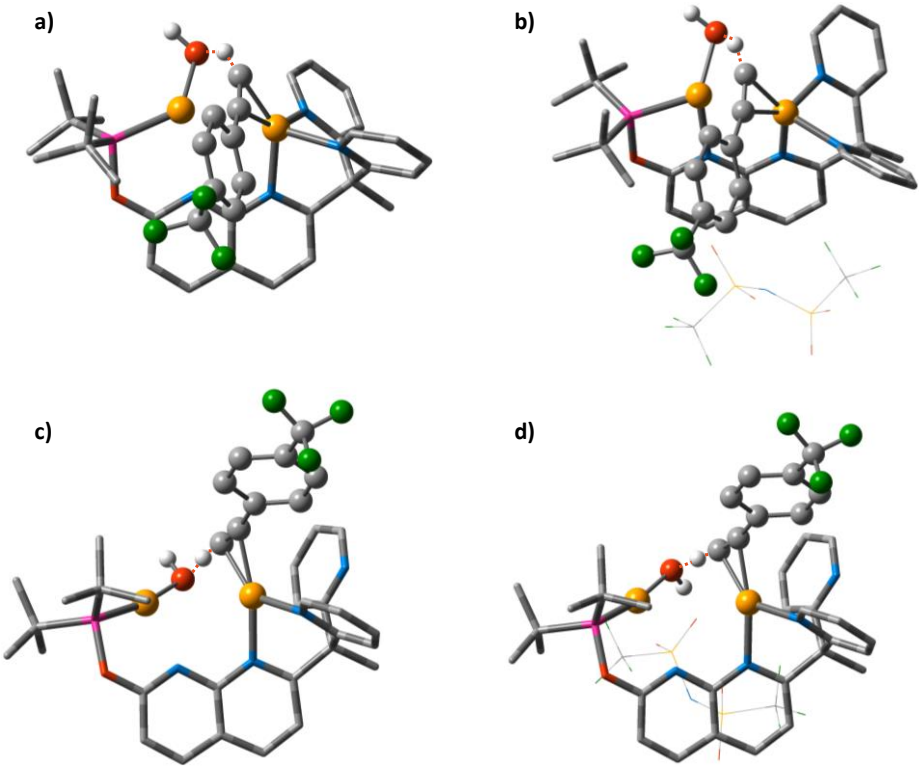

Figure V.22. 3D representation of a) TS_6, b) TS_{6C}, c) $TS_{6\beta}$ and d) $TS_{6\beta E}$. The red dashed lines account for the cleavage and formation of bonds between the hydroxyl and alkynyl moieties.

As **$TS_{6\alpha}$** and **$TS_{6\beta}$** have a low energy and are only 2.7 kcal/mol apart, they are both kept to examine the combined effects of the association with NTf_2^- and partial dissociation of DPEOPN on **TS_6**, creating the **$TS_{6\alpha X}$** and **$TS_{6\beta X}$** series (see Figures V.19 and V.20). The **$TS_{6\alpha X}$** series is spread on a short range of energy

distributed around **TS$_{6\alpha}$**, varying from 9.4 to 12.3 kcal/mol for **TS$_{6\alpha E}$** and **TS$_{6\alpha A}$**, respectively (blue dashed in Figure V.21). The geometry of these transitions states are similar to **TS$_{6\alpha}$**, with a difference in the bond lengths up to 0.05 Å maximum; except for two characteristics: the distance between the coppers and the position of the transferred proton. For the former, the length of this bond varies from 3.16 (**TS$_{6\alpha E}$**) to 3.58 Å (**TS$_{6\alpha A}$**), showing that the transition states remain very distorted compared to **4**$^{+}$ and **2**$^{+}$. The distance between the coppers correlates with the distance between Cu_1 and the naphthyridine backbone: when the latter increases, the former does as well. The position of the proton is closer to the alkynyl in **TS$_{6\alpha A}$** and **TS$_{6\alpha E}$**, while closer to the hydroxyl in the three other transition states. The counter-ion interacts mainly via dispersion in the **TS$_{6\alpha X}$** series but two other types of interactions are worth noting: an hydrogen bond between an oxygen of NTf_2^- and the hydroxyl in **TS$_{6\alpha A}$** and the coordination of NTf_2^- to Cu_2 (2.18 Å) in **TS$_{6\alpha E}$** via one of its oxygen.

In the **TS$_{6\beta X}$** series, the energy of the transition states are even lower, going from 5.3 to 11.1 kcal/mol (green dashed in Figure V.21). The lowest transition state of this series is **TS$_{6\beta E}$** (Figure V.22d). Its geometry is quite similar to **TS$_{6\beta}$** but with an elongated distance between Cu_1 and the naphthyridine backbone (2.84 Å versus 2.54 Å) leading to the coppers to be further apart (3.83 Å). The counter-ion is positioned along the naphthyridine backbone, allowing it to interact via dispersion with all parts of DPEOPN (phosphine, naphthyridine and dissociated pyridine) and doing a hydrogen bond with the hydroxyl via one of its oxygen (1.94 Å). This extremely distorted transition state is the lowest one for the second step the water assisted activation of alkynes.

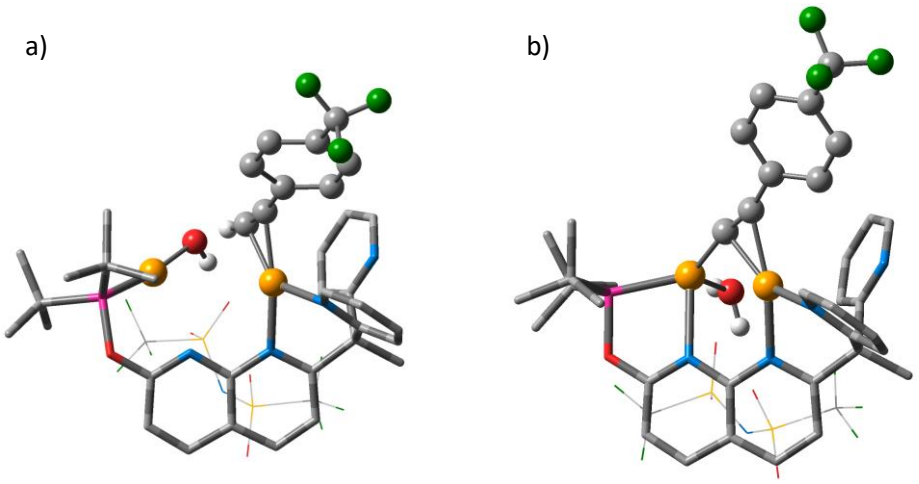

Figure V.23. 3D representation of the intermediates found via the IRC relaxation of $TS_{6\beta E}$: a) on the reactant side and b) on the product side.

Overall, the TS_6 series have much lower $\Delta G^{\ddagger}$ than the TS_5 series, with the lowest one being $TS_{6\beta E}$ with a barrier of 5.3 kcal/mol. Thus, the second barrier of the water-assisted mechanism is much lower than the first one (18.6 kcal/mol) suggesting that the rate determining step is the formation of $\mathbf{4}^{+}$. In this mechanism, as in the previous ones, the combined effects partial decoordination of DPEOPN and the ion-pairing with NTf_2^- are two key effects to lower the energy of the transition state, going from 14.3 to 5.3 kcal/mol. To be certain of the nature of these transition states, an IRC-driven relaxation were done on a selection of them, collected from both the TS_5 and TS_6 series, and additional intermediates were found for most of the transition states. For $TS_{6\beta E}$, there a two new intermediates, one before and one after the transition state. In the first one, the hydroxyl dissociate from Cu_2 as the alkyne coordinates via its π-system on it (Figure V.23a). The counter-ion does a hydrogen bond with the hydroxyl with one of its oxygen (2.01 Å). The energy of this intermediate is 4.8 kcal/mol higher than $\mathbf{4}_{pyrD}$ and $TS_{6\beta E}$ is less than 1 kcal/mol higher. The second intermediate (Figure V.23b) is appearing after the proton transfer and the alkynyl is bridging the two coppers while the water molecule is coordinated to Cu_1 (2.15 Å). NTf_2^- does two hydrogen bonds with H_2O via its oxygen atoms (2.15 and 1.73 Å). The energy of this second intermediate is -13.5 kcal/mol and after the dissociation of H_2O, $\mathbf{2}_B$ is formed

and is only 0.9 kcal/mol lower. The mechanism for this second step of the water-assisted catalyst is summarize in Figure V.24. Through this mechanism, the natural charge of H increases as it transfers from the alkyne to H_2O (+0.26 to +0.47) consistently with the electronegativity of the atoms it is bonded to (O_1 or C_2). The charge of O_2 diminishes (-1.14 to -0.94) as it dissociates from the coppers while the charge of C_2 increases (-0.22 to -0.62) as it dissociates from them.

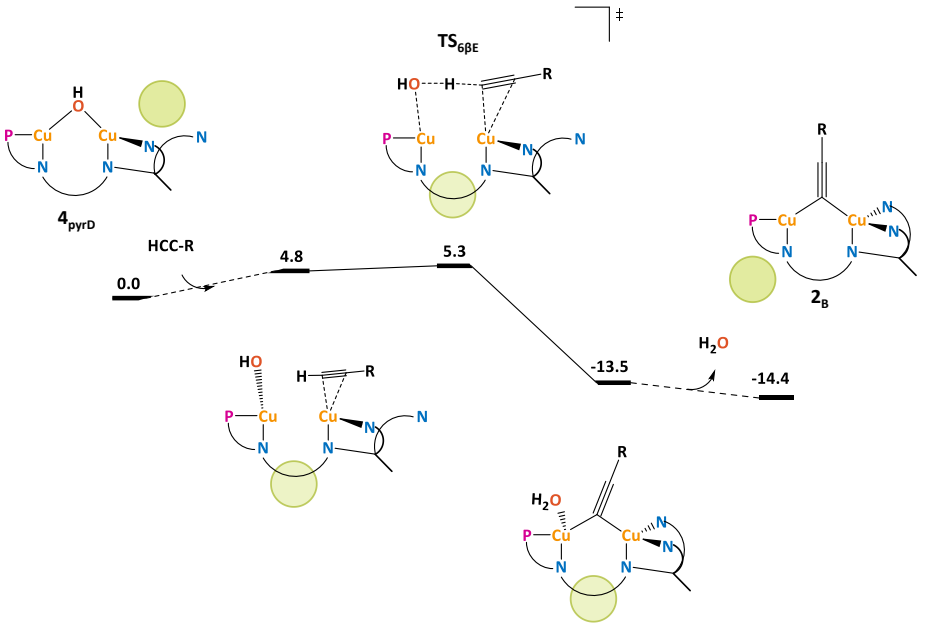

Figure V.24. Schematic representation of the mechanism of 4^+ to 2^+; the green circles represent the position of NTf_2^-.

b) - Descriptors analysis of the transition states

The 24 transition states computed for the step B of the water-assisted activation of alkynes are analysed using 16 descriptors, including:

- Position of NTf_2^-
- Distance between Cu_1 and Cu_2
- Distance between the C_2 and O_1

- Distance between H and C_2
- Distance between H and O_1
- Angle between P, Cu_1 and O_1
- Dihedral angle Cu_1-N_1-N_2-Cu_2
- Natural charge of Cu_1
- Natural charge of Cu_2
- Difference of natural charge between Cu_1 and Cu_2
- Natural charge of the C_2
- Natural charge of the O_1
- Difference of natural charge between C_2 and O_1
- Natural charge of H
- Difference of natural charge between H and C_2
- Difference of natural charge between H and O_1

In the following Figures V.25 to V. 30 and in the additional *Descriptors file* (see Annexes) are scattered plots of the descriptors analysis of the **TS_5** and **TS_6** series. All the transition states related to the **TS_5** series are represented in blue dots while the ones related to the **TS_6** series are in green dots. There are four main trends coming out from this descriptors analyses. First, all the transition states of the **TS_6** series have a lower energy than the ones of **TS_5** series (Figure V.25), demonstrating a clear preference for the alkyne coming toward the complex on the pyridines side. This is atypical as, so far, the phosphine side were the preferred spot for the bulkier reactant. A possible explanation is that while the alkynyl is supported by Cu_2, the π-system of the aryl ring can interact with the ^{t}Bu substituents of the phosphine (Figure V.22), while this is impossible if the alkynyl is coordinated to Cu_1. The second trend correspond to the correlation between large distortion in the transition state and low energy. This is evident from three descriptors: the distance between the coppers, the distance between C_2 and O_1 and the dihedral angle between the coppers and the nitrogens of the naphthyridine backbone (Figures V.26, V.27 and V.29). Surprisingly, the optimal distance between the coppers is almost

at 3.90 Å, which is extremely distorted in comparison of the optimum distance for the concerted mechanism (around 2.90 Å) where the reactants where bulkier. It could be due to the straightening of the coordination sphere of Cu_1: in the lowest transition states of the **TS_6** series, Cu_1 is dissociated from the naphthyridine backbone, and the further away it goes, the closer its coordination sphere is to linear. To show this, the angle between the phosphorus atom, Cu_1 and the oxygen of the hydroxyl has been added as a descriptor (Figure V.28). The R^2 value is significant (0.6558) and two kind of transition states can be observed. The first ones have a P-Cu_1-O_1 angle around 125° and correspond to transition states which are less distorted ones with a distance of 2.64 to 2.58 Å between the coppers and a distance between the naphthyridine backbone and Cu_1 from 2.10 to 2.71 Å. These transition states are also the ones with the highest energy. The second group have a P-Cu_1-O_1 angle around 165° and is composed of the most distorted transition states. Their distance between the coppers varies from 3.16 to 3.83 Å and the one between Cu_1 and the naphthyridine is from 2.47 to 3.35 Å away. These transition states are also the ones with the lowest energy. The amount of distortion needed to straighten the coordination sphere of Cu_1 is huge and it is unlikely to be accessible in the presence of a bulkier substrate, like the phenyl in the concerted mechanism. The third trend is the correlation between the decrease of the natural charge of Cu_1 and low-energy transition states (Figure V.30). In these transition states, one anion (hydroxyl or phenyl) is coordinated to each copper, inducing a lot of charge variation at the core of the transition states. Thus, the transition states stabilizing this polarization would lead to the lower energy. However, the energy range is large for each value of natural charge of Cu_1 and therefore no strong conclusion should be made from this descriptor. The last feature that arise from these figures is that the **TS_5** and **TS_6** form cluster in a majority of the descriptors. This can be explain the very different type of geometry observed in these series: compact for **TS_5** and distorted for **TS_6**.

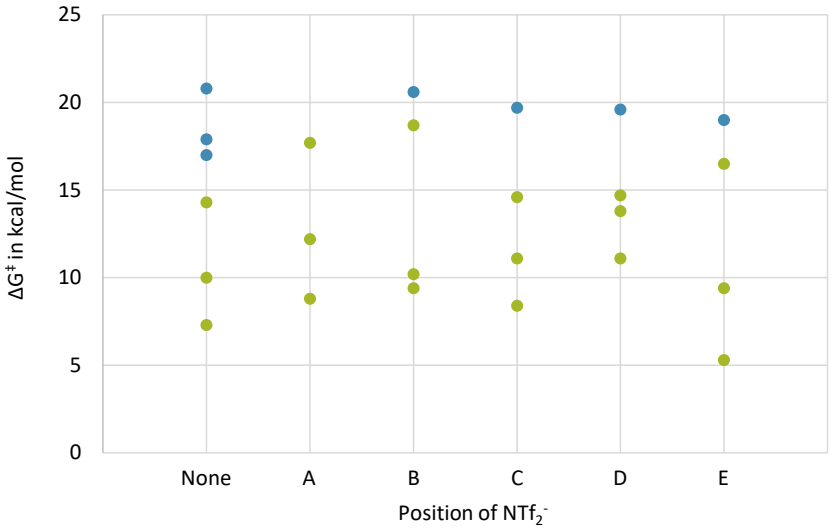

Figure V.25. Energy of the transition states as function of the position of NTf_2^-.

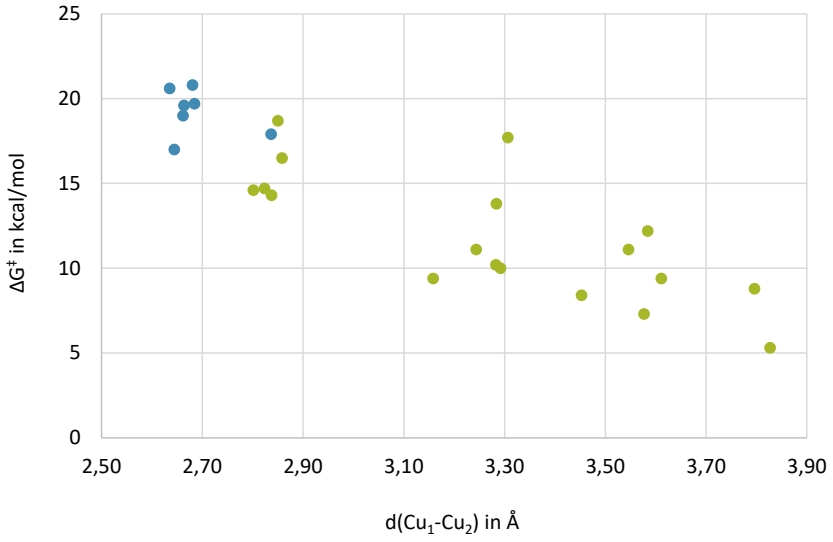

Figure V.26. Energy of the transition states as function of the distance between the two coppers, $R^2 = 0.7559$. No point has been removed.

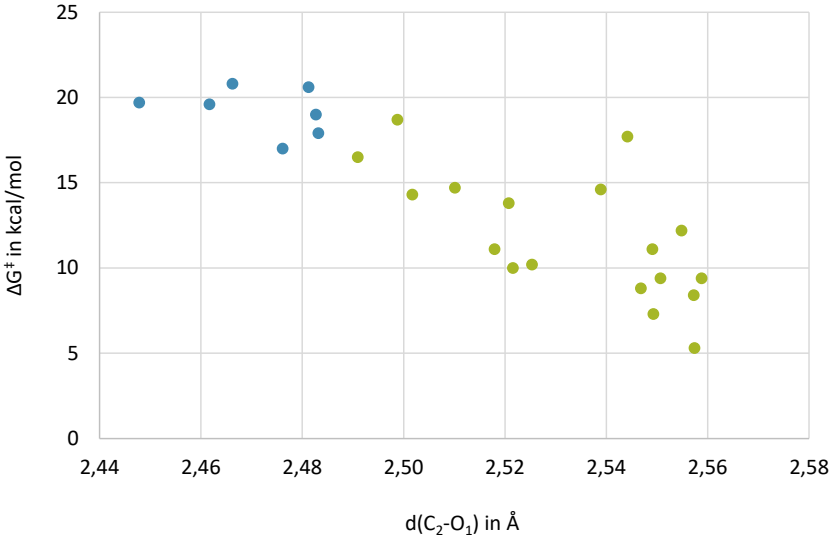

Figure V.27. Energy of the transition states as function of the distance between C_2 and O_1, $R^2 = 0.7178$. No point has been removed.

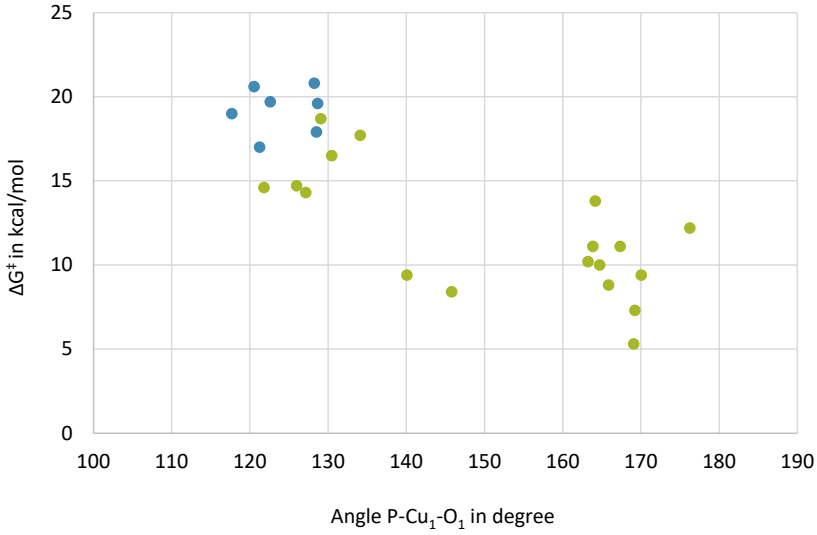

Figure V.28. Energy of the transition states as function of the angle between P, Cu_1 and O_1 and H, $R^2 = 0.6558$. No point has been removed.

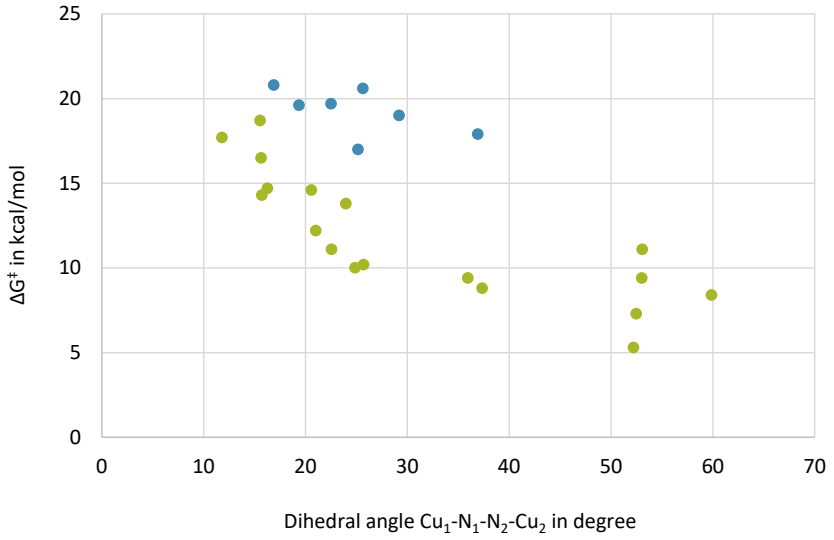

Figure V.29. Energy of the transition states as function of the dihedral angle between Cu_1, N_1, N_2 and Cu_2, $R^2 = 0.4572$. No point has been removed.

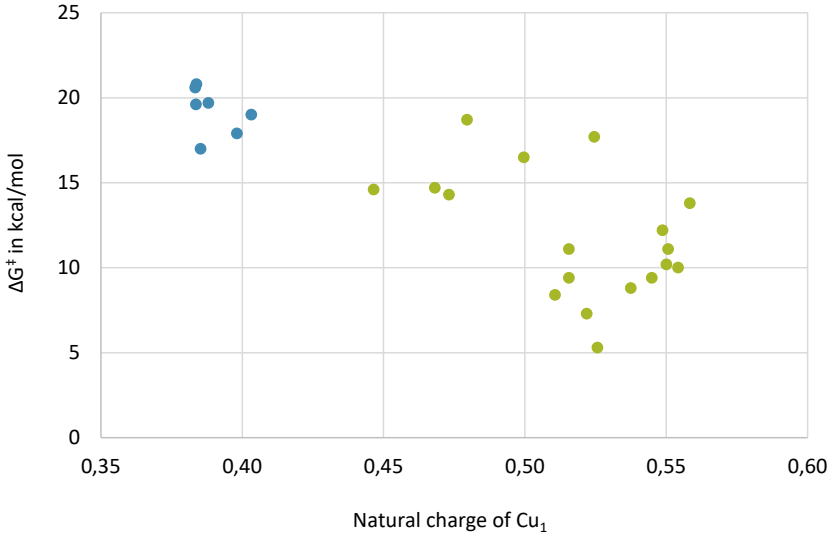

Figure V.30. Energy of the transition states as function of the natural charge of Cu_1, $R^2 = 0.6292$. No point has been removed.

4 - Microkinetics model

Before detailing the microkinetic models realized for this reaction, the full mechanism of the water assisted activation of alkynes by $\mathbf{1}^{+}$ is first summarized (Figure V.31). In step A, a water molecule approaches $\mathbf{1_C}$ on the pyridines side and transfers a proton to the phenyl bridging ligand in $\mathbf{TS_{3\beta E}}$. From this transition step, the reaction goes directly to the intermediate $\mathbf{4_D}$ and a molecule of benzene is liberated. Then, in step B, the alkyne also approaches the complex on the pyridines sides, leading to an intermediates where the hydroxyl is coordinated only to Cu_1 while the alkyne is coordinated via its π system to Cu_2. This intermediate is 4.8 kcal/mol higher than $\mathbf{4_D}$ and the following transition state is extremely easily accessible, as $\mathbf{TS_{6\beta E}}$ is only 0.5 kcal/mol higher. Going towards the products, another intermediate was found, where the alkynyl group is bridging the two coppers and the water molecule is still coordinated to Cu_1. As no transition state has been found, the water molecule is postulated to dissociate from $\mathbf{2}^{+}$ without a transition or with a very low-lying one (≤ 5 kcal/mol). After this dissociation the final product, $\mathbf{2_B}$, is formed. In this reaction, the rate determining step in the formation of $\mathbf{4_D}$ with a $\Delta G^{\neq}$ of 18.6 kcal/mol. The presence of NTf_2^- lower the energy of both the intermediates and the transition states and its position around the complexes is quite versatile. Apart from $\mathbf{1_C}$ and $\mathbf{2_B}$, all the intermediates and transition states have the back pyridine dissociated from Cu_2. Thus, the relevance of the partial dissociation of DPEOPN and of the ion-pairing is highlighted in this mechanism.

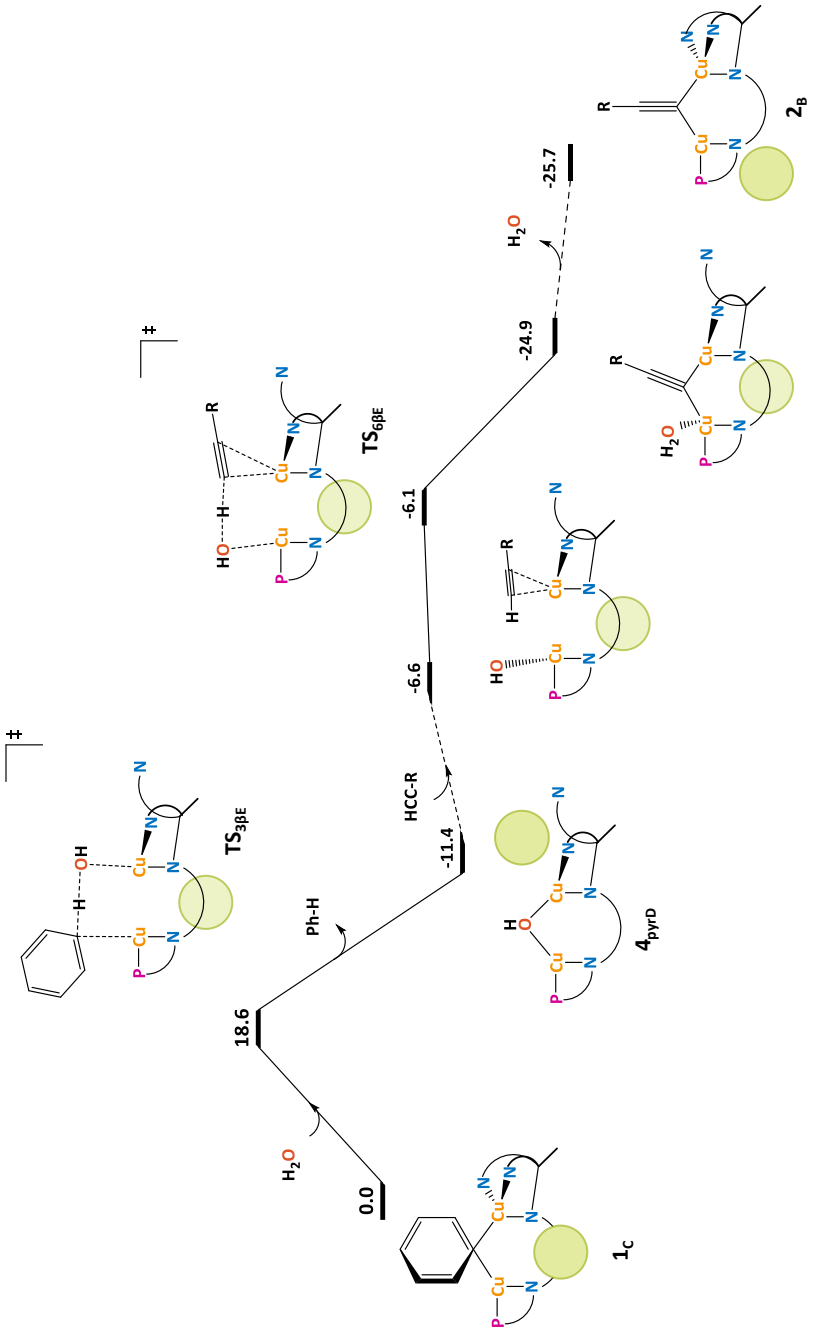

Figure V.31. Schematic representation of the mechanism of 1^+ to 2^+ catalyzed by water; the green circles represent the position of NTf_2^-.

This mechanism is used to create a microkinetics model to compute the conversion associated to it and to assess the error in the DFT barriers. Experimentally, the reaction reaches 50, 70 and 100 % conversion at 13, 20 and 60 minutes, respectively. To do the microkinetics, the same conditions as for the concerted reaction, and as in the in the kinetic experiments, were used: 10.0 mM of $\mathbf{1}^{+}$, 21.0 mM of alkyne, at 48.5°C in THF with 1 atm to which 1.5 equivalent of water were added relative to $\mathbf{1}^{+}$. The model comprise six elementary steps (Figure V.32). Four of them arise from the water assisted C-H activation described in this chapter. The first couple of elementary steps consist of the reaction of $\mathbf{1_C}$ to $\mathbf{4_D}$ via $\mathbf{TS_{3\beta E}}$ (step A), with a $\Delta G^{\ddagger}_{fA}$ of 18.6 kcal/mol for the forward step and a $\Delta G^{\ddagger}_{rA}$ of 30.0 kcal/mol for the reverse. The second couple of elementary step correspond to the reaction of $\mathbf{4_D}$ to $\mathbf{2_B}$ via $\mathbf{TS_{6\beta E}}$ (step B), with a barrier $\Delta G^{\ddagger}_{fB}$ of 5.3 kcal/mol and of 19.6 kcal/mol for the reverse elementary step $\Delta G^{\ddagger}_{rB}$. The last two elementary steps come from the concerted mechanism (discussed in IV) *i.e.* the reaction of $\mathbf{1_C}$ to $\mathbf{2_B}$ via $\mathbf{TS_{1\beta C}}$ and its reverse reaction. The energy barrier associated to these steps are 22.9 kcal/mol for $\Delta G^{\ddagger}_{fC}$ while the reverse step has a $\Delta G^{\ddagger}_{rC}$ of 48.6 kcal/mol. The coordination of the reactants and the dissociation of the products have been neglected as the energy barrier of such step is likely to be lower. The conversion is computed via a time course simulation, with one point every 30 seconds for 60 min.

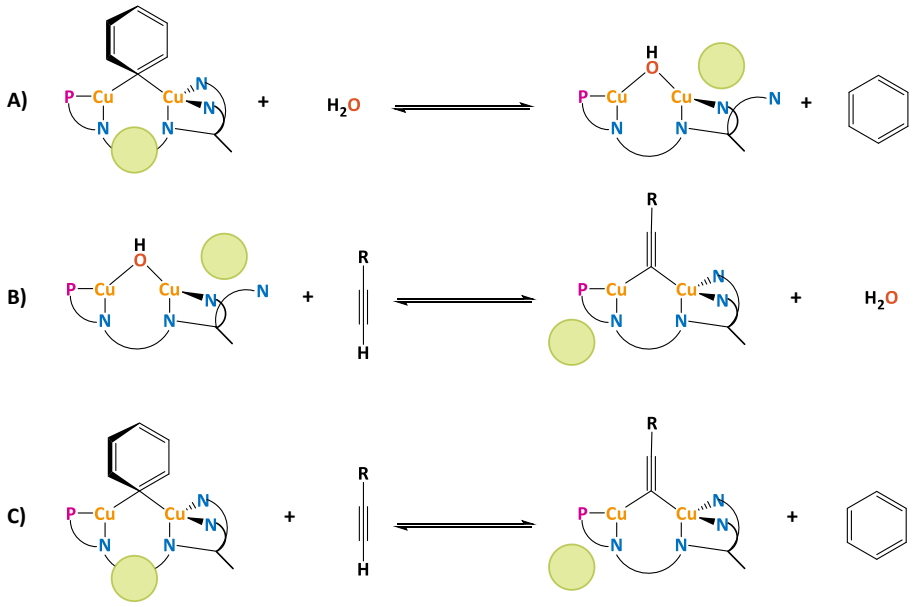

Figure V.32. Elementary reaction considered microkinetics model of the 1^+ to 2^+ catalysed by water.

First, the microkinetics simulation was run without any correction on the energetic barrier obtained by DFT, leading to 100% after only 13 minutes (Figure V.33). It indicates that the value of $\Delta G^{\ddagger}_{fA}$ is too low leading to the completion of the reaction in a sixth of the total time. The error cannot come from $\Delta G^{\ddagger}_{fC}$ as in the previous chapter, the conversion reached only around 10% at 60 minutes without energy corrections. To fit the DFT model the energy of $\Delta G^{\ddagger}_{fC}$ is lowered by 2.0 kcal/mol (as for the concerted mechanism) and the energy of $\Delta G^{\ddagger}_{fA}$ is gradually increased from +0.2 to +0.7 kcal/mol. The energy error that leads to the best model increased $\Delta G^{\ddagger}_{fA}$ by +0.5 kcal/mol: it reaches 50 and 70 % conversion at 13 and 20 minutes, as the experimental data. However, the full conversion is attained in 32 minutes which is faster than the experiments (60 minutes). It appears that the experimental kinetic involves at least two different regimes when our model only represent the first one. After 20 minutes, a new reaction or more stable intermediates causing catalyst poisoning dominate the kinetics of the reaction described in this chapter. This may be due to the high quantity of water present in the reaction mixture (1.5 equivalents relative to the complex).

	Conversion at 15 min	Conversion at 60 min
Experiment	50	100
DFT model	3.4	18.2
Fitted model (+0.2)	7.3	34.2
Fitted model (+0.3)	14.9	56.9
Fitted model (+0.4)	28.7	80.3
Fitted model (+0.5)	49.8	95.5
Fitted model (+0.6)	74.0	99 (at 66 min)
Fitted model (+0.7)	92.3	99 (at 30 min)

Table V.2. Comparison of the conversion between the experiments, the unfitted DFT model and the fitted model (error in kcal/mol).

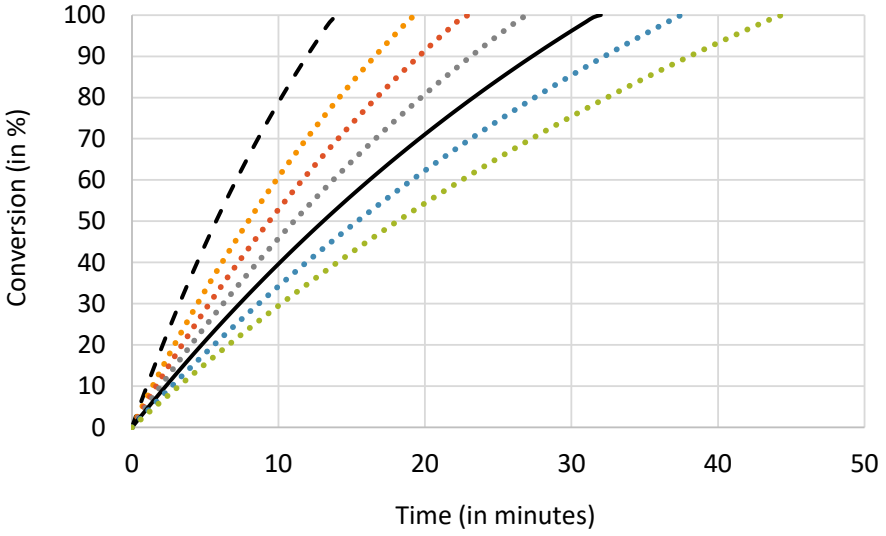

Figure V.33. Fitting of the DFT model (black dashed line) by increasing the energy of $\Delta G^{\ddagger}_{fA}$ by +0.2 (orange dots), +0.3 (red dots), +0.4 (grey dots), +0.5 (black line), +0.6 (blue dots) and +0.7 kcal/mol (green dots) and by lowering the energy of $\Delta G^{\ddagger}_{fA}$ by -2.0 kcal/mol .

VI - CuAAC reaction with 2^+ as catalyst

The catalytic ability of the di-copper DPEOPN based complexes was investigated using the CuAAC reaction. The motives to choose this reaction relies on three arguments. First, the CuAAC reaction is robust and selective, producing only 1,4 triazole and side products are usually not observed. Second, it involves alkynyl di-copper species as well as a C-H activation step similar to the one described in chapter IV. Finally, a similar 1,8 naphthyridine based di-copper complexes has been already used as catalyst for the CuAAC reaction.[45] Therefore, the complex **2^+** can be used to catalyse this reaction. Experimentally, the reaction can be done over a few hours in THF at 50°C, using the alkyne HCC(*p*-CF_3-C_6H_4) and the azide N_3(*p*-CH_3-C_6H_4). This chapter reports the study of the mechanism of the CuAAC using a robust di-copper catalyst with a well-defined structure, instead of simple copper salts. Through this chapter, the atoms and compounds will be labelled as shown in Figure VI.1 to ease the description of the intermediates and transition states. All the energy of the transition states reported in this chapter are gathered in tables in the annex A.

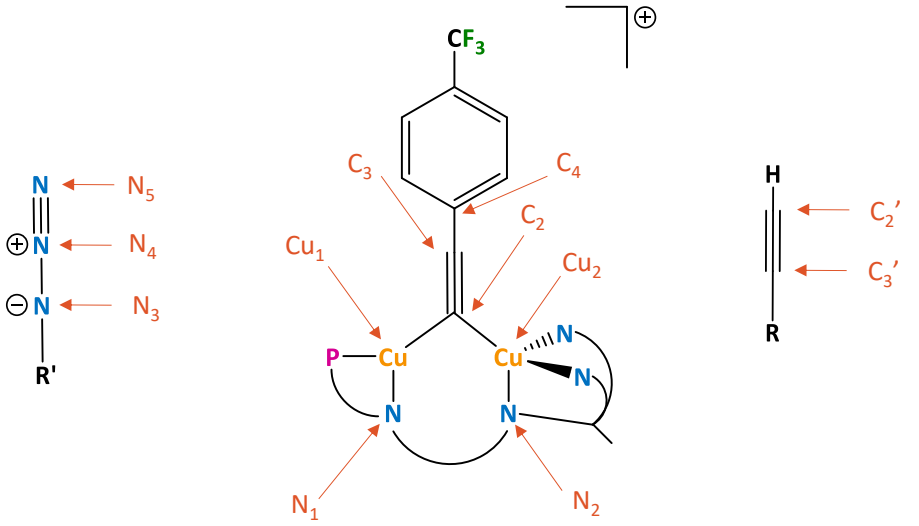

Figure VI.1. Labels of the key atoms in the CuAAC reaction catalysed by 2^+.

1 - The search of in-cycle intermediates

To explore the mechanism of the CuAAC reaction, intermediates were searched first and then the transition states that would connect them were investigated. In this first section, only the intermediates involved in the mechanism of the CuAAC reaction are reported.

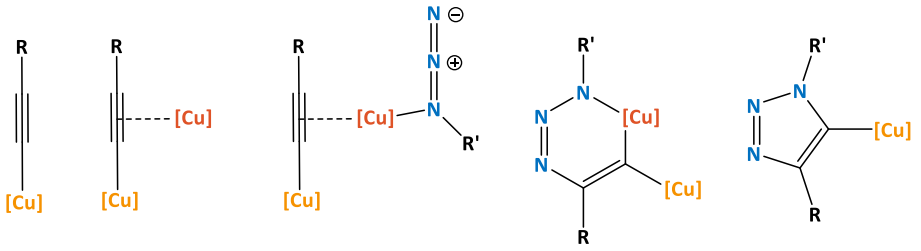

Figure VI.2. Commonly accepted intermediates for the CuAAC reaction.

This reaction is well known in the case of copper salt as catalyst and thus the key intermediates have been characterized, both experimentally and computationally[96–101] (Figure VI.2). Based on this knowledge, four intermediates are considered for a tentative cycle. The starting intermediate is **2**$^{+}$, with the alkynyl already bound to two coppers and thus the alkynyl do not need further activation as in the case of copper salts. The intermediate **2**$^{+}$ will not be described here as it has already been done in Chapter III. The second intermediate arise after the coordination of the azide to **2**$^{+}$. The third intermediate is a 6-membered ring metallocycle appearing after the formation of the first C-N bond. The fourth and last intermediate originates from the reductive elimination forming the second C-N bond and corresponds to a triazolyl bridging the two coppers. A proton transfer between this last intermediate and the alkyne regenerates **2**$^{+}$, releasing the 1,4 triazole product.

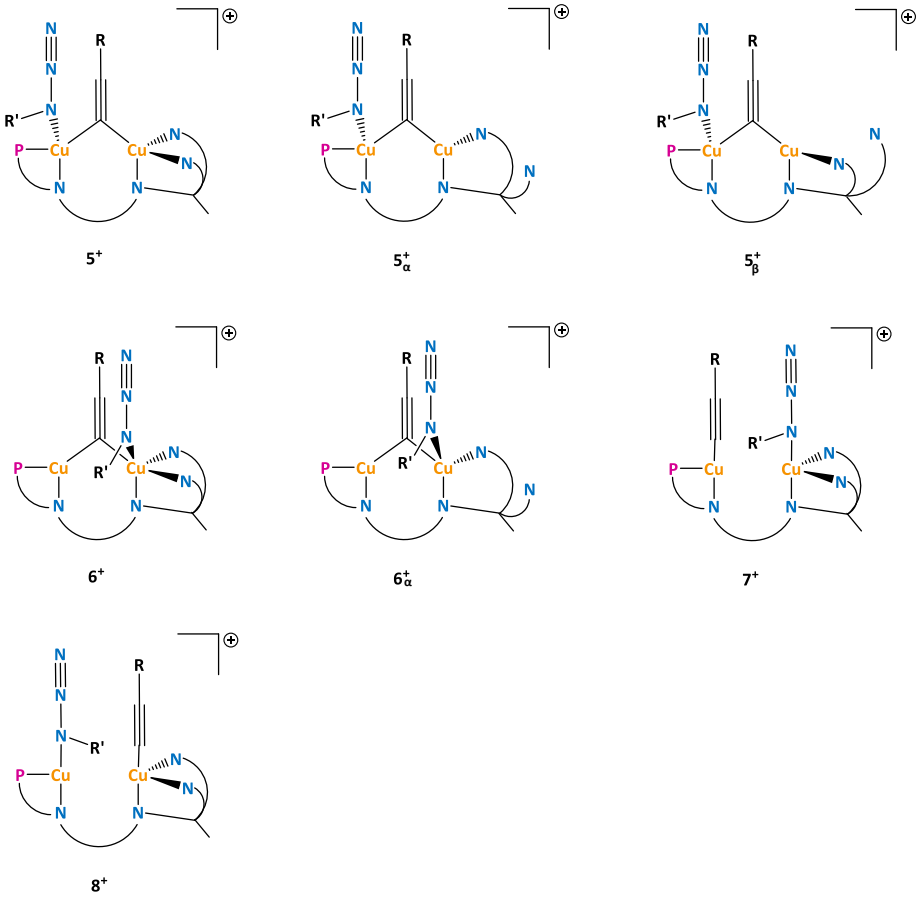

Figure VI.3. Tentative intermediates for the coordination of the azide to 2^+.

To find the intermediate where the azide is coordinated to $\mathbf{2}^+$, seven geometries were considered, as shown in Figure VI.3. Two variables were investigated: the coordination of the alkynyl; which can either bridge the coppers ($\mathbf{5}^+$ and $\mathbf{6}^+$) or not ($\mathbf{7}^+$ and $\mathbf{8}^+$); and on which copper the azide coordinates; either on the phosphine ($\mathbf{5}^+$ and $\mathbf{8}^+$) or on the pyridine side ($\mathbf{6}^+$ and $\mathbf{7}^+$). These four intermediates all converged into $\mathbf{5}^+$ (Figure VI.4a), indicating a clear preference for the alkynyl to bridge the coppers and highlighting the importance of the 2e3c interaction between the bridging ligand and the metal centres. The other clear feature is the preference of the azide to coordinate on the phosphine side, due to the higher steric hindrance

between the pyridines of DPEOPN and the aryl substituent of the azide, compared to the ^{t}Bu of the phosphine. The coordination of the azide (2.29 Å) on Cu_1 distorts slightly its coordination sphere: the phosphine is pushed outside of the axis containing DPEOPN and the coppers. This change is shown by the angle between Cu_2-Cu_1-P: 169.8° in $\mathbf{2}^+$ and 157.9° in $\mathbf{5}^+$. The other meaningful changes are the elongation of the distance between Cu_1 and the alkynyl (1.97 Å in $\mathbf{2}^+$ and 2.04 Å in $\mathbf{5}^+$) and of the distance between the coppers (2.38 Å in $\mathbf{2}^+$ and 2.46 Å in $\mathbf{5}^+$). Otherwise, all the other distances and angles are similar in both complexes. The coordination of the azide to $\mathbf{2}^+$ is thermoneutral, since $\mathbf{5}^+$ is only 0.2 kcal/mol higher in energy.

Complex	ΔG (kcal/mol)	Complex	ΔG (kcal/mol)
$\mathbf{5}^+$	0.0	$\mathbf{5}_{\alpha}^+$	2.3
$\mathbf{5}_{A}$	3.0	$\mathbf{5}_{\alpha A}$	2.2
$\mathbf{5}_{B}$	1.1	$\mathbf{5}_{\alpha B}$	4.8
$\mathbf{5}_{C}$	-2.7	$\mathbf{5}_{\alpha C}$	-0.1
$\mathbf{5}_{D}$	-0.4	$\mathbf{5}_{\alpha D}$	1.6
$\mathbf{5}_{E}$	-4.5	$\mathbf{5}_{\alpha E}$	-1.1

Complex	ΔG (kcal/mol)	Complex	ΔG (kcal/mol)
$\mathbf{5}_{\beta}^+$	2.2	$\mathbf{6}_{\alpha}^+$	5.9
$\mathbf{5}_{\beta A}$	2.4	$\mathbf{6}_{\alpha A}$	8.0
$\mathbf{5}_{\beta B}$	2.4	$\mathbf{6}_{\alpha B}$	6.2
$\mathbf{5}_{\beta C}$	-0.8	$\mathbf{6}_{\alpha C}$	-0.3
$\mathbf{5}_{\beta D}$	2.4	$\mathbf{6}_{\alpha D}$	7.6
$\mathbf{5}_{\beta E}$	-2.0	$\mathbf{6}_{\alpha E}$	4.5

Table VI.1. Free energy of the ion-paring of $\mathbf{5}^+$, $\mathbf{5}_{\alpha}^+$, $\mathbf{5}_{\beta}^+$ and $\mathbf{6}_{\alpha}^+$ with NTf_2^-.

The presence of the azide introduces steric bulk into the active centre and the partial dissociation of DPEOPN could yield different and more stable conformations. Thus, the effect of the partial dissociation of DPEOPN on $\mathbf{5}^+$ and $\mathbf{6}^+$ was also considered (Figure VI.3). Only two dissociations where considered: the rotation of the front pyridine **α** or of the back pyridine **β**, as the other dissociations usually yielded intermediates with higher energy (see Chapters III and V). Both dissociations were computed for $\mathbf{5}^+$ and only one for $\mathbf{6}^+$. The dissociation of the pyridine **β** was not considered for $\mathbf{6}^+$ as the steric

hindrance between the azide and the pyridine **α** would not decrease compared to $\mathbf{6}^+$ and thus the intermediate would converge into $\mathbf{5}_{\beta}^+$. Therefore, only the dissociation of the pyridine **α** was considered for $\mathbf{6}^+$.

These three intermediates have been obtained and their energy relative to $\mathbf{5}^+$ are gathered in Table VI.1. The dissociations are slightly endoergic for $\mathbf{5}^+$, with 2.3 and 2.2 kcal/mol for $\mathbf{5}_{\alpha}^+$ and $\mathbf{5}_{\beta}^+$, respectively. There are two main impacts on the geometry of $\mathbf{5}_{\alpha}^+$ (Figure VI.4b). First, the distance between the azide and Cu_1 increases to 2.42 Å, allowing the angle Cu_2-Cu_1-P straighten to 162.3°. The second is the elongation of the distance between the coppers by 0.2 Å to 2.67 Å. All the other distances are either the same as in $\mathbf{5}^+$ or only fluctuate by 0.05 Å. The dissociation of the pyridine **β** on $\mathbf{5}^+$ has the opposite effect (Figure VI.4c): the distance between Cu_1 and the azide shorten to 2.22 Å, increasing the bending of the Cu_2-Cu_1-P angle to 144.3°. The rest of the complex is not impacted by the dissociation. The intermediate $\mathbf{6}_{\alpha}^+$ is also higher in energy than $\mathbf{5}^+$, by 5.9 kcal/mol. In $\mathbf{6}_{\alpha}^+$, the azide is coordinated to Cu_2 (2.32 Å) instead of the pyridine **α** (Figure VI.4d), causing the elongation of the bond between the alkynyl and Cu_2 by 0.1 Å. Overall, these dissociation processes are easily accessible even at room temperature, without having considerable impacts on the geometry of the complexes.

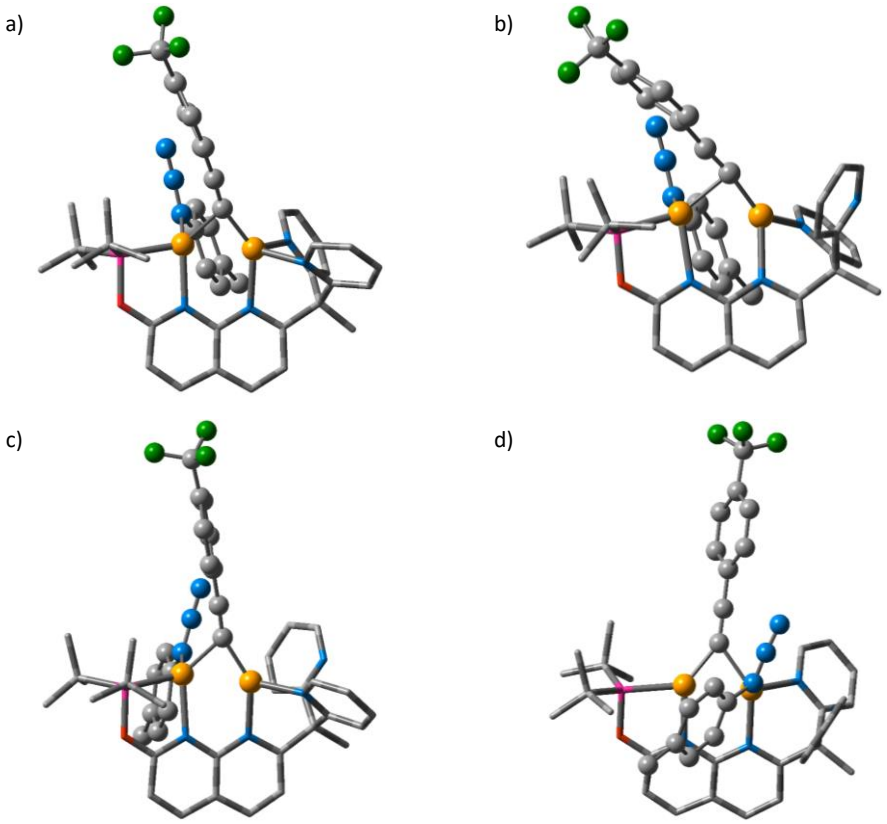

Figure VI.4 3D representation of a) 5^+, b) 5_α^+, c) 5_β^+ and d) 6_α^+.

As shown in the three previous chapters, the ion-pairing of the complexes with NTf_2^- dramatically affects both the energy and the geometry of complexes. Thus, it was also computed for $\mathbf{5}^+$, $\mathbf{5}_\alpha^+$, $\mathbf{5}_\beta^+$ and $\mathbf{6}_\alpha^+$, leading to the series $\mathbf{5}_X$, $\mathbf{5}_{\alpha X}$, $\mathbf{5}_{\beta X}$ and $\mathbf{6}_{\alpha X}$ where X stands for the position of the counter-ion around the complex (Figure III.8). All the energies are gathered in Table VI.1 and the energy reference is the addition of the energy of $\mathbf{5}^+$ and NTf_2^-. Overall, the ion-pairing has an important effect on the energies of these complexes, ranging from -4.5 to 8.0 kcal/mol, and eight associations are exergonic. For the four complexes, the positions of NTf_2^- yielding the lowest energies are **C** and **E**, in which the counter-ion is in the cavity created by the phosphine, the naphthyridine backbone and the pyridines of DPEOPN. The presence of NTf_2^- in the environment of $\mathbf{5}^+$, $\mathbf{5}_\alpha^+$, $\mathbf{5}_\beta^+$ and $\mathbf{6}_\alpha^+$ has little impact on their geometries;

the only important modification is the shortening of the distance between the coppers by 0.2 Å in $\mathbf{5}_{\alpha B}$. Thus, the energy differences observed for these series are mostly due to the weak interactions occurring between the complexes and the counter-ion. The most stable intermediate with the azide coordinated to $\mathbf{2}^{+}$ is $\mathbf{5}_{E}$, in which NTf_2^- is paired to the complex and DPEOPN is fully coordinated.

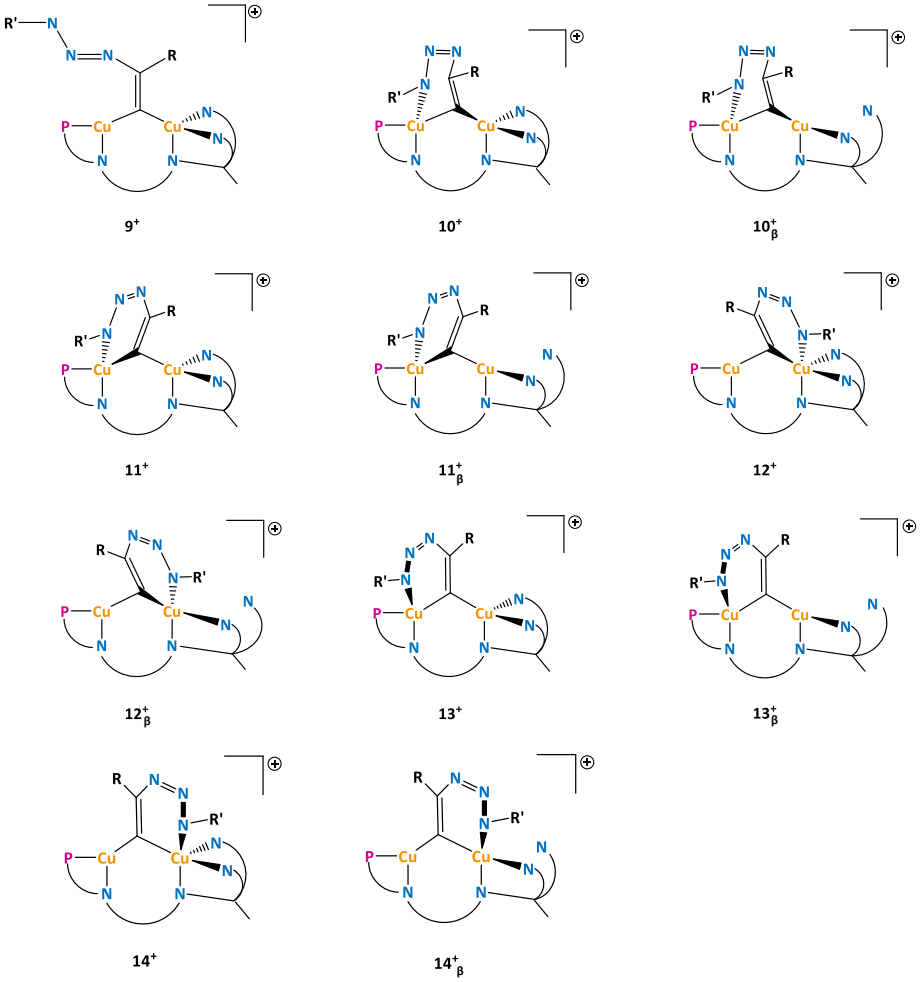

Figure VI.5. Tentative intermediates after the first C-N bond formation.

Then, the metallocycle intermediate, in which the first C-N is formed, was investigated (Figure VI.5). From the 11 attempts, ten converged to a complex where a triazolyl is bridging the two coppers, *i.e.* where the two C-N bonds are already formed (Figure VI6). Only $\mathbf{9}^{+}$ converges into an intermediate in which the carbons of the alkynyl and the nitrogens N_4 and N_5 of the azide form a 4-membered ring. The energy of $\mathbf{9}^{+}$ is 22.0 kcal/mol higher than $\mathbf{2}^{+}$ and as the two C-N bond are already formed, no further reactivity that could lead to the triazolyl seems plausible. Therefore, the intermediate $\mathbf{9}^{+}$ is considered irrelevant to this mechanism and no intermediate between the formations of the first and the second C-N bonds were found.

The last intermediate examined is the one where a triazolyl is bridging the coppers after the formations of the two C-N bond between the alkynyl and the azide. The only intermediate considered is $\mathbf{15}^{+}$ and its variations shown in Figure VI.6. The geometry of $\mathbf{15}^{+}$ is similar to the ones of $\mathbf{1}^{+}$ and $\mathbf{2}^{+}$: the pyridines and the naphthyridine backbone are coordinated symmetrically to the coppers, with 2.08 and 2.12 Å on average, respectively. The distance between the coppers is 2.40 Å and the triazolyl is bridging them symmetrically at 2.02 Å. The triazolyl is tilted one side toward on the naphthyridine backbone (Figure VI.7). As for all the other intermediates, the partial dissociation of DPEOPN was considered via the rotation of the pyridine **α** or **β**, leading to $\mathbf{15}_{\alpha}^{+}$ and $\mathbf{15}_{\beta}^{+}$. The dissociation does not affect the geometry of $\mathbf{15}^{+}$ as the biggest change is the slightly dissymmetric coordination of the coppers to the naphthyridine (2.16 and 2.08 Å for Cu_1 and Cu_2 in $\mathbf{15}_{\alpha}^{+}$). All the other distances and angles are similar to the ones in $\mathbf{15}^{+}$. The energy of these intermediates are also comparable to the one of $\mathbf{15}^{+}$, as $\mathbf{15}_{\alpha}^{+}$ and $\mathbf{15}_{\beta}^{+}$ are 1.5 and 2.9 kcal/mol higher, respectively.

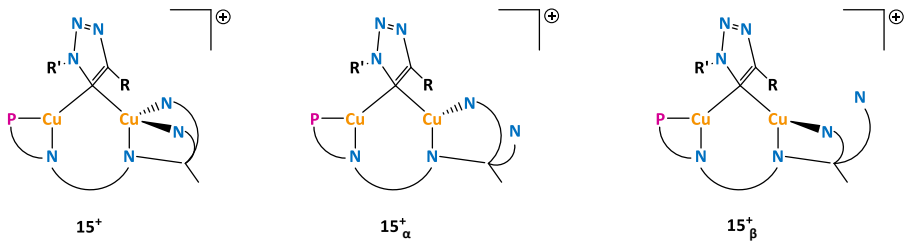

Figure VI.6. Tentative intermediates for the second C-N bond formation.

The effect of the ion-pairing with NTf_2^- on $\mathbf{15}^+$, $\mathbf{15}_\alpha^+$ and $\mathbf{15}_\beta^+$ was also investigated, leading to the series $\mathbf{15}_\mathbf{X}$, $\mathbf{15}_{\alpha\mathbf{X}}$ and $\mathbf{15}_{\beta\mathbf{X}}$, where X describes the position of NTf_2^- around the complexes (Figure III.8). As for $\mathbf{5}^+$, the association does not affect the geometry of the complexes as the larger fluctuation is observed in the $\mathbf{15}_{\alpha\mathbf{X}}$ series: the distance between Cu_1 and the naphthyridine backbone varies from 2.13 to 2.23 Å. The ion-pairing impacts the energy of $\mathbf{15}^+$, $\mathbf{15}_\alpha^+$ and $\mathbf{15}_\beta^+$, with energies varying between -3.6 and 5.0 kcal/mol (Table VI.2). The most stable positions are **C** and **E** for the three complexes, as for most intermediates. The lowest one is $\mathbf{15}_\mathbf{E}$, in which DPEOPN is fully coordinated to the coppers and the NTf_2^- is in the cavity created by DPEOPN.

Complex	ΔG (kcal/mol)
$\mathbf{15}^+$	0.0
$\mathbf{15}_\mathbf{A}$	2.7
$\mathbf{15}_\mathbf{B}$	0.3
$\mathbf{15}_\mathbf{C}$	-1.8
$\mathbf{15}_\mathbf{D}$	-1.7
$\mathbf{15}_\mathbf{E}$	-3.6

Complex	ΔG (kcal/mol)
$\mathbf{15}_\alpha^+$	1.5
$\mathbf{15}_{\alpha\mathbf{A}}$	2.1
$\mathbf{15}_{\alpha\mathbf{B}}$	-1.0
$\mathbf{15}_{\alpha\mathbf{C}}$	-3.3
$\mathbf{15}_{\alpha\mathbf{D}}$	1.3
$\mathbf{15}_{\alpha\mathbf{E}}$	-1.8

Complex	ΔG (kcal/mol)
$\mathbf{15}_\beta^+$	2.9
$\mathbf{15}_{\beta\mathbf{A}}$	5.0
$\mathbf{15}_{\beta\mathbf{B}}$	1.6
$\mathbf{15}_{\beta\mathbf{C}}$	0.4
$\mathbf{15}_{\beta\mathbf{D}}$	-
$\mathbf{15}_{\beta\mathbf{E}}$	0.2

Table VI.2. Free energy of the ion-paring for $\mathbf{15}^+$, $\mathbf{15}_{\alpha\mathbf{X}}$ and $\mathbf{15}_{\beta\mathbf{X}}$.

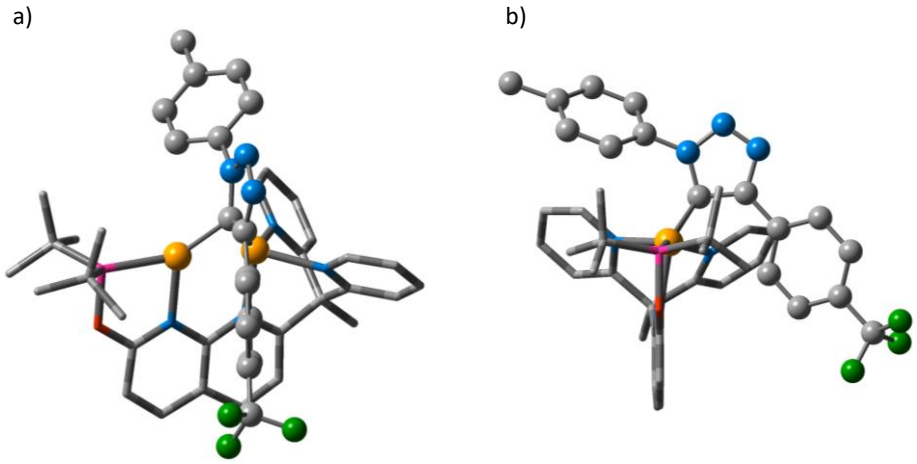

Figure VI.7. 3D representation of 15^+ from the a) front and b) side.

Over the four intermediates postulated to participate in the mechanism of the CuAAC reaction, only three, $\mathbf{2}^+$, $\mathbf{5}^+$ and $\mathbf{15}^+$ were found and they can be arranged in a tentative catalytic cycle (Figure VI.8). As it is, this mechanism involves three steps: A) the coordination of the azide to $\mathbf{2}^+$, B) the cyclisation between the alkynyl and the azide and C) the proton transfer from the alkyne to $\mathbf{15}^+$. The thermodynamic of this tentative catalytic cycle are promising as the coordination of the azide is thermoneutral; $\mathbf{5}_\mathbf{E}$ is -0.8 kcal/mol lower than $\mathbf{2}_\mathbf{B}$; and cyclisation step is very exergonic as $\mathbf{15}_\mathbf{E}$ is -53.9 kcal/mol lower than $\mathbf{2}_\mathbf{B}$. For these three intermediates, it is more advantageous for DPEOPN to be fully coordinated to the coppers and the association between the complexes and NTf_2^- is exergonic in all cases. The following sections of this chapter detail the search of transition states connecting these intermediates.

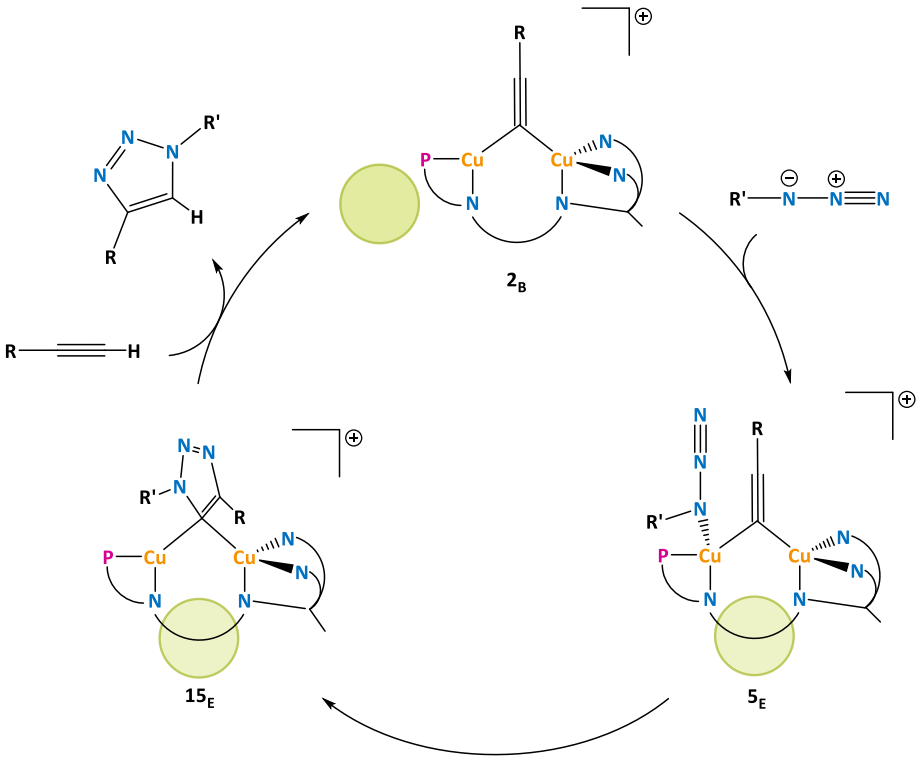

Figure VI.8. Postulated catalytic cycle for the Cu_2AAC reaction after exploring the stability of the potential intermediates.

2 - Step A: the coordination of the azide to 2^+

The first step of the catalytic cycle is the coordination of the azide to **2^+** (Figure VI.9). As there is often no or low-lying transition state for coordination step, a scan of the potential energy surface (PES) was done to check the presence of a transition state. The scan was done along the N_3-Cu_1 bond, with a point every 0.1 Å (Figure VI.10). Each point of the scan correspond to a constrained optimization in which all internal coordinates were relaxed except for N_3-Cu_1 and the energies reported are electronic since no frequency calculations were done.

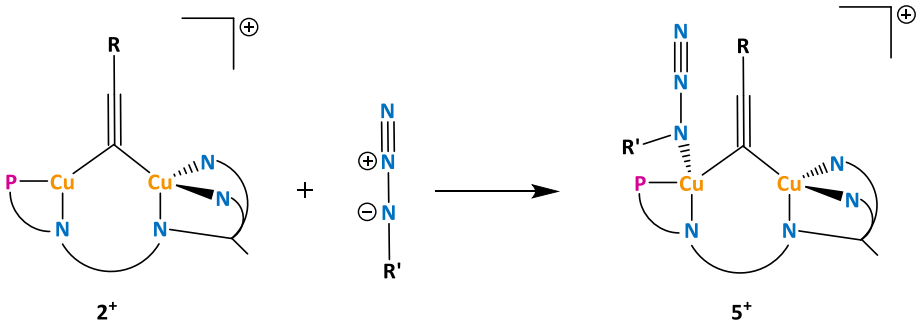

Figure VI.9. Step A: the azide coordination to 2^+.

The scan has no energy maximum and does not provide any evidence for the presence of a transition state on the PES. The minima around 2.30 Å correspond to the fully optimized geometry of $\mathbf{5}^+$. When the bond length diminish or augment, the electronic energy increases. A plateau in the energy is present around 3.00 Å and likely corresponds to the van der Waals complex of $\mathbf{5}^+$ and the azide. Overall, there is no clear indication of the presence of a transition state for this step and the energetic cost of this coordination step is postulated to originate only from the entropy penalty.

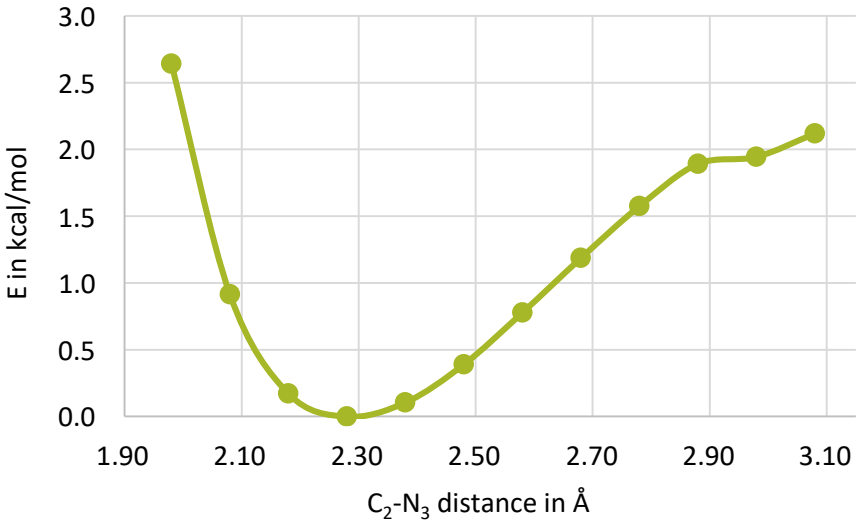

Figure VI.10. Scan of the electronic energy along the Cu_1-N bond in 5^+.

3 - Step B: the formation of the triazolyl complex 15^+

The second step of the CuAAC reaction consists of the cyclisation of the alkynyl and the azide ligands present in $\mathbf{5}^+$, forming the intermediate $\mathbf{15}^+$, in which a triazolyl is bridging the two coppers (Figure VI.11). None of the intermediates based on $\mathbf{6}^+$ (Figure VI.3) where considered as a starting point for this step as they all are higher in energy than the $\mathbf{5}^+$ ones. Overall, 18 transition states have been computed (Figures VI.12 and VI.13) and they form the $\mathbf{TS_7}$ series. In this section of the thesis, the energy references used to compare the energy of the transition states are either the energy of $\mathbf{5}^+$ or $\mathbf{5_E}$, depending on the presence of the counter-ion.

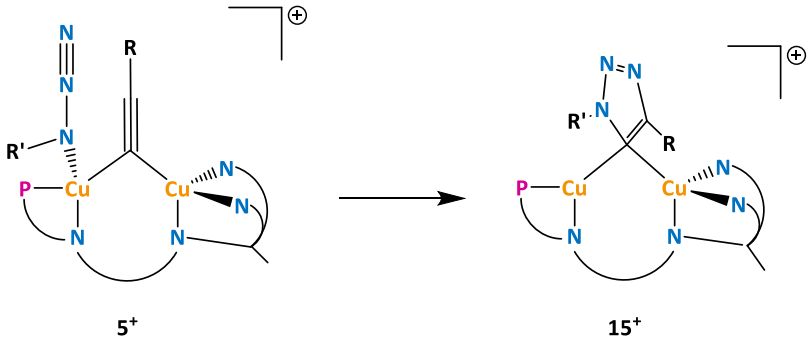

Figure VI.11. Step B of the catalytic cycle: triazolyl formation.

a) Search of the transition states

The simplest transition state for the cycloaddition is $\mathbf{TS_7}$, in which the effects of the partial dissociation of DPEOPN and of the ion-pairing with NTf_2^- are ignored. $\mathbf{TS_7}$ has a geometry close to the one of $\mathbf{5}^+$ as the coordination of the alkynyl and DPEOPN do not seems to be altered (Figure VI.15a). The naphthyridine and the pyridines coordinate symmetrically to the coppers with respective distances of 2.16 and 2.10 Å. The alkynyl is bridging the two coppers asymmetrically: the distance with Cu_1 is 0.14 Å longer than the one with Cu_2, due to the coordination of the azide to Cu_1. The azide is much closely coordinated than in $\mathbf{5}^+$ as the bond distance is shorten by 0.2 Å to 2.10 Å. This leads to an increase of the distance between the coppers to 2.59 Å, indicating that more distortions are needed to allow the azide closer to the coppers. The

two forming C-N bonds, *i.e.* N_3-C_2 and N_5-C_3, have very different lengths, with 2.87 Å for the former and 1.94 Å for the latter, but they are both involved in the imaginary frequency of the transition state. With the formation of these bonds, the alkynyl becomes "alkyl like" and the change in the nature of the multiple bond between C_2 and C_3 is apparent in the C_2-C_3-C_4 angle of 144.5°, compared to the 180.0° of the free alkyne. The energy of **TS_7** is 20.6 kcal/mol (in red in Figure VI.14). As for the previous series of transition states, the effects of the ion-pairing with NTf_2^-, of the partial dissociation of DPEOPN and of both combined are detailed in the next paragraphs.

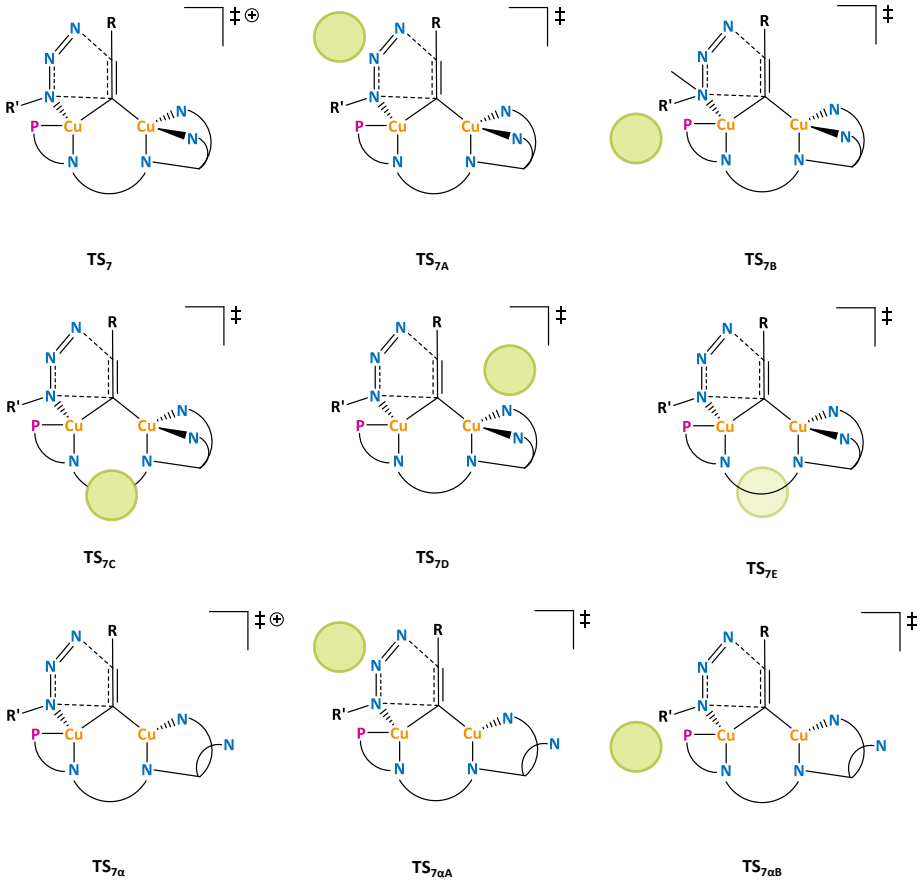

Figure VI.12 Schematic representations and labels of all the transition states computed for the TS_7 series; the green circles represent the position of NTf_2^- (1/2).

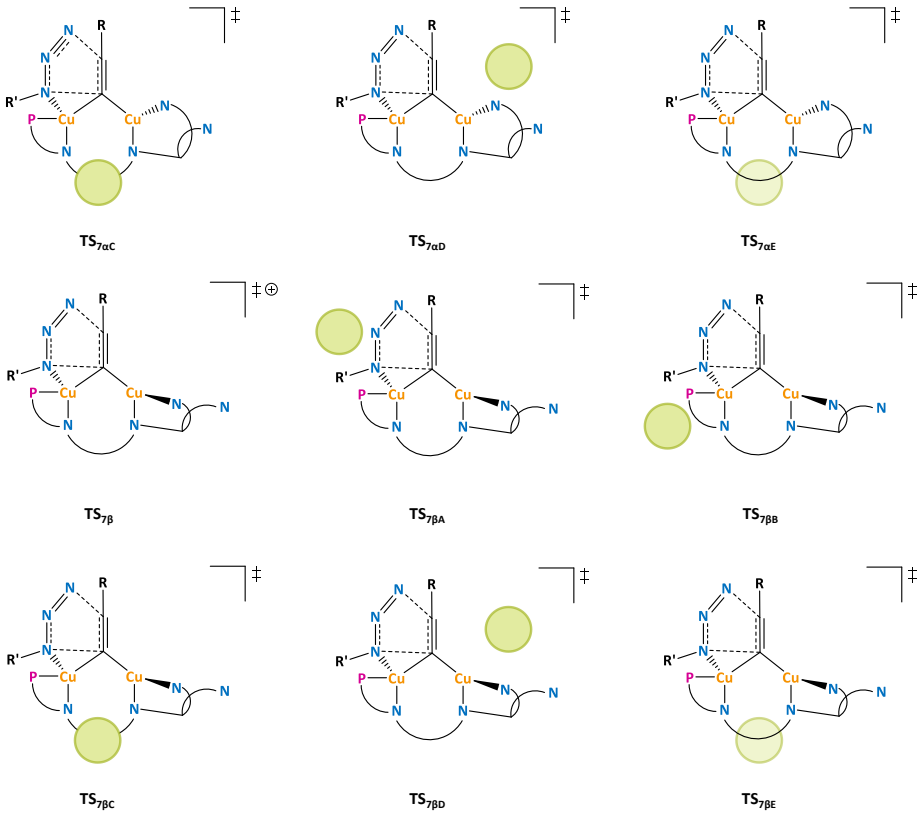

Figure VI.13. Schematic representations and labels of all the transition states computed for the TS_7 series; the green circles represent the position of NTf_2^- (2/2).

To examine the effect of the ion-paring, five positions of NTf_2^- around **TS_7** were investigated and led to the **TS_{7X}** transition states (Figure VI.12). The impact of this association on the geometry of **TS_7** is minimal as the most substantial deviations are in the range of ± 0.05 Å for the distances and of 2.5° for the angle C_2-C_3-C_4. However, the repercussion on the energy of these transition states are bigger: it ranges from 20.0 to 25.6 kcal/mol (red dashed in Figure VI.14). Thus, the association of NTf_2^- with **TS_7** is isoenergetic in one case (position **E**) and unfavourable in the others and the energy differences between the transition states arise from the various weak interactions with NTf_2^-. In the most stable transition state (**TS_{7E}**) the counter-ion is in the cavity created by the phosphine, the pyridine **β** and the naphthyridine backbone. In

addition to DPEOPN, NTf_2^- interacts with the toluene substituent of the azide as it is positioned below its aromatic ring (Figure VI.15b).

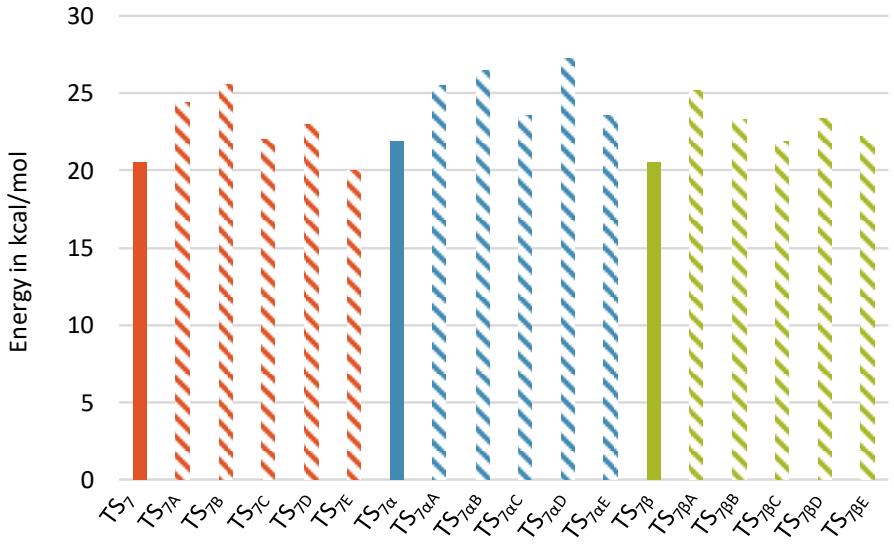

Figure VI.14. Free energy of all the transition states of the TS_7 series.

When the partial dissociation of DPEOPN in **TS_7** was investigated, only the dissociations of the pyridines were included, as they were the only considered for the intermediates, yielding **$TS_{7\alpha}$** and **$TS_{7\beta}$** (Figure VI.12 and VI.13). The dissociation has little impact on the geometry of the two transition states: the remaining bonds with DPEOPN are slightly shorter for Cu_2 and longer for Cu_1 (-0.08 Å and +0.06 Å for the naphthyridine core in **$TS_{7\beta}$**). Overall, the distances varies by less than 0.1 Å. These few modifications have no energetic impacts on **$TS_{7\beta}$** as its energy is 20.6 kcal/mol, like **TS_7**, and are slightly unfavourable for **$TS_{7\alpha}$**, with 21.9 kcal/mol.

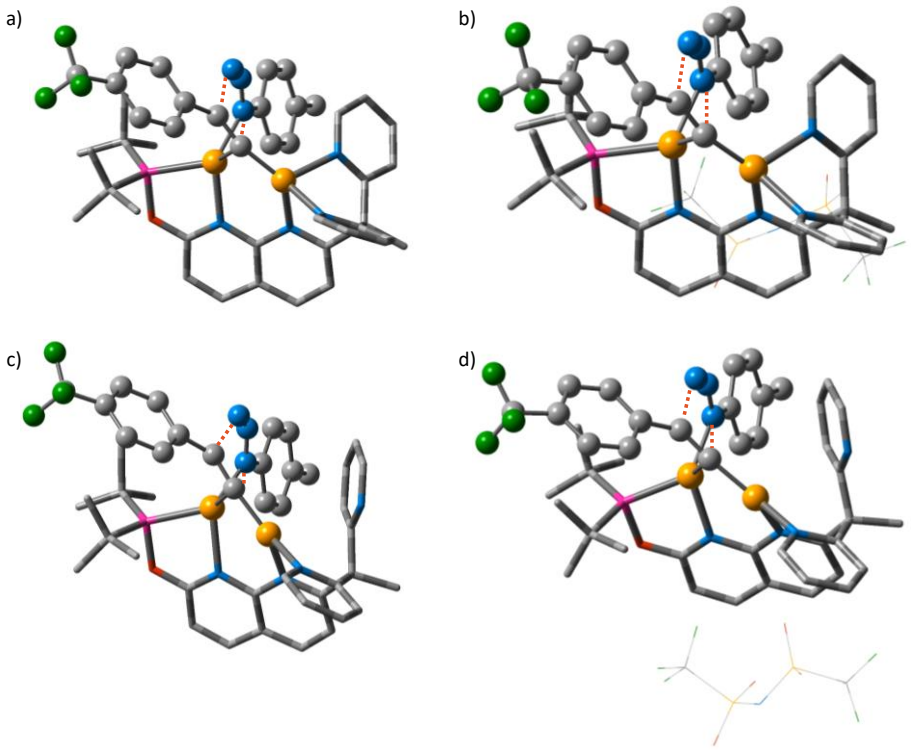

Figure VI.15. 3D representation of a) TS_7, b) TS_{7E}, c) $TS_{7\beta}$ and d) $TS_{7\beta C}$. The red dashed lines account for the formation of the two C-N bonds between the azide and alkynyl moieties.

Finally, the effects of the ion-pairing with NTf_2^- and of the partial dissociation of DPEOPN were examined simultaneously, leading to the **$TS_{7\alpha X}$** and **$TS_{7\beta X}$** series where X stands for the position of the counter-ion around the complex (Figures VI.12 and VI.13). The association between NTf_2^- and **$TS_{7\alpha X}$** is unfavourable as their energy ranges from 23.5 to 27.3 kcal/mol. The geometry of these transition states are not much influenced by the presence of the counter-ion; with distances varying less than 0.1 Å; and NTf_2^- do not interact directly with the metal centres. In the **$TS_{7\beta X}$** series, the association in the positions **A**, **B**, **C** and **E** do not lead to relevant changes in the geometry of **$TS_{7\beta}$**. However, in **$TS_{7\beta D}$**, NTf_2^- is above the pyridines arm and one of its CF_3 is close to the π system of the alkynyl (around 3.20 Å). As a result, the alkynyl bends more towards NTf_2^-, with a Cu_1-C_2-C_3 angle of 126.7° compared to 97.3° in

$TS_{7\beta}$, where the alkynyl bends more towards the phosphine. It also reduces the difference in the distances between the coppers and C_2 (1.97 and 1.90 Å with Cu_1 and Cu_2, respectively) and the distance between the coppers diminishes to 2.46 Å, which is close to the value in **5^+**. However, **$TS_{7\beta D}$** yields a barrier of 24.2 kcal/mol, showing that the geometry observed in most of the transition states in the **TS_7** series is preferable. The lowest position for NTf_2^- is **C**, in the cavity formed by DPEOPN, but on the side opposite to the coordination site of the azide. However, the association is still unfavourable, with 21.9 kcal/mol. The combination of the effects of the dissociation of DPEOPN and of the ion-paring with NTf_2^- do not yield favourable interactions in the case of **TS_7**.

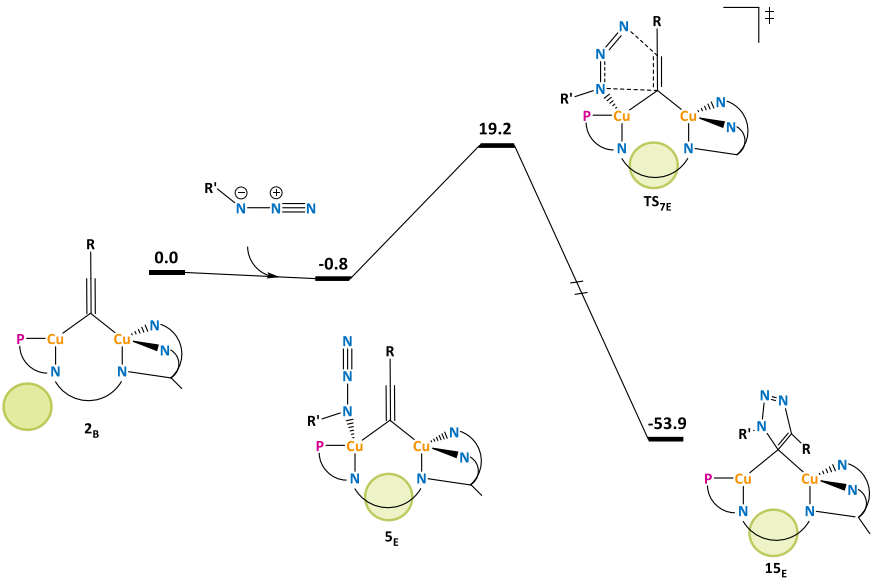

Figure VI.16. Schematic representation of the mechanism of the cyclisation of the CuAAC reaction; the green circles represent the position of NTf_2^-.

Overall, the transition states for the cyclisation step of the CuAAC reaction are in a low energy range of 20.0 to 27.3 kcal/mol, the lowest one being **TS_{7E}**. In this mechanism, the association of the transition states with NTf_2^- lowers their energy, whereas the partial decoordination of DPEOPN increases it. To be certain of the nature of these transition states, an IRC-driven relaxation were

done on a selection of them and no additional intermediates were found. The figure VI.16 summarizes the mechanism of the cyclisation **2**$^{+}$ with the azide.

b) Selectivity of the cycloaddition step

As stated in the introduction of this thesis, the CuAAC reaction is a selective copper catalysed version of the Huisgen addition. The mechanism and the origin of the selectivity of this reaction was already discuss in the case of the copper salt as catalyst.[176,177] With the DPEOPN catalyst, the reaction is also selective as no trace of the 1,5 triazole isomer has been detected experimentally.[45] Thus, the mechanism for the formation of the 1,5 triazole was computed to explain the selectivity in this case. Only the simpler case was consider: the counter-ion NTf_2^- is neglected and DPEOPN is fully coordinated to the coppers. For the 1,5 cycloaddition, the mechanism starts with **2**$^{+}$ and the azide separately and they form an adduct at 2.0 kcal/mol in which the azide do not coordinate to the copper but where its toluene substituent does a π-stacking interaction with the substituent of the alkynyl in **2**$^{+}$. However, the azide does coordinate to the copper on the phosphine side in the transition state (2.26 Å). The forming bond with C_2 is much shorter than the one in **TS$_7$** (2.09 versus 2.87 Å) while the bond with C_3 is elongated (2.19 versus 1.94 Å). This changes causes the transition state for the 1,5 cycloaddition to be 6.9 kcal/mol higher than **TS$_7$**. The triazolyl product is coordinated to the coppers at similar distance (2.02 Å) but its $ArCF_3$ substituent can do a C-H-π interaction with one of the pyridine (average distance of 2.80 Å). This 1,5 triazolyl complex is 9.4 kcal/mol higher than **15**$^{+}$. This higher energies for the 1,5 cycloaddition arise from increasing steric hindrance between the azide and the alkynyl as well as a stronger polarization. For example, the natural charge of Cu_1 is +0.29 in **TS$_7$** versus +0.79 in the transition state for the 1,5 cycloaddition (Table VI.3). This extra charge separation is apparent for most atoms in the active site in both the transition state and the 1,5 triazolyl complex. Thus, the 1,5 cycloaddition is thermodynamically and kinetically unfavourable compared to the 1,4 cycloaddition. These energies are consistent with the selectivity of the CuAAC reaction observed in the experiments with the DPEOPN di-copper catalyst.

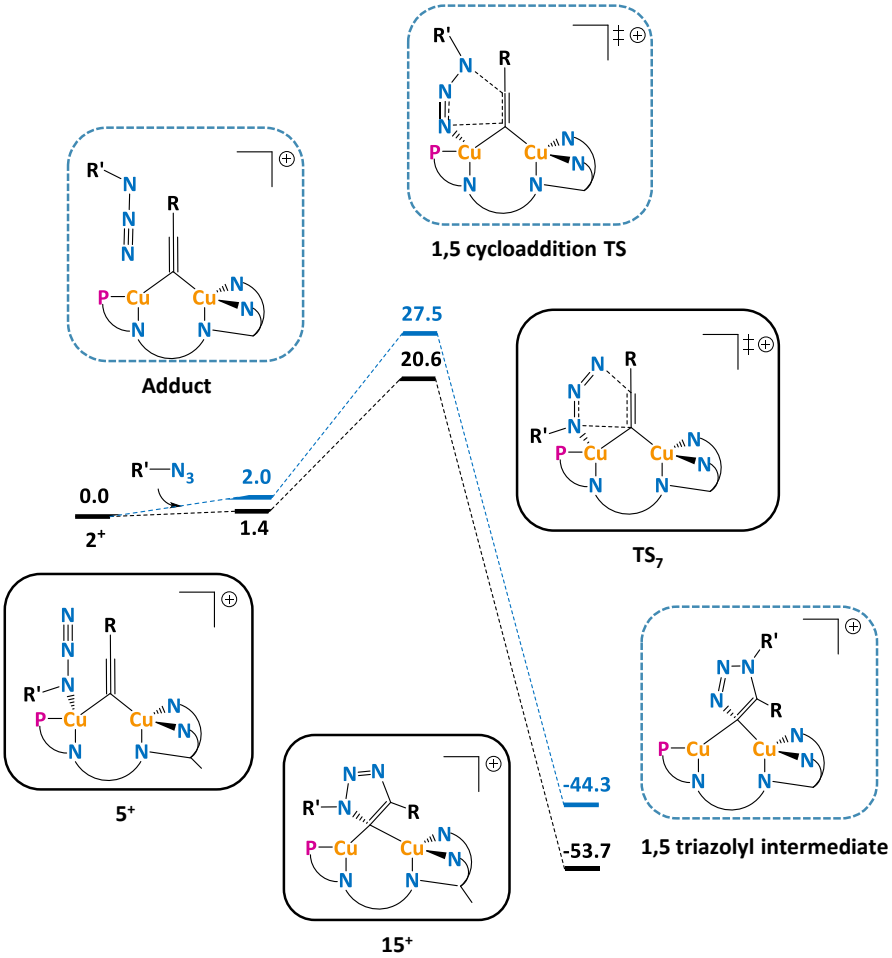

Figure VI.17. Cycloaddition mechanism to obtain the 1,4 (full black line) and 1,5 (dashed blue line) triazolyl di-copper complexes.

TS_7	Charge	1,5 isomer TS	Charge
Cu_1	+0.29	Cu_1	+0.79
Cu_2	+0.49	Cu_2	+0.88
C_1	-0.23	C_1	-0.58
C_2	-0.14	C_2	-0.05
N_1	-0.33	N_1	-0.20
N_2	+0.13	N_2	+0.12
N_3	-0.10	N_3	-0.25
15^+	**Charge**	**1,5 triazolyl intermediates**	**Charge**
Cu_1	+0.35	Cu_1	+0.70
Cu_2	+0.45	Cu_2	+0.84
C_1	-0.25	C_1	-0.46
C_2	0.00	C_2	+0.07
N_1	-0.18	N_1	-0.32
N_2	-0.09	N_2	-0.09
N_3	-0.27	N_3	-0.17

Table VI.3. Charge distribution along the pathways of the 1,4 and 1,5 cyclisations.

c) Descriptors analysis of the transition states

The 18 transition states obtained for the cyclisation step of the CuAAC were analysed using descriptors, defined by 15 different geometrical and electronical parameters, including:

- Position of NTf_2^-
- Distance between Cu_1 and Cu_2
- Distance between the C_2 and N_3
- Distance between the C_3 and N_5
- Distance between the C_2 and C_3
- Dihedral angle Cu_1-N_1-N_2-Cu_2
- Natural charge of Cu_1
- Natural charge of Cu_2

- Difference of natural charge between Cu_1 and Cu_2
- Natural charge of the C_2
- Natural charge of the C_3
- Natural charge of the N_3
- Natural charge of the N_5
- Difference of natural charge between C_2 and N_3
- Difference of natural charge between C_3 and N_5

In the additional *Descriptors file* (see annexes) are scatter plots showing the potential correlations between these descriptors and the energy barriers of the **TS_7** series. As previously stated, the lowest transitions states are taking into account the ion-pairing or the partial dissociation of DPEOPN even if the range of the energy in this series is quite narrow, from 20.0 to 27.3 kcal/mol. For comparison, the energy range was from 22.9 to 39.9 kcal/mol for the concerted mechanism of the C-H activation of alkyne (see Chapter IV). Another noticeable features is the small distortions the complex undergo during this cyclisation: the alkynyl is still bridging the coppers, in line with the short distance between the two metal centres (2.50 to 2.65 Å). The descriptor analysis did not reveal any clear trend as the highest R^2 value is 0.3162 for the natural charge of N_3.

4 - Step C: the regeneration of 2^+ from 15^+

The third and last step of the CuAAC reaction consists of the proton transfer between the alkyne and **15^+**, leading to the regeneration of **2^+** and the formation of the 1,4-triazole (Figure VI.18). In this section of the thesis, the energy references used to compare the energy of the transition states are either the energy of **15^+** or **15_E** plus the alkyne, depending on the presence of the counter-ion. For this step a concerted proton transfer was assumed, similarly to the one for the concerted activation of alkynes (see Chapter IV). There are four possible isomers for the transition state: depending on the positions of the triazolyl and of the alkynyl on the copper (**TS_8** and **TS_9** have alkynyl group on Cu_2 while it is on Cu_1 for **TS_{10}** and **TS_{11}**) and on the orientation

of the triazolyl compared to the alkynyl (the two $ArCF_3$ groups are close to each other like in **TS_9** and **TS_{11}**, or away from each other as from **TS_8** and **TS_{10}**). All these different series of transition states are described in this section.

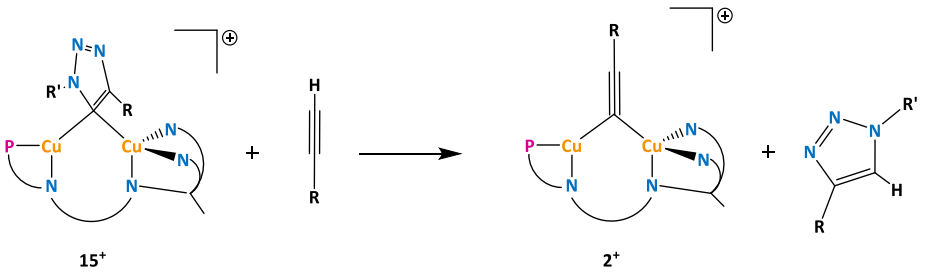

Figure VI.18. Step C of the CuAAC reaction: regeneration of 2^+.

a) Search of the transition states

The first series of isomers considered is **TS_8** and it contains 18 transition states (Figures VI.19 and VI.20). In this series, the alkynyl is coordinated to Cu_2 and the triazolyl on Cu_1, the latter is orientated so its tolyl substituent is near the alkynyl. The simplest transition state of this series is **TS_8** (Figure VI.22a), in which the effects of the partial dissociation of DPEOPN and of the ion-pairing with NTf_2^- are ignored. The distance between the coppers is 2.78 Å, which represent a distortion of 0.40 Å compared to **15^+** and **2^+**. Many transition states reported in this work have similar features or are even more distorted and considering the size of the substituents, **TS_8** is quite compact. The coordination of the pyridines to Cu_2 are symmetrical (2.09 Å in both cases) but the naphthyridine backbone is bound more tightly to Cu_2 than to Cu_1 (2.04 versus 2.22 Å). The alkynyl is coordinated to Cu_2 with the usual bond distance of 1.92 Å while the bond between Cu_1 and the triazolyl is elongated by 0.1 Å to 2.10 Å, due to steric interactions with the naphthyridine. The alkynyl is in the same plane as the coppers and the triazolyl is orientated toward the back, with its $ArCF_3$ substituent in the cavity **E** along the naphthyridine and close to the pyridine **β**. The tolyl substituent of the triazolyl is parallel to the $ArCF_3$ of the alkynyl (4.00 Å apart), suggesting the presence of a π-π interaction between them. The transferred proton is closer to the alkynyl than to the triazolyl, with 1.38 and 1.54 Å, respectively. The energy of **TS_8** is high, with

32.9 kcal/mol (red in Figure VI.21). The effect of the pairing with NTf_2^- and of the partial dissociation of DPEOPN are summarized in the following paragraphs.

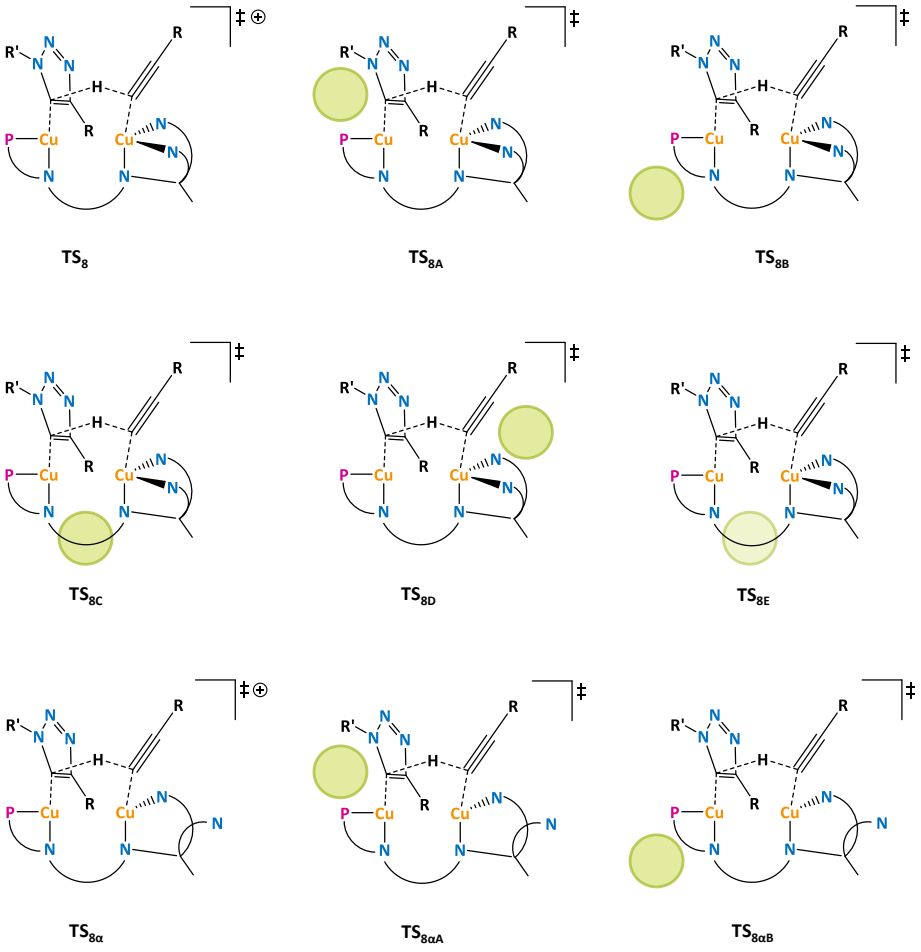

Figure VI.19. Schematic representations and labels of all the transition states computed for the TS_8 series; the green circles represent the position of NTf_2^- (1/2).

The counter-ion is added to **TS_8** to create the **TS_{8X}** series, with X describing the position of the counter-ion around the complex (**A** to **E** see Figure VI.19). The associations are unfavourable as the energies vary in the narrow range of 34.7 to 36.5 kcal/mol (red dashed in Figure VI.21). Overall, the geometry of **TS_8** is not impacted by the presence of the counter-ion as the biggest modification is the elongation of the distance between Cu_1 and the naphthyridine backbone (N_1) by 0.06 Å in **TS_{8A}**. Thus, the variation in energy are mainly due to the diverse interactions introduced by NTf_2^- depending on its position. It is worth noting that the two highest transition states, **TS_{8A}** with 35.1 and **TS_{8E}** with 36.5 kcal/mol, are the only ones in which the counter-ion interacts with the triazolyl. In the three remaining transition states, NTf_2^- interacts only with DPEOPN, and with the alkynyl ligand for **TS_{8C}**, leading to an energy of 34.7 kcal/mol in all cases. The associations of **TS_8** with NTf_2^- yield to barriers that are too high to be plausible.

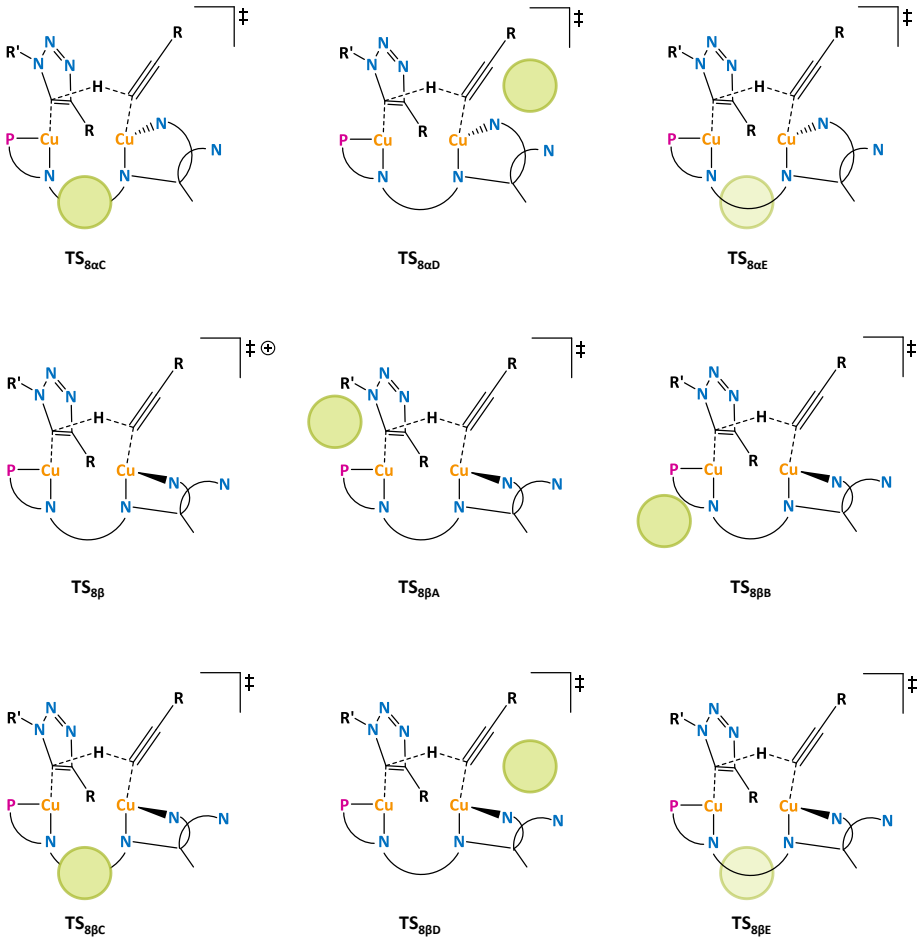

Figure VI.20. Schematic representations and labels of all the transition states computed for the TS_8 series; the green circles represent the position of NTf_2^- (2/2).

The impact of the partial dissociation of DPEOPN on **TS_8** was investigated via the dissociation of the pyridines **α** and **β** only, as for the intermediates and the cyclisation step, yielding **$TS_{8α}$** and **$TS_{8β}$** (Figure VI.22b). As for the ion-pairing, the geometry of **TS_8** is not affected by the dissociation in both cases, with changes below 0.05Å. The dissociations are unfavourable with an energy of 35.5 kcal/mol for both **$TS_{8α}$** and **$TS_{8β}$**. Thus, neither the effects of the ion-pairing nor the partial dissociation can lower the energy of **TS_8** alone.

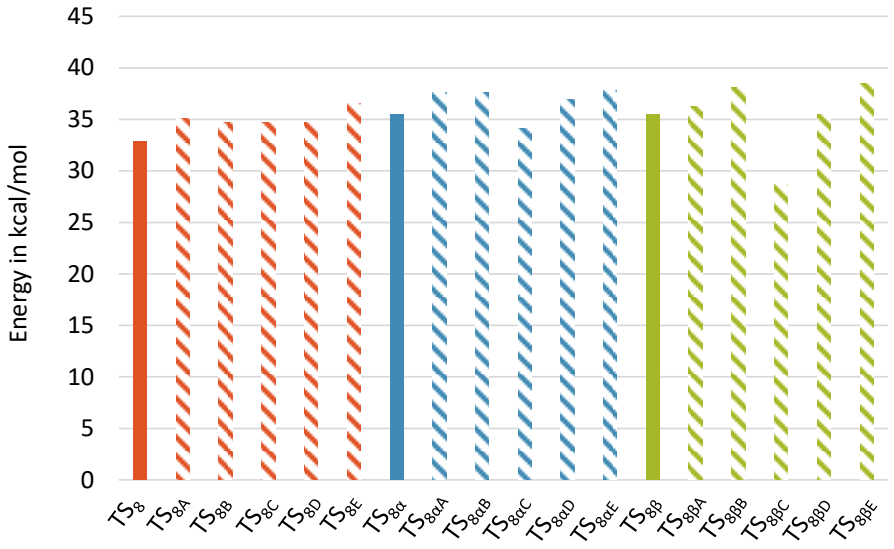

Figure VI.21. Free energy of all the transition states of the TS_8 series.

To complete the TS_8 series, the combined effects of the ion-paring with NTf_2^- and the partial dissociation of DPEOPN were considered together, leading to the series $TS_{8\alpha X}$ and $TS_{8\beta X}$ (Figures VI.19 and VI.20). The $TS_{8\alpha X}$ series is very similar to the previous transition states: the geometry is not impacted (less than 0.1 Å of difference) and the energy varies from 34.1 to 37.8 kcal/mol (dashed blue in Figure VI.21). The most stable one is $TS_{8\alpha C}$ and it is the only one for which the interaction of NTf_2^- with $TS_{8\alpha}$ is favourable (-1.4 kcal/mol). In $TS_{8\alpha C}$, NTf_2^- is in the cavity formed by the phosphine, the naphthyridine backbone and the dissociated pyridine **α** and it interacts only with these parts of $TS_{8\alpha}$. The transition states where NTf_2^- interacts with the triazolyl have high energy: between 36.9 and 37.8 kcal/mol for $TS_{8\alpha A}$, $TS_{8\alpha D}$ and $TS_{8\alpha E}$. The transition states in the $TS_{8\beta X}$ series are comprised within a large range of energies; 28.7 to 38.5 kcal/mol (dashed green in Figure VI.21) and their geometry are more varied than in the $TS_{8\alpha X}$ series. Compared to TS_8 and $TS_{8\beta}$, $TS_{8\beta A}$, $TS_{8\beta B}$ and $TS_{8\beta D}$ display no geometrical changes but $TS_{8\beta C}$ and $TS_{8\beta E}$ do (Figure VI.22c and d). $TS_{8\beta C}$ is much more distorted than other transition states in the series, with a distance between the coppers of 3.19 Å corresponding to an increase of 0.37 Å compared to $TS_{8\beta}$. This elongation comes from the loose

coordination of NTf_2^- to Cu_2 (2.40 Å) that forces it to come forward and thus lengthens the distance to Cu_1. It also leads to the elongation of the breaking bond between C_2' and H to 1.42 Å, meaning that the proton is now equidistant from the two carbons. Another dramatic change is the mode of coordination of the alkynyl: it is bonded to the two coppers in an asymmetric way, with distances of 2.17 and 2.00 Å from Cu_1 and Cu_2, respectively. The coordination of the triazolyl is less impacted as it only increases by 0.1 Å to 2.21 Å. Apart from coordination to Cu_2, NTf_2^- interacts with both arms of DPEOPN. All this features makes **$TS_{8\beta C}$** the lowest transition state of the **TS_8** series. **$TS_{8\beta E}$** is even more distorted than **$TS_{8\beta C}$**, with the distance between the coppers increasing to 3.88 Å and leading to the dissociation of Cu_1 from the naphthyridine backbone. This modification allows the coordination of NTf_2^- by one of its oxygens to Cu_1 (2.21 Å). As Cu_1 is further away from the naphthyridine backbone, there is more space for the triazolyl group and its bond to Cu_1 shortens to 2.01 Å. In this transition state, NTf_2^- interacts with the ^{t}Bu substituents of the phosphine and the $ArCF_3$ group of the triazolyl. These changes and new interactions on **$TS_{8\beta E}$** leads to the highest energy of the series **TS_8**, with 38.5 kcal/mol. Overall, the association with NTf_2^- and the partial dissociation of DPEOPN have little impact on the 18 transition states of the **TS_8** series, with the exception of **$TS_{8\beta C}$** and **$TS_{8\beta E}$**.

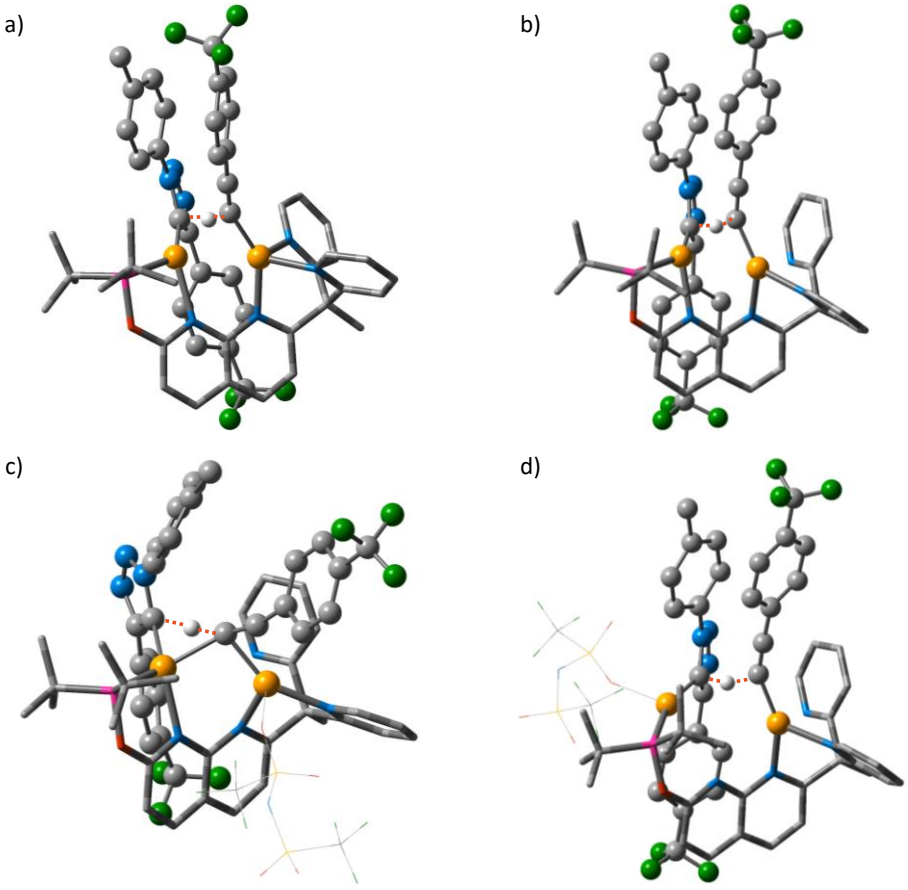

Figure VI.22. 3D representation of a) TS_8, b) $TS_{8\beta}$, c) $TS_{8\beta C}$ and d) $TS_{8\beta E}$. The red dashed lines account for the cleavage and formation of C-H bonds between the triazolyl and alkynyl moieties.

The second series isomer for the C-H activation step of the CuAAC reaction is the **TS_9**, which also contain 18 transition states (Figures VI.23 and VI.24). In this series, the triazolyl is coordinated to Cu_1 while the alkynyl is on Cu_2, as in **TS_8**, but the triazolyl has a different orientation: the $ArCF_3$ substituent is near the alkynyl group and the toluene substituent is facing the naphthyridine backbone. The simplest transition state of this series is **TS_9** (Figure VI.26a), in which the effects of the partial dissociation of DPEOPN and of the ion-pairing with NTf_2^- are neglected. The geometry of **TS_9** is similar to the one of **TS_8**: the naphthyridine backbone is coordinated asymmetrically to both coppers (2.19

and 2.04 Å for Cu_1 and Cu_2) and the pyridines are on average 2.10 Å away from Cu_2. The alkynyl has a typical bond length of 1.92 Å with Cu_2 while the bond between Cu_1 and the triazolyl is elongated to 2.09 Å. The proton is also similarly positioned between the alkynyl and the triazolyl (1.38 and 1.53 Å, respectively). The main difference with **TS_8** is the distance between the coppers, which is shorter in this instance with 2.69 Å. As a result, the $ArCF_3$ group of the triazolyl is closer to the alkynyl than in **TS_8** (ca. 3.50 Å versus 4.00 Å). The energy of **TS_9** is 33.0 kcal/mol which is equivalent to the one of **TS_8**.

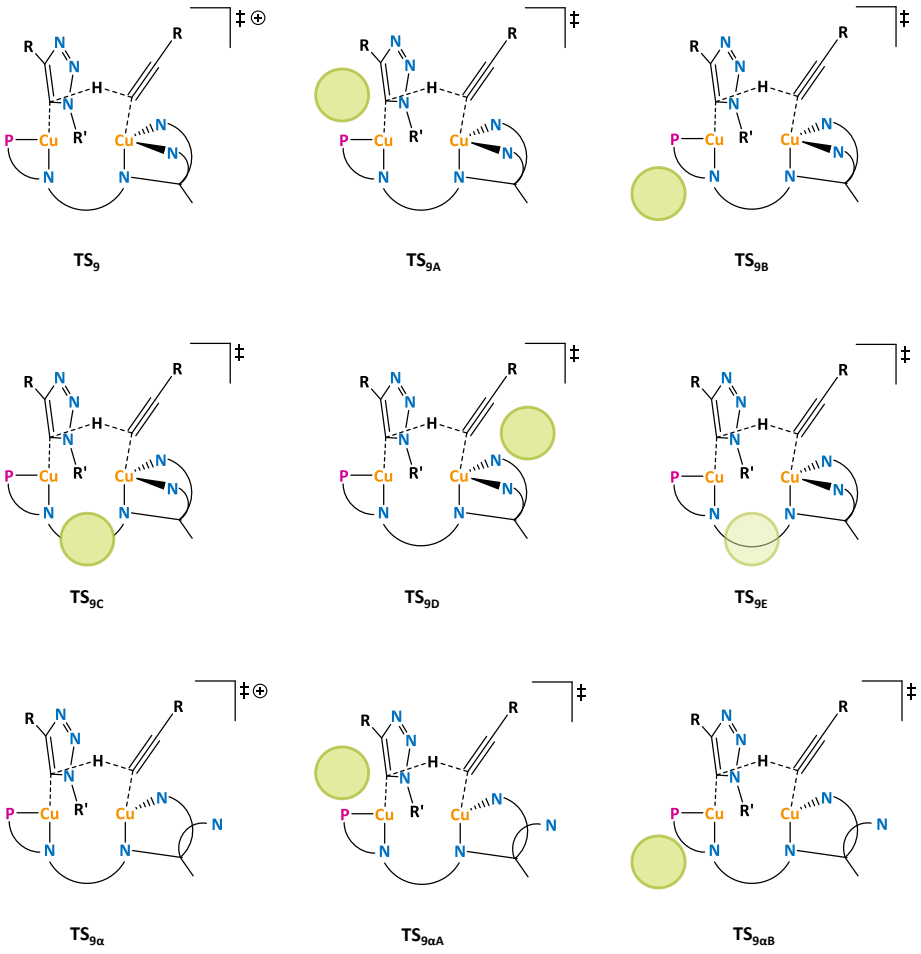

Figure VI.23. Schematic representations and labels of all the transition states computed for the TS_9 series; the green circles represent the position of NTf_2^- (1/2).

The association of **TS$_9$** with NTf_2^- yields the **TS$_{9X}$** series, comprising five transition states, with X labelling the different positions of the counter-ion around the complex (Figure VI.23). The energy of the transition states ranges from 30.0 to 36.5 kcal/mol (dashed red in Figure VI.25) and ion-pairing is only favourable in position **C**. The presence of NTf_2^- in the environment of **TS$_9$** has little impact on its geometry for the positions **A**, **B** and **D**. **TS$_{9C}$** has similar distances too but the orientation of the alkynyl is different as it bends forward over the counter-ion (2.50 Å apart, Figure VI.26b). The rest of the transition state is unchanged. **TS$_{9E}$** is impacted by the presence of NTf_2^- as it drags the triazolyl and Cu_1 away from the naphthyridine backbone, leading to an increased distance between the coppers of 2.83 Å. These changes lead to a high energy of 36.5 kcal/mol for **TS$_{9E}$**. In this case, the interaction between NTf_2^- and **TS$_9$** lowers the $\Delta G^{\ddagger}$ by 3.0 kcal/mol (**TS$_{9C}$**), it is however not low enough for this transition state to be accessible.

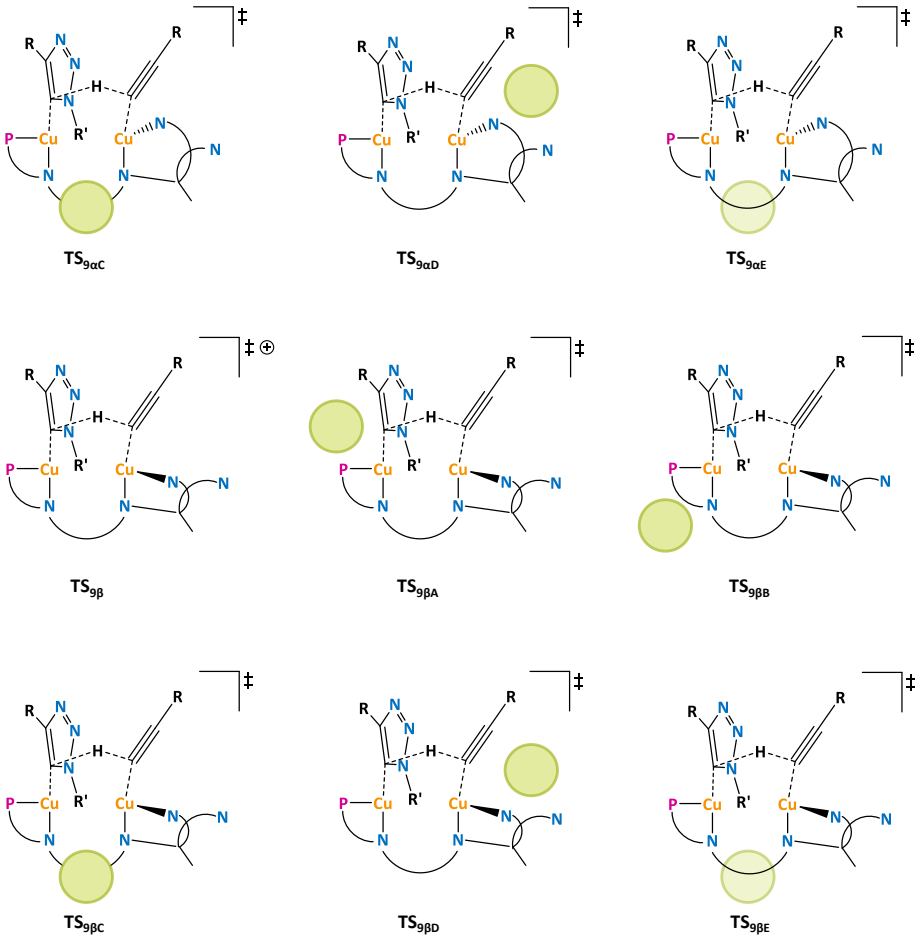

Figure VI.24. Schematic representations and labels of all the transition states computed for the TS_9 series; the green circles represent the position of NTf_2^- (2/2).

The partial dissociation of DPEOPN was investigated via the two transition states **$TS_{9\alpha}$** and **$TS_{9\beta}$**, in which one pyridine has dissociated from Cu_2 (Figures VI.23 and VI.24). The geometries of these transition states are not significantly reshaped as the most substantial change is the elongation of the distance between the coppers by 0.1 Å up to 2.77 Å in **$TS_{9\beta}$**. The dissociations increase the energy of **TS_9** to 35.1 and 35.8 kcal/mol for **$TS_{9\alpha}$** and **$TS_{9\beta}$**, respectively. It shows once more that the partial dissociation of DPEOPN is not able to lower the energy of the transition states on its own.

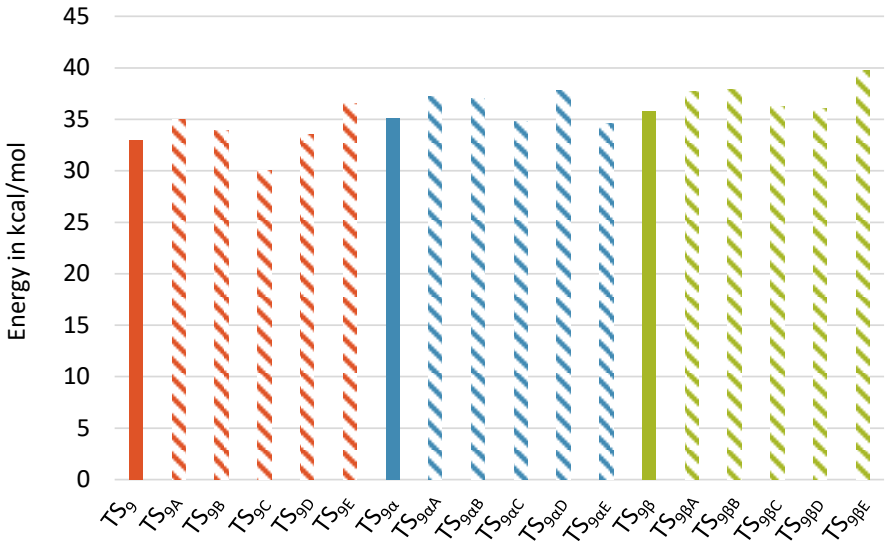

Figure VI.25. Free energy of all the transition states of the TS_9 series.

As **$TS_{9\alpha}$** and **$TS_{9\beta}$** are close in energy, they were both kept to examine the combined effects of the ion-pairing with NTf_2^- and the partial dissociation of DPEOPN on **TS_9**, leading to the series **$TS_{9\alpha X}$** and **$TS_{9\beta X}$** (Figures VI.23 and VI.24). The former series has an energy ranging from 34.6 to 37.8 kcal/mol (blue dashed in Figure VI.25). The most stable is **$TS_{9\alpha E}$** and it is the only case where the geometry of the transition state changes dramatically from **$TS_{9\alpha}$**: Cu_1 dissociates from the naphthyridine backbone (2.84 Å), increasing the distance between the coppers to 2.99 Å. As the complex is more open, the triazolyl is in a different position compared to the other transition states of the series. The $ArCF_3$ substituent is over the ^{t}Bu of the phosphine (3.50 Å on average) while the toluene substituent is almost parallel to the pyridine **β** (Figure VI.26d). The alkynyl also coordinates to the complex differently: it is bridging asymmetrically the coppers, with distances of 2.25 Å to Cu_1 and 2.02 Å to Cu_2, and its $ArCF_3$ substituent is in between the phosphine (around 2.50 Å) and the dissociated pyridine **α** (4.00 Å). In **$TS_{9\alpha E}$**, NTf_2^- is interacting only with the pyridine **β** and the toluene substituent of the triazolyl. The **$TS_{9\beta X}$** series is even higher in energy than **$TS_{9\alpha X}$,** ranging from 36.1 to 39.7 kcal/mol. The difference in energy inside this series comes from the different interactions with NTf_2^- as

they all have the same geometry as **$TS_{9\beta}$**. Overall, the **TS_9** series gives transition states with high energies and a low variety of geometrical characteristics. The lowest one is **TS_{9C}**, with 30.0 kcal/mol, which is 1.3 kcal/mol higher than **$TS_{8\beta C}$**.

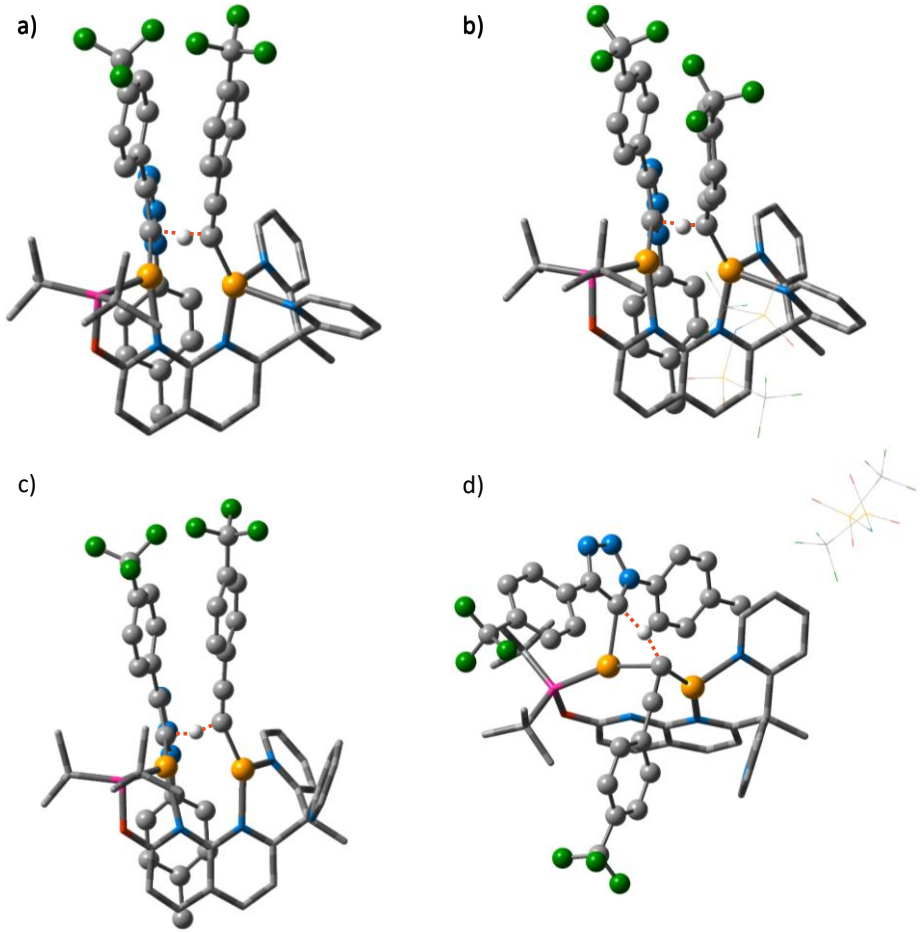

Figure VI.26. 3D representation of a) TS_9, b) TS_{9C}, c) $TS_{9\alpha}$ and d) $TS_{9\alpha E}$. The red dashed lines account for the cleavage and formation of C-H bonds between the triazolyl and alkynyl moieties.

The third isomer of the transition state for C-H activation step consists of the **TS_{10}** series and its 18 transition states (Figures VI.27 and VI.28). In this series, the alkynyl ligand is coordinated on Cu_1 while the triazolyl is on Cu_2. The latter is orientated so its toluene substituent is going upward near the substituent

of the alkynyl. The simplest transition state of this series is **TS_{10}** (Figure VI.30a), in which the effects of the partial dissociation of DPEOPN and of the ion-pairing with NTf_2^- are neglected. **TS_{10}** is distorted, with a distance between the coppers of 3.21 Å. This is caused by the coordination of the bulky triazolyl and the pyridines to Cu_2, forcing it to shift forward DPEOPN. It also leads to the elongation of the distance between Cu_2 and the naphthyridine backbone up to 2.44 Å. However, as there is less steric hindrance between the triazolyl and the naphthyridine backbone, it allows the triazolyl to closely coordinate to Cu_2 (2.00 Å), which is comparable to the distance in the intermediates **15^+**. The alkynyl is closely coordinated to Cu_1 as well, with a bond distances of 1.93 Å. The other ligands display normal bond distances with Cu_1: 2.28 Å for the phosphine and 2.07 Å with the naphthyridine backbone. The transferred proton is closer to the alkynyl than to the triazolyl, with distances of 1.35 versus 1.55 Å; *i.e.* the forming bond is longer than the breaking one. The tolyl substituent of the triazolyl is located between the two pyridines and is also close to the substituent of the alkynyl (around 3.40 Å) while the $ArCF_3$ substituent is positioned in the cavity formed by DPEOPN. The free energy barrier associated to **TS_{10}** is 33.6 kcal/mol (red in Figure VI.29), which is in the same energy range than **TS_8** and **TS_9**.

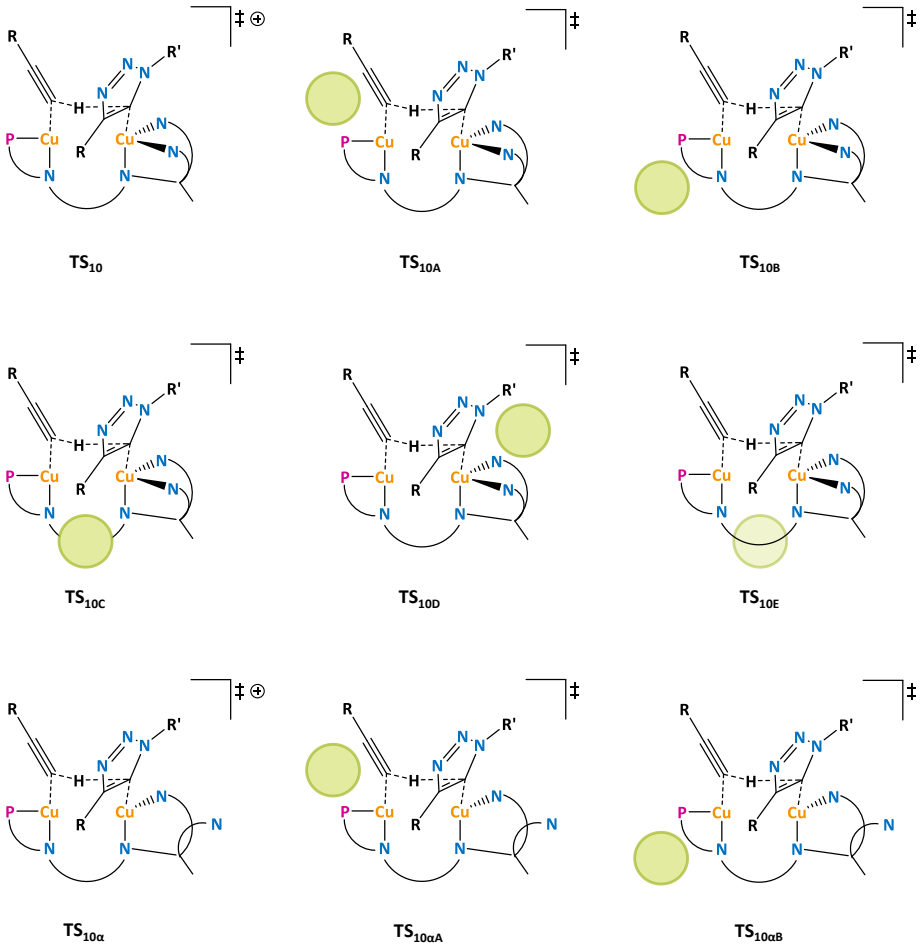

Figure VI.27. Schematic representations and labels of all the transition states computed for the TS_{10} series; the green circles represent the position of NTf_2^- (1/2).

The association of **TS_{10}** with NTf_2^- creates the **TS_{10X}** series, where X display the position of the counter-ion (Figure VI.27). These five transition states have an energy ranging from 33.1 to 37.7 kcal/mol (red dashed in Figure VI.29). The position **A** is the lowest and also is the one where the NTf_2^- coordinates to Cu_1 via one of its oxygens (2.18 Å). It causes a change in the way the naphthyridine coordinates to the coppers: it elongates by 0.1 Å with Cu_1 while it shortens to 2.20 Å with Cu_2. The last difference is the position of the proton which is now equidistant from the alkynyl and the triazolyl, with 1.42 and 1.45 Å,

respectively. In addition to be coordinated to Cu_1, NTf_2^- interacts with a ^tBu substituent of the phosphine, the alkynyl and the pyridine **β**. The **TS_{10B}**, **TS_{10C}**, **TS_{10D}** and **TS_{10E}** have geometries closer to **TS_{10}** with the only variation being the distance between Cu_2 and the naphthyridine ranging from 2.27 to 2.57 Å, causing the distance between the coppers to vary slightly. In these four transition states, NTf_2^- interacts only with the ligands. The association of **TS_{10}** with NTf_2^- do not stabilize the transition states and thus, their energy remains too high to be considered as a plausible pathway.

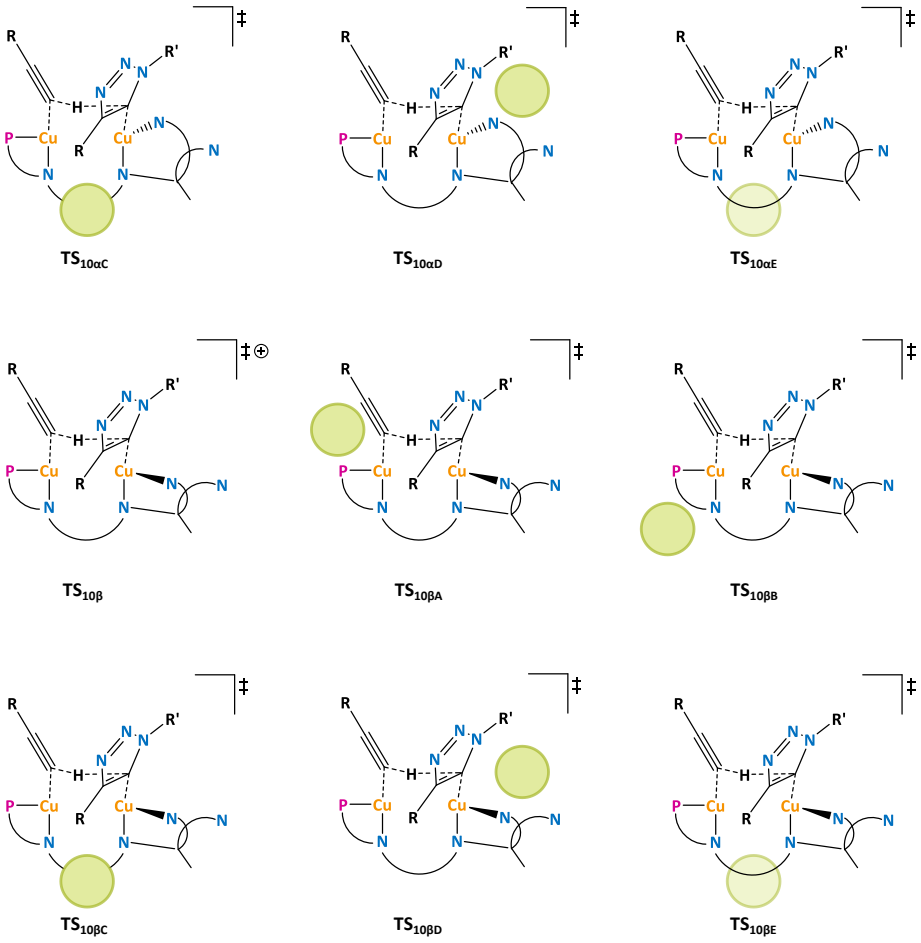

Figure VI.28. Schematic representations and labels of all the transition states computed for the TS_{10} series; the green circles represent the position of NTf_2^- (2/2).

The effect of the partial dissociation of DPEOPN was investigated, and as for **TS_8** and **TS_9**, only the dissociation of the pyridines were considered, leading to **$TS_{10\alpha}$** and **$TS_{10\beta}$** (Figures VI.27 and VI.28). The former is heavily influenced by the dissociation: the complex becomes more compact as the distance between the coppers shorten to 2.74 Å and the bond between Cu_2 and the naphthyridine backbone decreases by 0.3 Å to 2.15 Å. The dissociation of the pyridine **α** allows the complex to have more flexibility as the toluene substituent can take the space where the pyridine previously was (Figure VI.30c). A new interaction arises as the triazole cycle and the pyridine **α** are parallel and only 3.70 Å apart. These modifications do not stabilize **$TS_{10\alpha}$** as its energy is 35.0 kcal/mol. The second dissociation has fewer impact on the geometry of **TS_{10}**, even if it also gives the complex more flexibility. The distance between the coppers shortens to 3.09 Å and the distance between Cu_2 and the naphthyridine is shortened by 0.33 Å, meaning that this ligand is coordinated symmetrically to the coppers (2.11 Å). The rest of the bonds are not affected by the dissociation. The dissociation of the pyridine **β** is also unfavourable, with an energy of 37.7 kcal/mol for **$TS_{10\beta}$**.

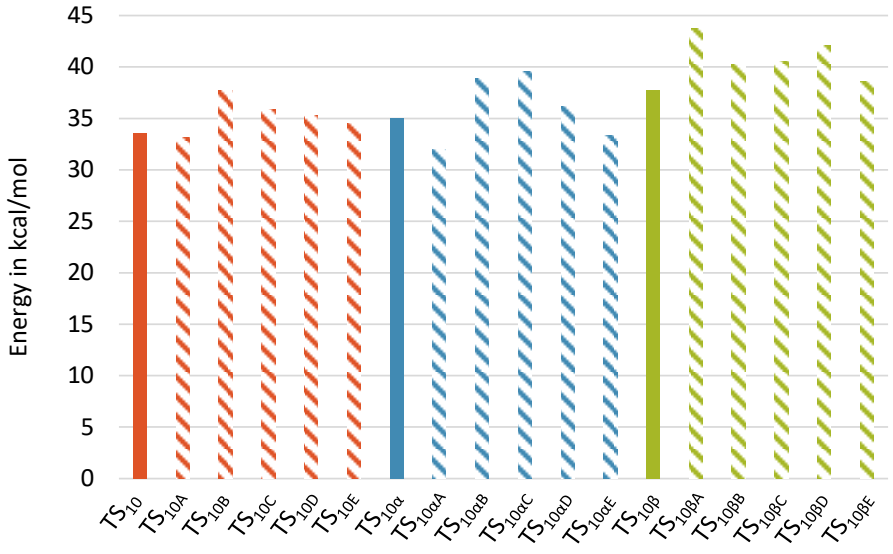

Figure VI.29. Free energy of all the transition states of the TS_{10} series.

The final series for **TS_{10}** consist of combining the effects of the ion-pairing with NTf_2^- and of the partial dissociation of DPEOPN, leading to the **$TS_{10\alpha X}$** and **$TS_{10\beta X}$** (Figures VI.27 and VI.28). The **$TS_{10\alpha X}$** transition states have energies ranging from 32.0 to 39.6 kcal/mol (blue dashed in Figure VI.29). The lowest one correspond to the position **A** and has similarities with **TS_{10A}**: NTf_2^- coordinates to Cu_1 at 2.19 Å which (Figure VI.30d) increases the distance between the metal and the naphthyridine to 2.17 Å. It also increases slightly the distance between the coppers by 0.07 Å. The rest of the complex is not impacted by the coordination of the counter-ion. The other **$TS_{10\alpha X}$** transition states have similar geometry to **$TS_{10\alpha}$** and NTf_2^- interacts only with the ligands. The association of **$TS_{10\beta}$** with NTf_2^- leads to five transition states with energies ranging from 36.6 kcal/mol for **$TS_{10\beta E}$** and 43.7 kcal/mol for **$TS_{10\beta C}$** (green dashed in Figure VI.29). The counter-ion does not interact directly with the metal centres and the differences in energy are mainly due to the different interactions between NTf_2^- and the ligands. Overall, the **TS_{10}** series produces 18 transition states that are high in energy, the lowest being **$TS_{10\alpha A}$** with 32.0 kcal/mol. Hence, the effects of the association with NTf_2^- and the partial dissociation of DPEOPN, either combined or separately, do not lead to any significant stabilisation.

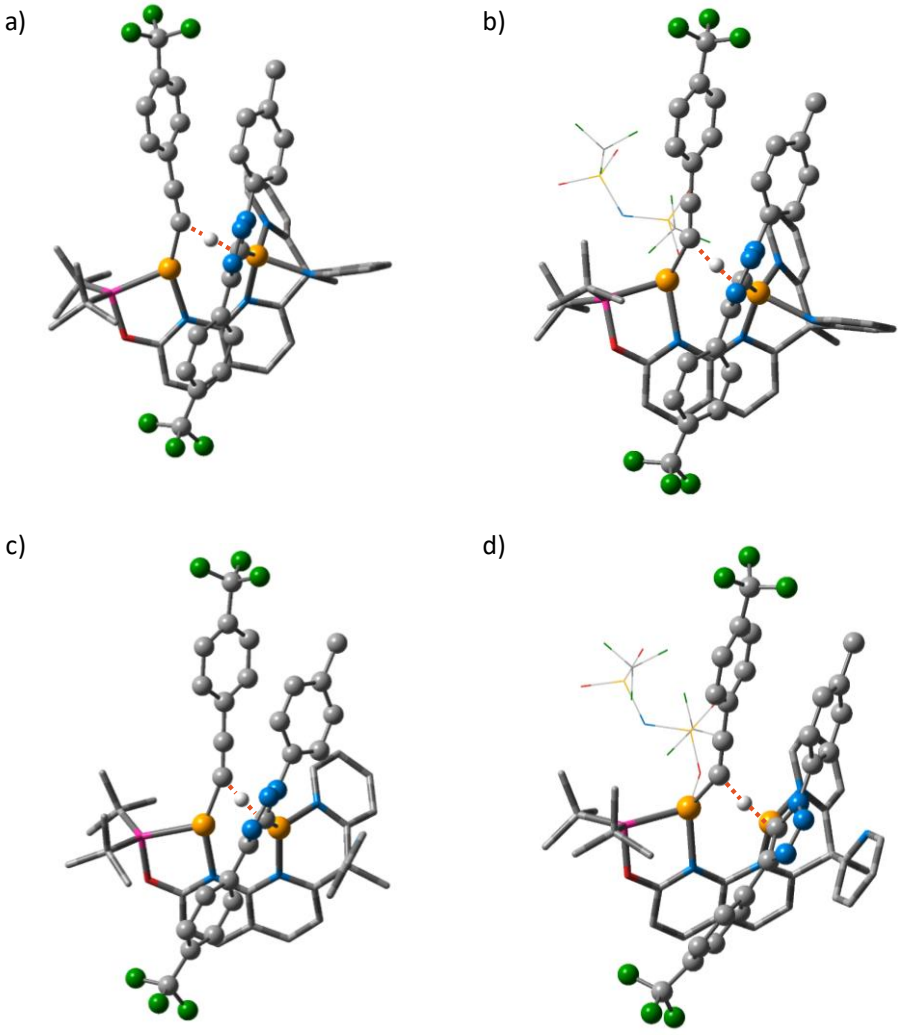

Figure VI.30. 3D representation of a) TS_{10}, b) TS_{10A}, c) $TS_{10\alpha}$ and d) $TS_{10\alpha A}$. The red dashed lines account for the cleavage and formation of C-H bonds between the triazolyl and alkynyl moieties.

The last series considered for the regeneration of $\mathbf{2}^{+}$ from $\mathbf{15}^{+}$ is $\mathbf{TS_{11}}$, which contains 18 transition states (Figure VI.31 and VI.32). In $\mathbf{TS_{11}}$, the alkynyl is coordinated to Cu_1 while the triazolyl is carried by Cu_2 and is orientated so its tolyl substituent faces the naphthyridine backbone. This transition state is distorted as the distance between the coppers is 3.13 Å. However, both

coppers are still coordinated to the naphthyridine backbone, with bond distance of 2.07 and 2.24 Å for Cu_1 and Cu_2, respectively. The elongation of the distance between the metal centres comes from Cu_2 shifting off the naphthyridine plane due to the presence of the very bulky triazolyl. The triazolyl and the alkynyl have bond distances similar those in the corresponding bridging intermediates $\mathbf{2}^+$ and $\mathbf{15}^+$: 1.99 and 1.92 Å, respectively. As in $\mathbf{TS_{10}}$, the transferred proton is closer to the alkynyl (1.37 Å) than the triazolyl (1.55 Å). The $ArCF_3$ substituent is 3.50 Å away from the substituent of the alkynyl (Figure VI.34a) while the tolyl substituent is parallel to the naphthyridine backbone (around 3.50 Å). The energy associated to $\mathbf{TS_{11}}$ is 34.7 kcal/mol (red in Figure VI.33), the highest of the four isomers considered for this C-H activation step.

The association of the counter-ion with $\mathbf{TS_{11}}$ creates the $\mathbf{TS_{11X}}$ series where X stands for the position of NTf_2^- around the complex (Figure VI.31). For four of these transition states ($\mathbf{TS_{11A}}$, $\mathbf{TS_{11B}}$, $\mathbf{TS_{11C}}$ and $\mathbf{TS_{11D}}$) the association is isoenergetic or unfavourable since their energies range from 34.9 to 37.6 kcal/mol (dashed red in Figure VI.33). Their geometries are not impacted by the presence of NTf_2^-, which interacts only with the ligands. However, $\mathbf{TS_{11E}}$ does a favourable association with NTf_2^-, with a $\Delta G^{\ddagger}$ of 33.6 kcal/mol. The counter-ion coordinates to Cu_1 via one of its oxygen (2.19 Å). It causes a change in the way the coppers coordinate to the naphthyridine backbone: the distance with Cu_1 elongates to 2.15 Å while the distance with Cu_2 decreases to 2.16 Å, leading to symmetrical coordination (Figure VI.34b). The distance between the coppers elongates slightly to 3.19 Å. These changes affect the position of the proton relatively to the alkynyl and the triazolyl as it becomes equidistant, with 1.44 and 1.48 Å, respectively. The associations of the counter-ion with $\mathbf{TS_{11}}$ do not lead to any significant stabilization and the energies are still much higher than $\mathbf{TS_{8\beta C}}$, the most stable transition state so far with 28.7 kcal/mol.

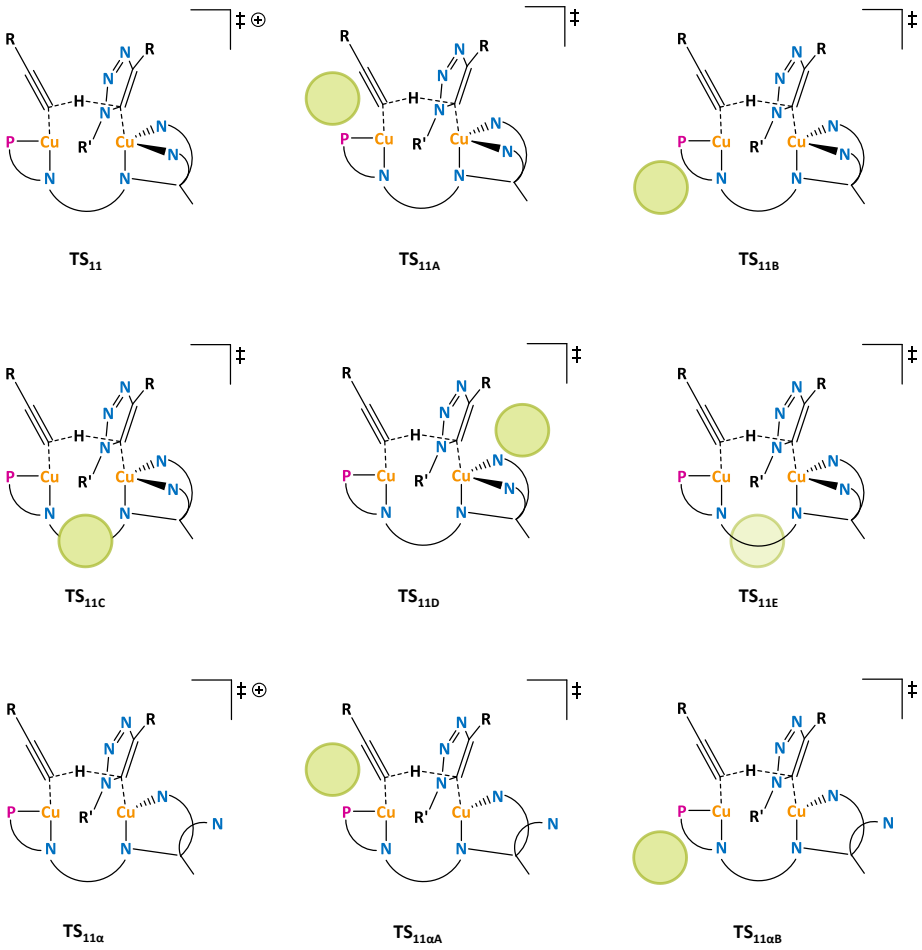

Figure VI.31. Schematic representations and labels of all the transition states computed for the TS_{11} series; the green circles represent the position of NTf_2^- (1/2).

The next effect to be considered on **TS_{11}** is the partial dissociation of DPEOPN and as for previous isomers, only the dissociation of one pyridine at a time was computed, leading to **$TS_{11\alpha}$** and **$TS_{11\beta}$**. The former is hugely affected by the dissociation as the $ArCF_3$ substituent of the triazolyl fills the pocket open by dissociated the pyridine **α** (Figure VI.34c), like for **$TS_{10\alpha}$**. This new flexibility allows the two coppers to be much closer, as shown by the inter-atomic distance of 2.72 Å. It also reduces the distance between Cu_2 and the naphthyridine to 2.14 Å, due to reduced steric hindrance between the

triazolyl and DPEOPN. The dissociation of the pyridine **α** is unfavourable as the energy of $\mathbf{TS_{11\alpha}}$ is 35.4 kcal/mol. The dissociation of the pyridine **β** has a softer impact on the geometry as the biggest change is the shortening of the bond between Cu_2 and the naphthyridine backbone by 0.15 Å. All the other bonds undergo modifications smaller than 0.05 Å. The energy of $\mathbf{TS_{11\beta}}$ is even higher, with 37.9 kcal/mol. Thus, the partial dissociation do not appears to lower the energy barrier associated to $\mathbf{TS_{11}}$.

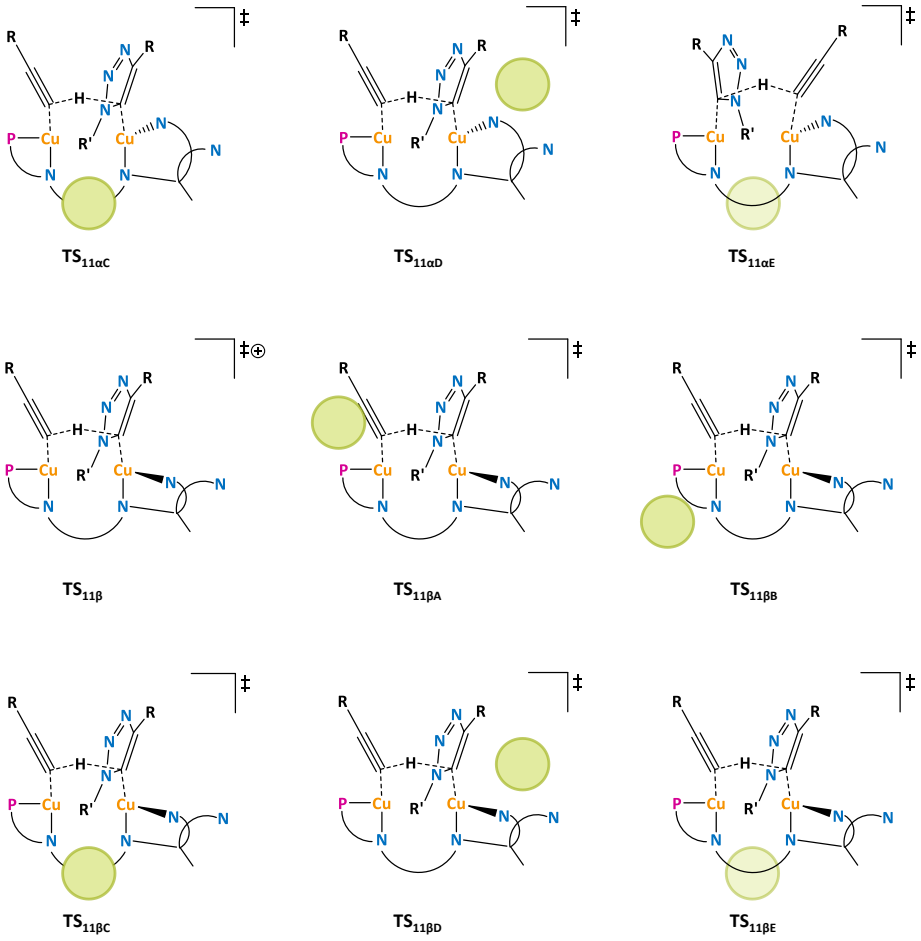

Figure VI.32. Schematic representations and labels of all the transition states computed for the TS_{11} series; the green circles represent the position of NTf_2^- (2/2).

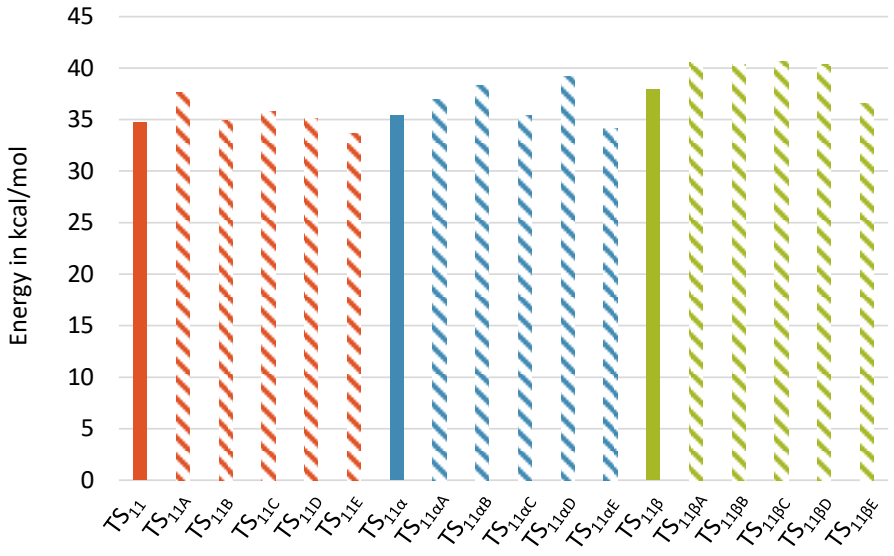

Figure VI.33. Free energy of all the transition states of the TS_{11} series.

Finally, the effects of the association with NTf_2^- and the partial dissociation of DPEOPN on **TS_{11}** were combined, creating the **$TS_{11\alpha X}$** and **$TS_{11\beta X}$** series. The former series comprise five transitions states with geometries similar to the one of **$TS_{11\alpha}$**. NTf_2^- interacts with the ligands; DPEOPN, the alkynyl and/or the triazolyl depending of its position and it coordinates to Cu_1 only in **$TS_{11\alpha E}$** (2.21 Å) without changing its geometry (Figure VI.34d). The energy of these transition states range from 34.1 kcal/mol for **$TS_{11\alpha E}$** to 39.2 kcal/mol for **$TS_{11\alpha D}$** (blue dashed in VI.33). In the **$TS_{11\beta X}$** series, three transition states (**$TS_{11\beta B}$**, **$TS_{11\beta C}$** and **$TS_{11\beta D}$**) have very similar geometries and energies to **$TS_{11\beta}$**, as they are ranging from 40.3 to 40.6 kcal/mol (green dashed in VI.33). In these transition states, NTf_2^- interacts only with the ligands and not directly with the metal centres. However, in **$TS_{11\beta A}$** and **$TS_{11\beta E}$**, the counter-ion coordinates to Cu_1 (2.21 and 2.25 Å, respectively). In both cases, the coordination leads to an increased distance between the coppers to 3.27 Å, affecting the coordination sphere of Cu_1. In **$TS_{11\beta A}$**, the bond with the naphthyridine backbone elongates by 0.1 Å while the coordination of the alkynyl changes from σ to π in **$TS_{11\beta E}$**. The energy of these transition states are 40.5 and 36.6 kcal/mol, respectively. Overall, the transition states that compose the **TS_{11}** series are high in energy

and the effects of the ion-pairing with NTf_2^- and/or the partial dissociation of DPEOPN do not lower the energy of **TS_{11}** significantly.

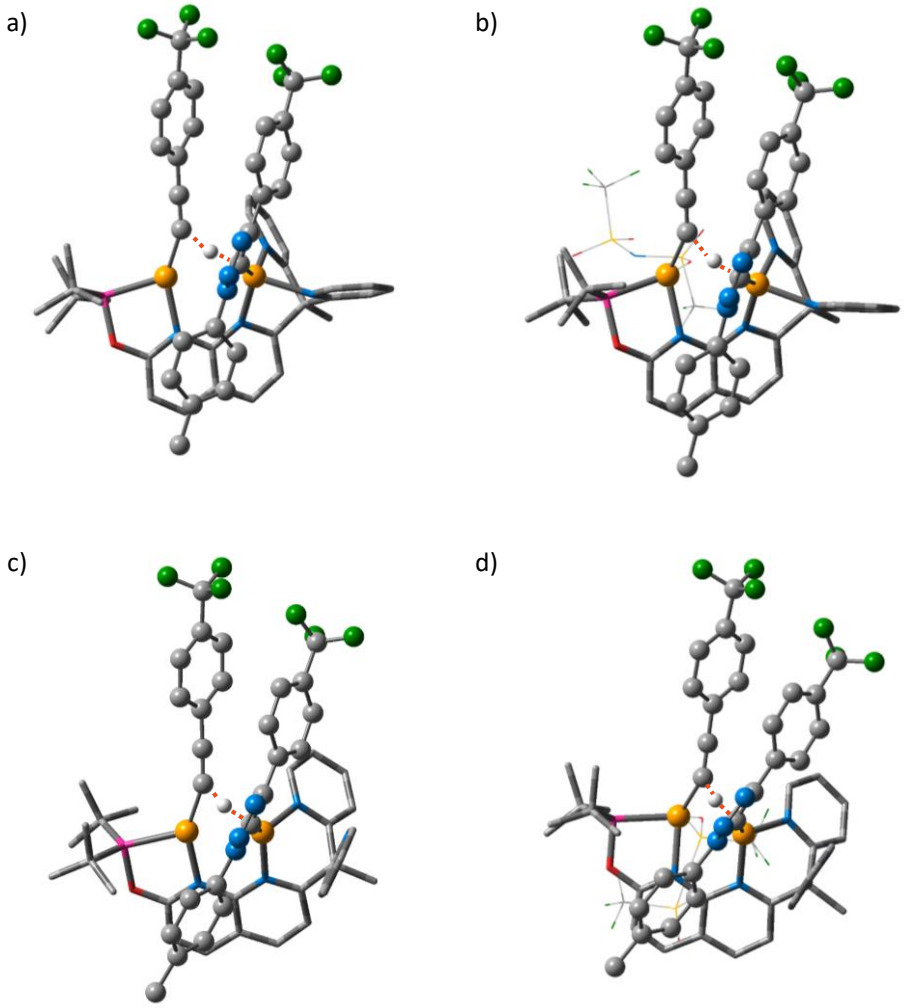

Figure VI.34. 3D representation of a) TS_{11}, b) TS_{11E}, c) $TS_{11\alpha}$ and d) $TS_{11\alpha E}$. The red dashed lines account for the cleavage and formation of C-H bonds between the triazolyl and alkynyl moieties.

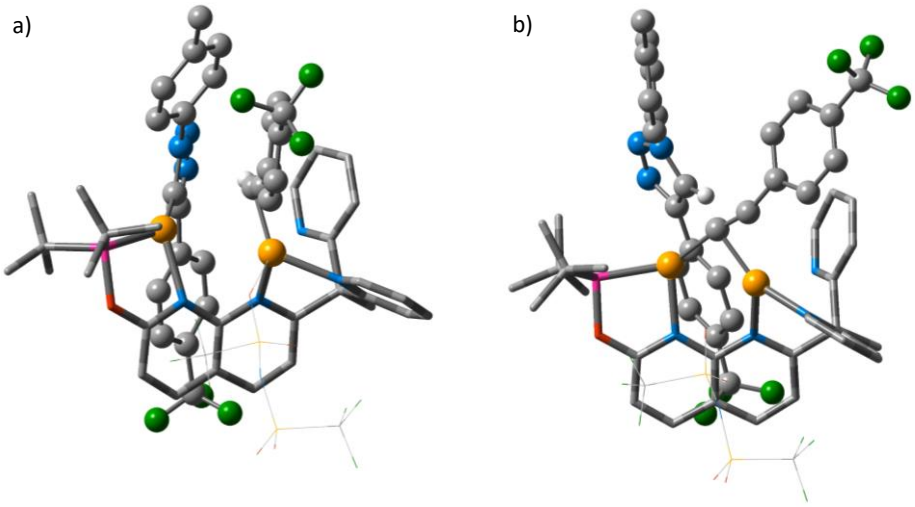

Figure VI.35. 3D representation of the intermediates on reactant (a) and product (b) sides.

Overall, the transition states for the regeneration of $\mathbf{2}^{+}$ have high energies, from 28.7 to 42.1 kcal/mol. The lowest one is $\mathbf{TS_{8\beta c}}$, in which the alkynyl is coordinated to Cu_2 while the triazolyl is on Cu_1 with its tolyl substituent oriented towards the $ArCF_3$ group of the alkynyl. The importance of the ion-pairing and of the partial dissociation of DPEOPN are once more highlighted as the pyridine **β** is not bound to Cu_2 while NTf_2^- is. To be certain of the nature of these transition states, an IRC-driven relaxation was done on a selection of them. Two additional intermediates were found for $\mathbf{TS_{8\beta c}}$ (Figure VI.35). From $\mathbf{15}^{+}$, there is an intermediate at 9.7 kcal/mol in which the alkyne is coordinated to Cu_2 via its π-system (2.00 Å to C_2' and 2.07 Å to C_3'). To allow the alkyne to coordinate, the triazolyl dissociates from Cu_2 and thus is only bound to Cu_1 (1.96 Å). The second intermediate is after $\mathbf{TS_{8\beta c}}$, at -10.0 kcal/mol. In this one, the 1,4 triazole is formed and dissociated from the complex. The alkynyl is bridging the coppers asymmetrically: in σ mode to Cu_1 (1.89 Å) and in a π mode to Cu_2 (2.06 Å on average). The other important feature of these intermediates is that the counter-ion remains close to Cu_2 (2.22 and 2.51 Å for the pre-reactant and pre-product). The figure VI.36 summarizes the mechanism of the regeneration of $\mathbf{2}^{+}$ starting from $\mathbf{15}^{+}$.

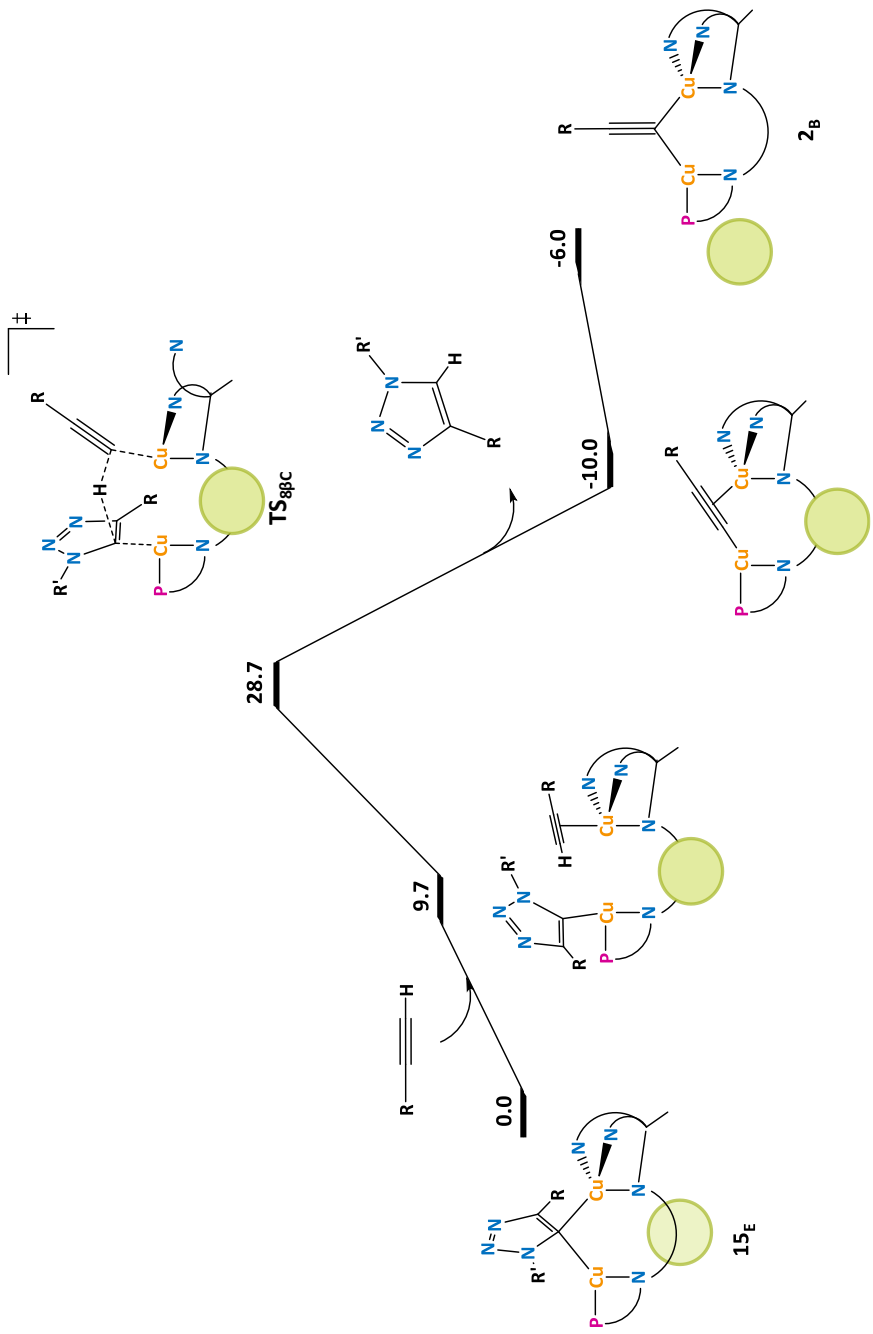

Figure VI.36. Schematic representation of the mechanism of the C-H activation of the CuAAC reaction; the green circles represent the position of NTf_2^-.

b) Descriptors analysis of the transition states

For this C-H activation step, 72 transition states were computed and analysed using 15 descriptors, both geometrical and electronical. These descriptors include:

- Position of NTf_2^-
- Distance between Cu_1 and Cu_2
- Distance between the C_2 and C_2'
- Distance between H and C_2
- Distance between H and C_2'
- Dihedral angle Cu_1-N_1-N_2-Cu_2
- Natural charge of Cu_1
- Natural charge of Cu_2
- Difference of natural charge between Cu_1 and Cu_2
- Natural charge of the C_2
- Natural charge of the C_2'
- Difference of natural charge between C_2 and C_2'
- Natural charge of H
- Difference of natural charge between H and C_2
- Difference of natural charge between H and C_2'

In the additional *Descriptors file* (see annexes) are scatter plots showing the potential correlations between these descriptors and the energy barriers of the transition states series **TS_8**, **TS_9**, **TS_{10}** and **TS_{11}**. All the lowest-energy transition states include the effect of the ion-paring, often combined with the partial dissociation of DPEOPN. The descriptor analysis did not reveal any specific trends as the highest R^2 value is 0.3232 for the natural charge of C_2. However it is worth noticing that the transition states for this step have very varied geometries, as shown by the distance between the coppers changing

within a wide range of 2.60-3.90 Å. No clustering was observed in the scatter plots either.

5 - The poisoning of 2^+

The last topic investigated for the CuAAC reaction is the poisoning of the catalytic system. The major source of potential poisoning is the coordination of the azide to **2^+**, which can occur in ways hampering the cycloaddition to the alkynyl. Thus, the ten off-cycle adducts shown on Figure VI.37 were computed. The energy reference for this section is **5^+** and the energies of the adducts are gathered in Table VI.4. Three of them did not converged into intermediates where the azide is coordinated to **2^+** and thus, **16_α^+**, **17_α^+** and **19^+** were discarded. The remaining adducts converged in four different intermediates.

The first one arise from the calculation of **16^+**, **17^+** and **18^+**. In this intermediate, the azide is loosely coordinated to Cu_1 by N_5 (2.35 Å) and its tolyl substituent is orientated toward the pyridines arm (Figure VI.38b). The coordination of the azide induces an asymmetry in the coordination of the alkynyl to the coppers, with a longer distance to Cu_1 than Cu_2 (2.01 and 1.94 Å). The only difference between this three adducts is the orientation of the alkynyl: it bend over the phosphine in **16^+** while it is straight in **17^+** and **18^+**. Their respective energies are 4.1, 3.6 and 3.8 kcal/mol. As **17^+** is the most stable one, it was the only one kept to investigate the effect on the ion-pairing with NTf_2^-, leading to the **17_X** series (X = A to E, see Figure III.8). The overall geometries of the transition states of this series are similar to the one of **17^+** with the exception of the bond between Cu_1 and the azide, which varies from 2.28 Å for the position **E** to 2.47 Å for **C**. The energy is ranging from -1.0 to 5.6 kcal/mol (Table VI.4), the lowest one being **17_C**. The position **A** did not converge.

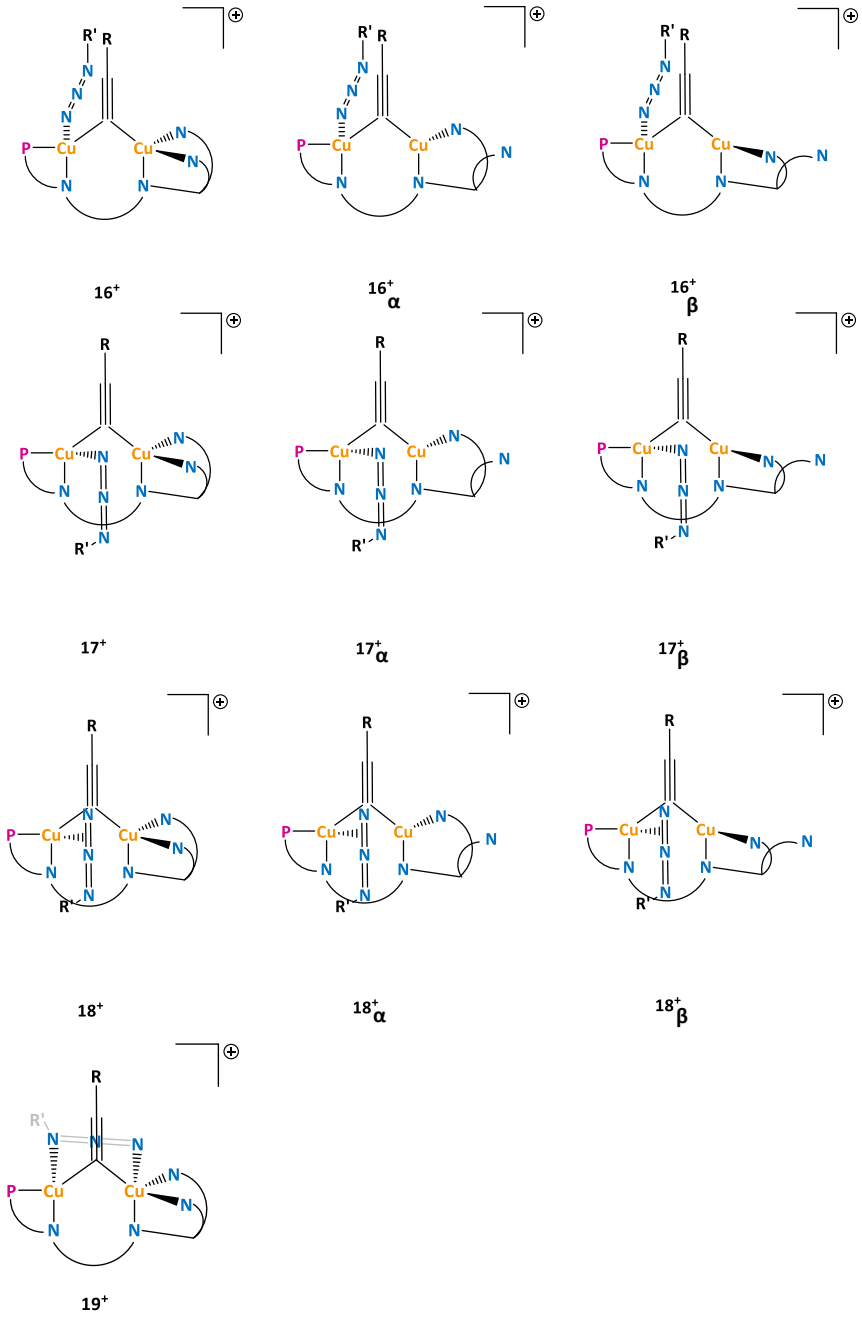

Figure VI.37. Schematic representations and labels of the off-cycle adducts of the CuAAC reaction.

The second intermediate comes from the converged geometry of $\mathbf{18}_{\alpha}^{+}$. It has a geometry similar to $\mathbf{17}^{+}$ but with the pyridine **α** dissociated (Figure VI.38d). The rest of the geometrical characteristics vary within a range of only 0.1 Å relative to $\mathbf{17}^{+}$. The dissociation of the pyridine **α** is endoergic as the energy of $\mathbf{18}_{\alpha}^{+}$ is 5.3 kcal/mol, which is 1.7 kcal/mol higher than $\mathbf{17}^{+}$. When $\mathbf{18}_{\alpha}^{+}$ is paired with NTf_2^-, only the position **E** leads to an intermediate in which the azide is coordinated to $\mathbf{2}^{+}$. The ion-pairing has a minimal effect on the geometry as the only relevant change in $\mathbf{18}_{\alpha E}$ is the slight shortening of the bond between the azide and Cu_1 to 2.35 Å. The energy of $\mathbf{18}_{\alpha E}$ (5.0 kcal/mol) is similar to the one of $\mathbf{18}_{\alpha}^{+}$.

Complex	ΔG (kcal/mol)	Complex	ΔG (kcal/mol)
$\mathbf{16}_{\beta}^{+}$	3.1	$\mathbf{17}^{+}$	3.6
$\mathbf{16}_{\beta A}$	6.2	$\mathbf{17}_{A}$	-
$\mathbf{16}_{\beta B}$	3.1	$\mathbf{17}_{B}$	1.2
$\mathbf{16}_{\beta C}$	-	$\mathbf{17}_{C}$	-1.4
$\mathbf{16}_{\beta D}$	2.7	$\mathbf{17}_{D}$	2.3
$\mathbf{16}_{\beta E}$	1.1	$\mathbf{17}_{E}$	5.2

Complex	ΔG (kcal/mol)	Complex	ΔG (kcal/mol)
$\mathbf{17}_{\beta}^{+}$	4.2	$\mathbf{18}_{\alpha}^{+}$	5.3
$\mathbf{17}_{\beta A}$	4.1	$\mathbf{18}_{\alpha A}$	-
$\mathbf{17}_{\beta B}$	-	$\mathbf{18}_{\alpha B}$	-
$\mathbf{17}_{\beta C}$	1.5	$\mathbf{18}_{\alpha C}$	-
$\mathbf{17}_{\beta D}$	5.8	$\mathbf{18}_{\alpha D}$	-
$\mathbf{17}_{\beta E}$	-0.4	$\mathbf{18}_{\alpha E}$	5.0

Table VI.4. Free energy of ion-paring for $\mathbf{16}_{\beta}^{+}$, $\mathbf{17}^{+}$, $\mathbf{17}_{\beta}^{+}$ and $\mathbf{18}_{\alpha}^{+}$.

The third intermediate is $\mathbf{16}_{\beta}^{+}$, in which the azide is strongly coordinated to Cu_1 (2.12 Å) and orientated such as the nitrogens are perpendicular to the naphthyridine backbone (Figure VI.38a). The other features of this adduct are the same as these of $\mathbf{17}^{+}$ but with the pyridine **β** dissociated. The energy of $\mathbf{16}_{\beta}^{+}$ is 3.1 kcal/mol. The association of $\mathbf{16}_{\beta}^{+}$ with NTf_2^- lead to the $\mathbf{16}_{\beta X}$ series. The position **C** optimized in a complex in which the azide is not coordinated to the coppers but the counter-ion is. Thus, this position was discarded. Of the four remaining associations, three have the same geometry as $\mathbf{16}_{\beta}^{+}$: $\mathbf{16}_{\beta B}$,

$16_{\beta D}$ and **$16_{\beta E}$**. For **$16_{\beta A}$**, the presence of NTf_2^- induce the elongation of the distances of Cu_1 with the azide and with Cu_2, by 0.15 and 0.22 Å, respectively. The alkynyl bends over the phosphine and NTf_2^-, changing its coordination mode from a σ,σ to a σ,π. The energies of the **$16_{\beta X}$** series are ranging from 1.5 to 6.5 kcal/mol, with **E** being the most stable position for the counter-ion.

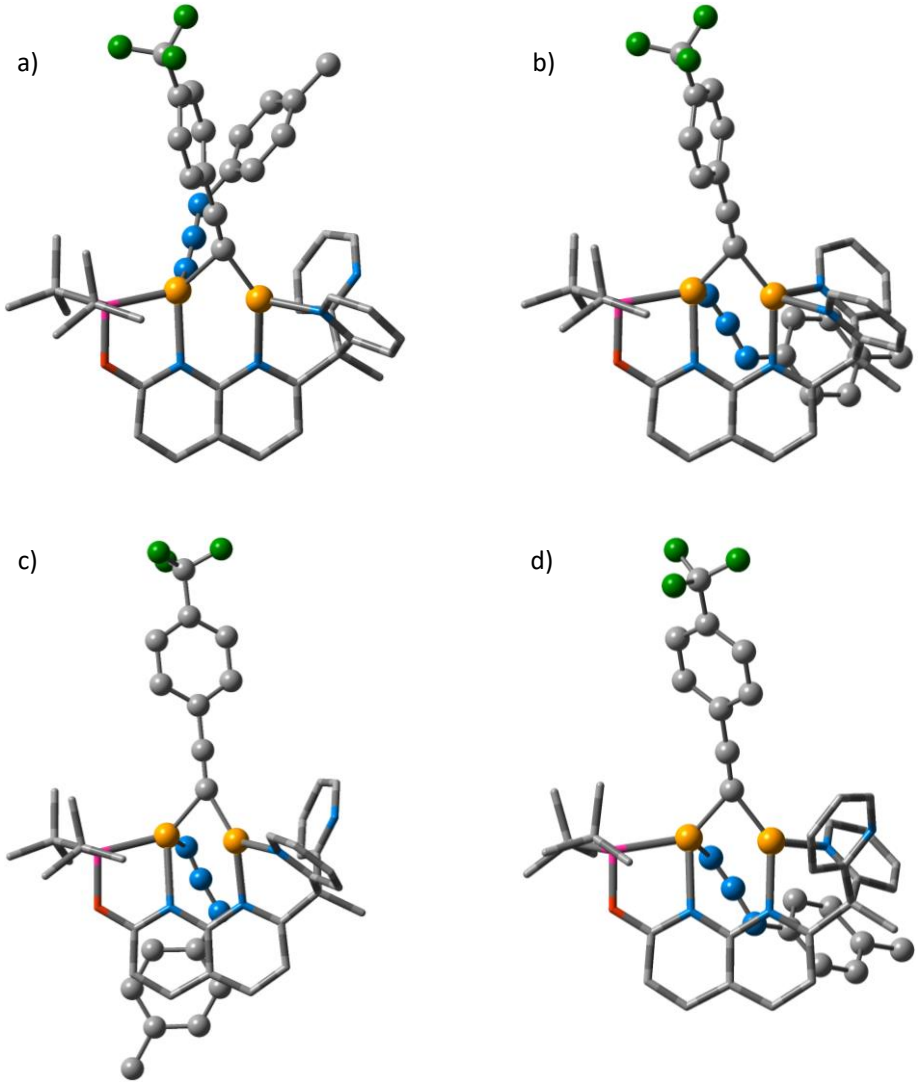

Figure VI.38. 3D representations of the off-cycle adducts a) 16_{β}^+, b) 17^+, c) 17_{β}^+ and d) 18_{α}^+.

The last intermediate was obtained from the two adducts, $\mathbf{17_{\beta}^{+}}$ and $\mathbf{18_{\beta}^{+}}$, in which the azide is coordinated to Cu_1 (2.22 Å) and the tolyl substituent is orientated toward the phosphine (Figure VI.38c). The relatively close coordination of the azide causes the elongation of the bonds of Cu_1 with the naphthyridine backbone and the alkynyl, with 2.28 and 2.02 Å. The energy of $\mathbf{17_{\beta}^{+}}$ and $\mathbf{18_{\beta}^{+}}$ are 4.1 and 4.3 kcal/mol, respectively. Thus, $\mathbf{17_{\beta}^{+}}$ was kept to investigate the effect of the association with NTf_2^- on this intermediate, leading to the series $\mathbf{17_{\beta X}}$. The position **B** could not be converged. For $\mathbf{17_{\beta C}}$, $\mathbf{17_{\beta D}}$ and $\mathbf{17_{\beta E}}$, the ion-pairing do not impact the geometry that remains similar to $\mathbf{17_{\beta}^{+}}$. However the presence of NTf_2^- introduces several changes in $\mathbf{17_{\beta A}}$: the alkynyl bends over it and the phosphine, inducing an asymmetric coordination to the coppers (2.03 and 1.89 Å for Cu_1 and Cu_2) and increase the distance between the coppers to 2.62 Å. To accommodate the new position of the alkynyl, Cu_1 nearly dissociates from the naphthyridine backbone (2.43 Å). The energy range for this series is -0.4 to 5.8 kcal/mol(Table VI.4), $\mathbf{17_{\beta E}}$ being the lowest one.

Overall, four adducts ($\mathbf{16_{\beta}^{+}}$, $\mathbf{17^{+}}$, $\mathbf{17_{\beta}^{+}}$ and $\mathbf{18_{\alpha}^{+}}$) were obtained for the CuAAC reaction and their energies are higher than that of $\mathbf{5^{+}}$. The association with the counter-ion leads to a couple of intermediates with lower energy: $\mathbf{17_C}$ and $\mathbf{17_{\beta E}}$, with -1.4 and -0.4 kcal/mol, respectively. However, none of the off-cycle adducts are more stable than $\mathbf{5_E}$. Therefore, there is no poisoning found for the CuAAC reaction and the rate determining step remains the C-H activation of the alkyne.

6 - Summary of the mechanism of the CuAAC reaction

The CuAAC reaction starts with the coordination of the azide on Cu_1 in $\mathbf{2_B}$, forming $\mathbf{5_E}$. This first step is thermoneutral (-0.8 kcal/mol) and there is no barrier other than the energy cost originating from the entropy penalty. Then, the alkynyl and azide ligands undergo a cycloaddition to create two C-N bonds in $\mathbf{TS_{7E}}$. This first transition step is low in energy, with a barrier of 20.0 kcal/mol, and leads to the formation of the intermediate $\mathbf{15_E}$, which is very exergonic (-53.9 kcal/mol). The third and last step of the CuAAC reaction consists of a proton transfer from the alkyne to the triazolyl in $\mathbf{15_E}$,

regenerating $\mathbf{2_B}$ and producing the 1,4 triazole product. This step involves the highest energy barrier (28.7 kcal/mol), which is associated to the transition state $\mathbf{TS_{8\beta C}}$. In this mechanism, the counter-ion plays a key role since it is bound to the coppers core in the lowest-energy transition state and the two intermediates directly connected to it. There is also a clear preference for the position of NTf_2^- around the complexes: the cavity formed by the arms of DPEOPN (positions **C** and **E**) with the exception of $\mathbf{2_B}$. The partial dissociation of DPEOPN is also an important effect as it allow to lower the energy of $\mathbf{TS_{8\beta C}}$ by 6.0 kcal/mol compared to $\mathbf{TS_{8C}}$, its fully coordinated equivalent. The full mechanism of the CuAAC reaction is summarized in the Figure VI.39.

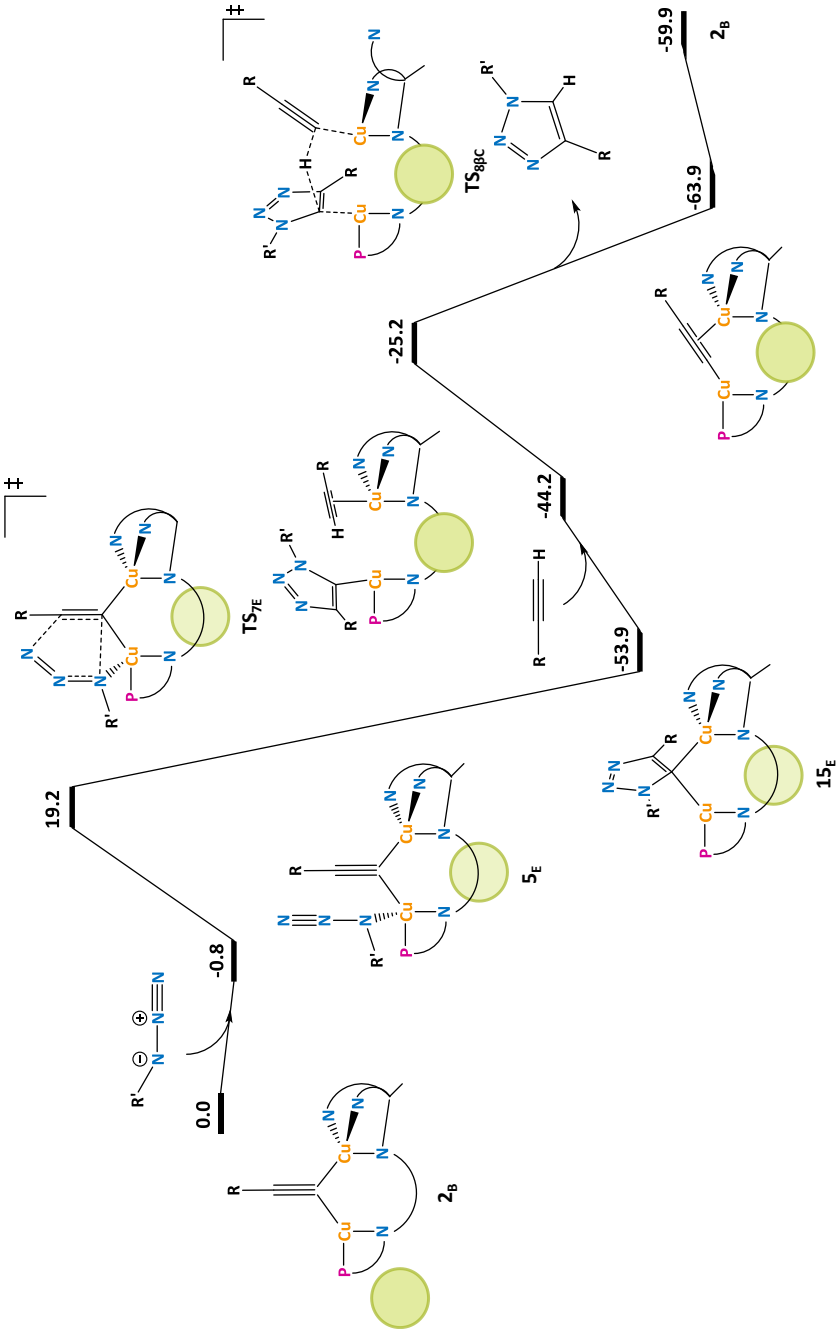

Figure VI.39. Schematic representation of the mechanism of the CuAAC reaction; the green circles represent the position of NTf_2^{-}

VII - Ligand design: modifications on DPEOPN

In this chapter, the chelating ligand DPEOPN was modified to assess its influence on the reactivity of this type of complexes. Each part of the ligand (phosphine, naphthyridine, pyridines arm) was modified one by one, to know the origin of the differences observed. For the sake of simplicity, the effects of the ion-pairing between the complex and the counter-ion and of the partial dissociation of the chelating ligand are neglected as they would create an extremely large number of combinations.

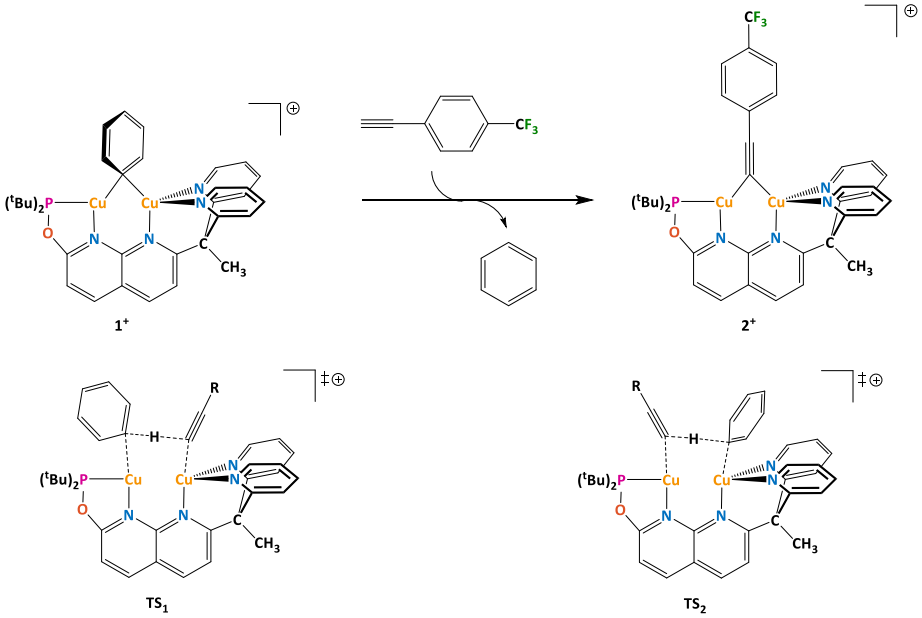

Figure VII.1. The C-H activation of alkynes reaction used for ligand design.

To investigate the effects of the chelating, the C-H activation of alkyne by **1**$^{+}$ is used as a model reaction (see chapter IV and Figure VII.1). This choice was motivated by three reasons. First, this reaction is the most studied one, by both experiments and computations, and thus is the one that our model represents most accurately. Second, the CuAAC reaction includes a C-H activation step that is also the rate determining step and thus, it is reasonable to assume that the best ligand for the activation of alkynes would also be

efficient for the CuAAC reaction. Third, the mechanism of this reaction is a concerted proton transfer, removing potential complexities such as a change of the most stable species in a catalytic process or a multistep reaction. For each new ligand, two intermediates will be computed (with a phenyl or an alkynyl bridging the coppers), as well as two transition states (with the phenyl and alkynyl substituents on different coppers), as shown in Figure VII.1. To ease the description of the complexes and transition states in this chapter, the key atoms are labelled as shown in Figure VII.2. All the energy of the transition states reported in this thesis are listed in tables in the annex A.

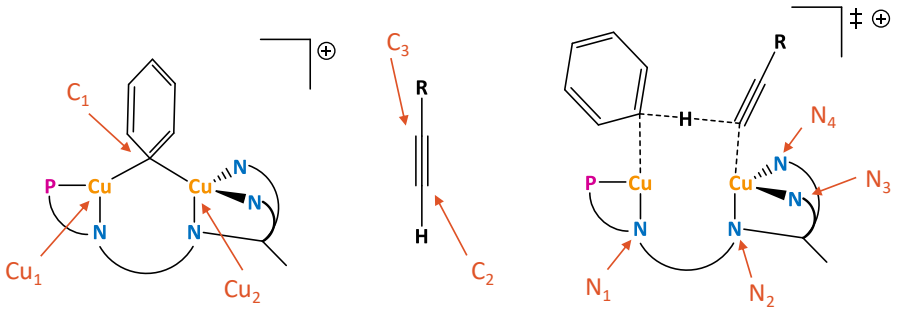

Figure VII.2. Labels of the key atoms in this chapter.

1 - Symmetrical ligands based on DPEOPN

The DPEOPN ligand has two different arms on its naphthyridine backbone: a phosphine and a pyridines one. The easiest modification to implement is to make ligands with either two phosphines or two pyridines arms[148] (Figure VII.3). The complexes emerging from these ligands are labelled **AX$_Y$**, where **X** equal to **1**$^+$ or **2**$^+$ depending if a phenyl or an alkynyl is bridging the coppers and **Y** is either **PR3** or **pyr** depending of the arms of the ligand.

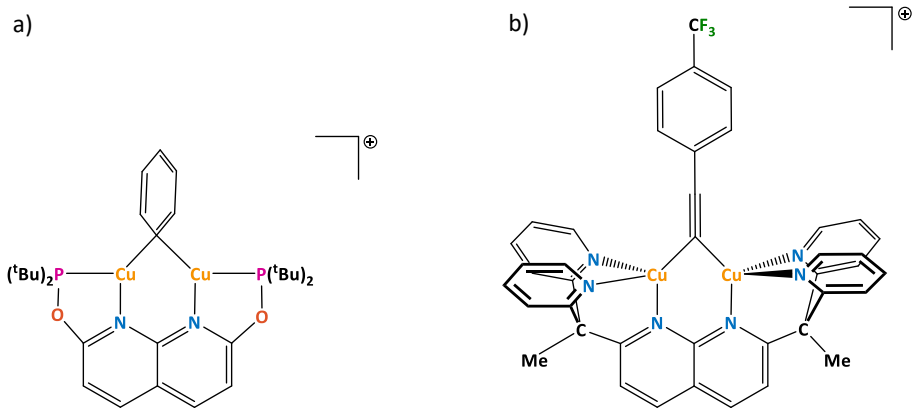

Figure VII.3. Complexes $A1^{+}_{PR3}$ and $A2^{+}_{pyr}$ with symmetrical chelating ligands.

The complexes $\mathbf{A1}^{+}_{PR3}$ and $\mathbf{A1}^{+}_{pyr}$ share common features with $\mathbf{1}^{+}$. First, they all have a distance between the coppers of 2.39 Å and their chelating ligand is fully coordinated. Next, the distance between the different parts of the chelating ligand and the coppers are also similar to $\mathbf{1}^{+}$: 2.14 Å with the naphthyridine, 2.26 Å for the phosphines in $\mathbf{A1}^{+}_{PR3}$ and 2.12 Å for the pyridines in $\mathbf{A1}^{+}_{pyr}$. The phenyl is bridging the coppers symmetrically at 2.02 Å but is orientated in different ways. In $\mathbf{A1}^{+}_{PR3}$, the phenyl is in the plane of the naphthyridine backbone while it bends out of it for $\mathbf{1}^{+}$ (14.6°) and even more for $\mathbf{A1}^{+}_{pyr}$ (26.7°, see Figure VII.4a). These different bendings of the phenyl illustrate how the bulk of the phosphine and pyridines arms are orientated: the ^{t}Bu substituents point toward the exterior of the active site while the pyridines hinder the copper on which they are coordinated, hence inducing more distortion than the phosphine.

The two complexes with the alkynyl bridging the coppers, $\mathbf{A2}^{+}_{PR3}$ and $\mathbf{A2}^{+}_{pyr}$, also display similarities with $\mathbf{2}^{+}$. The ligands are all coordinated and orientated in similar ways. The bond distances involving the chelating ligand are not reported here as they are equivalent to the μ-phenyl complexes (see above). The alkynyl coordinates symmetrically to the coppers at 1.96 Å on average (Figure VII.4b). The thermodynamics of the proton transfer reaction between the alkyne and $\mathbf{A1}^{+}_{Y}$, leading to $\mathbf{A2}^{+}_{Y}$, is exergonic with -20.2, -24.8 and -25.8 kcal/mol for $\mathbf{A2}^{+}_{PR3}$, $\mathbf{2}^{+}$ and $\mathbf{A2}^{+}_{pyr}$, respectively.

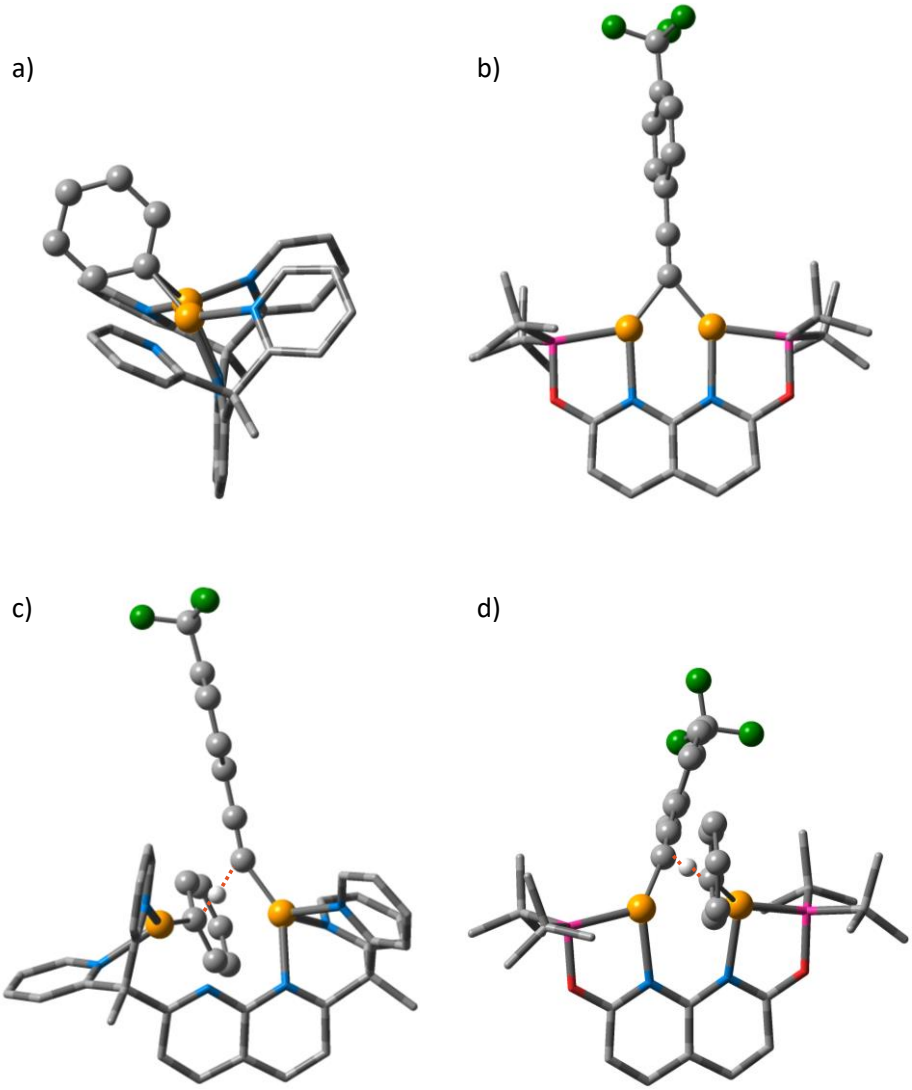

Figure VII.4. 3D representation of the complexes a) $A1^{+}_{pyr}$ and b) $A2^{+}_{PR3}$ and of the transition states c) TS_{A1pyr} and d) TS_{A1PR3}. The red dashed lines account for the cleavage and formation of C-H bonds between the phenyl and alkynyl moieties.

The C-H activation of an alkyne by $\mathbf{A1^{+}_{Y}}$ is assumed to undergo a concerted mechanism (Figure VII.1) leading to $\mathbf{A2^{+}_{Y}}$. Unlike for the DPEOPN complexes, there is only one transition state possible ($\mathbf{TS_{A1Y}}$) from $\mathbf{A1^{+}_{Y}}$ to $\mathbf{A2^{+}_{Y}}$, as both sides of the chelating ligand are the same *i.e.* the two coppers are equivalent.

TS_{A1PR3} (Figure VII.4d) is significantly distorted compared to the reactant and product (+0.28 Å for the distance between the coppers) but not enough to induce the partial dissociation of the chelating ligand. The distances between the chelating ligand and the coppers are similar to the ones reported for **$A1^{+}_{PR3}$**. The phenyl bonds to Cu_1 at 2.05 Å, while the alkynyl coordinates Cu_2 at 2.02 Å and its $ArCF_3$ substituent is near one of the ^{t}Bu substituents of the phosphine. The proton is closer to the alkynyl (1.35 Å) than the phenyl (1.63 Å). All these characteristics are similar to those of **TS_1**. The energy of this transition state is however significantly higher than **TS_1**, with 31.2 kcal/mol versus of 27.1 kcal/mol. **TS_{A1pyr}** is much more distorted than **TS_{A1PR3}**, due to the dissociation of Cu_1 from the naphthyridine backbone (2.75 Å), caused by the steric hindrance between the phenyl and the pyridines, as in **TS_2**. As a result, the distance between the coppers increases to 3.55 Å (Figure VII.4c). The remaining bond between the chelating ligand and the coppers are in the same range as observed in the corresponding intermediates except for the bond between one of the pyridine and Cu_1 which is slightly shorter (2.04 Å). The phenyl and the alkynyl are both tightly bound to their respective copper with distances of 1.95 and 1.92 Å. The transferred proton is also closer to the alkynyl than to the phenyl (1.36 versus 1.87 Å). The energy of **TS_{A1pyr}** is 24.0 kcal/mol, which is significantly lower than **TS_1**, **TS_2** and **TS_{A1PR3}**. The Table VII.1 shows the local natural charge of the coppers and the energy of **TS_1**, **TS_2**, **TS_{A1PR3}** and **TS_{A1pyr}**. It seems that the energy of the transition states correlates to the charge of the coppers: the highest transition state (**TS_{A1PR3}**) is the one with the less positively charged coppers. Conversely, the lowest transition state (**TS_{A1pyr}**) is the one where the coppers are the most positively charged. The transition states are computed in THF, a polar solvent, and thus the transition states that separate the charges best leads to the lower energy.

Transition state	$\Delta G^{\ddagger}$	Natural charge of Cu_1	Natural charge of Cu_2
TS_1	27.1	0.30	0.51
TS_2	27.3	0.48	0.59
TS_{A1PR3}	31.2	0.36	0.32
TS_{A1pyr}	24.0	0.62	0.55
TS_{A1Til}	27.6	0.55	0.53

Table VII.1. Free energy and natural charges of the coppers in TS_1, TS_2, TS_{A1PR3}, TS_{A1pyr} and TS_{A1Til}.

It is worth mentioning that the Tilley group synthesized another symmetrical 1,8-naphthyridine based complexes with two pyridines arms.[45] However, instead of the methyl group, there is a fluorine atom on the sp^3 carbon connecting the pyridines to the backbone. Thus, the intermediates and the transition state (labelled $\mathbf{A1^+_{Til}}$, $\mathbf{A2^+_{Til}}$ and $\mathbf{TS_{A1Til}}$) for the activation of alkyne was also computed for this ligand. The intermediates $\mathbf{A1^+_{Til}}$ and $\mathbf{A2^+_{Til}}$ are very similar to $\mathbf{A1^+_{pyr}}$ and $\mathbf{A2^+_{pyr}}$ and therefore will not be describe here. The thermodynamic of the reaction is -25.8 kcal/mol which is the exactly the same as for the methylated version of the ligand (see above). The transition state $\mathbf{TS_{A1Til}}$ also has several common features with $\mathbf{TS_{A1pyr}}$ (Figure VII.5): Cu_1 is dissociated from the naphthyridine backbone (2.42 Å), increasing the distance between the coppers to 3.20 Å. The remaining distances are the same as in $\mathbf{TS_{A1pyr}}$. The energy of $\mathbf{TS_{A1Til}}$ is 27.6 kcal/mol and is 3.6 kcal/mol higher than $\mathbf{TS_{A1pyr}}$. In $\mathbf{TS_{A1Til}}$, there is less charge separation than in $\mathbf{TS_{A1pyr}}$ (see the natural charge ofCu_1 and Cu_2 in Table VII.1) leading to a higher barrier.

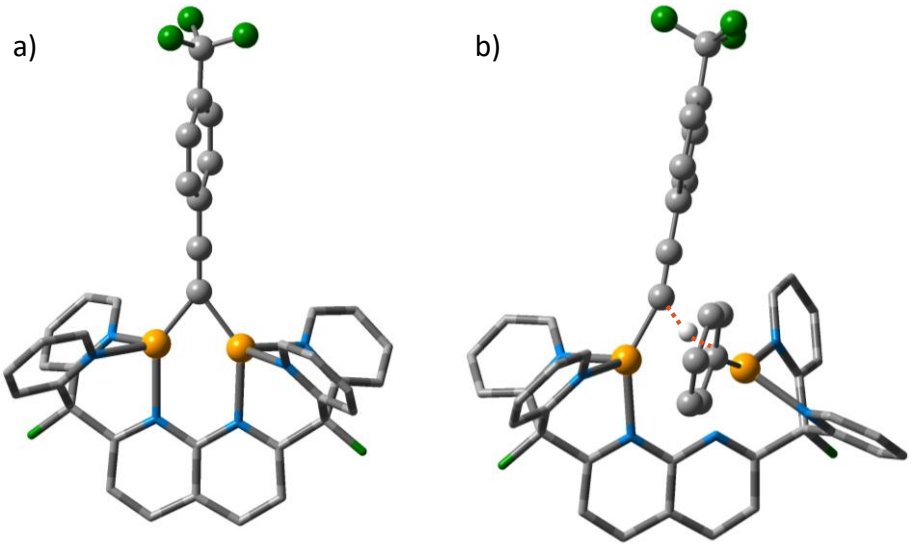

Figure VII.5. 3D representation of a) $A2^{+}_{TiI}$, b) TS_{A1TiI}. The red dashed lines account for the cleavage and formation of C-H bonds between the phenyl and alkynyl moieties.

2 - Modification of the phosphine

The second series of modifications of DPEOPN concerns the functionalisation of the phosphine. In addition to the original ^{t}Bu, eight substituents were chosen: five alkanes (Me, Et, ^{i}Pr, Cy and Ad) and three alkyls (*p*-Ph-NO_2, Ph and *p*-Ph-OMe). The complexes belonging to this series are label $\mathbf{BX_R}$, where X is $\mathbf{1}^{+}$ or $\mathbf{2}^{+}$ and **R** is the abbreviation of the phosphine substituents (Figure VII.6).

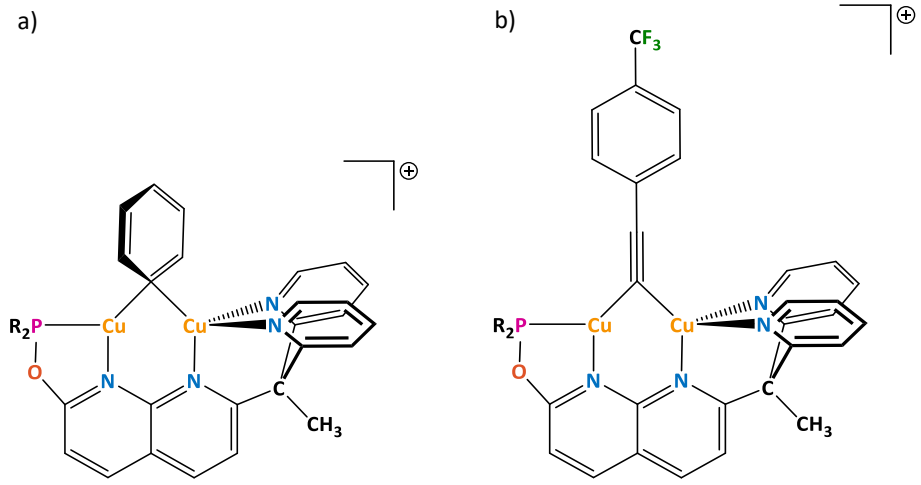

Figure VII.6. Reactant and products of the C-H activation of alkyne via a dicopper complex; a) $B1^{+}_{R}$ and b) $B2^{+}_{R}$ with R = Me, Et, ^{i}Pr, ^{t}Bu, Cy, Ad, Ph, *p*-Ph-NO_2 and *p*-Ph-OMe.

All the $\mathbf{B1^{+}_{R}}$ intermediates have very similar geometries: the distance between the coppers is 2.38 Å and the chelating ligand is all fully coordinated on them. The bond distances for the phosphine, the naphthyridine backbone and the pyridines to the corresponding copper are 2.25, 2.14 and 2.10 Å on average. The orientation of the phosphine changes for the three biggest substituents (^{t}Bu, Cy and Ad): instead of pointing to the side, one of the substituent is filling the space in front of the naphthyridine allowing the other to point away from the active site and thus reducing the steric hindrance (comparison between Figure VII.7a and b). The phenyl is bridging symmetrically the coppers at 2.02 Å and is orientated on one side of the naphthyridine (Figure VII.7b). Overall the largest variation in the key distances is observed for the Cu_1-N_1 bond with a range of 0.07 Å. The only geometrical properties influenced by the different substituents of the phosphine is the R-P-R angle which varies as follow: *p*-Ph-NO_2 < Me ≈ Ph < Et < Ad < *p*-Ph-OMe ≈ Cy < ^{i}Pr < ^{t}Bu. Most of these angles are ranging from 103.4° to 107.6°, except for ^{t}Bu which has a larger angle of 115.8°.

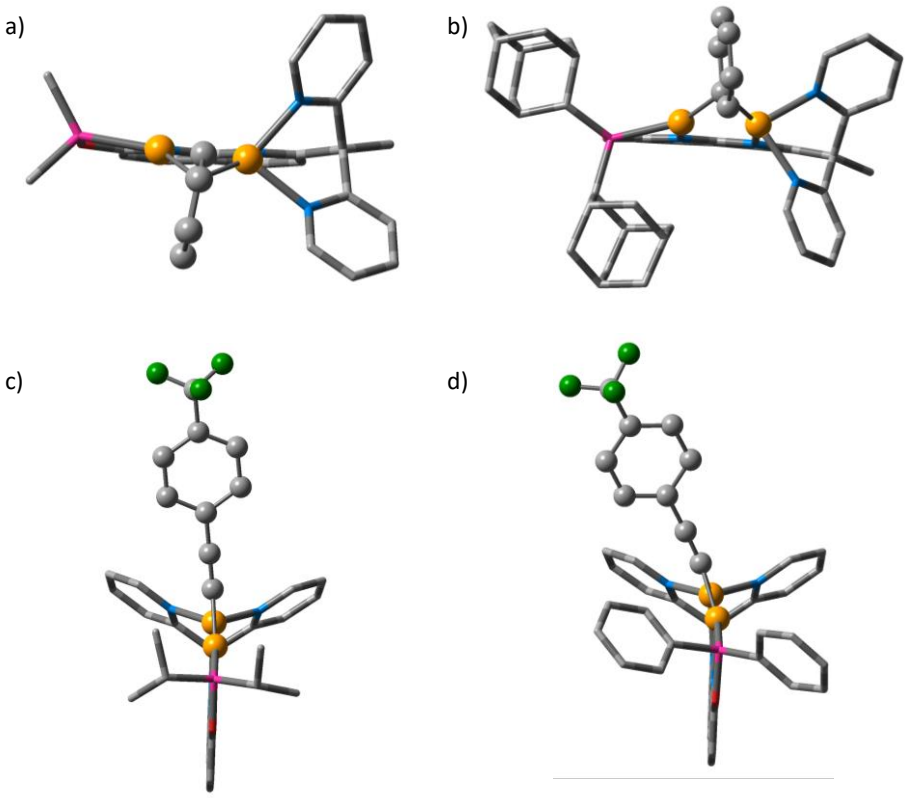

Figure VII.7. 3D representation of a) $B1^{+}_{Me}$, b) $B1^{+}_{Ad}$, c) $B2^{+}_{iPr}$ and d) $B2^{+}_{Ph}$.

Similar observation can be made for the $\mathbf{B2^{+}_{R}}$ complexes: the distance between the coppers is 2.38 Å and the distances with the chelating ligand are 2.26, 2.10 and 2.08 Å for the phosphine, the naphthyridine backbone and the pyridines, respectively. The orientation of the phosphine changes for the three biggest R substituents (^{t}Bu, Cy and Ad) in the same way as in the $\mathbf{B1^{+}_{R}}$ complexes. The alkynyl is bridging the coppers evenly at 1.95 Å on average. In most cases, the alkynyl is orientated in the plane of the naphthyridine but in 3 cases (Cy, Ph and *p*-$PhNO_2$) the alkynyl bends outside of the plane (Figure VII.7c and d). As for the $\mathbf{B1^{+}_{R}}$ complexes, the only change caused by the substituents is the R-P-R angle, which followed the same trend and varied from 103.7° to 108.0° for all, with the exception of ^{t}Bu which has an angle of 116.0°. Considering the thermochemistry of the C-H activation of alkynes by

B1$^{+}_{R}$, the reaction is exergonic and the energy ranges from -22.6 kcal/mol for **B2**$^{+}_{Ad}$ and **B2**$^{+}_{p\text{-Ph-NO2}}$ to -24.9 kcal/mol for **B2**$^{+}_{p\text{-Ph-OMe}}$.

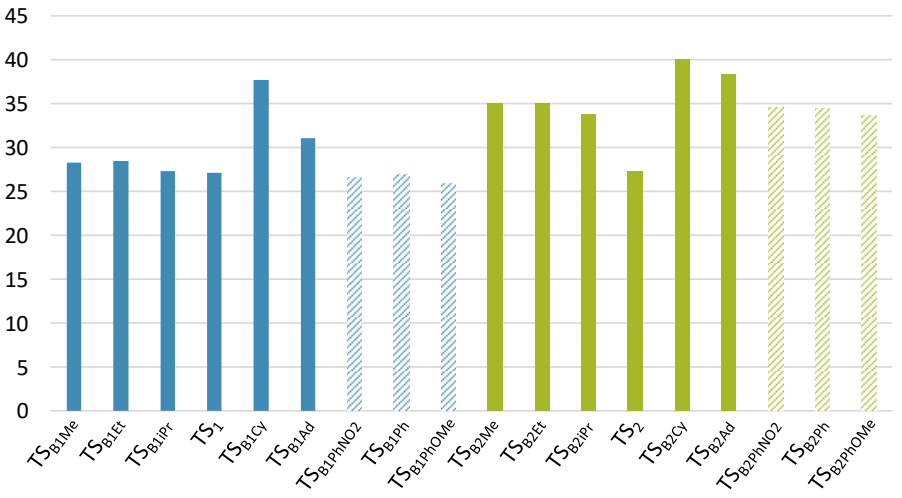

Figure VII.8. Free energy of all the transition states of the TS$_{B1R}$ (blue) and TS$_{B2R}$ (green) series relative to B1$^{+}_{R}$; plain colours correspond to alkane substituents and the dashed colours to alkyl substituents.

In this series, the ligands are unsymmetrical and thus there are two different isomers for the transition state connecting **B1**$^{+}_{R}$ to **B2**$^{+}_{R}$, as for DPEOPN (Figure VII.1), and they are labelled **TS$_{B1R}$** and **TS$_{B2R}$** depending on the coordination of the phenyl to either Cu_1 or Cu_2, respectively. The energy of these transition states are gathered in the Figure VII.8. The transition states in the **TS$_{B1R}$** series can be split in two groups, depending on the nature of R. The ones with alkane substituents share common features: a long distance between the coppers (2.88 to 3.02 Å), except for **TS$_{B1Ad}$** which has a shorter distance of 2.77 Å. The chelating ligand is still fully coordinated to the metal centres, with a slight asymmetry in the coordination of the naphthyridine (around +0.1 Å for N_1 compared to N_2). The phenyl is coordinated to Cu_1 at 2.01 Å on average and is outside of the naphthyridine plane (Figure VII.9a). The alkynyl is coordinated to Cu_2 at 1.93 Å and bends over the phosphine so its $ArCF_3$ substituent interacts with it (around 3,00 Å apart for **TS$_{B1Et}$**). The energy of these transition states decreases from Me/Et to ^{i}Pr/^{t}Bu (Figure VII.8), likely

due to the increasing interactions between the R substituents and the alkynyl. The two bulkiest substituents have higher energies, with 31.1 and 37.7 kcal/mol for Ad and Cy, respectively. This significant energy increase is due to the high steric hindrance generated by these substituents that cannot be counterbalanced by the creation of new weak interactions with the other part of the complex. The three transition states with the alkyl substituents have an overall similar geometry to the alkane ones except for the orientation of the alkynyl. Instead of being tilted over the phosphine, the $ArCF_3$ substituent of the alkynyl do a π-stacking interaction with one of the R substituent of the phosphine (3.60 Å apart on average). In $\mathbf{TS_{B1}}$*p*-Ph-NO2 and $\mathbf{TS_{B1Ph}}$, the alkynyl is in the cavity formed by the chelating ligand around the coppers, while it is on top of the R substituent in $\mathbf{TS_{B1}}$*p*-Ph-OMe (Figure VII.9c and d). The energies of these transition states are lower than the alkane ones, ranging from 25.9 kcal/mol for $\mathbf{TS_{B1}}$*p*-Ph-OMe to 26.9 kcal/mol for $\mathbf{TS_{B1Ph}}$.

All the transition states in the $\mathbf{TS_{B2R}}$ series have similar characteristics: for all except $\mathbf{TS_2}$ (R=^{t}Bu, which is not describe here, see chapter IV) the phenyl is bridging the two coppers (Figure VII.10a) despite the large variations in the distance between the metals (from 2.71 to 3.30 Å). The bridge is symmetrical in five transition states versus three unsymmetrical ($\mathbf{TS_{B2Cy}}$, $\mathbf{TS_{B2Ad}}$ and $\mathbf{TS_{B2Ph}}$). The preferred position for the alkynyl is with its $ArCF_3$ substituent parallel to the pyridine **β** (the pyridine containing N_4 in Figure VII.2), with which it does a π-stacking interaction as they are 3.50 to 3.70 Å apart. The two exceptions are $\mathbf{TS_{B2Cy}}$ and $\mathbf{TS_{B2Ph}}$. In the former, the alkynyl is not interacting with the chelating ligand at all while it is parallel to the naphthyridine (3.30 Å) in the latter, showing the presence of the π-stacking interaction (Figure VII.10c and d). The energies of these transition states are all higher than their $\mathbf{TS_{B1R}}$ equivalents by few kcal/mol, with the exception of $\mathbf{TS_2}$, which has the same energy as $\mathbf{TS_1}$ (27.3 and 27.1 kcal/mol, respectively). The overall range for the $\mathbf{TS_{B2R}}$ series is from 27.3 to 40.0 kcal/mol.

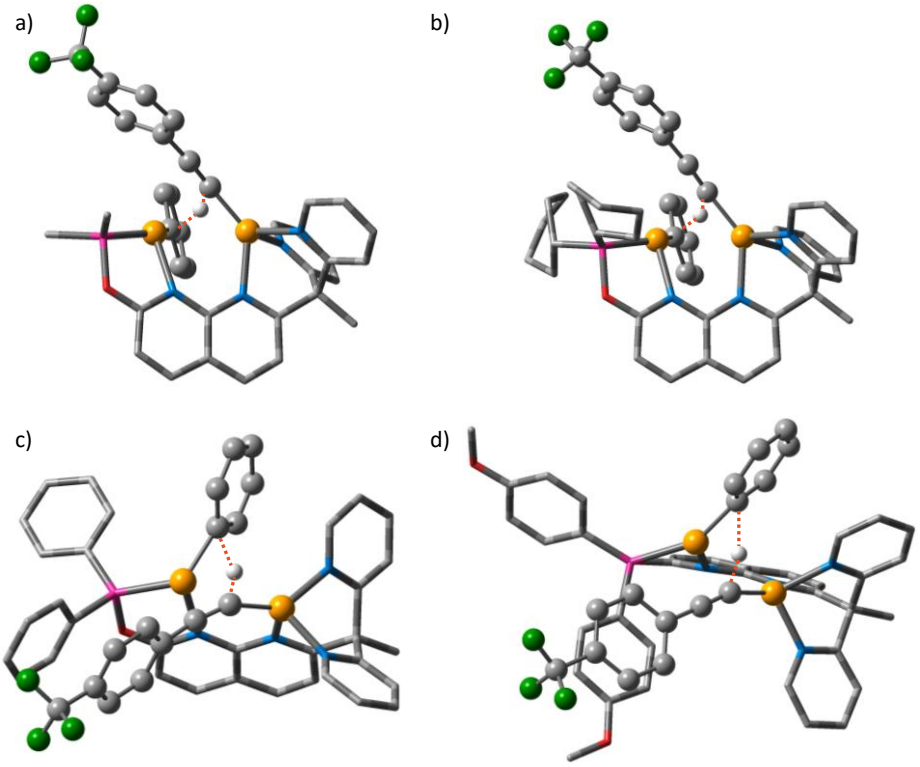

Figure VII.9. 3D representation of a) TS_{B1Me}, b) TS_{B1Cy}, c) TS_{B1Ph} and d) $TS_{B1p\text{-}Ph\text{-}OMe}$. The red dashed lines account for the cleavage and formation of C-H bonds between the phenyl and alkynyl moieties.

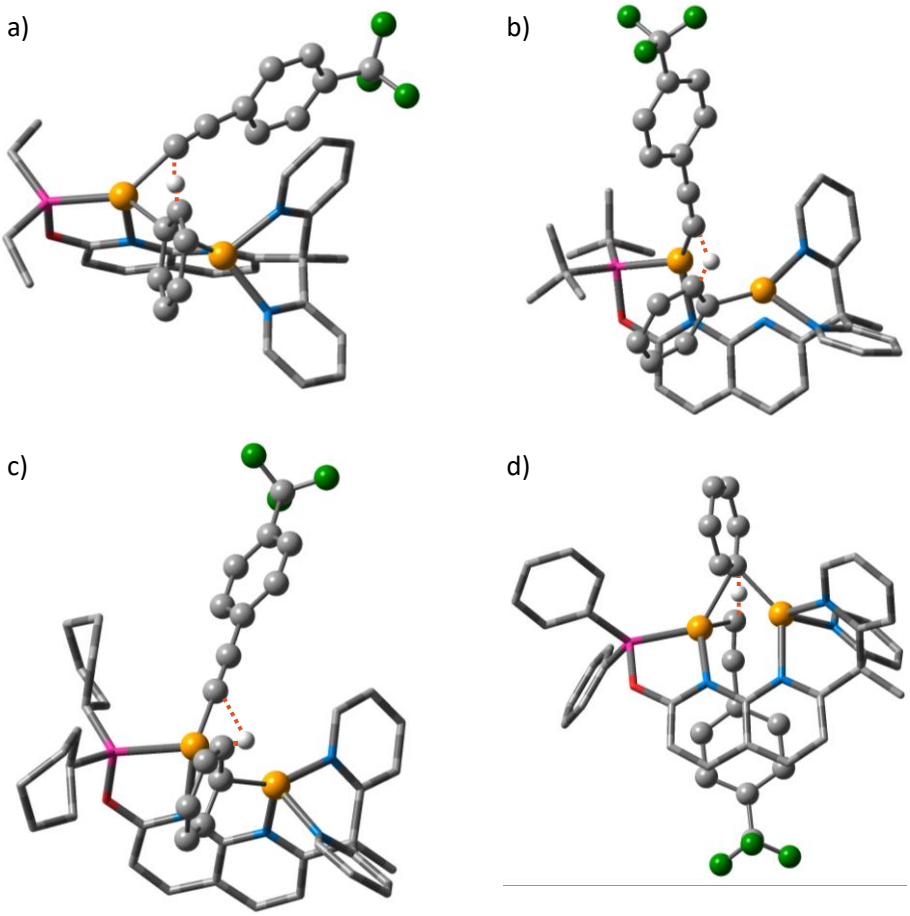

Figure VII.10. 3D representation of a) TS_{B2Et}, b) TS_2, c) TS_{B2Cy} and d) TS_{B2Ph}. The red dashed lines account for the cleavage and formation of C-H bonds between the phenyl and alkynyl moieties.

The two series of transition states **TS_{B1R}** and **TS_{B2R}** were analysed with the descriptors approach used in the previous chapters to find correlations between the energy of the transition states and geometrical and electronical parameters. Some descriptors will be considered in each subsections of this chapter (black dots, see below) and other are specific to each subsections (grey squares, see below for the phosphine case):

- Distance between Cu_1 and Cu_2

- Natural charge of Cu_1
- Natural charge of Cu_2
- Difference of natural charge between Cu_1 and Cu_2
- Dihedral angle Cu_1-N_1-N_2-Cu_2
- Distance Cu and C_1
- Distance Cu and C_2
- Distance C_1 and H
- Distance C_2 and H
- Natural charge of the C_1
- Natural charge of the C_2
- Natural charge of H
- Distance between Cu_1 and P
- Natural charge of P
- Angle R-P-R

In the Figure VII.11 and in the additional *Descriptors file* (see annexes), are scattered plots of the descriptors analysis of the **TS_{B1R}** and **TS_{B2R}** series. All the transition states related to the **TS_{B1R}** series are represented in blue dots while the **TS_{B2R}** are in green. The main feature of this descriptor analysis is that there is no parameters that strongly correlate to the energies. The only one display a moderate correlation is the natural charge with C_2, the carbon of the alkynyl coordinated to the copper, with a R^2 of 0.57 (Figure VII.11). It could indicate that more the carbon is charge negatively, lower the transition state energy will be, *i.e.* better the charge separation is and easier the transfer of the proton from C_2 to C_1 is. However, the correlation for this parameters is only moderate and the span of the energy barriers is wide for each values of the charge and thus, no strong conclusions can be made.

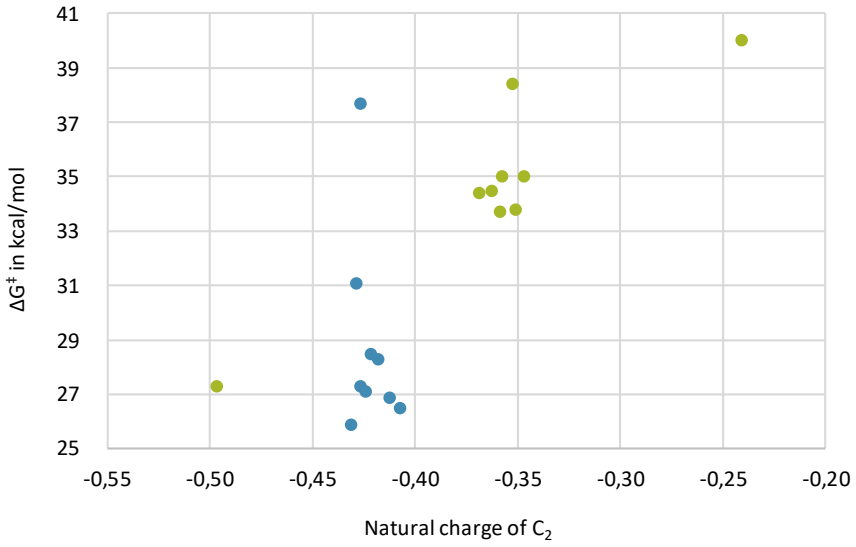

Figure VII.11. Energy of the transition states as function of the natural charge of C_2, $R^2 = 0.5676$. No point has been removed.

3 - Modification of the naphthyridine

The third series of modifications of DPEOPN involves the functionalisation of the naphthyridine backbone. No geometrical changes are done near the active site but the electronic properties are tuned with the addition of an -NO_2 or -OMe group instead of a hydrogen in the para position relative to the coordinating nitrogen (Figure VII.12). The complexes belonging to this series are label **CX_Y**, where **X** is **1^+** or **2^+** and **Y** is the abbreviation of the naphthyridine substituents.

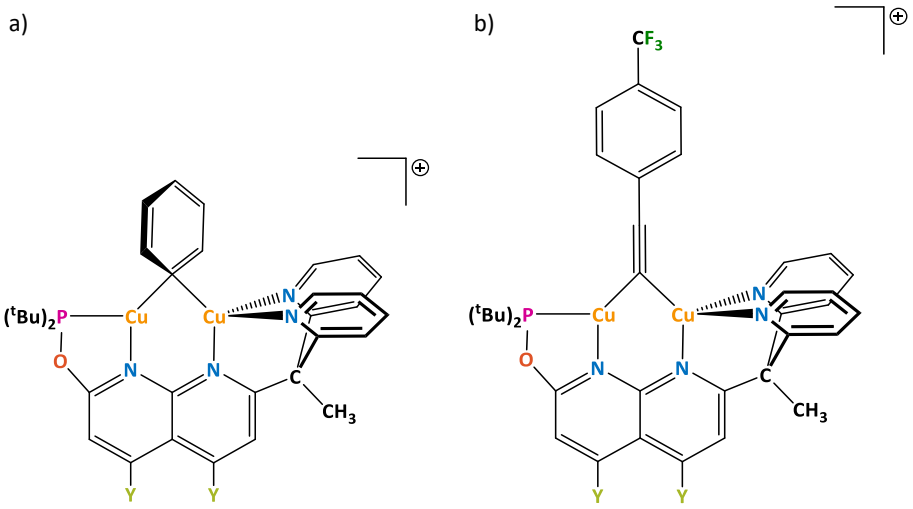

Figure VII.12. Reactant and products of the C-H activation of alkyne via a dicopper complex; a) $C1^{+}_{Y}$ and b) $C2^{+}_{Y}$ with Y = NO_2, H and OMe.

The intermediates $\mathbf{C1}^{+}_{Y}$ and $\mathbf{C2}^{+}_{Y}$ are both very similar to $\mathbf{1}^{+}$ and $\mathbf{2}^{+}$: in both cases the distance between the coppers is 2.38 Å and the chelating ligands are all fully coordinated to them. The phosphine and the pyridine have no variation in their bonding distances to the coopers while the distance to the naphthyridine varies slightly, even if the largest variation is 0.07 and 0.05 Å for $\mathbf{C1}^{+}_{Y}$ and $\mathbf{C2}^{+}_{Y}$. In both cases, the phenyl and the alkynyl are symmetrically bridging the coppers, at 2.02 and 1.95 Å, respectively. Figure VII.13 displays an example of each of these complexes. The thermodynamics of the reaction from $\mathbf{C1}^{+}_{Y}$ to $\mathbf{C2}^{+}_{Y}$ is exergonic, with ΔG = -24.3, -24.8 and -25.1 kcal/mol for **Y** = NO_2, H and OMe, within a narrow energy range of 0.8 kcal/mol.

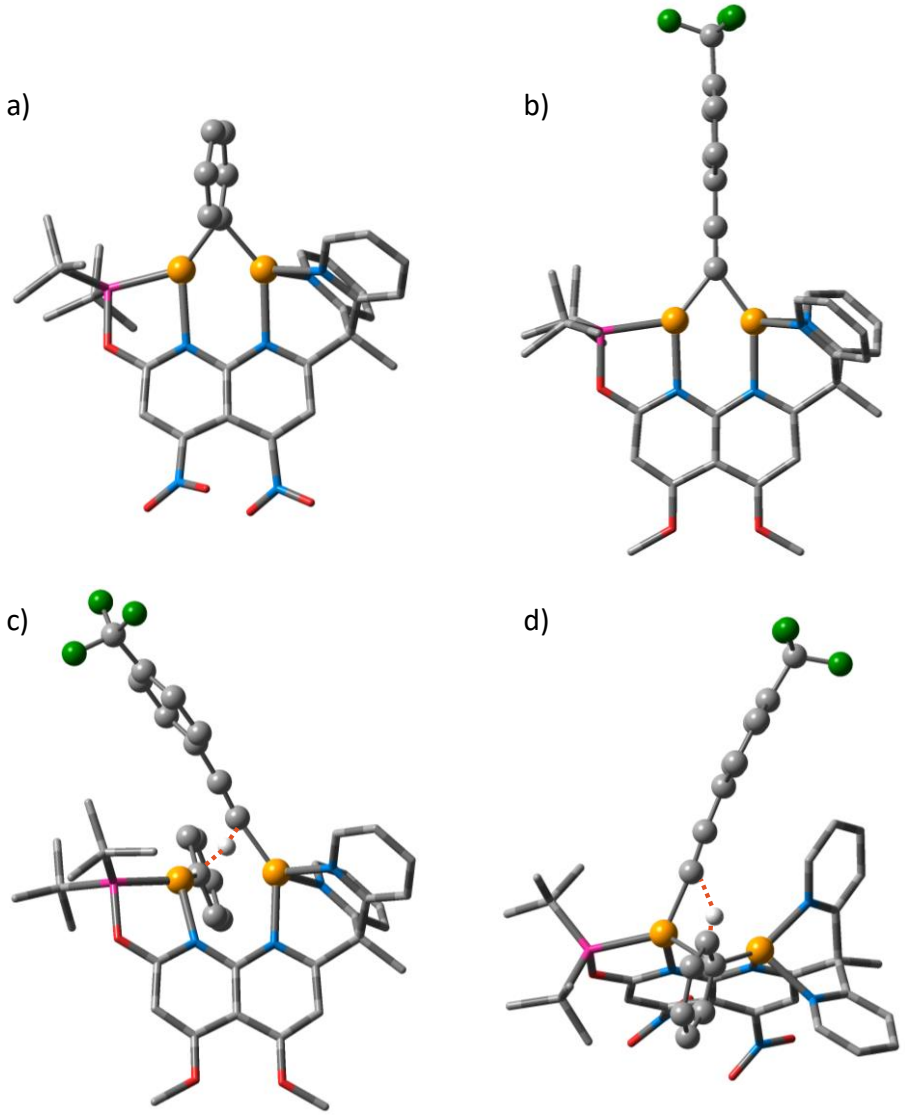

Figure VII.13. 3D representation of a) $C1^{+}_{NO2}$ b) $C2^{+}_{OMe}$, c) TS_{C1OMe} and d) TS_{C2NO2}. The red dashed lines account for the cleavage and formation of C-H bonds between the phenyl and alkynyl moieties.

The proton transfer connecting $\mathbf{C1^{+}_{Y}}$ to $\mathbf{C2^{+}_{Y}}$ proceed via two different transition states: the alkyne coordinates either on pyridine side ($\mathbf{TS_{C1Y}}$) or on the phosphine one ($\mathbf{TS_{C2Y}}$). The energy of these transition states are gathered

on Figure VII.14. The transition states $\mathbf{TS_{C1R}}$ are very similar to $\mathbf{TS_1}$: the chelating ligand is fully coordinated to the coppers, the distance between Cu_1 and the phenyl is 2.01 Å while Cu_2 and the alkynyl are 1.93 Å apart and its $ArCF_3$ substituent is above the phosphine (Figure VII.13c). The only difference between these three transition states is the distance between the coppers (2.98, 2.88 and 2.82 Å for $\mathbf{TS_{C1NO2}}$, $\mathbf{TS_1}$ and $\mathbf{TS_{C1OMe}}$), due to the elongation or shortening of the bond between Cu_1 and N_1. The energy of these transition states are 27.8, 27.1 and 26.5 kcal/mol for $\mathbf{TS_{C1NO2}}$, $\mathbf{TS_1}$ and $\mathbf{TS_{C1OMe}}$, respectively; correlating to the distance between the coppers and the electronic donor ability of the substituent Y.

The transition states $\mathbf{TS_{C2Y}}$ are very different from $\mathbf{TS_2}$ and from each other. $\mathbf{TS_{C2NO2}}$ is less distorted than $\mathbf{TS_2}$, with a distance between the coppers of only 2.84 Å versus 3.08 Å, allowing the chelating ligand to be fully coordinated to the coppers (Figure VII.13d). The phenyl ligand is strongly coordinated to Cu_2 (1.99 Å) and loosely to Cu_1 (2.36 Å), displaying a weak bridge between the coppers. The alkynyl is coordinated to Cu_1 at 1.97 Å. The energy of $\mathbf{TS_{C2NO2}}$ is 31.7 kcal/mol, which is 4.4 kcal/mol higher than $\mathbf{TS_2}$. $\mathbf{TS_{C2OMe}}$ has a geometry very similar the ones of the $\mathbf{TS_{B2R}}$ series, with the phenyl bridging the coppers evenly (2.14 and 2.11 Å for Cu_1 and Cu_2, respectively) and the alkynyl orientated in a way that allows it to do a π-stacking interaction with the pyridine **β** (3.70 Å apart). This transition state is even higher in energy, with 35.8 kcal/mol. Thus, the transition states from $\mathbf{TS_{C1Y}}$ appear to be lower in energy than the $\mathbf{TS_{C2Y}}$ ones, the lowest being $\mathbf{TS_{C1OMe}}$ (26.5 kcal/mol).

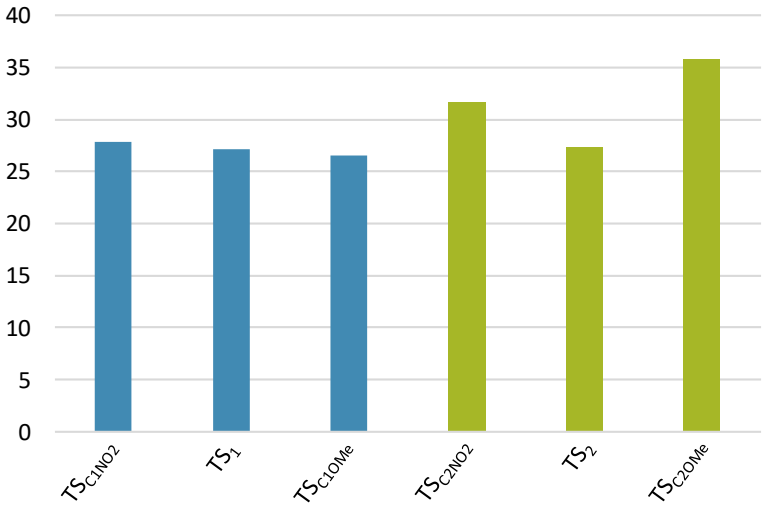

Figure VII.14. Free energy of all the transition states of the TS_{C1Y} (blue) and TS_{C2Y} (green) series

4 - Modifications on the pyridines arm

a) Modifications of the pyridines

The fourth series of modifications of DPEOPN regards the functionalisation of the two pyridines. As for the modifications of the naphthyridine backbone, the electronic properties of the pyridines are altered with the addition of an $-NO_2$ or -OMe group instead of a hydrogen in the para position compared to the coordinating nitrogen (Figure VII.15). Two different sets of complexes where investigated, the $\mathbf{DX_Y}$ series which has two pyridines and the $\mathbf{EX_Y}$ series in which the pyridine **β** (the pyridine containing N_4 in Figure VII.2) was replaced by a methyl (**X** is $\mathbf{1}^+$ or $\mathbf{2}^+$ and **Y** is the abbreviation of the pyridine substituent). This last series was inspired on the dissociation of the **β** pyridine observed in the DPEOPN complexes and described in the previous chapters.

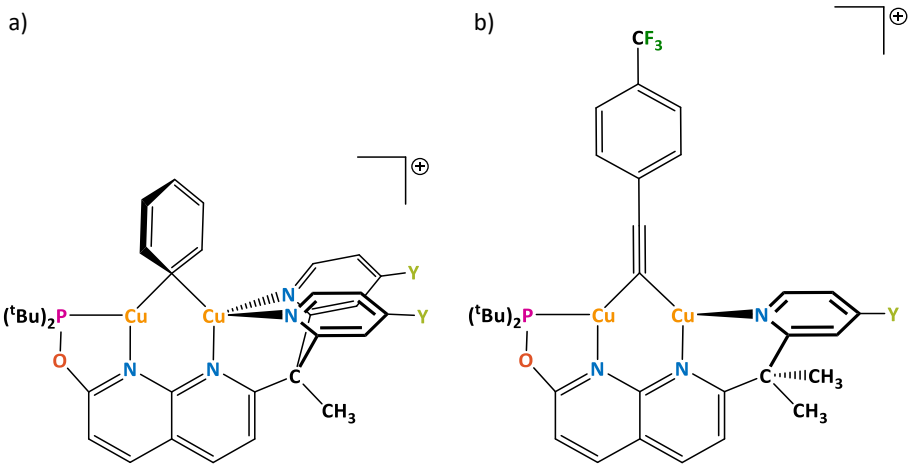

Figure VII.15. Reactant and products of the C-H activation of alkyne via a dicopper complexes a) $D1^{+}_{Y}$ and b) $E2^{+}_{Y}$, with Y = NO_2, H and OMe.

The three $\mathbf{D1^{+}_{Y}}$ intermediates are all very similar (Figure VII.16a): the distance between the coppers is 2.38 Å and the chelating ligand is fully coordinated to them. The phosphine has the longer bond distance with 2.25 Å while the naphthyridine and the pyridines are shorter, with an average of 2.14 and 2.10 Å, respectively. The phenyl is bridging symmetrically the coppers (2.02 Å) and is tilted outside of the naphthyridine plane. The geometry of the $\mathbf{E1^{+}_{Y}}$ complexes is not much impacted by the loss of one pyridine compared to their $\mathbf{D1^{+}_{Y}}$ equivalent. The only noticeable differences are: 1) the asymmetrical coordination of the naphthyridine to the coppers, with distances in $\mathbf{E1^{+}_{H}}$ of 2.17 and 2.08 Å for the Cu_1-N_1 and Cu_2-N_2 bonds, respectively. 2) The phenyl bridge is not tilted out from the naphthyridine plane (Figure VII.16b), as there is less steric hindrance with the chelating ligand. These small geometry changes are similar to the subtle distortion of the DPEOPN complexes caused by the dissociation of the pyridine **β**.

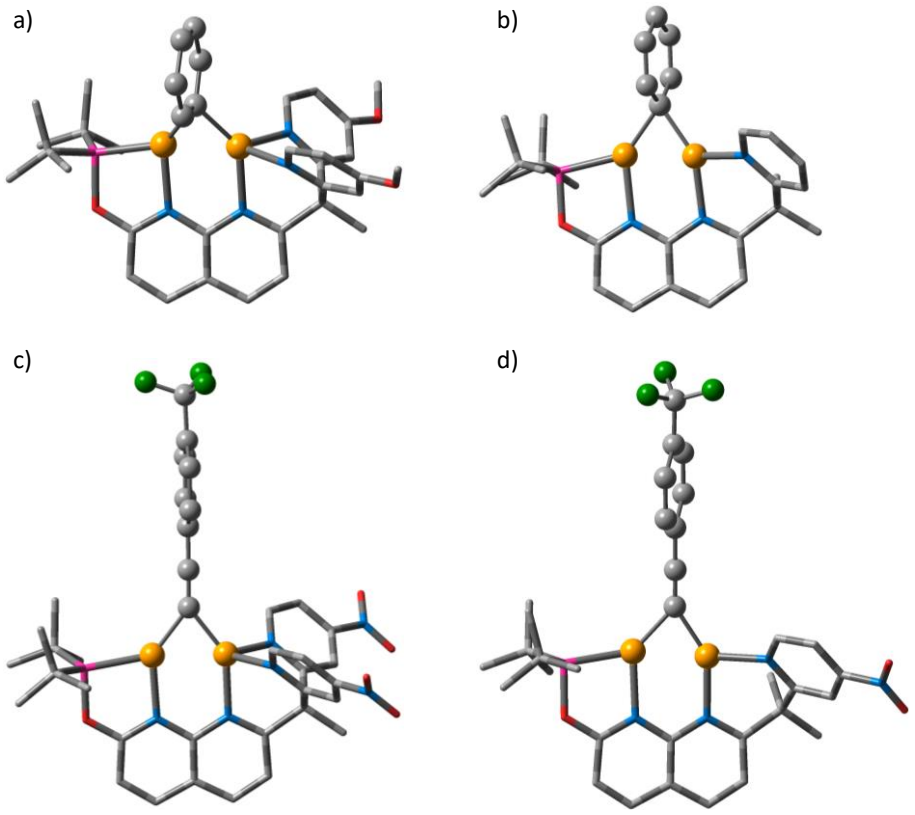

Figure VII.16. 3D representation of a) $D1^{+}_{OMe}$, b) $E1^{+}_{H}$ c) $D2^{+}_{NO2}$ and d) $E2^{+}_{NO2}$.

The same trends are observed for the $\mathbf{D2^{+}_{Y}}$ and $\mathbf{E2^{+}_{Y}}$ complexes: the overall geometry is the same for both series even if the latter is slightly more distorted. For example, the dihedral angle Cu_1-N_1-N_2-Cu_2 is -0.2° on average for the $\mathbf{D2^{+}_{Y}}$ complexes and 10.2° for the $\mathbf{E2^{+}_{Y}}$. The coordination to naphthyridine to the coppers is slightly asymmetric, with distance differences of 0.04 and 0.10 Å between for N_1 and N_2 in $\mathbf{D2^{+}_{NO2}}$ and $\mathbf{E2^{+}_{NO2}}$, respectively. The shared features among the two series comprise the distance between the coppers of 2.38 Å and the fully coordinated chelating ligands (2.25 Å for the phosphine and 2.06 Å on average for the pyridine). The alkynyl is bridging symmetrically the coppers at 1.95 Å on average and is unbend (Figure VII.16c and d). The $\mathbf{D2^{+}_{Y}}$ complexes are more exergonic than the $\mathbf{E2^{+}_{Y}}$ ones as their

energies are ranging from -23.9 to -24.8 kcal/mol and from -20.2 to 21.4 kcal/mol, compared to their respective phenyl-bridged complexes.

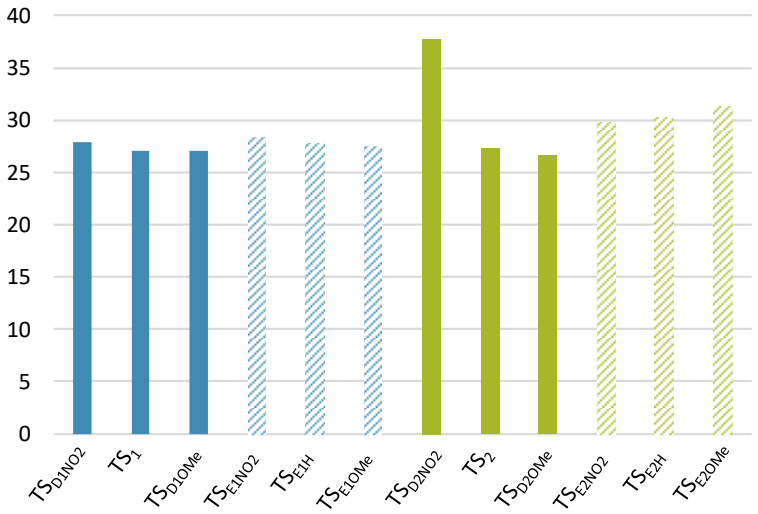

Figure VII.17. Free energy of all the transition states of the series TS_{D1Y} (plain blue), TS_{E1Y} (dashed blue), TS_{D2Y} (plain green) and TS_{E2Y} (dashed green).

For this series, the transition state linking **$D1^+_Y$** and **$E1^+_Y$** to **$D2^+_Y$** and **$E2^+_Y$** has also two isomers: the ones were the alkyne attacks from the pyridines or the phosphine sides, leading to **TS_{D1Y}** and **TS_{D2Y}** for the ligands with two pyridines and to **TS_{E1Y}** and **TS_{E2Y}** for the ligands with only one pyridine. The six transition states of the **TS_{D1Y}** and **TS_{E1Y}** series have many common features: the distance between the coppers varies only by ±0.05 Å around 2.92 Å and the chelating ligands are fully coordinated to the coppers, with asymmetric bonding of the naphthyridine (+0.1 Å longer for the Cu_1-N_1 bond compared to the Cu_2-N_2 one). The distance between Cu_1 and the phenyl is 2.01 Å for the **TS_{D1Y}** series, while the distance is elongated to 2.08 Å for the **TS_{E1Y}**. The only major differences between these two series are the coordination mode and the orientation of the alkynyl. In **TS_{D1Y}**, it coordinates to Cu_2 in a σ mode via C_2 and its $ArCF_3$ substituent is tilted toward the phosphine (Figure VII.18a), while it coordinates via its π system on Cu_2 in **TS_{E1Y}** (2.05 and 2.08 Å for C_2 and C_3) and its $ArCF_3$ substituent is above the pyridine (Figure VII.18b). The energy of

these six transition states are ranging from 27.1 to 28.3 kcal/mol, and for each Y substituent the transition state from the series D is lower than the one from the series E (Figure VII.17). The other noticeable trend is that the lowest-energy transition state in each series is the one with the donor substituent -OMe on the pyridine and the higher one has the acceptor substituent -NO_2. However, with such small range of energy (1.2 kcal/mol), it is difficult to conclude that the substituent with the most electron donating character will yield the lowest energy barriers since the smallest error in the estimation of the DFT energies could reverse this trend.

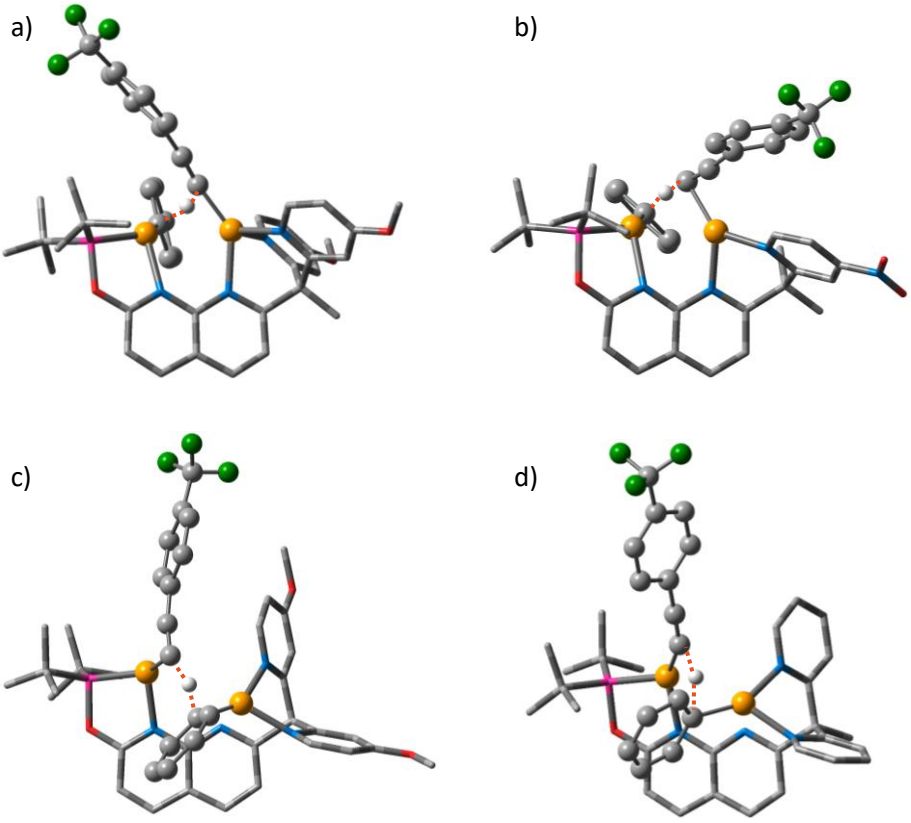

Figure VII.18. 3D representation of a) TS_{D1OMe}, b) TS_{E1NO2}, c) TS_{D2OMe} and d) TS_2. The red dashed lines account for the cleavage and formation of C-H bonds between the phenyl and alkynyl moieties.

As for the previous modifications of DPEOPN, the **TS_{D2Y}** and **TS_{E2Y}** series exhibit a large variety of geometries, with the distance between the coppers in the wide range of 2.75 to 4.04 Å. Their corresponding energies vary from 26.6 to 37.8 kcal/mol (Figure VII.17). In this case, all geometries are significantly different and therefore, only the lowest-energy one will be describe here (**TS_{D2OMe}** in Figure VII.18c). **TS_{D2OMe}** is extremely distorted and has the longest distance between the coppers (4.04 Å), due to the dissociation of Cu_2 from the naphthyridine (2.77 Å) as the arm carrying the pyridine rotates forward, resembling **TS_2** (Figure VII.18d). The effect on the coordination sphere of Cu_2 is minimal as the remaining distances with the metal are 2.06 and 1.99 Å for the pyridines and the phenyl, respectively. The alkynyl coordinates on Cu_1 via its π-system and its $ArCF_3$ substituent is above the phosphine, differing from **TS_2**, in which the alkynyl is bound to Cu_1 in a σ mode. The proton is equidistant from the two carbons, at 1.44 Å. Overall, in this series of modifications, the lowest-energy transition state is **TS_{D2OMe}** with 26.6 kcal/mol.

From the four series **TS_{D1Y}**, **TS_{D2Y}**, **TS_{E1Y}** and **TS_{E2Y}**, twelve transition states were computed and analysed to search for correlation between their properties and energy. The chosen properties include the general parameters described in the section VII.2, plus the following:

- Natural charge of the N_3
- Natural charge of the N_4
- Angle between N_3-Cu_2-N_4
- Distance between N_3 and Cu_2
- Distance between N_4 and Cu_2

In the additional *Descriptors file* (see annexes), are scattered plots of the descriptors analysis of the **TS_{D1Y}**, **TS_{D2Y}**, **TS_{E1Y}** and **TS_{E2Y}**. Two descriptors features a good correlation with the energies of the transition states: the distance between Cu_2 and N_4 and the angle N_3-Cu_2-N_4 (see below). It is important to notice that these descriptors concern geometric properties involving the pyridine **β** and thus involve only the six transition states from the **TS_{D1Y}** and **TS_{D2Y}** series. After a closer look to these graphics, one point is

an outlier compare to the other transition states ($\mathbf{TS_{D2NO2}}$ with 37.8 kcal/mol) and seems to be at the origin of the correlation. Thus, the descriptors analysis on the transition states issued from the modifications of the pyridine do not lead to any clear correlation between the energy and any descriptors and the only parameters that show a significant R^2 arise from a mathematical artefact.

b) Replacement of the pyridines by imines

The fifth modification of the DPEOPN ligand concerns the replacement of the pyridines by imines (Figure VII.19). The number of atoms between the naphthyridine backbone and the coordinating nitrogens is kept constant relative to DPEOPN to have chelating ligands with a relatively similar shape and flexibility. The imine is functionalize with five different groups: Me, Et, ^{i}Pr, ^{t}Bu and Ph, chosen to vary the size and orientation of the bulk around Cu_2. As in the previous section, two series of complexes were designed: $\mathbf{FX_R}$ which has two imines and $\mathbf{GX_R}$ which has only one (with **X** = $\mathbf{1}^+$ or $\mathbf{2}^+$ and R = Me, Et, ^{i}Pr, ^{t}Bu, Ph).

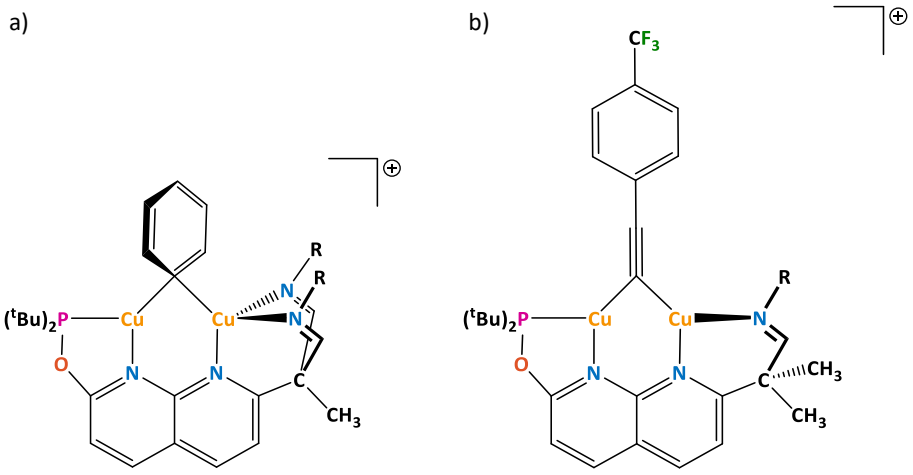

Figure VII.19. Reactant and products of the C-H activation of alkyne via a dicopper complex: a) $\mathbf{F1^+_R}$ and b) $\mathbf{G2^+_R}$ with R = Me, Et, ^{i}Pr, ^{t}Bu and Ph.

The complexes $\mathbf{F1^+_R}$ and $\mathbf{G1^+_R}$ have very similar characteristics: the distance between the metal centres varies from 2.36 to 2.43 Å, with the $\mathbf{F1^+_R}$ complexes tending to have longer distances than the $\mathbf{G1^+_R}$. The chelating ligands are all

fully coordinated to the coppers: the phosphine bonds to Cu_1 at 2.25 Å, the bonds with the naphthyridine are asymmetric (Cu_2-N_2 is 0.1 Å longer than Cu_1-N_1) and the imines coordinate to Cu_2 at 2.10 Å in $\mathbf{F1^+_R}$ and 2.03 Å in $\mathbf{G1^+_R}$. The phenyl bridges the coppers symmetrically with a bond distance of 2.02 Å on average over the two series. Its orientation changes with the size of the R substituent of the imine. For R = Me and Et, the phenyl is in the plane of the naphthyridine while it slightly bends out of it to interact with the imines for R = ^{i}Pr and Ph (Figure VII.20a). For R = ^{t}Bu, the phenyl is also outside of the plane of the naphthyridine but on the opposite side of the imine for $\mathbf{G1^+_{tBu}}$ (Figure VII.20b) and the imine arm shifts to make space on one side in $\mathbf{F1^+_{tBu}}$ for the phenyl.

The $\mathbf{F2^+_R}$ and $\mathbf{G2^+_R}$ complexes are even more alike as the distance between the coppers varies only from 2.39 to 2.41 Å. The naphthyridine backbone is symmetrically coordinated to the coppers with a bond distance of 2.11 Å on average, except for $\mathbf{F2^+_{iPr}}$ and $\mathbf{F2^+_{tBu}}$, in which the Cu_1-N_1 bond is shorter by 0.1 Å. The phosphine is bound to Cu_1 at 2.25 Å and the imine to Cu_2 with a distance of 2.09 Å for $\mathbf{F2^+_R}$ and 2.03 Å for the $\mathbf{G2^+_R}$. The alkynyl is bonded symmetrically to the coppers (1.96 Å) and is orientated in the plane of the naphthyridine in all complexes except for $\mathbf{F2^+_{Ph}}$ in which the $ArCF_3$ substituent bends over the imines (Figure VII.20c and d). The thermodynamics of the activation of alkynes is exergonic and the $\mathbf{F2^+_R}$ complexes are more stable than the $\mathbf{G2^+_R}$ ones, with the energies ranging from -22.5 to -27.0 kcal/mol for $\mathbf{F2^+_R}$ and from -20.7 to -21.8 kcal/mol for $\mathbf{G2^+_R}$.

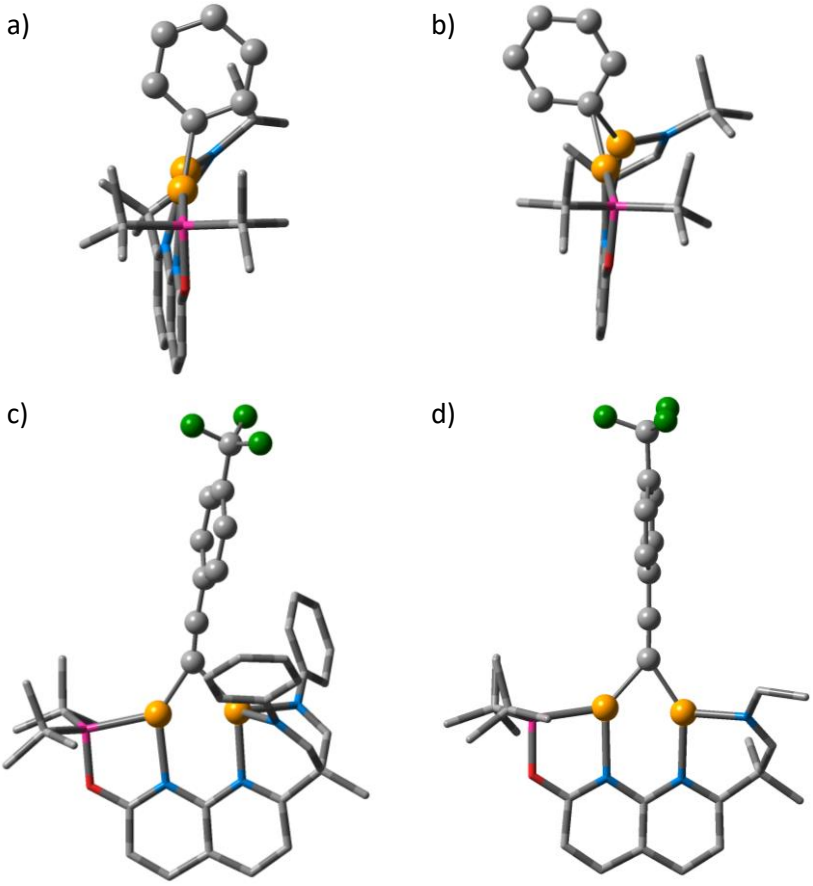

Figure VII.20. 3D representation of a) $F1^{+}_{iPr}$, b) $G1^{+}_{tBu}$ c) $F2^{+}_{Ph}$ and d) $G2^{+}_{Et}$.

The proton transfer connecting $\mathbf{F1^{+}_{R}}$ and $\mathbf{G1^{+}_{R}}$ to $\mathbf{F2^{+}_{R}}$ and $\mathbf{G2^{+}_{R}}$ can proceed via two transition states: the alkyne arrives either on the pyridine side of the complexes ($\mathbf{TS_{F1R}}$ and $\mathbf{TS_{G1R}}$) or on the phosphine one ($\mathbf{TS_{F2R}}$ and $\mathbf{TS_{G2R}}$). The energy of all these transition states are gathered in Figure VII.21. $\mathbf{TS_{F1R}}$ and $\mathbf{TS_{G1R}}$ have similar bonding between the chelating ligand and the coppers, but the asymmetrical bonding to the naphthyridine backbone is accentuated for $\mathbf{TS_{G1R}}$ (2.20 Å to N_1 and 2.14 Å to N_2 in $\mathbf{TS_{F1Me}}$ versus 2.22 and 2.05 Å for $\mathbf{TS_{G1Me}}$). In all these cases, the phenyl is only bound to Cu_1 with an average distance of 2.01 Å. The main difference between $\mathbf{TS_{F1R}}$ and $\mathbf{TS_{G1R}}$ is the coordination of the alkynyl to Cu_2. In $\mathbf{TS_{F1R}}$, it coordinates in a σ mode via C_2 (1.96 Å on average) and its $ArCF_3$ substituent bends over the phosphine (Figure VII.22a). In $\mathbf{TS_{G1R}}$,

the coordination mode is also σ (except for **TS_{G1iPr}** which has a π mode) but the substituent of the alkynyl points toward the top of the complex and does not interact with the chelating ligand (Figure VII.22b). The energy of the transition states of **TS_{F1R}** are either lower or equivalent to the one of **TS_{G1R}** (R = Me and Ph). The overall range of energy is quite narrow, from 26.2 to 29.9 kcal/mol. The lowest for each series are **TS_{F1iPr}** with 26.2 kcal/mol and **TS_{G1Ph}** 28.8 kcal/mol.

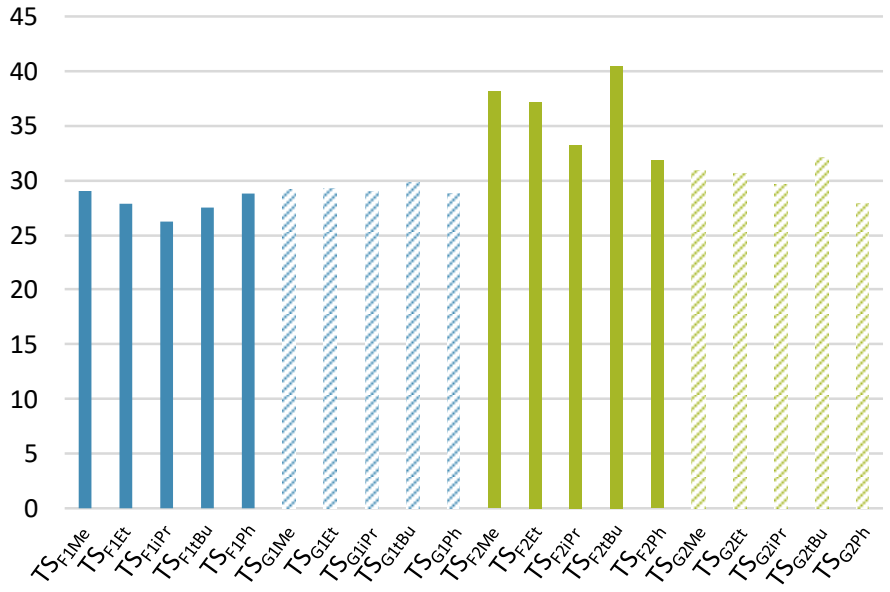

Figure VII.21. Free energy of all the transition states of the series TS_{F1Y} (plain blue), TS_{G1Y} (dashed blue), TS_{F2Y} (plain green) and TS_{G2Y} (dashed green).

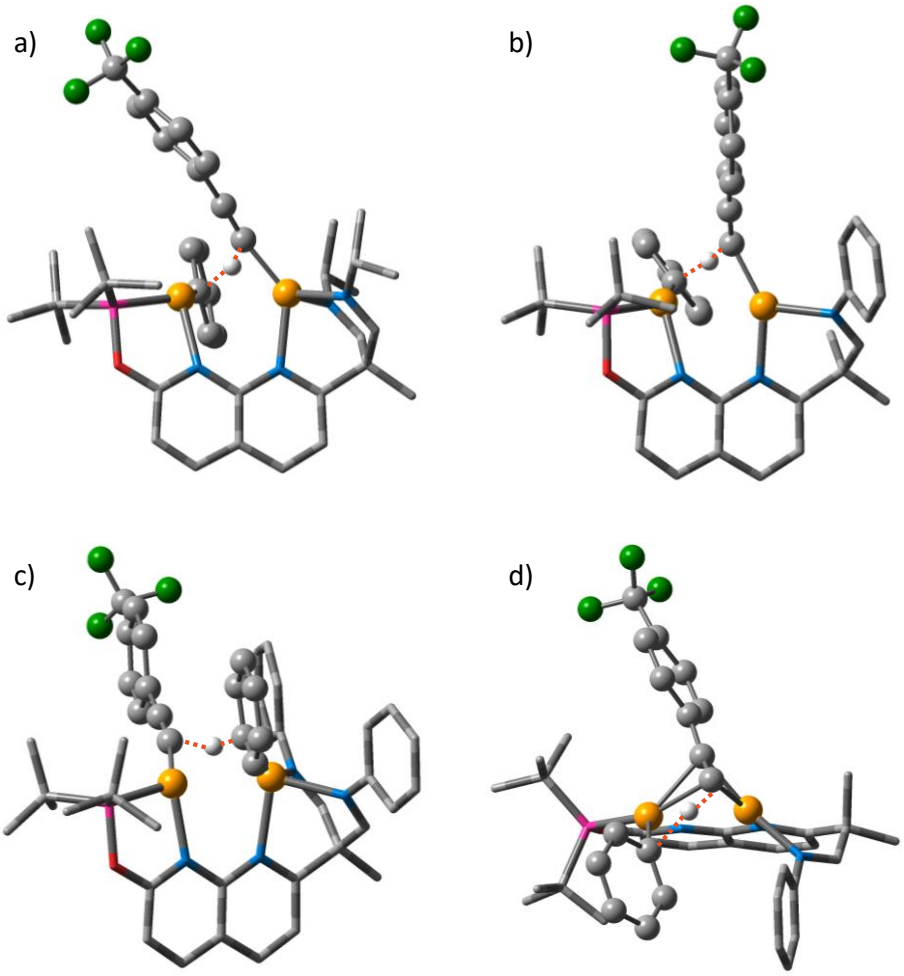

Figure VII.22. 3D representation of a) TS_{F1iPr}, b) TS_{G1Ph}, c) TS_{F2Ph} and d) TS_{G2Ph}. The red dashed lines account for the cleavage and formation of C-H bonds between the phenyl and alkynyl moieties.

The second series of transition states, **TS_{F2R}** and **TS_{G2R}**, contains a very large variety of geometries: the phenyl bridges the coppers in **TS_{F2Me}** and **TS_{F2Ph}** (Figure VII.22c) while the alkynyl is bridging them in **TS_{G2Ph}**. When there is no bridge, the phenyl coordinates on Cu_2 and the alkynyl on Cu_1 with a large variety of mode of coordination (σ or π) and of orientation of its substituent (in the cavity formed by the chelating ligand, along the naphthyridine or above the imines). Overall, the energies of these transition states are higher than

those of **TS_{F1R}** and **TS_{G1R}**, ranging from 27.9 to 40.5 kcal/mol. The lowest one is **TS_{G2Ph}**, in which the alkynyl is bridging the coppers via its π system and the phenyl is coordinated to Cu_1 and orientated above the phosphine (Figure VII.22d). To allow this geometry, Cu_1 dissociates from the naphthyridine (3.03 Å).

From these four series, **TS_{F1R}**, **TS_{F2R}**, **TS_{G1R}** and **TS_{G2R}**, twenty transition states were computed and analysed to search for correlation between properties and their energy. The properties chosen include the general parameters described in the section VII.2 plus the following:

- Natural charge of the N_3
- Natural charge of the N_4
- Angle between N_3-Cu_2-N_4
- Distance between N_3 and Cu_2
- Distance between N_4 and Cu_2

In the Figures VII.23 and in the additional *Descriptors file* (see annexes), are scattered plots of the descriptors analysis of the **TS_{F1R}**, **TS_{F2R}**, **TS_{G1R}** and **TS_{G2R}** series (in blue, green, orange and red, respectively). Only one descriptors, the distance between Cu and C_2, yields a significant correlation (Figure VII.23). The energy of the transition states are lower when the alkyne coordinates strongly to the copper, *i.e.* when the alkyne is well activated. The three other descriptors that show moderate correlation are the distances C_1-H and C_2-H and the angle N_3-Cu_2-N_4. The two distances are complementary as the energy of the transition states are lower when the transferred proton is closer to the alkynyl (with a moderately activated C_2-H around 1.20 Å) than to the phenyl (best around 2.00 Å). This is consistent with most of the transition states described in this thesis: the energy is lower when the geometry is closer to reactants than to products. The angle N_3-Cu_2-N_4 seems to show a correlation between a larger angle, *i.e.* distortion to create space around the active site, and the transition states with lower energies. However, the energy span is quite broad over all the angles and thus no strong conclusion can be made.

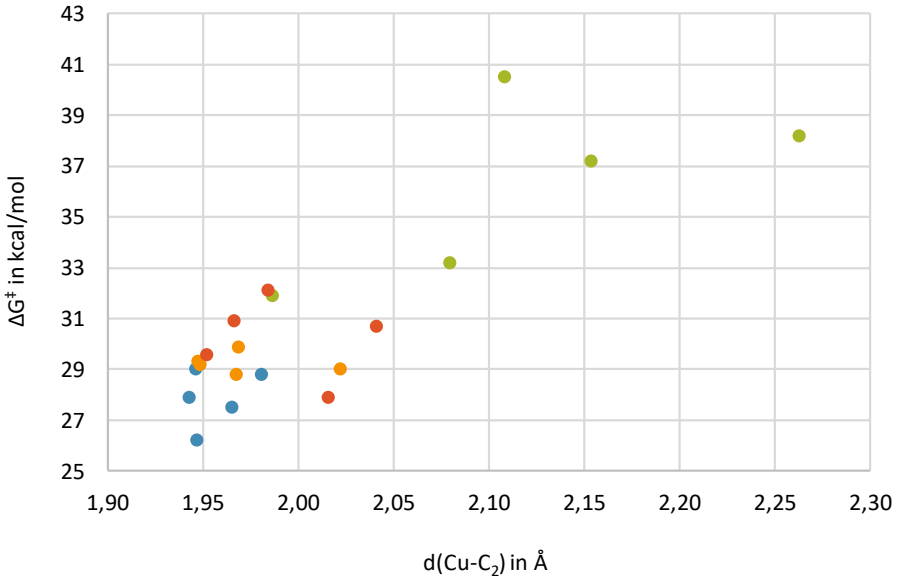

Figure VII.23. Energy of the transition states as function of the distance between Cu and C_2, R^2 = 0.6961. No point has been removed.

c) Replacement of the pyridines by amines

The last modification of DPEOPN reported in this chapter is the replacement of the two pyridines by amines (Figure VII.24). As for the imine, the number of atoms between the naphthyridine backbone and the coordinating nitrogens is kept constant relative to DPEOPN. The amine is functionalized with five groups: Me, Et, ^{i}Pr, ^{t}Bu and Ph. As for the imine modification, this arm of the ligand can have one or two amines, leading to the complexes $\mathbf{HX_R}$ and $\mathbf{IX_R}$, respectively (with **X** = $\mathbf{1}^+$ or $\mathbf{2}^+$ and R = Me, Et, ^{i}Pr, ^{t}Bu, Ph).

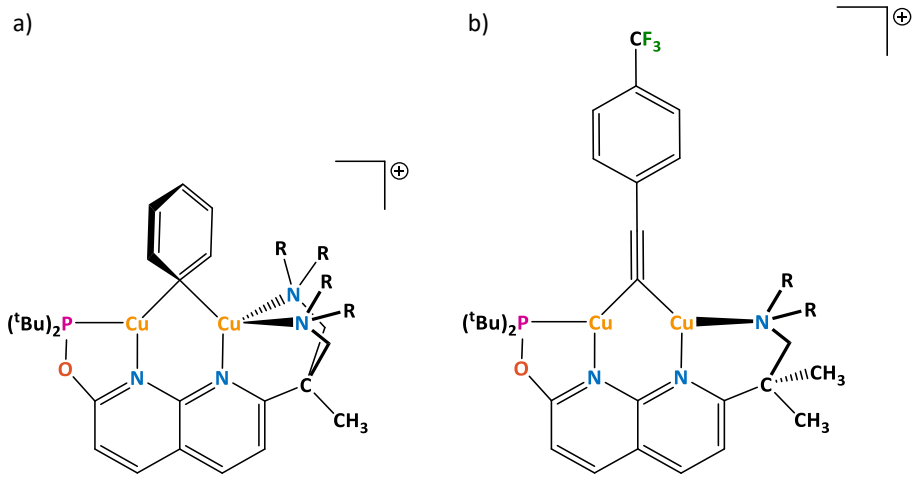

Figure VII.24. Reactant and products of the C-H activation of alkyne via a dicopper complex; a) $H1^{+}_{R}$ and b) $I2^{+}_{R}$ with R = Me, Et, ^{i}Pr, ^{t}Bu and Ph.

$\mathbf{H1^{+}_{R}}$ and $\mathbf{I1^{+}_{R}}$ complexes are relatively similar: the Cu_1-Cu_2 distance is ranging in between 2.35 and 2.42 Å, the Cu_1-P distance has the same value measured in most systems (2.25 Å), the naphthyridine backbone is asymmetrically coordinated to the coppers in most cases (except $\mathbf{H1^{+}_{Me}}$ and $\mathbf{H1^{+}_{Et}}$), with a maximum difference in bond distances of 0.2 Å. The phenyl is bridging the coppers symmetrically in all complexes, with a bond distance of 2.02 Å. The main difference among these complexes is the coordination of the amine(s) to Cu_2. In the $\mathbf{H1^{+}_{R}}$ series, only the two smallest substituents (Me and Et) allow for the coordination of both amines. When the size of the substituent increases, one of the amines dissociates to ease the steric hindrance between their substituents (Figure VII.25a). The amine in the $\mathbf{I1^{+}_{R}}$ complexes is always coordinated to Cu_2 (Figure VII.25b) as there is less hindrance with the rest of the chelating ligand. In most complexes, the R substituents of the amine interact with the phenyl as there are close to each other (around to 2.50 Å in $\mathbf{H1^{+}_{tBu}}$).

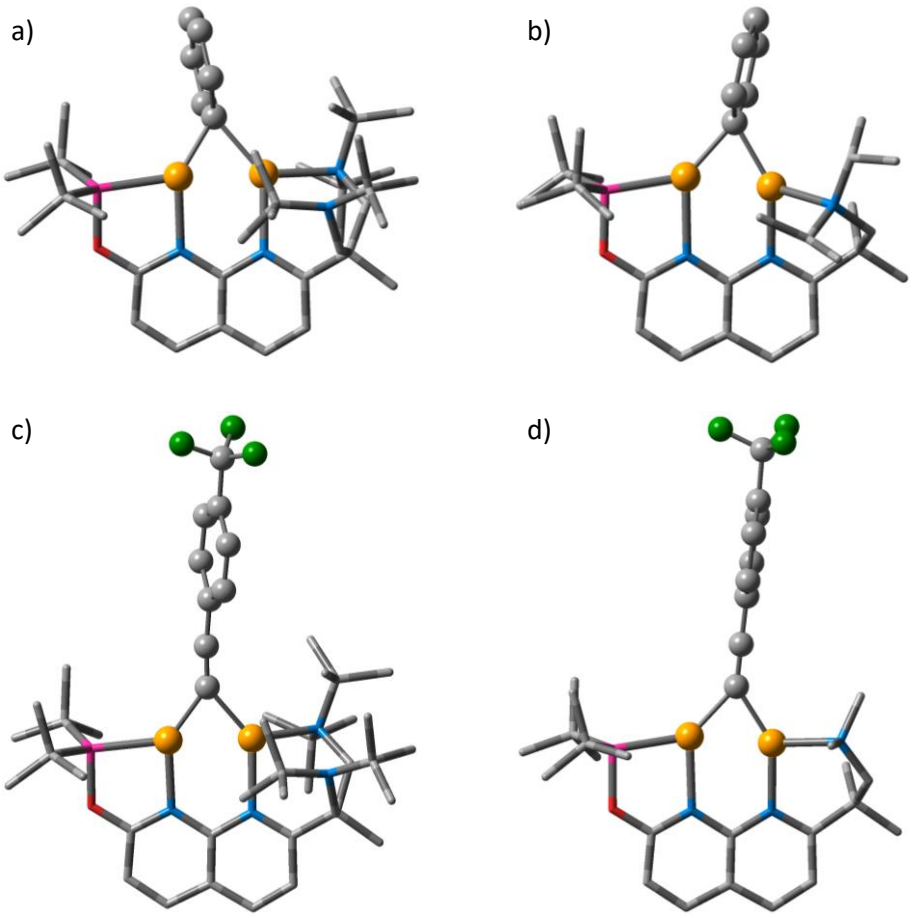

Figure VII.25. 3D representation of a) $H1^{+}_{tBu}$, b) $I1^{+}_{iPr}$ c) $H2^{+}_{tBu}$ and d) $I2^{+}_{Me}$.

The features observed for the phenyl bridging complexes are also mostly valid for the alkynyl series $\mathbf{H2^{+}_{R}}$ and $\mathbf{I2^{+}_{R}}$. The main difference between them is also how the amines coordinate to Cu_2. For the ligands with two amines, only $\mathbf{H2^{+}_{Me}}$ and $\mathbf{H2^{+}_{Et}}$ show an even coordination of the amines to Cu_2 (2.15 and 2.20 Å, respectively). The bond of Cu_2 with one of the amine is elongated for R = ^{i}Pr and Ph (2.36 and 2.32 Å) but not completely broken. There is a clear dissociation (3.79 Å) of one of the amines only for $\mathbf{H2^{+}_{tBu}}$, which has the bulkiest R substituent (Figure VII.25c). This difference is likely due to the size of the bridging ligand: the alkynyl do not create much steric hindrance compared to the phenyl, as the bulk of its substituent is placed far from the

bimetallic core. In the $\mathbf{I2^+_R}$ complexes, the amine is always fully coordinated to Cu_2 (Figure VII.25d).

The proton transfer connecting $\mathbf{H1^+_R}$ and $\mathbf{I1^+_R}$ to $\mathbf{H2^+_R}$ and $\mathbf{I2^+_R}$, can proceed via two distinct transition states, depending on whether the alkyne arrives on the complex from the pyridine side ($\mathbf{TS_{H1R}}$/$\mathbf{TS_{I1R}}$) or from the phosphine side ($\mathbf{TS_{H2R}}$/$\mathbf{TS_{I2R}}$). The $\mathbf{TS_{H1R}}$ series, can be split in two depending on the size of the amine. For the two smaller ones, with R = Me and Et, the chelating ligand is fully coordinated to the coppers, with an asymmetry for the naphthyridine backbone (2.21 and 2.08 Å for N_1-Cu_1 and N_2-Cu_2 in $\mathbf{TS_{H1Et}}$, respectively). The phenyl is bound to Cu_1 at 2.03 Å and points toward the outside of the active site. The alkynyl coordinates to Cu_2 in σ mode (1.92 Å) and bends over the phosphine (Figure VII.26a). The transferred proton is closer to the alkynyl than the phenyl (1.30 versus 1.79 Å on average). The energy of these two transition states are 29.0 and 31.7 kcal/mol for $\mathbf{TS_{H1Me}}$ and $\mathbf{TS_{H1Et}}$, respectively. The remaining three $\mathbf{TS_{H1R}}$ (R = ^{i}Pr, ^{t}Bu and Ph) share common features: one of the amines is dissociated from Cu_2, as in the intermediates $\mathbf{H1^+_R}$, due to their bulky substituents. The alkynyl coordinates to Cu_2 in σ mode but its $ArCF_3$ substituent is between the phosphine and the amine (Figure VII.26b). In both $\mathbf{TS_{H1tBu}}$ and $\mathbf{TS_{H1Ph}}$, the bond between the naphthyridine backbone and Cu_1 is broken, with distances of 2.58 and 2.96 Å, respectively. The energy of these three transition states are 27.0, 27.7 and 29.5 kcal/mol for $\mathbf{TS_{H1iPr}}$, $\mathbf{TS_{H1tBu}}$ and $\mathbf{TS_{H1Ph}}$ (Figure VII.27), respectively.

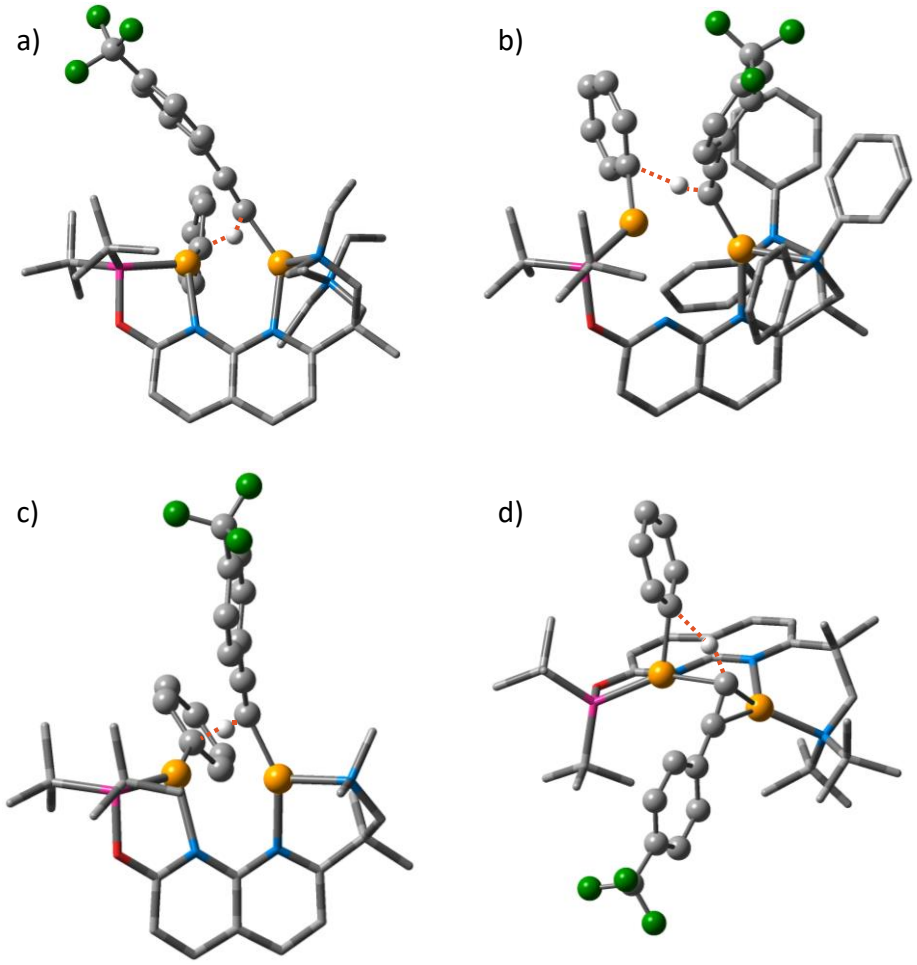

Figure VII.26. 3D representation of a) TS_{H1Et}, b) TS_{H1Ph}, c) TS_{I1Me} and d) TS_{I1tBu}. The red dashed lines account for the cleavage and formation of C-H bonds between the phenyl and alkynyl moieties.

The geometry of the transition states in the TS_{I1R} series differs: TS_{I1Me}, TS_{I1Et} and TS_{I1iPr} have a geometry similar to TS_{H1Me}, in which only the orientation of the alkynyl differs as its do not bend over the phosphine (Figure VII.26c). They all have similar energy, with 28.5, 28.4 and 28.1 kcal/mol for TS_{I1Me}, TS_{I1Et} and TS_{I1iPr}, respectively. TS_{I1tBu} is the lowest transition state of all the tried modifications of DPEOPN with an energy of 19.3 kcal/mol. In this transition state the chelating ligand and the phenyl are both coordinated as in TS_{I1Me} and

the only change is the coordination of the alkynyl. It is bonded to Cu_2 via its π system (2.02 and 2.22 Å to C_2 and C_3) and it is also coordinated to Cu_1 via C_2 (2.18 Å), bridging the two coppers. The $ArCF_3$ substituent of the alkynyl is between the amine and the phosphine (Figure VII.26d). In **TS_{I1Ph}**, the amine has dissociated from Cu_2 (3.55 Å) so the alkynyl can coordinate via its π system instead and its substituent is above the amine. This transition state is the highest of the **TS_{I1R}** series with 29.4 kcal/mol.

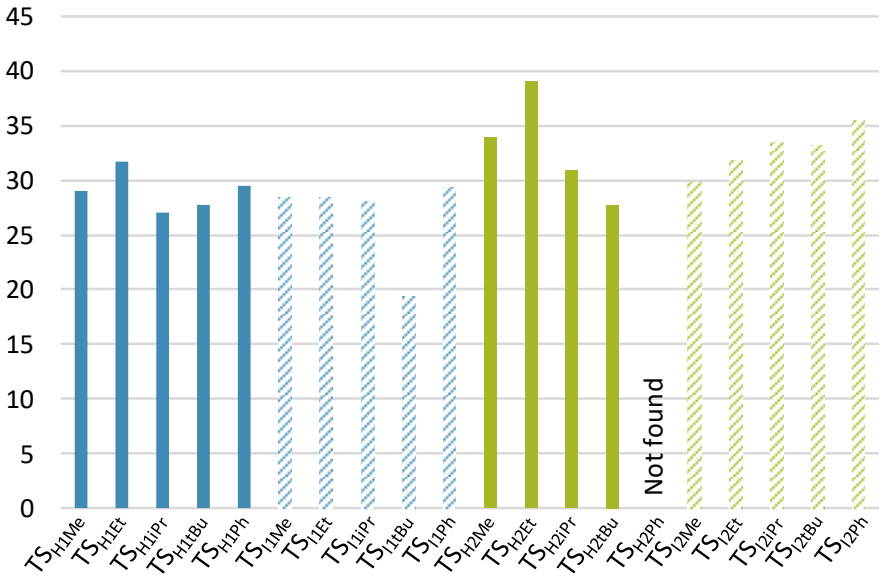

Figure VII.27. Free energy of all the transition states of the series TS_{H1Y} (plain blue), TS_{I1Y} (dashed blue), TS_{H2Y} (plain green) and TS_{I2Y} (dashed green).

The transition state based on **TS_2** also displays a large variety of geometries. For the **TS_{H2R}** series, only four transition states were obtained as **TS_{H2Ph}** did not converge. Out of these four, the chelating ligand is fully coordinated to the coppers only in **TS_{H2Me}**. In **TS_{H2Et}**, Cu_1 dissociate from the naphthyridine backbone to allow the alkynyl to coordinate via its π system (2.13 and 2.25 Å for C_2 and C_3) while its $ArCF_3$ substituent is above the phosphine (Figure VII.28a). As often in this type of transition states, the proton is equidistant from the alkynyl and the phenyl, with 1.41 and 1.47 Å, respectively. The energy of **TS_{H2Et}** is particularly high with 39.0 kcal/mol. In **TS_{H2iPr}** and **TS_{H2tBu}**,

one of the amines has to dissociate due to its bulk (Figure VII.28b), as for the intermediates **H1$^{+}_{R}$**. In these two transition states and in **TS$_{H2Me}$**, the alkynyl coordinates to Cu_1 in a σ mode (2.00 Å on average) and its substituent does not interact with any other part of the complex. The transferred proton is closer to the alkynyl than to the phenyl (1.26 and 1.66 Å in **TS$_{H2tBu}$**). The energy of these is lower, ranging from 27.8 to 33.9 kcal/mol, with the energy lowering with the increased size of the R substituents of the amine.

The **TS$_{I2R}$** series has more homogeneous characteristics, with energies ranging from 29.9 to 35.4 kcal/mol. **TS$_{I2Ph}$** has the highest energy while **TS$_{I2Me}$** has the lowest and is the only one described here. The chelating ligand is fully coordinated to the coppers with a slight asymmetry in the coordination of the naphthyridine (2.14 and 2.05 Å for N_1 and N_2, respectively) while the amine is bound to Cu_2 at 2.18 Å, yielding to a short distance between the coppers of 2.75 Å. The alkynyl is bound to Cu_1 at 1.97 Å in σ mode and there is no close interaction between its substituent and the rest of the complex. The phenyl coordinates to Cu_2 on the same side as the amine at 1.96 Å. The proton is again closer to the alkynyl (1.31 Å) than to the phenyl (1.73 Å). The series **TS$_{H2R}$** and **TS$_{I2R}$**, involving the second isomer of the transition states for the amine modification of DPEOPN lead to transition states higher in energy than the series for the first isomer (**TS$_{H1R}$** and **TS$_{I1R}$**), with 27.0 kcal/mol for **TS$_{H1iPr}$** and 19.3 kcal/mol for **TS$_{I1tBu}$**.

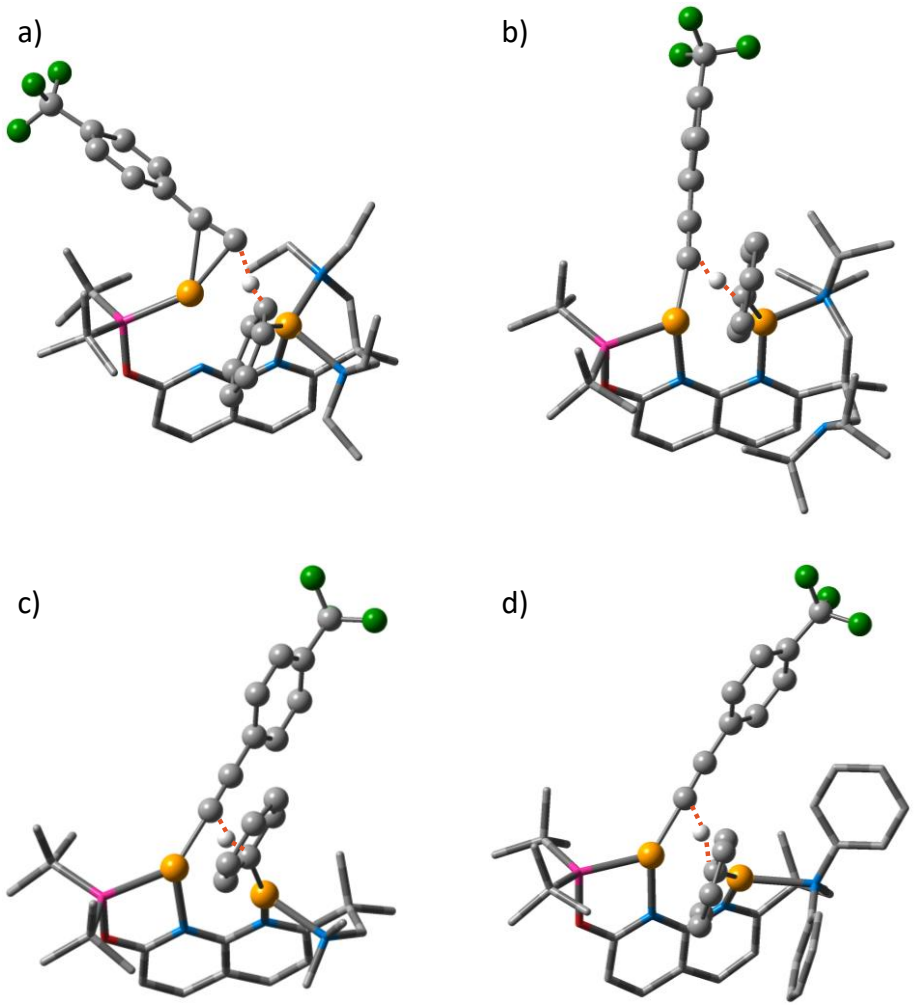

Figure VII.28. 3D representation of a) TS_{H2Et}, b) TS_{H2iPr}, c) TS_{I2Me} and d) TS_{I2Ph}. The red dashed lines account for the cleavage and formation of C-H bonds between the phenyl and alkynyl moieties.

Nineteen transition states were computed for the replacement of the pyridine by amines in DPEOPN. They were analysed to search for correlation between properties and their energy. The properties chosen include the general parameters described in the section VII.2 plus the following:

- Natural charge of the N_3
- Natural charge of the N_4
- Angle between N_3-Cu_2-N_4
- Distance between N_3 and Cu_2
- Distance between N_4 and Cu_2

In the Figures VII.29 and VII.30 and in the additional *Descriptors file* (see annexes), are scattered plots of the descriptors analysis of the $\mathbf{TS_{H1R}}$, $\mathbf{TS_{H2R}}$, $\mathbf{TS_{I1R}}$ and $\mathbf{TS_{I2R}}$ series (in blue, green, orange and red, respectively). Two descriptors showed a moderate correlation with the energies of the transition states. The first one is the natural charge of H: the energy of the transition states decreases when the positive charge of H is higher, with the highest value around 0.32. This descriptors shows that the more the transferred hydrogen atom is "proton-like" the faster the reaction is. The distance between C_2 and H is the second descriptor with moderately good R^2 (0.5556). It shows that the shorter this distance is (down to 1.20 Å in this case), the lower the energy of the transition state will be. It seems that the lower the transition state has "reactant like" geometry. This is a common feature for low-lying transition states across the different reactions reported in this thesis.

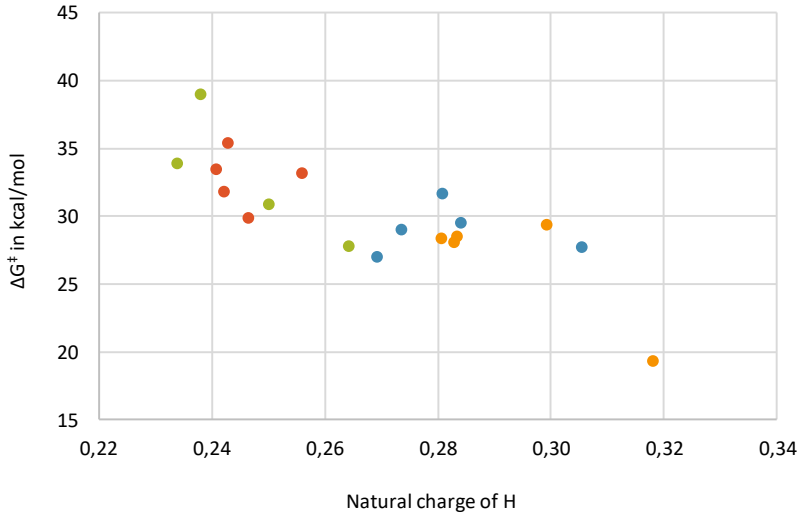

Figure VII.29. Energy of the transition states as function of the natural charge of H, R^2 = 0.6270. No point has been removed.

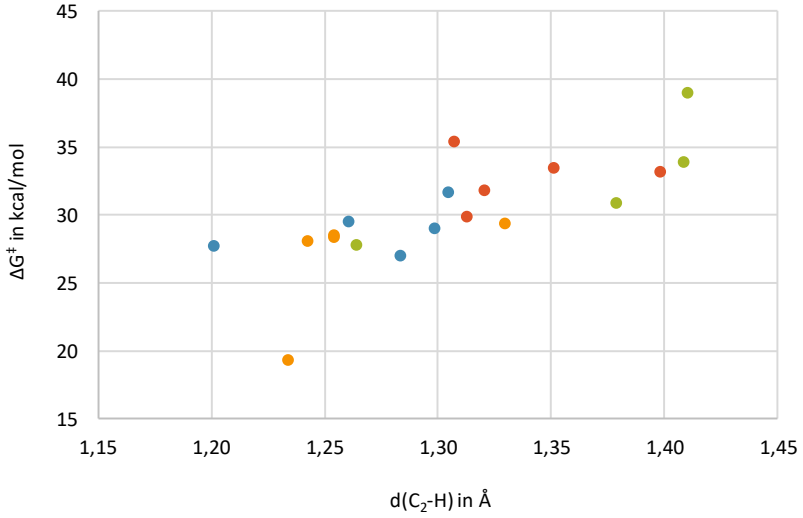

Figure VII.30. Energy of the transition states as function of the distance between C_2 and H, R^2 = 0.5556. No point has been removed.

5 - General remarks on ligand design

This chapter on the ligand design of 1,8-naphthyridine based on DPEOPN will be concluded with several remarks:

- 74 transition states were computed and their energy vary from 19.3 kcal/mol for $\mathbf{TS_{I1tBu}}$ to 40.5 kcal/mol for $\mathbf{TS_{F2tBu}}$, leading to a large overall range of 21.2 kcal/mol. However, the majority of the transition states (65) have energies within a narrower range of 11.8 kcal/mol, from 24.0 to 35.8 kcal/mol.
- 9 transitions states are lower than $\mathbf{TS_1}$: $\mathbf{TS_{A1pyr}}$, $\mathbf{TS_{B1p\text{-}Ph\text{-}NO2}}$, $\mathbf{TS_{B1Ph}}$, $\mathbf{TS_{B1p\text{-}Ph\text{-}OMe}}$, $\mathbf{TS_{C1OMe}}$, $\mathbf{TS_{D2OMe}}$, $\mathbf{TS_{F1iPr}}$, $\mathbf{TS_{H1iPr}}$ and $\mathbf{TS_{I1tBu}}$. At the exception of $\mathbf{TS_{D2OMe}}$, they all correspond to the isomer where the phenyl coordinates on Cu_1, independently of the nature and size of the different part of the chelating ligand.
- Overall, the results suggest that more donating ligands (OMe versus H and NO_2) lead to transition states with a lower energy.
- There is a balance between steric hindrance and favourable weak interaction involving the chelating ligand: the transition states are stabilized when the substituent of the chelating ligands are neither too small (R = Me, Et) nor too large (R = Cy,Ad). The balance seems to be R = iPr, Ph and tBu, where the phenyl and alkynyl can interact with the substituents without too much steric hindrance.
- This chapter should be considered as a preliminary work on ligand design based on DPEOPN for C-H activation reactions. All the reported transition states neglects two effects; the association with the counter-ion and the partial dissociation of the chelating ligand; which can impact the energy, affecting the trends observed in this chapter. The goal here were to search for possible candidate for a future study of this type of ligand, requiring more automation of transition states search and in deep statistical analysis.

VIII - Conclusions and Outlook

The main conclusions on the properties and reactivity of the dicopper DPEOPN complexes are:

- These complexes are labile since the DPEOPN ligand can undergo various partial dissociations. These allow the coordination sphere of the complexes to adapt to the presence of other ligands and to the approach of reactants.

- The counter-ion (NTf_2^-) of these dicopper complexes needs to be included in the computations to represent properly their reactivity.

- There is a subtle balance between steric hindrance and attractive weak interactions between the different ligands and the counter-ion.

- The $[Cu_2(\mu\text{-Ph})(DPEOPN)]^+$ complex (**1**$^+$) can activate the C-H bond of alkynes via a concerted proton transfer. This reaction can be catalyzed by water, decoupling the protonation of the phenyl and the deprotonation of the alkyne in two steps.

- The $[Cu_2(\mu\text{-Alk})(DPEOPN)]^+$ complex (**2**$^+$) catalyses the CuAAC reaction. The mechanism of this catalytic cycle differs from the same reaction done with Cu^{II} salts as catalysts. The cycloaddition reaction occurs in one concerted step, instead of two, due to the bulk of DPEOPN around the dicopper centre. The rate determining step is the protonation of the triazolyl, occurring similarly to the C-H bond activation of alkynes by **1**$^+$. In **2**$^+$**,** the flexibility of the metal core is

restricted by the bulky nature of the reactants, yielding higher energy barriers.

- The C-H activation of alkynes is favoured when the naphthyridine ligand carries donating substituents on either the aromatic rings or the chelating arms. This further opens the possibility of designing more reactive complexes.

To continue the work done on this project, several directions are possible:

- The DFT mechanisms, especially for the water catalyzed C-H activation of alkyne and the CuAAC reaction, could be refined when more experimental data becomes available.

- Due to the large amount of different geometries for each complex (partial dissociation of DPEOPN, positions of the counter-ion, approaches and coordination mode of the reactants), the calculations and the analysis of the results can highly benefit from automation measures facilitating the design of new catalysts.

- Several other naphthyridine based catalyst are available experimentally and they are efficient for cyclisation reactions and/or C-H activations. It would be interesting to compare their efficiency and reactivity to $\mathbf{1}^{+}$ and $\mathbf{2}^{+}$ on the reactions presented in this thesis.

- Since $\mathbf{2}^{+}$ catalyses the CuAAC reaction, it may also be active in similar reactions. The Kinugasa reaction is a good candidate as it requires a

Cu^{I} catalyst for the cycloaddition of an alkyne to a nitrone. This reaction leads to different diastereomers and the differentiation of the coppers in the DPEOPN complexes could be efficient at promoting selectivity.

Annexes

In addition to the annexes present in this thesis, two files contain materials related to this thesis:

- The figures of the description analysis of the transition states (Descriptors.pdf)
- The cartesian coordinates of the geometry of all the intermediates and transition states mention in this thesis (Geometries.xyz)

Both files can be found here: https://doi.org/10.5281/zenodo.5236129

A - Summary of the energy of the transitions states

1 - Chapter IV: C-H activation of alkyne with 1^+

The energy reference for these transition states are either $\mathbf{1}^+$ or $\mathbf{1_C}$ plus the alkyne, depending on the absence/presence of the counter-ion NTf_2^-.

TS	$\Delta G^‡$	TS	$\Delta G^‡$	TS	$\Delta G^‡$
$\mathbf{TS_1}$	27.1	$\mathbf{TS_{1\beta}}$	28.9	$\mathbf{TS_{2D}}$	31.8
$\mathbf{TS_{1\_THF}}$	30.2	$\mathbf{TS_{1\beta A}}$	24.2	$\mathbf{TS_{2E}}$	29.4
$\mathbf{TS_{1A}}$	33.3	$\mathbf{TS_{1\beta B}}$	28.3	$\mathbf{TS_{2\alpha}}$	30.7
$\mathbf{TS_{1B}}$	29.4	$\mathbf{TS_{1\beta C}}$	22.9	$\mathbf{TS_{2\alpha A}}$	33.1
$\mathbf{TS_{1C}}$	26.5	$\mathbf{TS_{1\beta D}}$	30.3	$\mathbf{TS_{2\alpha B}}$	33
$\mathbf{TS_{1D}}$	26.5	$\mathbf{TS_{1\beta E}}$	24.7	$\mathbf{TS_{2\alpha C}}$	30.1
$\mathbf{TS_{1E}}$	26.5	$\mathbf{TS_2}$	27.3	$\mathbf{TS_{2\alpha D}}$	33.4
$\mathbf{TS_{1\_arm}}$	39.9	$\mathbf{TS_{2A}}$	35.2	$\mathbf{TS_{2\alpha E}}$	26.7
$\mathbf{TS_{1\_armTHF}}$	36.5	$\mathbf{TS_{2B}}$	35.8	$\mathbf{TS_{2\beta}}$	35.2
$\mathbf{TS_{1\alpha}}$	34.5	$\mathbf{TS_{2C}}$	31.1		

2 - Chapter V: C-H activation of alkyne catalyzed by H_2O

The energy reference for the transition states of the step A are either $\mathbf{1}^+$ or $\mathbf{1_C}$ plus H_2O, depending on the absence/presence of the counter-ion NTf_2^-.

TS	$\Delta G^‡$	TS	$\Delta G^‡$	TS	$\Delta G^‡$
$\mathbf{TS_3}$	23.0	$\mathbf{TS_{3\beta}}$	20.7	$\mathbf{TS_{4\alpha}}$	22.1
$\mathbf{TS_{3A}}$	23.8	$\mathbf{TS_{3\beta A}}$	18.9	$\mathbf{TS_{4\alpha A}}$	23.9
$\mathbf{TS_{3B}}$	24.3	$\mathbf{TS_{3\beta B}}$	22.0	$\mathbf{TS_{4\alpha B}}$	25.1
$\mathbf{TS_{3C}}$	24.6	$\mathbf{TS_{3\beta C}}$	19.7	$\mathbf{TS_{4\alpha C}}$	20.2
$\mathbf{TS_{3D}}$	24.7	$\mathbf{TS_{3\beta D}}$	24.9	$\mathbf{TS_{4\alpha D}}$	25.5
$\mathbf{TS_{3E}}$	23.1	$\mathbf{TS_{3\beta E}}$	18.6	$\mathbf{TS_{4\alpha E}}$	23.0
$\mathbf{TS_{3\alpha}}$	23.5	$\mathbf{TS_4}$	23.6	$\mathbf{TS_{4\beta}}$	20.8
$\mathbf{TS_{3\alpha A}}$	25.9	$\mathbf{TS_{4A}}$	19.6	$\mathbf{TS_{4\beta A}}$	20.6
$\mathbf{TS_{3\alpha B}}$	24.8	$\mathbf{TS_{4B}}$	25.8	$\mathbf{TS_{4\beta B}}$	21.7
$\mathbf{TS_{3\alpha C}}$	22.0	$\mathbf{TS_{4C}}$	24.0	$\mathbf{TS_{4\beta C}}$	20.0
$\mathbf{TS_{3\alpha D}}$	24.6	$\mathbf{TS_{4D}}$	24.7	$\mathbf{TS_{4\beta D}}$	24.1
$\mathbf{TS_{3\alpha E}}$	22.1	$\mathbf{TS_{4E}}$	22.6	$\mathbf{TS_{4\beta E}}$	23.8

The energy reference for the transition states of the step B are either $\mathbf{4^{+}_{pyr}}$ or $\mathbf{4_{pyrD}}$ plus the alkyne, depending on the absence/presence of the counter-ion NTf_2^-.

TS	$\Delta G^{‡}$	TS	$\Delta G^{‡}$	TS	$\Delta G^{‡}$
$\mathbf{TS_5}$	17	$\mathbf{TS_{6A}}$	17.7	$\mathbf{TS_{6\alpha D}}$	13.8
$\mathbf{TS_{5A}}$	-	$\mathbf{TS_{6B}}$	18.7	$\mathbf{TS_{6\alpha E}}$	9.4
$\mathbf{TS_{5B}}$	20.6	$\mathbf{TS_{6C}}$	14.6	$\mathbf{TS_{6\beta}}$	7.3
$\mathbf{TS_{5C}}$	19.7	$\mathbf{TS_{6D}}$	14.7	$\mathbf{TS_{6\beta A}}$	8.8
$\mathbf{TS_{5D}}$	19.6	$\mathbf{TS_{6E}}$	16.5	$\mathbf{TS_{6\beta B}}$	9.4
$\mathbf{TS_{5E}}$	19	$\mathbf{TS_{6\alpha}}$	10	$\mathbf{TS_{6\beta C}}$	8.4
$\mathbf{TS_{5\alpha}}$	20.8	$\mathbf{TS_{6\alpha A}}$	12.2	$\mathbf{TS_{6\beta D}}$	11.1
$\mathbf{TS_{5\beta}}$	17.9	$\mathbf{TS_{6\alpha B}}$	10.2	$\mathbf{TS_{6\beta E}}$	5.3
$\mathbf{TS_6}$	14.3	$\mathbf{TS_{6\alpha C}}$	11.1		

3 - Chapter VI: CuAAC reaction with DPEOPN based catalyst

The energy reference for the transition states of the cyclisation step are either $\mathbf{5^{+}}$ or $\mathbf{5_E}$, depending on the absence/presence of the counter-ion NTf_2^-.

TS	$\Delta G^{‡}$	TS	$\Delta G^{‡}$	TS	$\Delta G^{‡}$
$\mathbf{TS_7}$	20.6	$\mathbf{TS_{7\alpha}}$	21.9	$\mathbf{TS_{7\beta}}$	20.6
$\mathbf{TS_{7A}}$	24.4	$\mathbf{TS_{7\alpha A}}$	25.5	$\mathbf{TS_{7\beta A}}$	25.2
$\mathbf{TS_{7B}}$	25.6	$\mathbf{TS_{7\alpha B}}$	26.5	$\mathbf{TS_{7\beta B}}$	23.3
$\mathbf{TS_{7C}}$	22.0	$\mathbf{TS_{7\alpha C}}$	23.5	$\mathbf{TS_{7\beta C}}$	21.9
$\mathbf{TS_{7D}}$	23.0	$\mathbf{TS_{7\alpha D}}$	27.3	$\mathbf{TS_{7\beta D}}$	23.4
$\mathbf{TS_{7E}}$	20.0	$\mathbf{TS_{7\alpha E}}$	23.5	$\mathbf{TS_{7\beta E}}$	22.2

The energy reference for the transition states of the C-H activation step are either **15**$^{+}$ or **15**$_{E}$ plus the alkyne, depending on the absence/presence of the counter-ion NTf_2^-.

TS	$\Delta G^{‡}$	TS	$\Delta G^{‡}$	TS	$\Delta G^{‡}$
TS$_{8}$	32.9	**TS$_{9α}$**	35.1	**TS$_{10β}$**	37.7
TS$_{8A}$	35.1	**TS$_{9αA}$**	37.2	**TS$_{10βA}$**	43.7
TS$_{8B}$	34.7	**TS$_{9α}$B**	37.0	**TS$_{10βB}$**	40.3
TS$_{8C}$	34.7	**TS$_{9αC}$**	34.8	**TS$_{10βC}$**	40.5
TS$_{8D}$	34.7	**TS$_{9αD}$**	37.8	**TS$_{10βD}$**	42.1
TS$_{8E}$	36.5	**TS$_{9αE}$**	34.6	**TS$_{10βE}$**	38.6
TS$_{8α}$	35.5	**TS$_{9β}$**	35.8	**TS$_{11}$**	34.7
TS$_{8αA}$	37.6	**TS$_{9βA}$**	37.7	**TS$_{11A}$**	37.6
TS$_{8αB}$	37.6	**TS$_{9βB}$**	37.9	**TS$_{11B}$**	34.9
TS$_{8αC}$	34.1	**TS$_{9βC}$**	36.2	**TS$_{11C}$**	35.8
TS$_{8αD}$	36.9	**TS$_{9βD}$**	36.1	**TS$_{11D}$**	35.1
TS$_{8αE}$	37.8	**TS$_{9βE}$**	39.7	**TS$_{11E}$**	33.6
TS$_{8β}$	35.5	**TS$_{10}$**	33.6	**TS$_{11α}$**	35.4
TS$_{8βA}$	36.3	**TS$_{10A}$**	33.1	**TS$_{11αA}$**	37.0
TS$_{8βB}$	38.1	**TS$_{10B}$**	37.7	**TS$_{11αB}$**	38.3
TS$_{8βC}$	28.7	**TS$_{10C}$**	35.9	**TS$_{11αC}$**	35.4
TS$_{8βD}$	35.5	**TS$_{10D}$**	35.3	**TS$_{11αD}$**	39.2
TS$_{8βE}$	38.5	**TS$_{10E}$**	34.5	**TS$_{11αE}$**	34.1
TS$_{9}$	33.0	**TS$_{10α}$**	35.0	**TS$_{11β}$**	37.9
TS$_{9A}$	35.0	**TS$_{10αA}$**	32.0	**TS$_{11βA}$**	40.5
TS$_{9B}$	33.9	**TS$_{10αB}$**	38.9	**TS$_{11βB}$**	40.4
TS$_{9C}$	30.0	**TS$_{10αC}$**	39.6	**TS$_{11βC}$**	40.6
TS$_{9D}$	33.5	**TS$_{10αD}$**	36.2	**TS$_{11βD}$**	40.3
TS$_{9E}$	36.5	**TS$_{10αE}$**	33.3	**TS$_{11βE}$**	36.6

The energy reference for these transition state are their corresponding phenyl bridging complex plus the alkyne.

TS	$\Delta G^{\ddagger}$	TS	$\Delta G^{\ddagger}$	TS	$\Delta G^{\ddagger}$
TS_{1}	27.1	TS_{G1Et}	29.3	TS_{D2NO2}	37.8
TS_{A1PR3}	31.2	TS_{G1iPr}	29.0	TS_{D2OMe}	26.6
TS_{A1Pyr}	24.0	TS_{G1tBu}	29.9	TS_{E2NO2}	29.8
TS_{A1Til}	27.6	TS_{G1Ph}	28.8	TS_{E2H}	30.3
TS_{B1Me}	28.3	TS_{H1Me}	29.0	TS_{E2OMe}	31.3
TS_{B1Et}	28.5	TS_{H1Et}	31.7	TS_{F2Me}	38.2
TS_{B1iPr}	27.3	TS_{H1iPr}	27.0	TS_{F2Et}	37.2
TS_{B1Cy}	37.7	TS_{H1tBu}	27.7	TS_{F2iPr}	33.2
TS_{B1Ad}	31.1	TS_{H1Ph}	29.5	TS_{F2tBu}	40.5
$TS_{B1PhNO2}$	26.5	TS_{I1Me}	28.5	TS_{F2Ph}	31.9
TS_{B1Ph}	26.9	TS_{I1Et}	28.4	TS_{G2Me}	30.9
$TS_{B1PhOMe}$	25.9	TS_{I1iPr}	28.1	TS_{G2Et}	30.7
TS_{C1NO2}	27.8	TS_{I1tBu}	19.3	TS_{G2iPr}	29.6
TS_{C1OMe}	26.5	TS_{I1Ph}	29.4	TS_{G2tBu}	32.1
TS_{D1NO2}	27.9	TS_{2}	27.3	TS_{G2Ph}	27.9
TS_{D1OMe}	27.1	TS_{B2Me}	35.0	TS_{H2Me}	33.9
TS_{E1NO2}	28.3	TS_{B2Et}	35.0	TS_{H2Et}	39.0
TS_{E1H}	27.8	TS_{B2iPr}	33.8	TS_{H2iPr}	30.9
TS_{E1OMe}	27.5	TS_{B2Cy}	40.0	TS_{H2tBu}	27.8
TS_{F1Me}	29.0	TS_{B2Ad}	38.4	TS_{H2Ph}	-
TS_{F1Et}	27.9	$TS_{B2PhNO2}$	34.5	TS_{I2Me}	29.9
TS_{F1iPr}	26.2	TS_{B2Ph}	34.4	TS_{I2Et}	31.8
TS_{F1tBu}	27.5	$TS_{B2PhOMe}$	33.7	TS_{I2iPr}	33.5
TS_{F1Ph}	28.8	TS_{C2NO2}	31.7	TS_{I2tBu}	33.2
TS_{G1Me}	29.2	TS_{C2OMe}	35.8	TS_{I2Ph}	35.4

Bibliography

1. Chakrabarti, P. Interaction of metal ions with carboxylic and carboxamide groups in protein structures. *Protein Eng.* **4**, 49–56 (1990).
2. Lipscomb, W. N. & Sträter, N. Recent Advances in Zinc Enzymology. *Chem. Rev.* **96**, 2375–2434 (1996).
3. Sousa, S. F., Fernandes, P. A. & Ramos, M. J. The Carboxylate Shift in Zinc Enzymes: A Computational Study. *J. Am. Chem. Soc.* **129**, 1378–1385 (2007).
4. Sträter, N., Lipscomb, W. N., Klabunde, T. & Krebs, B. Two-Metal Ion Catalysis in Enzymatic Acyl- and Phosphoryl-Transfer Reactions. *Angew. Chem. Int. Ed. Engl.* **35**, 2024–2055 (1996).
5. Dapporto, P., Ghilardi, C. A., Mealli, C., Orlandini, A. & Pacinotti, S. Low-Temperature (163 K) Structure of 1,8-Naphthyridine, C8H6N2. *Acta Crystallogr.* **40**, 891–894 (1984).
6. Evens, G. & Caluwe, P. Poly(1,8-naphthyridines) and 1,9,10-Anthyridines: Model Systems for 'Black Orlon'. *Macromolecules* **12**, 803–808 (1979).
7. Singh, P., Clearfield, A. & Bernal, I. THE CRYSTAL AND MOLECULAR STRUCTURE OF AN OCTACOORDINATED IRON(II) COMPOUND—TETRAKIS(1,8-NAPHTHYRIDINE)Fe(II) PERCHLORATE. *J. Coord. Chem.* **1**, 29–37 (1971).
8. Bodner, R. L. & Hendricker, D. G. Complexes of 1,8-naphthyridines. VII. Eight coordinate transition metal perchlorate complexes of 1,8-naphthyridine. *Inorg. Chem.* **12**, 33–37 (1973).
9. Clearfield, A., Gopal, R. & Olsen, R. W. Crystal Structure of Hexakis (1,8-naphthyridine) praseodymium (III) Perchlorate. **16**, 911–915 (1977).
10. Gatteschi, D., Mealli, C. & Sacconi, L. Synthesis and Characterization of the Mixed-Valence Copper Complex Trichlorobis (4-methyl-1,8-naphthyridine) dicopper. *Inorg. Chem.* **15**, 2774–2778 (1976).
11. Mealli, C. & Zanobini, F. X-Ray Crystal Structure of the Antiferromagnetic Binuclear Dichloro-μ-dichloro-μ-di(1,8-naphthyridine)-dicopper Complex. *J. Chem. Soc. Chem. Commun.* 97–98 (1982).
12. Tikkanen, W. R. *et al.* Synthesis, characterization, and x-ray molecular structures of mono- and dinuclear copper complexes with 2,7-bis(2-pyridyl)-1,8-naphthyridine. *Inorg. Chem.* **23**, 3633–3638 (1984).
13. Sacconi, Luigi., Mealli, Carlo. & Gatteschi, Dante. Synthesis and characterization of 1,8-Naphthyridine Complexes of 1.5-Valent Nickel. *Inorg. Chem.* **13**, 1985–1991 (1974).
14. Aghabozorg, H., Palenik, R. C. & Palenik, G. J. Synthesis and Structure of Hexaaquanickel(II)Tris(1,8-naphthyridine-2,7-dicarboxylato) dinickelate(II) Pentahydrate. *Inorg. Chem.* **24**, 4214–4216 (1985).
15. Thummel, R. P., Lefoulon, F., Williamson, D. & Chavan, M. Polyaza Cavity-Shaped Molecules. 7. Dirhodium Complexes of Triaza and Tetraaza Cavities. *Inorg. Chem.* **25**, 1675–1679 (1986).
16. Tikkanen, W. R., Binamira-Soriaga, E., Kaska, W. C. & Ford, P. C. Crescent-Shaped Dinuclear Complexes: a Dirhodium(II) Complex of the New Tetradentate Ligand 2,7-

bis(2-pyridyl)-1,8-naphthyridine (bpnp), [Rh2(bpnp)(μ-CH3CO2)3](PF6). *Inorg. Chem.* **22**, 1147–1148 (1983).

17. Baker, A. T., Tikkanen, W. R., Kaska, W. C. & Ford, P. C. Observation of both Bridging and Chelating Modes of the 2-(2-pyridyl)-1,8-naphthyridine Ligand (pynp) in a Single Dirhodium(II) Complex: X-ray Structure of [Rh2(pynp)3Cl2][PF6]2.CH3CN. *Inorg. Chem.* **23**, 3254–3256 (1984).
18. Collin, J.-P. *et al.* Synthesis and Electrochemical Characterization of Binuclear Rhodium and Ruthenium Complexes with 1,8-naphthyridine-2,7-dicarboxylate. X-ray Molecular Structure of Tris(μ-acetato)(1,8-naphthyridine-2,7-dicarboxylato) diruthenium. *Inorg. Chem.* **29**, 2238–2241 (1990).
19. Tikkanen, W. R., Binamira-Soriaga, E., Kaska, W. C. & Ford, P. C. Preparation and Spectral and Electrochemical Characterization of Dirhodium(II) Complexes with Bridging 1,8-Naphthyridine Ligands: 2,7-Bis(2-pyridyl)-1,8-naphthyridine, 5,6-Dihydrodipyrido[2,3-b:3',2'-j][1,10] phenanthroline, 2-(2-Pyridyl)-1,8 naphthyridine, and 1,8-Naphthyridine. X-ray Crystal Structure of Tris(μ-acetato)(2,7-bis(2-pyridyl)-1,8 naphthyridine) dirhodium(II) Hexafluorophosphate. *Inorg. Chem.* **23**, 141–146 (1984).
20. Balch, A. L. & Cooper, R. D. Bidentate Amines as Bridges Between M(CO)2Cl (M = Rh OR Ir) Units. *J. Organomet. Chem.* **169**, 97–105 (1979).
21. He, C., DuBois, J. L., Hedman, B., Hodgson, K. O. & Lippard, S. J. A Short Copper-Copper Distance in a (μ-1,2-Peroxo)dicopper(II) Complex Having a 1,8-Naphthyridine Unit as an Additional Bridge. *Angew. Chem.* **113**, 1532–1535 (2001).
22. He, C. & Lippard, S. J. Design and Synthesis of Multidentate Dinucleating Ligands Based on 1,8-Naphthyridine. *Tetrahedron* **56**, 8245–8252 (2000).
23. He, C. *et al.* Diiron Complexes of 1,8-Naphthyridine-Based Dinucleating Ligands as Models for Hemerythrin. *J. Am. Chem. Soc.* **122**, 12683–12690 (2000).
24. He, C. & Lippard, S. J. Modeling Carboxylate-Bridged Dinuclear Active Sites in Metalloenzymes Using a Novel Naphthyridine-Based Dinucleating Ligand. *J. Am. Chem. Soc.* **122**, 184–185 (2000).
25. He, C. & Lippard, S. J. Synthesis and Characterization of Several Dicopper (I) Complexes and a Spin-Delocalized Dicopper(I,II) Mixed-Valence Complex Using a 1,8-Naphthyridine-Based Dinucleating Ligand. *Inorg. Chem.* **39**, 5225–5231 (2000).
26. Brodsky, C. N. *et al.* Oxygen activation at a dicobalt centre of a dipyridylethane naphthyridine complex. *Dalton Trans.* **47**, 11903–11908 (2018).
27. Su, X.-J. *et al.* Electrocatalytic Water Oxidation by a Dinuclear Copper Complex in a Neutral Aqueous Solution. *Angew. Chem.* **127**, 4991–4996 (2015).
28. Jin, Q., Li, J., Ariafard, A., Canty, A. J. & O'Hair, R. A. Formation and reactions of the 1, 8-naphthyridine (napy) ligated geminally dimetallated phenyl complexes [(napy)Cu2(Ph)]+, [(napy)Ag2(Ph)]+ and [(napy)CuAg(Ph)]+. *Eur. J. Mass Spectrom.* **25**, 30–43 (2019).
29. Jin, Q., Li, J., Ariafard, A., Canty, A. J. & O'Hair, R. A. Substituent effects in the decarboxylation reactions of coordinated arylcarboxylates in dinuclear copper complexes, [(napy)Cu2(O2CC6H4X)]+. *Eur. J. Mass Spectrom.* **23**, 351–358 (2017).

30. Dutta, I., De, S., Yadav, S., Mondol, R. & Bera, J. K. Aerobic oxidative coupling of alcohols and amines towards imine formation by a dicopper(I,I) catalyst. *J. Organomet. Chem.* **849–850**, 117–124 (2017).
31. Dutta, I. *et al.* Acceptorless Dehydrogenation of Alcohols on a Diruthenium(II,II) Platform. *Organometallics* **35**, 1505–1513 (2016).
32. Saha, B., Wahidur Rahaman, S. M., Daw, P., Sengupta, G. & Bera, J. K. Metal-Ligand Cooperation on a Diruthenium Platform: Selective Imine Formation through Acceptorless Dehydrogenative Coupling of Alcohols with Amines. *Chem. - Eur. J.* **20**, 6542–6551 (2014).
33. Maity, A. K., Zeller, M. & Uyeda, C. Carbene Formation and Transfer at a Dinickel Active Site. *Organometallics* **37**, 2437–2441 (2018).
34. Powers, I. G., Andjaba, J. M., Luo, X., Mei, J. & Uyeda, C. Catalytic Azoarene Synthesis from Aryl Azides Enabled by a Dinuclear Ni Complex. *J. Am. Chem. Soc.* **140**, 4110–4118 (2018).
35. Steiman, T. J. & Uyeda, C. Reversible Substrate Activation and Catalysis at an Intact Metal− Metal Bond Using a Redox-Active Supporting Ligand. *J. Am. Chem. Soc.* **137**, 6104–6110 (2015).
36. Zhou, Y.-Y., Hartline, D. R., Steiman, T. J., Fanwick, P. E. & Uyeda, C. Dinuclear Nickel Complexes in Five States of Oxidation Using a Redox-Active Ligand. *Inorg. Chem.* **53**, 11770–11777 (2014).
37. Kwon, D.-H., Proctor, M., Mendoza, S., Uyeda, C. & Ess, D. H. Catalytic Dinuclear Nickel Spin Crossover Mechanism and Selectivity for Alkyne Cyclotrimerization. *ACS Catal.* **7**, 4796–4804 (2017).
38. Pal, S. & Uyeda, C. Evaluating the Effect of Catalyst Nuclearity in Ni-Catalyzed Alkyne Cyclotrimerizations. *J. Am. Chem. Soc.* **137**, 8042–8045 (2015).
39. Pal, S., Zhou, Y.-Y. & Uyeda, C. Catalytic Reductive Vinylidene Transfer Reactions. *J. Am. Chem. Soc.* **139**, 11686–11689 (2017).
40. Zhou, Y.-Y. & Uyeda, C. Reductive Cyclopropanations Catalyzed by Dinuclear Nickel Complexes. *Angew. Chem. Int. Ed.* **55**, 3171–3175 (2016).
41. Zhou, Y.-Y. & Uyeda, C. Catalytic reductive [4+1]-cycloadditions of vinylidenes and dienes. *Science* **363**, 857–862 (2019).
42. Hartline, D. R., Zeller, M. & Uyeda, C. Well-Defined Models for the Elusive Dinuclear Intermediates of the Pauson–Khand Reaction. *Angew. Chem. Int. Ed.* **55**, 6084–6087 (2016).
43. Behlen, M. J. & Uyeda, C. C2-Symmetric Dinickel Catalysts for Enantioselective [4+1]-Cycloadditions. *J. Am. Chem. Soc.* **142**, 17294–17300 (2020).
44. Saha, S., Kaur, M. & Bera, J. K. Fluorinated Anions Promoted “on Water” Activity of Di- and Tetranuclear Copper(I) Catalysts for Functional Triazole Synthesis. *Organometallics* **34**, 3047–3054 (2015).
45. Ziegler, M. S., Lakshmi, K. V. & Tilley, T. D. Dicopper Cu(I)Cu(I) and Cu(I)Cu(II) Complexes in Copper-Catalyzed Azide−Alkyne Cycloaddition. *J. Am. Chem. Soc.* 5378–5386 (2017).
46. Understanding C−H Bond Activation on a Diruthenium(I) Platform.pdf.

47. Sarkar, M., Doucet, H. & Bera, J. K. Room temperature C–H bond activation on a [PdI–PdI] platform. *Chem. Commun.* **49**, 9764–9766 (2013).
48. Kounalis, E., Lutz, M. & Broere, D. L. J. Cooperative H2 Activation on Dicopper(I) Facilitated by Reversible Dearomatization of an "Expanded PNNP Pincer" Ligand. *Chem. – Eur. J.* **25**, 13280–13284 (2019).
49. Kounalis, E., Lutz, M. & Broere, D. L. J. Tuning the Bonding of a μ-Mesityl Ligand on Dicopper(I) through a Proton-Responsive Expanded PNNP Pincer Ligand. *Organometallics* **39**, 585–592 (2020).
50. Ziegler, M. S., Levine, D. S., Lakshmi, K. V. & Tilley, T. D. Aryl Group Transfer from Tetraarylborato Anions to an Electrophilic Dicopper(I) Center and Mixed-Valence μ-Aryl Dicopper(I,II) Complexes. *J. Am. Chem. Soc.* **138**, 6484–6491 (2016).
51. Ziegler, M. S. *et al.* Dicopper Alkyl Complexes: Synthesis, Structure, and Unexpected Persistence. *Organometallics* **37**, 2807–2823 (2018).
52. Deolka, S. *et al.* Metal–metal cooperative bond activation by heterobimetallic alkyl, aryl, and acetylide PtIICuI complexes. *Chem. Sci.* **11**, 5494–5502 (2020).
53. Isaac, J. A. *et al.* High-valence CuIICuIII species in action: demonstration of aliphatic C–H bond activation at room temperature. *Chem. Commun.* **55**, 12711–12714 (2019).
54. Boettger, Rud. Ueber die Einwirkung des Leuchtgases auf verschiedene Salzsolutionen, insbesondere auf eine ammoniakalische Kupferchlorürlösung. *Ann. Chem. Pharm.* **109**, 351–362 (1859).
55. Chui, S. S. Y., Ng, M. F. Y. & Che, C.-M. Structure Determination of Homoleptic AuI, AgI, and CuI Aryl/Alkylethynyl Coordination Polymers by X-ray Powder Diffraction. *Chem. - Eur. J.* **11**, 1739–1749 (2005).
56. Xie, Y.-P. *et al.* Assembly of Cu(I) Alkynyl Complexes: From Cluster to Infinite Cluster-Based Framework. *Cryst. Growth Des.* **19**, 5791–5797 (2019).
57. Thompson, J. S., Bradley, A. Z., Park, K.-H., Dobbs, K. D. & Marshall, W. Copper(I) Complexes with Bis(trimethylsilyl)acetylene: Role of Ancillary Ligands in Determining π Back-Bonding Interactions. *Organometallics* **25**, 2712–2714 (2006).
58. Srebro, M. & Mitoraj, M. Role of Ancillary Ligands in a Description of Copper(I)−Bis(trimethylsilyl)acetylene bonding. A Theoretical Study. *Organometallics* **28**, 3650–3655 (2009).
59. Oguadinma, P. O. & Schaper, F. π Back-Bonding in Dibenzyl-β-diketiminato Copper Olefin Complexes. *Organometallics* **28**, 6721–6731 (2009).
60. Pernicone, N. C., Geri, J. B. & York, J. T. Examining the impact of ancillary ligand basicity on copper(I)–ethylene binding interactions: a DFT study. *Theor. Chem. Acc.* **131**, 1105 (2012).
61. Díez-González, S. Copper(I)–Acetylides: Access, Structure and Relevance in Catalysis. in *Advances in Organometallic Chemistry* vol. 66 93–141 (Elsevier, 2016).
62. Buschbeck, R., Low, P. J. & Lang, H. Homoleptic transition metal acetylides. *Coord. Chem. Rev.* **255**, 241–272 (2011).

63. Adeleke, A. F., Brown, A. P. N., Cheng, L.-J., Mosleh, K. A. M. & Cordier, C. J. Recent Advances in Catalytic Transformations Involving Copper Acetylides. *Synthesis* **49**, 790–801 (2017).
64. Lang, H., Jakob, A. & Milde, B. Copper(I) Alkyne and Alkynide Complexes. *Organometallics* **31**, 7661–7693 (2012).
65. Sakata, K. & Nishibayashi, Y. Mechanism and reactivity of catalytic propargylic substitution reactions via metal–allenylidene intermediates: a theoretical perspective. *Catal. Sci. Technol.* **8**, 12–25 (2018).
66. Glaser, C. Beiträge zur Kenntniss des Acetenylbenzols. *Berichte Dtsch. Chem. Ges.* **2**, 422–424 (1869).
67. Hay, A. S. Oxidative Coupling of Acetylenes. II. *J. Org. Chem.* **27**, 3320–3321 (1962).
68. Akhtar, R. & Zahoor, A. F. Transition metal catalyzed Glaser and Glaser-Hay coupling reactions: Scope, classical/green methodologies and synthetic applications. *Synth. Commun.* **50**, 3337–3368 (2020).
69. Jover, J., Spuhler, P., Zhao, L., McArdle, C. & Maseras, F. Toward a mechanistic understanding of oxidative homocoupling: the Glaser–Hay reaction. *Catal. Sci. Technol.* **4**, 4200–4209 (2014).
70. Vilhelmsen, M. H., Jensen, J., Tortzen, C. G. & Nielsen, M. B. The Glaser-Hay Reaction: Optimization and Scope Based on 13C NMR Kinetics Experiments. *Eur. J. Org. Chem.* **2013**, 701–711 (2013).
71. Fomina, L., Vazquez, B., Tkatchouk, E. & Fomine, S. The Glaser reaction mechanism. A DFT study. *Tetrahedron* **58**, 6741–6747 (2002).
72. Seavill, P. W., Holt, K. B. & Wilden, J. D. Investigations into the mechanism of copper-mediated Glaser–Hay couplings using electrochemical techniques. *Faraday Discuss.* **220**, 269–281 (2019).
73. Lampkowski, J. S., Villa, J. K., Young, T. S. & Young, D. D. Development and Optimization of Glaser-Hay Bioconjugations. *Angew. Chem. Int. Ed.* **54**, 9343–9346 (2015).
74. Yin, C. *et al.* Butterfly-Like Tetranuclear Copper(I) Clusters for Efficient Alkyne Homocoupling Reactions. *Eur. J. Inorg. Chem.* **2021**, 392–397 (2021).
75. Kinugasa, M. & Hashimoto, S. The Reactions of Copper(I) Phenylacetylide with Nitrones. *J. Chem. Soc. Chem. Commun.* **8**, 466–467 (1972).
76. Stecko, S., Furman, B. & Chmielewski, M. Kinugasa reaction: an 'ugly duckling' of β-lactam chemistry. *Tetrahedron* **70**, 7817–7844 (2014).
77. Popik, O., Grzeszczyk, B., Staszewska-Krajewska, O., Furman, B. & Chmielewski, M. Synthesis of β-lactams via diastereoselective, intramolecular Kinugasa reactions. *Org. Biomol. Chem.* **18**, 2852–2860 (2020).
78. Kutaszewicz, R. *et al.* Bypassing the stereoselectivity issue: transformations of Kinugasa adducts from chiral alkynes and non-chiral acyclic nitrones. *Org. Biomol. Chem.* **17**, 6251–6268 (2019).
79. Lo, M. M.-C. & Fu, G. C. Cu(I)/Bis(azaferrocene)-Catalyzed Enantioselective Synthesis of β-Lactams via Couplings of Alkynes with Nitrones. *J. Am. Chem. Soc.* **124**, 4572–4573 (2002).

80. Darroudi, M., Sarrafi, Y. & Hamzehloueian, M. Theoretical exploration of mechanism of carbapenam formation in catalytic Kinugasa reaction. *Tetrahedron* **73**, 1673–1681 (2017).
81. Santoro, S., Liao, R.-Z., Marcelli, T., Hammar, P. & Himo, F. Theoretical Study of Mechanism and Stereoselectivity of Catalytic Kinugasa Reaction. *J. Org. Chem.* **80**, 2649–2660 (2015).
82. Malig, T. C., Yu, D. & Hein, J. E. A Revised Mechanism for the Kinugasa Reaction. *J. Am. Chem. Soc.* **140**, 9167–9173 (2018).
83. Michael, A. Ueber die Einwirkung von Diazobenzolimid auf Acetylendicarbonsäuremethylester. *J. Für Prakt. Chem.* **48**, 94–95 (1893).
84. Huisgen, R. 1,3-Dipolar Cycloadditions by Rolf Huisgen. *Proc. Chem. Soc.* 357–396 (1961).
85. Huisgen, R. Concerted nature of 1,3-dipolar cycloadditions and the question of diradical intermediates. *J. Org. Chem.* **41**, 403–419 (1976).
86. Huisgen, R. 1,3-Dipolar Cycloadditions. Past and Future. *Angew. Chem. Int. Ed.* **2**, 565–598 (1963).
87. Huisgen, R. Kinetics and Mechanism of 1,3-Dipolar Cycloadditions. *Angew. Chem. Int. Ed.* **2**, 633–645 (1963).
88. Huisgen, R. Kinetics and reaction mechanisms: selected examples from the experience of forty years. *Pure Appl. Chem.* **61**, 613–628 (1989).
89. Singh, M. S., Chowdhury, S. & Koley, S. Progress in 1,3-dipolar cycloadditions in the recent decade: an update to strategic development towards the arsenal of organic synthesis. *Tetrahedron* **72**, 1603–1644 (2016).
90. Breugst, M. & Reissig, H. The Huisgen Reaction: Milestones of the 1,3-Dipolar Cycloaddition. *Angew. Chem. Int. Ed.* **59**, 12293–12307 (2020).
91. Polansky, O. E. & Schuster, P. CALCULATION Of TRANSITION STATE ENERGIES BY MEANS OF SIMPIE QUANTUM MECHANICAL LC-METHODS (Transition State Energies of 1,3 Dipolar Additions). *Tetrahedron Lett.* **30**, 2019–2022 (1964).
92. Vilhena, F. S., Bickelhaupt, F. M. & Carneiro, J. W. M. Regio- and Stereoselectivity in 1,3-Dipolar Cycloadditions: Activation Strain Analyses for Reactions of Hydrazoic Acid with Substituted Alkenes. *Eur. J. Org. Chem.* **2017**, 4313–4318 (2017).
93. Breugst, M., Huisgen, R. & Reissig, H.-U. Regioselective 1,3-Dipolar Cycloadditions of Diazoalkanes with Heteroatom-Substituted Alkynes: Theory and Experiment. *Eur. J. Org. Chem.* **2018**, 2477–2485 (2018).
94. Tornøe, C. W., Christensen, C. & Meldal, M. Peptidotriazoles on Solid Phase: [1,2,3]-Triazoles by Regiospecific Copper(I)-Catalyzed 1,3-Dipolar Cycloadditions of Terminal Alkynes to Azides. *J. Org. Chem.* **67**, 3057–3064 (2002).
95. Rostovtsev, V. V., Green, L. G., Fokin, V. V. & Sharpless, K. B. A Stepwise Huisgen Cycloaddition Process: Copper(I)-Catalyzed Regioselective 'Ligation' of Azides and Terminal Alkynes. *Angew. Chem.* **114**, 2708–2711 (2002).
96. Haldón, E., Nicasio, M. C. & Pérez, P. J. Copper-catalysed azide–alkyne cycloadditions (CuAAC): an update. *Org. Biomol. Chem.* **13**, 9528–9550 (2015).

97. Hein, J. E. & Fokin, V. V. Copper-catalyzed azide–alkyne cycloaddition (CuAAC) and beyond: new reactivity of copper(I) acetylides. *Chem. Soc. Rev.* **39**, 1302–1315 (2010).
98. Bock, V. D., Hiemstra, H. & van Maarseveen, J. H. CuI-Catalyzed Alkyne–Azide "Click" Cycloadditions from a Mechanistic and Synthetic Perspective. *Eur. J. Org. Chem.* **2006**, 51–68 (2006).
99. Zhu, L., Brassard, C. J., Zhang, X., Guha, P. M. & Clark, R. J. On the Mechanism of Copper(I)-Catalyzed Azide-Alkyne Cycloaddition. *Chem. Rec.* **16**, 1501–1517 (2016).
100. Meldal, M. & Diness, F. Recent Fascinating Aspects of the CuAAC Click Reaction. *Trends Chem.* **2**, 569–584 (2020).
101. Díez-González, S. Well-defined copper(I) complexes for Click azide–alkyne cycloaddition reactions: one Click beyond. *Catal. Sci. Technol.* **1**, 166–178 (2011).
102. Kolb, H. C., Finn, M. G. & Sharpless, K. B. Click Chemistry: Diverse Chemical Function from a Few Good Reactions. *Angew. Chem. Int. Ed.* **40**, 2004–2021 (2001).
103. Patil, P. C. & Luzzio, F. A. Alternate pathway for the click reaction of 2-(2-azidophenyl)-4,5-diaryloxazoles. *Tetrahedron Lett.* **59**, 3458–3460 (2018).
104. Peng, H. *et al.* An unexpected copper catalyzed 'reduction' of an arylazide to amine through the formation of a nitrene intermediate. *Tetrahedron* **69**, 5079–5085 (2013).
105. Yoo, E. J. *et al.* Copper-Catalyzed Synthesis ofN-Sulfonyl-1,2,3-triazoles: Controlling Selectivity. *Angew. Chem. Int. Ed.* **46**, 1730–1733 (2007).
106. Yoo, E. J. *et al.* Mechanistic Studies on the Cu-Catalyzed Three-Component Reactions of Sulfonyl Azides, 1-Alkynes and Amines, Alcohols, or Water: Dichotomy via a Common Pathway. *J. Org. Chem.* **73**, 5520–5528 (2008).
107. Sultana, J. & Sarma, D. Ag-catalyzed azide-alkyne cycloaddition: copper free approaches for synthesis of 1,4-disubstituted 1,2,3-triazoles. *Catal. Rev.* **62**, 96–117 (2020).
108. McNulty, J., Keskar, K. & Vemula, R. The First Well-Defined Silver(I)-Complex-Catalyzed Cycloaddition of Azides onto Terminal Alkynes at Room Temperature. *Chem. - Eur. J.* **17**, 14727–14730 (2011).
109. Zhang, L. *et al.* Ruthenium-Catalyzed Cycloaddition of Alkynes and Organic Azides. *J. Am. Chem. Soc.* **127**, 15998–15999 (2005).
110. Wang, C., Ikhlef, D., Kahlal, S., Saillard, J.-Y. & Astruc, D. Metal-catalyzed azide-alkyne "click" reactions: Mechanistic overview and recent trends. *Coord. Chem. Rev.* **316**, 1–20 (2016).
111. Hong, L., Lin, W., Zhang, F., Liu, R. & Zhou, X. Ln[N(SiMe3)2]3-catalyzed cycloaddition of terminal alkynes to azides leading to 1,5-disubstituted 1,2,3-triazoles: new mechanistic features. *Chem. Commun.* **49**, 5589 (2013).
112. Ding, S., Jia, G. & Sun, J. Iridium-Catalyzed Intermolecular Azide-Alkyne Cycloaddition of Internal Thioalkynes under Mild Conditions. *Angew. Chem.* **126**, 1908–1911 (2014).
113. Boz, E. & Tüzün, N. Ş. Reaction mechanism of ruthenium-catalyzed azide–alkyne cycloaddition reaction: A DFT study. *J. Organomet. Chem.* **724**, 167–176 (2013).
114. Brotherton, W. S. *et al.* Apparent Copper(II)-Accelerated Azide−Alkyne Cycloaddition. *Org. Lett.* **11**, 4954–4957 (2009).

115. Himo, F. *et al.* Copper(I)-Catalyzed Synthesis of Azoles. DFT Study Predicts Unprecedented Reactivity and Intermediates. *J. Am. Chem. Soc.* **127**, 210–216 (2005).
116. Nolte, C., Mayer, P. & Straub, B. F. Isolation of a Copper(I) Triazolide: A "Click" Intermediate. *Angew. Chem. Int. Ed.* **46**, 2101–2103 (2007).
117. Calvo-Losada, S., Pino, M. S. & Quirante, J. J. On the regioselectivity of the mononuclear copper-catalyzed cycloaddition of azide and alkynes (CuAAC). A quantum chemical topological study. *J. Mol. Model.* **20**, 2187–2193 (2014).
118. Rodionov, V. O., Fokin, V. V. & Finn, M. G. Mechanism of the Ligand-Free CuI-Catalyzed Azide-Alkyne Cycloaddition Reaction. *Angew. Chem.* **117**, 2250–2255 (2005).
119. Straub, B. F. μ-Acetylide and μ-alkenylidene ligands in "click" triazole syntheses. *Chem. Commun.* 3868–3870 (2007).
120. Ahlquist, M. & Fokin, V. V. Enhanced Reactivity of Dinuclear Copper(I) Acetylides in Dipolar Cycloadditions. *Organometallics* **26**, 4389–4391 (2007).
121. Kamata, K., Nakagawa, Y., Yamaguchi, K. & Mizuno, N. 1,3-Dipolar Cycloaddition of Organic Azides to Alkynes by a Dicopper-Substituted Silicotungstate. *J. Am. Chem. Soc.* **130**, 15304–15310 (2008).
122. Cantillo, D. *et al.* Assessing the whole range of CuAAC mechanisms by DFT calculations—on the intermediacy of copper acetylides. *Org. Biomol. Chem.* **9**, 2952–2958 (2011).
123. Straub, B. F., Bessel, M. & Berg, R. Dicopper Catalysts for the Azide Alkyne Cycloaddition: A Mechanistic DFT Study. in *Modeling of Molecular Properties* (ed. Comba, P.) 207–214 (Wiley-VCH Verlag GmbH & Co. KGaA, 2011).
124. Calvo-Losada, S., Pino-González, M. S. & Quirante, J. J. Rationalizing the Catalytic Activity of Copper in the Cycloaddition of Azide and Alkynes (CuAAC) with the Topology of ∇2ρ(r) and ∇∇2ρ(r). *J. Phys. Chem. B* **119**, 1243–1258 (2015).
125. Özkılıç, Y. & Tüzün, N. Ş. A DFT Study on the Binuclear CuAAC Reaction: Mechanism in Light of New Experiments. *Organometallics* **35**, 2589–2599 (2016).
126. Kalvet, I. *et al.* NMR and DFT Study of the Copper(I)-Catalyzed Cycloaddition Reaction: H/D Scrambling of Alkynes and Variable Reaction Order of the Catalyst. *ChemCatChem* **8**, 1804–1808 (2016).
127. Jin, L., Tolentino, D. R., Melaimi, M. & Bertrand, G. Isolation of bis(copper) key intermediates in Cu-catalyzed azide-alkyne "click reaction". *Sci. Adv.* **1**, e1500304 (2015).
128. Buckley, B. R., Dann, S. E. & Heaney, H. Experimental Evidence for the Involvement of Dinuclear Alkynylcopper(I) Complexes in Alkyne-Azide Chemistry. *Chem. - Eur. J.* **16**, 6278–6284 (2010).
129. Kuang, G.-C. *et al.* Experimental Investigation on the Mechanism of Chelation-Assisted, Copper(II) Acetate-Accelerated Azide–Alkyne Cycloaddition. *J. Am. Chem. Soc.* **133**, 13984–14001 (2011).
130. Worrell, B. T., Malik, J. A. & Fokin, V. V. Direct Evidence of a Dinuclear Copper Intermediate in Cu(I)-Catalyzed Azide-Alkyne Cycloadditions. *Science* **340**, 457–460 (2013).

131. Makarem, A., Berg, R., Rominger, F. & Straub, B. F. A Fluxional Copper Acetylide Cluster in CuAAC Catalysis. *Angew. Chem. Int. Ed.* **54**, 7431–7435 (2015).
132. Iacobucci, C., Reale, S., Gal, J.-F. & De Angelis, F. Dinuclear Copper Intermediates in Copper(I)-Catalyzed Azide-Alkyne Cycloaddition Directly Observed by Electrospray Ionization Mass Spectrometry. *Angew. Chem. Int. Ed.* **54**, 3065–3068 (2015).
133. Iacobucci, C., Lebon, A., De Angelis, F. & Memboeuf, A. CuAAC Click Reactions in the Gas Phase: Unveiling the Reactivity of Bis-Copper Intermediates. *Chem. - Eur. J.* **22**, 18690–18694 (2016).
134. Özen, C. & Tüzün, N. Ş. Mechanism of CuAAC reaction: In acetic acid and aprotic conditions. *J. Mol. Catal. Chem.* **426**, 150–157 (2017).
135. Shao, C. *et al.* Copper(I) Acetate: A Structurally Simple but Highly Efficient Dinuclear Catalyst for Copper-Catalyzed Azide-Alkyne Cycloaddition. *Adv. Synth. Catal.* **352**, 1587–1592 (2010).
136. Jin, L., Romero, E. A., Melaimi, M. & Bertrand, G. The Janus Face of the X Ligand in the Copper-Catalyzed Azide−Alkyne Cycloaddition. *J. Am. Chem. Soc.* **137**, 15696–15698 (2015).
137. Lewis, W. G., Magallon, F. G., Fokin, V. V. & Finn, M. G. Discovery and Characterization of Catalysts for Azide−Alkyne Cycloaddition by Fluorescence Quenching. *J. Am. Chem. Soc.* **126**, 9152–9153 (2004).
138. Chan, T. R., Hilgraf, R., Sharpless, K. B. & Fokin, V. V. Polytriazoles as Copper(I)-Stabilizing Ligands in Catalysis. *Org. Lett.* **6**, 2853–2855 (2004).
139. Rodionov, V. O., Presolski, S. I., Gardinier, S., Lim, Y.-H. & Finn, M. G. Benzimidazole and Related Ligands for Cu-Catalyzed Azide−Alkyne Cycloaddition. *J. Am. Chem. Soc.* **129**, 12696–12704 (2007).
140. Rodionov, V. O., Presolski, S. I., Díaz Díaz, D., Fokin, V. V. & Finn, M. G. Ligand-Accelerated Cu-Catalyzed Azide−Alkyne Cycloaddition: A Mechanistic Report. *J. Am. Chem. Soc.* **129**, 12705–12712 (2007).
141. Presolski, S. I., Hong, V., Cho, S.-H. & Finn, M. G. Tailored Ligand Acceleration of the Cu-Catalyzed Azide−Alkyne Cycloaddition Reaction: Practical and Mechanistic Implications. *J. Am. Chem. Soc.* **132**, 14570–14576 (2010).
142. Díez-González, S., Correa, A., Cavallo, L. & Nolan, S. P. (NHC)Copper(I)-Catalyzed [3+2] Cycloaddition of Azides and Mono- or Disubstituted Alkynes. *Chem. - Eur. J.* **12**, 7558–7564 (2006).
143. Díez-González, S. & Nolan, S. P. [(NHC)2Cu]X Complexes as Efficient Catalysts for Azide-Alkyne Click Chemistry at Low Catalyst Loadings. *Angew. Chem.* **120**, 9013–9016 (2008).
144. Berg, R. *et al.* Highly Active Dinuclear Copper Catalysts for Homogeneous Azide-Alkyne Cycloadditions. *Adv. Synth. Catal.* **354**, 3445–3450 (2012).
145. Gonda, Z. & Novák, Z. Highly active copper-catalysts for azide-alkynecycloaddition. *Dalton Trans.* **39**, 726–729 (2010).
146. Wang, F., Fu, H., Jiang, Y. & Zhao, Y. Quick and highly efficient copper-catalyzed cycloaddition of aliphatic and aryl azides with terminal alkynes “on water”. *Green Chem.* **10**, 452–456 (2008).

147. de Boer, S. Y., Gloaguen, Y., Lutz, M. & van der Vlugt, J. I. CuI click catalysis with cooperative noninnocent pyridylphosphine ligands. *Inorganica Chim. Acta* **380**, 336–342 (2012).
148. Davenport, T. C. & Tilley, T. D. Dinucleating Naphthyridine-Based Ligand for Assembly of Bridged Dicopper(I) Centers: Three-Center Two-Electron Bonding Involving an Acetonitrile Donor. *Angew. Chem.* **123**, 12413–12416 (2011).
149. Davenport, T. C. & Tilley, T. D. Dinuclear first-row transition metal complexes with a naphthyridine-based dinucleating ligand. *Dalton Trans.* **44**, 12244–12255 (2015).
150. Davenport, T. C., Ahn, H. S., Ziegler, M. S. & Tilley, T. D. A molecular structural analog of proposed dinuclear active sites in cobalt-based water oxidation catalysts. *Chem. Commun.* **50**, 6326–6329 (2014).
151. Nicolay, A. *et al.* Isomerism and dynamic behavior of bridging phosphaalkynes bound to a dicopper complex. *Chem. Sci.* **11**, 1607–1616 (2020).
152. Nicolay, A. & Tilley, T. D. Selective Synthesis of a Series of Isostructural MIICuI Heterobimetallic Complexes Spontaneously Assembled by an Unsymmetrical Naphthyridine-Based Ligand. *Chem. – Eur. J.* **24**, 10329–10333 (2018).
153. Nicolay, A. *et al.* Unsymmetrical Naphthyridine-Based Dicopper(I) Complexes - Synthesis, Stability, and Carbon−Hydrogen Bond Activations. *Organometallics* **40**, 1866–1873 (2021).
154. Koch, W. & Holthausen, M. C. *A Chemist's Guide to Density Functional Theory*. (Wiley, 2001).
155. Cramer, C. J. *Essentials of computational chemistry: theories and models*. (Wiley, 2004).
156. Jensen, F. *Introduction to computational chemistry*. (John Wiley & Sons, 2007).
157. Tomasi, J., Mennucci, B. & Cammi, R. Quantum Mechanical Continuum Solvation Models. *Chem. Rev.* **105**, 2999–3094 (2005).
158. Filot, I. A. W. *Introduction to microkinetic modeling.pdf*. (Eindhoven, 2018).
159. Besora, M. & Maseras, F. Microkinetic modeling in homogeneous catalysis. *WIREs Comput. Mol. Sci.* **8**, e1372 (2018).
160. Miehlich, B., Savin, A., Stoll, H. & Preuss, H. Results obtained with the correlation energy density functionals of becke and Lee, Yang and Parr. *Chem. Phys. Lett.* **157**, 200–206 (1989).
161. Becke, A. D. Density-functional thermochemistry. III. The role of exact exchange. *J. Chem. Phys.* **98**, 5648–5652 (1993).
162. Boese, A. D. & Martin, J. M. L. Development of density functionals for thermochemical kinetics. *J. Chem. Phys.* **121**, 3405–3416 (2004).
163. Yanai, T., Tew, D. P. & Handy, N. C. A new hybrid exchange–correlation functional using the Coulomb-attenuating method (CAM-B3LYP). *Chem. Phys. Lett.* **393**, 51–57 (2004).
164. Zhao, Y. & Truhlar, D. G. The M06 suite of density functionals for main group thermochemistry, thermochemical kinetics, noncovalent interactions, excited states, and transition elements: two new functionals and systematic testing of four M06-class functionals and 12 other functionals. *Theor. Chem. Acc.* **120**, 215–241 (2008).

165. Yu, H. S., He, X., Li, S. L. & Truhlar, D. G. MN15: A Kohn–Sham global-hybrid exchange–correlation density functional with broad accuracy for multi-reference and single-reference systems and noncovalent interactions. *Chem. Sci.* **7**, 5032–5051 (2016).
166. Adamo, C. & Barone, V. Toward reliable density functional methods without adjustable parameters: The PBE0 model. *J. Chem. Phys.* **110**, 6158–6170 (1999).
167. Tao, J., Perdew, J. P., Staroverov, V. N. & Scuseria, G. E. Climbing the Density Functional Ladder: Nonempirical Meta–Generalized Gradient Approximation Designed for Molecules and Solids. *Phys. Rev. Lett.* **91**, 146401 (2003).
168. Staroverov, V. N., Scuseria, G. E., Tao, J. & Perdew, J. P. Comparative assessment of a new nonempirical density functional: Molecules and hydrogen-bonded complexes. *J. Chem. Phys.* **119**, 12129 (2003).
169. Grimme, S., Antony, J., Ehrlich, S. & Krieg, H. A consistent and accurate *ab initio* parametrization of density functional dispersion correction (DFT-D) for the 94 elements H-Pu. *J. Chem. Phys.* **132**, 154104 (2010).
170. Frisch, M. J. *et al. Gaussian 16*. (Gaussian, Inc., 2016).
171. Weigend, F. & Ahlrichs, R. Balanced basis sets of split valence, triple zeta valence and quadruple zeta valence quality for H to Rn: Design and assessment of accuracy. *Phys. Chem. Chem. Phys.* **7**, 3297–3305 (2005).
172. Cossi, M., Rega, N., Scalmani, G. & Barone, V. Energies, structures, and electronic properties of molecules in solution with the C-PCM solvation model. *J. Comput. Chem.* **24**, 669–681 (2003).
173. Barone, V. & Cossi, M. Quantum Calculation of Molecular Energies and Energy Gradients in Solution by a Conductor Solvent Model. *J. Phys. Chem. A* **102**, 1995–2001 (1998).
174. Glendening, E. D. *et al. NBO 7.0.* (Theoretical Chemistry Institute, University of Wisconsin, 2018).
175. Hoops, S. *et al.* COPASI--a COmplex PAthway SImulator. *Bioinformatics* **22**, 3067–3074 (2006).
176. Ben El Ayouchia, H., Bahsis, L., Anane, H., Domingo, L. R. & Stiriba, S.-E. Understanding the mechanism and regioselectivity of the copper(I) catalyzed [3 + 2] cycloaddition reaction between azide and alkyne: a systematic DFT study. *RSC Adv.* **8**, 7670–7678 (2018).
177. Calvo-Losada, S. & Quirante, J. J. Exploring the regioselectivity in the cycloaddition of azides to alkynes catalyzed by dinuclear copper clusters (Cu2AAC reaction) using the topologies of ∇2ρ(r) and ∇∇2ρ(r). *J. Mol. Model.* **23**, 337 (2017).